Carbonate-Ceramic Dual-Phase Membranes for High Temperature Carbon Dioxide Separation

by

Matthew Anderson

A Dissertation Presented in Partial Fulfillment
of the Requirements for the Degree
Doctor of Philosophy

Approved April 2011 by the
Graduate Supervisory Committee:

Jerry Lin, Chair
Terry Alford
Kaushal Rege
James Anderson
Daniel Rivera

ARIZONA STATE UNIVERSITY

May 2011

ABSTRACT

Emission of CO_2 into the atmosphere has become an increasingly concerning issue as we progress into the 21st century Flue gas from coal-burning power plants accounts for 40% of all carbon dioxide emissions. The key to successful separation and sequestration is to separate CO_2 directly from flue gas (10-15% CO_2, 70% N_2), which can range from a few hundred to as high as 1000°C. Conventional microporous membranes (carbons/silicas/zeolites) are capable of separating CO_2 from N_2 at low temperatures, but cannot achieve separation above 200°C.

To overcome the limitations of microporous membranes, a novel ceramic-carbonate dual-phase membrane for high temperature CO_2 separation was proposed. The membrane was synthesized from porous $La_{0.6}Sr_{0.4}Co_{0.8}Fe_{0.2}O_{3-\delta}$ (LSCF) supports and infiltrated with molten carbonate ($Li_2CO_3/Na_2CO_3/K_2CO_3$). The CO_2 permeation mechanism involves a reaction between CO_2 (gas phase) and $O^=$ (solid phase) to form $CO_3^=$, which is then transported through the molten carbonate (liquid phase) to achieve separation.

The effects of membrane thickness, temperature and CO_2 partial pressure were studied. Decreasing thickness from 3.0 to 0.375 mm led to higher fluxes at 900°C, ranging from 0.186 to 0.322 $mL \cdot min^{-1} \cdot cm^{-2}$ respectively. CO_2 flux increased with temperature from 700 to 900°C. Activation energy for permeation was similar to that for oxygen ion conduction in LSCF. For partial pressures above 0.05 atm, the membrane exhibited a nearly constant flux. From these

observations, it was determined that oxygen ion conductivity limits CO_2 permeation and that the equilibrium oxygen vacancy concentration in LSCF is dependent on the partial pressure of CO_2 in the gas phase.

Finally, the dual-phase membrane was used as a membrane reactor. Separation at high temperatures can produce warm, highly concentrated streams of CO_2 that could be used as a chemical feedstock for the synthesis of syngas (H_2 + CO). Towards this, three different membrane reactor configurations were examined: 1) blank system, 2) LSCF catalyst and 3) 10% Ni/γ-alumina catalyst. Performance increased in the order of blank system < LSCF catalyst < Ni/γ-alumina catalyst. Favorable conditions for syngas production were high temperature (850°C), low sweep gas flow rate (10 $mL \cdot min^{-1}$) and high methane concentration (50%) using the Ni/γ-alumina catalyst.

The following chapters within this dissertation are modified versions of papers or reviews that have been published or are to be submitted for publication in the very near future in the journals indicated.

Chapter 1

Anderson, M., & Lin, Y. S. (2011). Inorganic membranes for carbon dioxide separation from flue gas. *Reviews in Chemical Engineering*, to be submitted.

Chapter 2

Anderson, M., & Lin, Y. S. (2010). Carbonate-ceramic dual-phase membrane for carbon dioxide separation. *Journal of Membrane Science*, 357, 122-129.

Chapter 3

Anderson, M., Norton, T., Villarreal, A., & Lin, Y. S. (2011). Carbon dioxide permeation through carbonate-ceramic dual-phase membranes. *AIChE Journal*, to be submitted.

Chapter 4

Anderson, M., Norton, T., Seshadri, S., & Lin, Y. S. (2011). Carbon dioxide capture and dry reforming of methane for synthesis of syngas by a carbonate-ceramic dual-phase membrane reactor. *Journal of Membrane Science*, to be submitted.

DEDICATION

To my family

John R. Anderson
Susan E. Anderson
Jeremy D. Anderson
Lindsay H. Anderson

ACKNOWLEDGMENTS

First and foremost, I would like to dedicate this dissertation to my family, for whom without, my pursuit of this degree would not be possible. Their constant love, support and encouragement have been a true blessing and helped me get through some of the difficult times during my time as a graduate student at Arizona State University. To my dad, John; mother, Susan; brother, Jeremy; and sister, Lindsay – I say thank you from the bottom of my heart for everything you have done for me over the years. I also wish acknowledge my extended family; grandmother Phyllis Rasch, aunts and uncles and cousins who also did their part to encourage me in those times of need. Sadly, my grandfather, Lloyd Rasch, as well as my grandparents, John and Hilda Anderson, are no longer alive, but they too have had and will continue to have a profound impact in my life going forward.

I would also like to thanks my advisor, Dr. Jerry Lin, for his guidance and support during my time as graduate student. I was the first Arizona State student to be advised by Dr. Lin at Arizona State University back when he arrived in 2005. He gave me the opportunity to work on research that was both exciting, educational and cutting edge. His research and management methods, leadership, and positive attitude will continue to influence me throughout my career. I should also acknowledge Dr. Terry Alford, Dr. James Anderson, Dr. Kaushal Rege, and Dr. Daniel Rivera for taking the time and effort to serve on my committee and for their invaluable input that helped improve the quality of my work. Special thanks

are also given to Mr. Fred Peña, whose assistance and friendship over the years was invaluable to me. The time an effort spent by Mr. Peña on building new and troubleshooting old laboratory equipment/projects will not be forgotten.

Finally, I would like to extend my appreciation to all those I have worked with over the years. Of those people, one deserves specific mention – Shriya Seshadri. Shriya and I became great friends during our time in Dr. Lin's lab, and it was a great benefit to both of us to have such a good friend by each other's side while pursuing this degree. She was there for me during some of the hard times, and like my family, helped keep me positive throughout the process. Her joyful attitude and carefree outlook on life made it fun to go to lab on a daily basis. And, no matter what happens after we graduate and leave Arizona State, the special bond Shriya and I formed while working in Dr. Lin's lab will be something I treasure – forever.

The other students in Dr. Lin's lab also made coming to work each day an enjoyable experience. Not only did we become great friends in the work environment, our friendships carried on outside of the lab. We will all remain friends due to the special bonds we created while at Arizona State University.

Shriya Seshadri	Tyler Norton	Jose Ortiz Landeros
Teresa Rosa	Bo Lv	Armando Villarreal
Carrie Eggen	Xiaoli Ma	Chao Ji
Deepak Singh	Vineet Gupta	Duo Li
Zhenxia Zhao	Dr. Wanqin Jin	Dr. Jiansheng Li

Dr. Qinghua Yin	Dr. Wenhui Yuan	Dr. Ke Zhang
Dr. Xuefeng Zhu	Dr. Mikel Duke	Dr. Jessica Abraham
Dr. Xiaotong Wei	Dr. Jay Kniep	Dr. Masakoto Kanezashi
Dr. Haibing Wang		

TABLE OF CONTENTS

Page

Chapter Page

Chapter Page

Chapter Page

Appendices Page

LIST OF TABLES

Table Page

Table Page

LIST OF FIGURES

Figure Page

Figure Page

Figure Page

Figure Page

Figure Page

Chapter 1

GENERAL INTRODUCTION: INORGANIC MEMBRANES FOR CARBON DIOXIDE SEPARATION FROM FLUE GAS

1.1 Introduction

Emission of carbon dioxide (CO_2) and other greenhouse gases into the atmosphere has become an increasingly concerning issue as we progress further into the 21st century. The presence of such gases in the atmosphere is believed to be a significant contributor to the global warming phenomenon. In the thousands of years prior to the Industrial Revolution, the concentration of CO_2 in the atmosphere was within a range of 280 ± 20 ppm [Indermühle et al., 1999]. By 2005, that number had reached 379 ppm [Solomon et al., 2007]. This leads credence to the belief that the increase of CO_2 concentration is chiefly anthropogenic. Continued increases in atmospheric concentration could lead to catastrophic planetary changes, such as increased surface temperatures and rises in sea level [Solomon et al., 2007]. Despite efforts to mitigate emissions, the concentration of CO_2 continues to rise, and at an increasing rate at that. With the continued dependence on fossil fuels by developed nations and growing need by those in third world countries, the problem only figures to get worse before it gets better. Accordingly, methods to alleviate emissions of carbon dioxide have become a focal point of research within the academic community.

Large point sources such as flue gas from coal burning electrical power plants are the main contributors to the problem. In fact, flue gas accounts for

roughly 40% of all CO_2 emissions [Merkel et al., 2010]. The key to successful separation and sequestration is to separate CO_2 directly from flue gas. Flue gas is primarily composed of nitrogen and carbon dioxide with temperatures ranging from a few hundred to as high as 1000°C depending on the location of the gas within the power plant. Highly acidic compounds such as SO_x and NO_x are also present and can further complicate issues with regards to CO_2 removal [Draper and Leer, 2000].

It is highly desirable to separate CO_2 without having to cool the gas, but the high temperature and acidic nature make separation under such conditions a difficult and/or expensive problem to tackle. Aaron and Tsouris have published a comprehensive review that delves into the potential methods of CO_2 removal from flue gas [Aaron and Tsouris, 2005]. Separation methods such as amine absorption, cryogenic distillation and membranes have been examined for this purpose. At present, the most widely used processes to separate CO_2 from flue gas are amine solvent absorption and cryogenic distillation. These two methods are capable of achieving high purities of separation (99%+), but amine solvents are expensive and require constant regeneration or recharging. Cryogenic distillation is very energy intensive, and therefore, rather expensive, because the gas(es) must be cooled considerably to achieve separation. To conserve energy and limit costs, it is highly desirable to separate CO_2 from flue gas at high temperatures, a requirement for which the use of membranes is particular promising. Membrane separation is a steady state process and has a limited

number of moving parts in comparison to liquid solvent absorption and cryogenic distillation. Furthermore, membranes are capable of separating gases from high throughput streams (i.e., flue gas). A review by Figueroa et al. has identified CO_2 selective membranes as promising means for CO_2 capture from pre- and post-combustion processes [Figueroa et al., 2008]. Figure 1.1 shows typical flow diagrams for pre- and post- combustion processes that include some aspect of CO_2 capture [Kanniche et al., 2010].

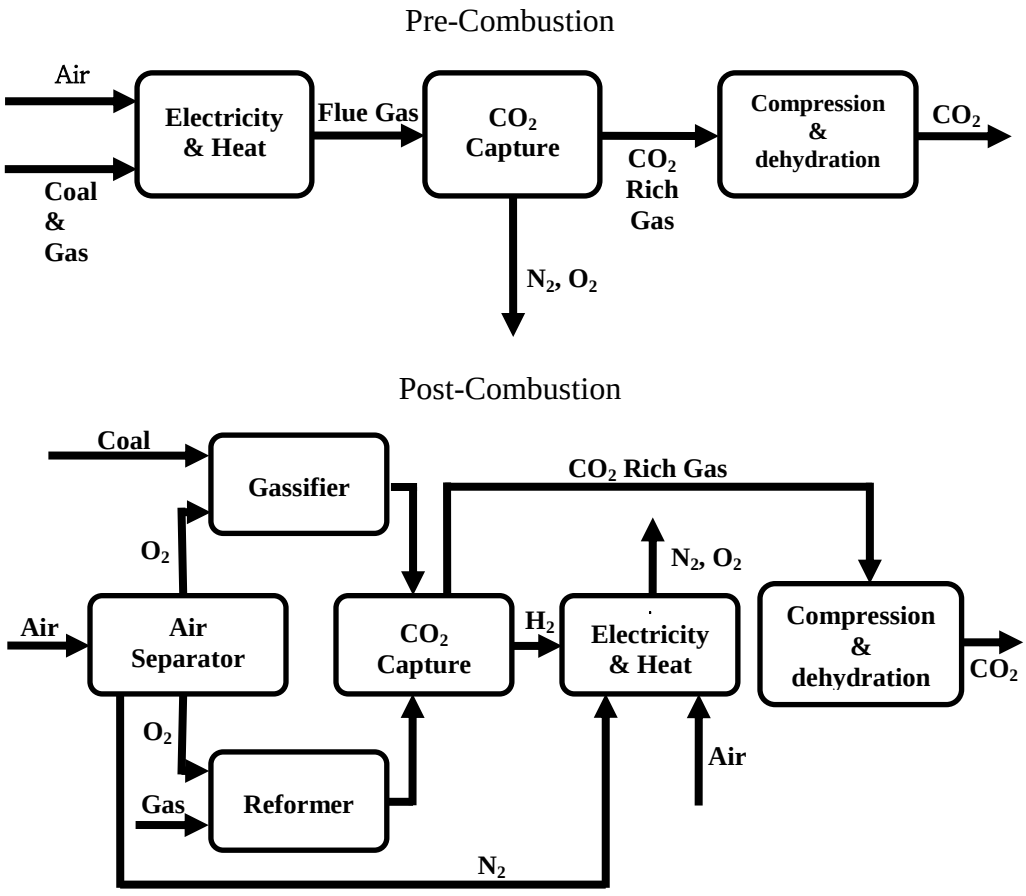

Figure 1.1 Process flow diagrams for pre- and post-combustion processes with CO_2 capture

The majority of academic research with regards to membranes has centered on the use of polymers to accomplish a majority of separations, including that of carbon dioxide. In comparison to inorganic membranes, polymeric membranes are easier and cheaper to manufacture. A comprehensive literature review on polymeric membranes for CO_2 removal from flue gas has been written by Powell and Qiao [Powell and Qiao, 2006]. In addition, membranes (organic and inorganic) designed for pre-combustion CO_2 capture have been reviewed at length by Scholes et al. [Scholes et al., 2010].

The purpose of this introduction is to examine the use of inorganic membranes for CO_2 and N_2 separation. Such membranes could possibly be applied to carbon dioxide removal from flue gas. Inorganic membranes can withstand the high temperature and harsh chemical conditions that accompany flue gas, thus making these materials more suitable candidates than their polymer counterparts for this purpose. Discussion of conventional microporous (γ-alumina, carbon, silica and zeolite) and unconventional (perovskite, dual-phase) membranes will be included. Recommendations for future research with regards to CO_2 and N_2 separation will also be offered.

1.2 Inorganic membrane overview

1.2.1 Membrane classifications and transport mechanisms

Inorganic membranes are often comprised of metals, glasses or ceramic materials that have exceptional mechanical, chemical and especially thermal stability over their polymer counterparts [Bhave, 1991; Hsieh, 1996]. These

characteristics make them ideal candidates for separation of gas mixtures, particularly those at high temperatures. The major disadvantages that inorganic membranes have in comparison to formed by polymers are that they are more costly and can be difficult to prepare without defects.

Inorganic membranes are categorized based on their defining pore size. The IUPAC designations for the different classifications are shown in Table 1.1.

Table 1.1 Membrane classifications based on pore diameter

Membrane Classification	Pore Diameter
Macroporous	> 50 nm
Mesoporous	2 – 50 nm
Microporous	< 2 nm
Dense[1]	≈ 0 nm

Most research has focused on the use of microporous membranes (i.e., carbons, silicas and zeolites) in order to take advantage of surface diffusion and the difference in kinetic diameter between CO_2 (0.33 nm) and N_2 (0.364). However, some recent success has also been achieved using dense, dual-phase membranes. On the other hand, macro- and mesoporous membranes (i.e., γ-alumina) offer little in terms of separation effectiveness, as will be elucidated to later.

The decision regarding which type of membrane to use involves a delicate and sometimes complex trade-off between permeance ($mol \cdot m^{-2} \cdot Pa^{-1} \cdot s^{-1}$) and

[1] The pore size of a dense membrane need only be smaller than the kinetic diameter of the smallest permeant.

selectivity/permselectivity/separation factor (α)[2]. Mesoporous membranes offer large permeances, but low separation factors that boarder on Knudsen selectivity, whereas microporous membranes generally have lower permeances but higher separation factors. Dense membranes tend to have the lowest permeances, but separation factors can be much higher than those found in mesoporous or microporous membranes. Macroporous membranes cannot effectively separate gases; hence they are mainly used as supports for meso-, microporous and dense membranes due to their low resistance to gas flow. Table 1.2 summarizes the different membrane classifications and the typical CO_2 permeances and CO_2/N_2 separation factors that are generally achieved from each.

Table 1.2 Membrane classifications & typical α_{CO_2/N_2} *separation characteristics*

Membrane Classification	Pore Diameter	Typical CO_2 Permeance[3] ($mol \cdot m^{-2} \cdot Pa^{-1} \cdot s^{-1}$)	α_{CO_2/N_2}
Mesoporous	2 – 50 nm	10^{-6}-10^{-7}	10^{0}
Microporous	< 2 nm	10^{-7}-10^{-9}	10^{1}-10^{2}
Dense	≈ 0 nm	$< 10^{-8}$	$> 10^{2}$

Understanding the transport mechanisms through porous inorganic membranes is important towards determining which type is likely to offer the best result. The five most recognized methods of transport though porous inorganic

[2] *Permselectivity* is the ratio of permeance values obtained from single gas permeation measurements. *Selectivity* is the ratio obtained from binary gas separation. *Separation factor* is determined from binary gas separation and takes into account the mole ratios of the gases in the retentate and permeate.

[3] Values listed in Table 1 are not all inclusive, but are typical of what is normally seen for each classification. Some membranes may outperform the typical values listed within the table.

membranes are 1) viscous flow, 2) Knudsen diffusion, 3) single layer adsorption (surface diffusion), 4) multilayer adsorption (capillary condensation) and 5) molecular sieving. These mechanisms are visually depicted in Figure 1.2 [Bhave, 1991].

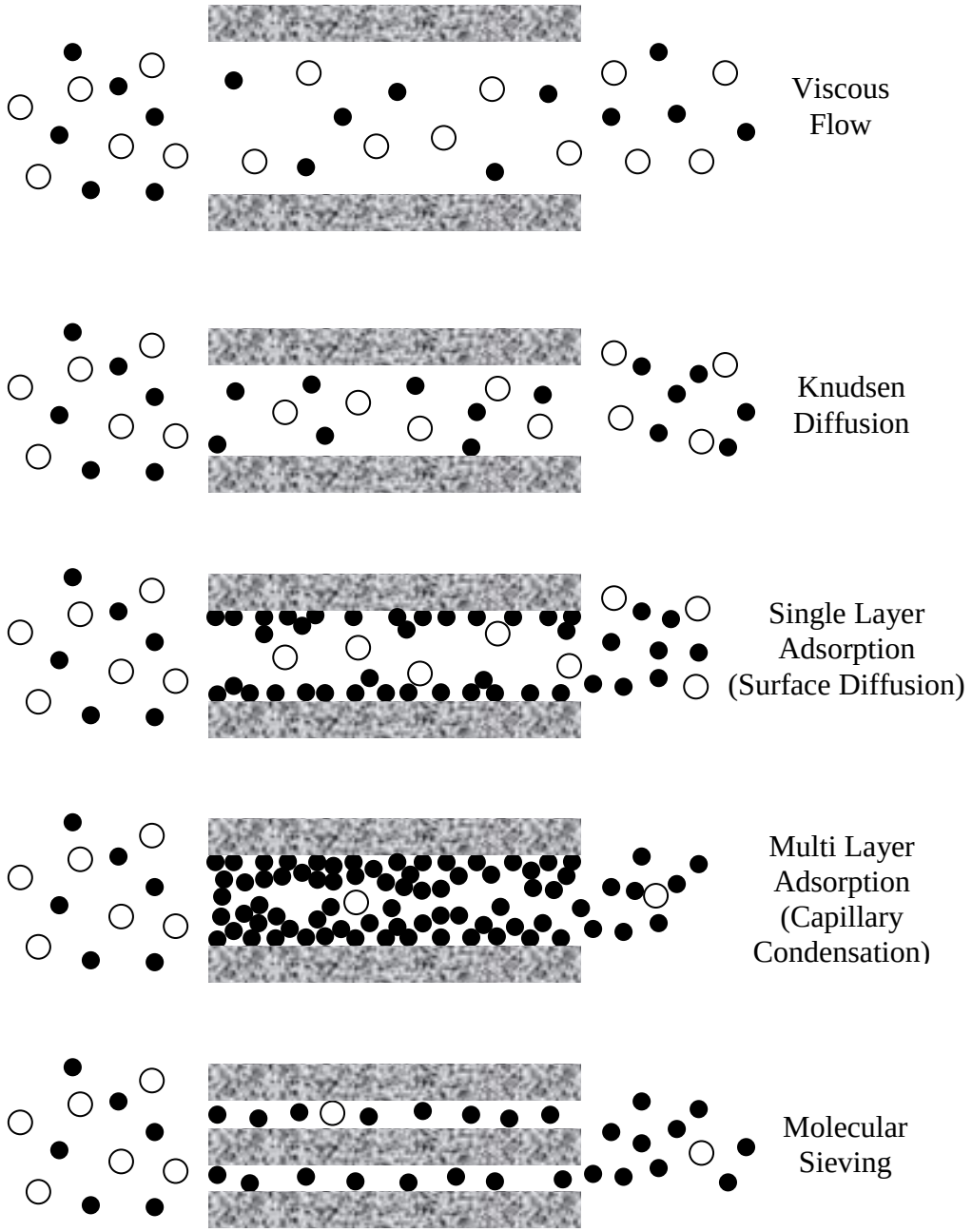

Figure 1.2 Transport mechanisms through macro-, meso- and microporous membranes. A) Viscous diffusion, B) Knudsen diffusion, C) Single layer adsorption, D) Multilayer adsorption & E) Molecular sieving

Only three of the five mechanisms shown in Figure 1.2 are relevant for CO_2 and N_2 separation. Vicious flow (A) does not effectively separate gases because it occurs as a result of either macropores ($d_p \geq 50$ nm) or large defects within the membrane. Separation by Knudsen diffusion (B) is based on molecule-surface interactions occurring more often than molecule-molecule collisions. In order to figure out which is more likely, one must determine the Knudsen number. The Knudsen number is the mean free path (λ) of a gas molecule divided by the average pore diameter (d_p) of the membrane [Noble and Stern, 1995]:

$$Kn = \frac{\lambda}{d_p} \tag{1.1}$$

$$\lambda = \frac{16\eta}{5\pi P_m}\sqrt{\frac{\pi RT}{2M}} \tag{1.2}$$

where P_m is the mean pressure of the system, T is the temperature, M and η are the molecular weight and viscosity of the permeating gas and R is the universal gas constant. If λ is much greater than d_p (i.e., Kn >> 1), Knudsen diffusion is the predominant transport mechanism. This mechanism is primarily seen in membranes that contain mesopores (50 nm < d_p < 2 nm), but more so towards the smaller end of the spectrum. For cases when the Knudsen diffusion is the dominant mode of transport, the separation factor (α_{ij}) can be correlated to the molecular weights of the two permeating gases [Noble and Stern, 1995]:

$$\alpha_{ij} = \sqrt{\frac{M_j}{M_i}} \tag{1.3}$$

Separation via Knudsen diffusion is limited, as performance is inversely proportional to the square root of the molecular weights of the permeating gases. This fact makes it extremely difficult to separate gases of similar molecular weights. Pure Knudsen diffusion would result in a CO_2 (M_w = 44.01 g·mol^{-1}) and N_2 (M_w = 28.01 g·mol^{-1}) separation factor of just 0.80, meaning that the lighter nitrogen molecules are preferentially separated over the heavier CO_2 molecules. This mode of transport is more useful when separating lighter gas molecules such as hydrogen (M_w = 2.016 g·mol^{-1}) from heavier ones (i.e., carbon dioxide). In that case, the H_2/CO_2 Knudsen selectivity would be 4.7.

1.2.2 Transport through microporous membranes

The majority of research for CO_2 and N_2 separation has focused on the use of microporous membranes (d_p < 2 nm). These membranes can be tailored to have pore sizes that are just slightly larger than the size of the permeating molecules. When the membrane pore diameter and permeating molecules are similar in size, single and/or multilayer adsorption and diffusion can become an effective means of separation. This mode of transport is especially common when separating carbon dioxide because it is prone to surface adsorption on carbons, silicas and zeolites.

Molecular sieving is another method by which CO_2 can be separated from N_2 in microporous membranes. Essentially, a molecular sieve separates gases based on molecular size, just as mesh sieves separate particles based on size. Theoretically, a perfect molecular sieving membrane would allow for permeation

of just CO_2 and have an infinite CO_2/N_2 separation factor. However, the proximity in kinetic diameter between CO_2 (0.33 nm) and N_2 (0.364 nm) make fabrication of a perfect molecular sieve a difficult task. A 'perfect' molecular sieve membrane would have to be completely free of defects and need to have the narrowest of pore size distributions. In terms of inorganic membranes, this is fabrication of a perfect molecular sieve is currently not within the capabilities of researchers.

Lin et al. published a lengthy review on microporous membranes, including the theory behind the permeation mechanisms through such [Lin et al., 2002]. The work published by Lin et al. is especially useful, as it discusses the permeation mechanisms in low and high temperature regimes – both of which are pertinent to CO_2 removal from flue gas. Furthermore, the review also looks at the mechanisms for both single and binary component permeation.

For single component permeation through a microporous membrane having only minor defects, a simplified version of the Dusty-Gas model [Lin and Burggraaf, 1993] can be used:

$$F = \alpha + \beta\left(\frac{P_f + P_p}{2}\right) \tag{1.4}$$

where F is permeance and P_f and P_p represent the feed and permeate pressures. The Dusty-Gas model considers the contribution of viscous flow through defects and Knudsen diffusion through meso- and large micropores. Knudsen diffusion and viscous flow are represented respectively by α ($mol \cdot m^{-2} \cdot s^{-1} \cdot Pa^{-1}$) and β

(mol·m^{-2}·s^{-1}·Pa^{-2}) in Equation 1.4. The values of α and β can be calculated from the following equations [Lin and Burggraaf, 1993]:

$$\alpha = 1.06\left(\frac{1}{L}\right)\left(\frac{\varepsilon}{\tau}\right)\frac{r_p}{\sqrt{RTM_w}} \tag{1.5}$$

$$\beta = 0.125\left(\frac{1}{L}\right)\left(\frac{\varepsilon}{\tau}\right)\frac{r_p^2}{\eta RT} \tag{1.6}$$

where L is the thickness of the membrane, ε is the porosity, τ is pore tortuosity, η and M_w are the viscosity and molecular weight of the permeating species, r_p is the size of the average pore radius of the membrane, T is the temperature of the system and R is the universal gas constant.

As mentioned prior, viscous flow and Knudsen diffusion are not effective methods for separation of CO_2 and N_2. As such, separation with microporous membranes having defects is unlikely to offer high CO_2/N_2 separation factors. On the other hand, effective CO_2 separation can be achieved using *defect-free* microporous membranes. For defect-free microporous membranes, steady state single gas permeation is determined from integration of the following:

$$F = \frac{\phi}{L\left(P_f - P_p\right)}\int_{q_f}^{q_p} D_c \Gamma \, dq \tag{1.7}$$

where ϕ is a geometric correction factor that accounts for both membrane porosity (ε) and tortuosity (τ), D_c is the corrected diffusivity of the permeating species and Γ is the thermodynamic correlation factor. The limits of integration in Equation 1.7, q_p and q_f, refer to the concentration of the permeating species in the permeate and feed respectively. In order to solve the above equation, additional

information is required pertaining to the adsorption of the permeating species with regards to the material used to synthesize the membrane. The adsorption equilibrium of various microporous materials can be described by a Langmuir isotherm [Yang, 1987; Do, 1998]:

$$\frac{q}{q_o} = \theta = \frac{KP}{1+KP} \tag{1.8}$$

where K refers to the Langmuir adsorption constant of the gas in question, P is the pressure of the system and θ represents the relative occupancy of the permeating species. The thermodynamic correlation coefficient (Γ) in Equation 1.7 and relative occupancy (θ) in Equation 1.8 can be defined as:

$$\Gamma_{ij} = \theta_i \frac{\partial \ln P_i}{\partial \theta_j} \quad \text{for i, j} = 1,2,...\text{n} \tag{1.9}$$

$$\theta_i = f\left(p_1, p_2, ...p_n\right) \quad \text{for i, j} = 1,2,...\text{n} \tag{1.10}$$

The thermodynamic correlation coefficient can only be determined if the relationship between partial pressure (P_i) and concentration of the permeating species in the membrane is known. Assuming this information is available or can be determined, the thermodynamic correlation coefficient can be calculated:

$$\Gamma = \frac{1}{1-\theta} \tag{1.11}$$

The diffusion of gases within the micropores of inorganic membranes has been studied extensively. Xiao and Wei determined that the diffusivity of a single species could be predicted by using the following relationship [Xiao and Wei, 1992]:

$$D = g_d \lambda \mu e^{\frac{-E_d}{RT}} \tag{1.12}$$

where g_d is a probability factor, λ is the free length of diffusion, μ is the velocity of the diffusing gas molecules and E_d is the activation energy for diffusion of the gas in question. However, as mentioned prior, there are two separate diffusion regimes to consider – one at low and another at high temperature.

At low temperature, adsorption and surface diffusion are likely to be the dominant transport mechanism. Equation 1.13 can be used to calculate the surface diffusion coefficient (D_s) at low temperature [Xiao and Wei, 1992]:

$$D_s = g_d \lambda^2 \mu(\theta) e^{\left(\frac{-E_d}{RT}\right)} \tag{1.13}$$

Here, E_d represents the energy barrier for diffusion on the internal pore surface within the membrane. As temperature increases, the adsorbing molecules (in this case, CO_2), are not as likely to be attracted to the pore wall. Movement within the pores occurs only if the energy barrier (E_d) is exceeded. In this regime, diffusion of the gas within the pores is often referred to as gas translation diffusion. The gas translation diffusivity (D_{GT}) at high temperature is determined from:

$$D_{GT} = g_d d_p \left(\frac{8RT}{\pi M}\right)^{1/2} e^{\left(\frac{-E_d}{RT}\right)} \tag{1.14}$$

It should clarified that Equations 1.13 and 1.14 are only valid for describing diffusion coefficients for non-polar molecules such as CO_2 [Xiao and Wei, 1992; Xiao and Wei, 1992]. Therefore, these equations are considered valid for the current discussion.

In the Langmuir regime, the (J_s) flux of a single species can be described by either relationship shown in Equation 1.15. The equations hold true if diffusivity (D_c) is independent of concentration.

$$J_s = \rho \varepsilon q_s \frac{D_c}{L}\left(\frac{1+KP_f}{1+KP_p}\right) \text{ or } J_s = \rho \varepsilon q_s \frac{D_c}{L}\left(\frac{1-\theta_p}{1+\theta_f}\right) \tag{1.15}$$

The above equations can be further simplified if the adsorption isotherm of the permeating gas is linear (1 >> KP). In Henry's regime, q = KP (where K = q_sb). These simplifications can be used to describe the flux in Henry's regime:

$$J_s = \rho \varepsilon q_s \frac{D_c}{L} K\left(P_f - P_p\right) \tag{1.16}$$

In the high temperature regime, the value of K can be determined using the van't Hoff-type relationship. Similarly, the Arrhenius equation can be used to describe D_c. These equations establish the temperature dependency of J_s.

$$K = K_o e^{\left(\frac{Q_a}{RT}\right)} \tag{1.17}$$

$$D_c = D_{c,o} e^{\left(\frac{-E_d}{RT}\right)} \tag{1.18}$$

where Q_a represents the heat of adsorption of the permeating species and E_d is the activation energy of diffusion within the micropores of the membrane. Substituting Equations 1.17 and 1.18 into 1.15 gives the permeation flux of CO_2 in the Langmuir region, whereas substitution into Equation 1.16 gives the same for Henry's regime. These are shown respectively as Equations 1.19 and 1.20 – both of which are valid under the assumption that the permeate pressure, P_p, is zero (vacuum).

$$J_s = \frac{\rho \varepsilon q_s}{L} D_{c,o} e^{\left(\frac{-E_d}{RT}\right)} \cdot \ln\left(1 + K_o P_f e^{\left(\frac{Q_a}{RT}\right)}\right) \tag{1.19}$$

$$J_s = \frac{\rho \varepsilon q_s}{L} K_o D_{c,o} e^{\left(\frac{Q_a}{RT} - \frac{E_a}{RT}\right)} P_f \tag{1.20}$$

Again, these two equations model low temperature permeation of non-polar species within defect free microporous membranes [Lin et al., 2002].

At high temperature, a portion (or all) of the permeating species in the micropores desorbs from the pore walls (q_g). The remnants remain adsorbed on the pore surface (q_a). At this stage, gas translation diffusion becomes the dominant mode of transport through the membrane. In this case, permeation flux can be obtained by substituting Equation 1.14, which solves for the diffusivity in the gas translation regime (D_{GT}), into Equation 1.7. If the thermodynamic correlation coefficient is assumed to be 1 and if q_g is approximately equivalent to P/RT, then the expression for the flux in the gas translation (J_{GT}) regime becomes:

$$J_{GT} = \frac{\rho \varepsilon g_d d_p}{L} \left(\frac{8}{\pi MRT}\right)^{1/2} e^{\left(\frac{-E_d}{RT}\right)} P_f \tag{1.21}$$

This equation is applicable for permeation in which RT is greater than Q_a. For cases in which K and Q_a are large, and RT < Q_a, molecules desorb inside the micropores of the membrane. After desorption, q_g > P/RT, $q_a = q_{sat}KP/(1+KP)$ and $q_g \approx q_a \exp(-\Delta E_d/RT)$. Using Equations 1.1 and 1.14, the expression for the flux for gas translational diffusion regime is described by [Xiao and Wei, 1992; Xiao and Wei, 1992]:

$$J_{GT} \approx \frac{\rho \varepsilon g_d d_p}{L}\left(\frac{8RT}{\pi M}\right)^{1/2} q_{sat} K_o e^{\left(\frac{Q_a - \Delta E_d - E_d}{RT}\right)} P_f \qquad (1.22)$$

Some work has been done that indicates the total permeation flux (J_T) is actually dependent on both of the flux due to surface diffusion (J_s) and gas translation diffusion (J_{GT}) [Baker et al., 1997; Burggraaf, 1999]. From this, the total permeation flux (J_T) for a single comment in both Langmuir and Henry's regimes can be calculated from Equations 1.24 and 1.25 respectively.

$$J_T = J_s + J_{GT} \qquad (1.23)$$

$$J_T = \frac{\rho \varepsilon q_s}{L} D_{c,o} e^{\left(\frac{-E_d}{RT}\right)} \cdot \ln\left(1 + K_o P_f e^{\left(\frac{Q_a}{RT}\right)}\right) + \frac{\rho \varepsilon g_d d_p}{L}\left(\frac{8RT}{\pi M}\right)^{1/2} q_{sat} K_o e^{\left(\frac{Q_a - \Delta E_d - E_d}{RT}\right)} P_f \qquad (1.24)$$

$$J_T = \frac{\rho \varepsilon q_s}{L} K_o D_{c,o} e^{\left(\frac{Q_a}{RT} - \frac{E_a}{RT}\right)} P_f + \frac{\rho \varepsilon g_d d_p}{L}\left(\frac{8RT}{\pi M}\right)^{1/2} q_{sat} K_o e^{\left(\frac{Q_a - \Delta E_d - E_d}{RT}\right)} P_f \qquad (1.25)$$

For single gas permeation, the permselectivity (α) of CO_2/N_2 can be determined by simply using the ratios of the flux for each individual component (i.e., $\alpha = J_{CO_2}/J_{N_2}$).

Equations 1.4 through 1.25 represent single gas permeation through defect-free inorganic microporous membranes at high and low temperature.

It is also necessary to model binary gas mixtures (i.e., CO_2 and N_2) to observe how the presence of another component, in this case, N_2, affects

permeation of CO_2 and vice versa. The expressions used to model binary gas permeation are shown in the equations below [Krishna et al., 1999]:

$$(J) = -\rho\left[B_{ij}\right]^{-1}\left[\Gamma\right]\frac{d\theta}{dz} \tag{1.26}$$

$$B_{ij} = \frac{1}{D_{1z}} + \sum_{\substack{j=1 \\ j\neq 1}}^{n}\frac{\theta_j}{D_{ij}}, B_{ij} = -\frac{\theta_i}{D_{ij}} \quad \text{for i, j} = 1,2,...\text{n} \tag{1.27}$$

Equation 1.26 is the explicit flux equation in n-dimensional matrix notation in rectangular coordinates for a single dimension. To determine flux of multiple species, the Langmuir isotherms and diffusivities of each must be known. Multicomponent Langmuir adsorption can be determined using the following relationship [Kapteijn et al., 1995, van de Graaf et al., 1999]:

$$\theta_i = \frac{q_i}{q_s, i} = \frac{K_i P_i}{1 + \sum_{i=1}^{n} K_i P_i} \tag{1.28}$$

Assuming intermolecular reaction is negligible in the absence of D_{ij}, Equations 1.26-1.28 can be combined to arrive at the following equations which represent the binary permeation fluxes through a defect-free microporous membrane:

$$J_1 = -\rho q_{s,1}\left(\frac{D_1}{1-\theta_1-\theta_2}\right)\left[(1-\theta_2)\frac{\partial\theta_1}{\partial z} + \theta_1\frac{\partial\theta_2}{\partial z}\right] \tag{1.29}$$

$$J_2 = -\rho q_{s,2}\left(\frac{D_2}{1-\theta_1-\theta_2}\right)\left[(1-\theta_1)\frac{\partial\theta_2}{\partial z} + \theta_2\frac{\partial\theta_1}{\partial z}\right] \tag{1.30}$$

For binary component permeation, the selectivity is simply determined from the ratio of the permeation fluxes of each species. Selectivity is often reported for equimolar feed mixtures of CO_2 and N_2. However, for binary mixtures in which

the feed compositions are not equimolar, it is often useful to report the separation factor. The binary separation factor (α_{ij}) is defined by:

$$\alpha_{ij} = \frac{\left(Y_i / Y_j\right)}{\left(X_i / X_j\right)} \tag{1.31}$$

where Y_i and Y_j are the mole fractions of species i and j in the retentate while X_i and X_j are the mole fractions of each species in the permeate.

1.3 Conventional inorganic membranes

1.3.1 γ-Alumina membranes

Use of γ-alumina membranes as a primary means to separate CO_2 has been limited due to the borderline mesoporous nature of these materials. By borderline, it is meant that these membranes are often on the fringe of being microporous, with pore sizes often measuring between 2 and 3 μm. Membranes with this pore size classification are likely to have high permeances and poor separation factors that are governed by mainly by Knudsen diffusion. Early work on the use of γ-alumina membranes for CO_2 separation was studied by Keizer et al. [Keizer et al., 1988]. Magnesium oxide (MgO) was included in a 4 μm thick supported γ-alumina membrane to create basic sites to which CO_2 would be attracted. At low temperatures, the MgO-γ-alumina membrane exhibited some surface diffusion characteristics within the modified layer, leading to a CO_2/N_2 separation factor of about 1.1 at 30°C. As the temperature approached 100°C, the separation factor dropped and was equivalent to Knudsen selectivity (0.80). Work on the MgO/γ-alumina was extended by Uhlhorn et al., who found that the

adsorption of CO_2 within the pores was partially irreversible [Uhlhorn et al., 1989]. This partial irreversibility caused the heat of adsorption of CO_2 to increase, thus leading to lower permeation fluxes through the membrane.

A few years later, Ma et al. impregnated iron and aluminum oxide catalysts within γ-alumina layers to augment separation [Ma et al., 1992]. High catalyst loads were seen to have a detrimental effect on permeation. Maximum separation efficiency occurred at a catalyst loading of 4.59×10^{-4} mol·m^{-2}. An unmodified γ-alumina membrane (no catalyst impregnation) had a very low CO_2/N_2 permselectivity of 0.7 at room temperature. The membranes impregnated with iron oxide and aluminum oxide had higher CO_2/N_2 values of 1.68 and 1.5 respectively. The increase in permselectivity was attributed to the increased surface adsorption of CO_2 as a result of the inclusion of the catalyst. The adsorption of CO_2 somewhat mired transport of N_2, hence leading to increased permselectivities in comparison to the unmodified membrane.

Cho et al. produced 2 and 5 μm thick γ-alumina membranes by coating a boehmite sol on tubular α-alumina supports [Cho et al., 1995]. Permeation of CO_2 for unmodified γ-alumina membranes were observed to be pressure independent, but was found to be a function of the square root of temperature. These permeation characteristics are indicative of Knudsen diffusion. In an effort to improve the membrane, calcium oxide (CaO) was incorporated into the γ-Al_2O_3 framework to induce interaction with CO_2. However, despite the inclusion of CaO, no improvement in permselectivity was observed between 25 and 400°C.

The lack of improvement was likely a result of the low permeation temperatures in the study because the reaction kinetics of CaO are slow below 500°C. Silica was then added to the γ-alumina network to produce better separation characteristics. For single gas permeation, the CO_2/N_2 permselectivity at room temperature was only 1.4 and decreased towards Knudsen selectivity as temperature increased. Separation was improved by using a binary mixture of CO_2 and N_2. For a feed ratio of 0.26 (CO_2:N_2), the CO_2 and N_2, the separation factor was found to be 1.72 at room temperature and decreased only slightly to 1.5 at 400°C. The increase in the binary separation factor over permselectivity was a result of surface adsorption and diffusion of CO_2 and concurrent blockage of N_2.

To improve CO_2 separation of a γ-alumina membrane, Hyun et al. modified the surface by the silane coupling technique with phenyltriethoxysilane [Hyun et al., 1996]. The membrane exhibited a separation factor of 1.7 at 90°C, and transport was mainly attributed to surface diffusion of CO_2 along the pore walls. Performance was dictated by the hydroxylation tendency of the support and the number of special functional groups coupled to the γ-alumina layer. Finally, CO_2 separation using a Pd modified γ-alumina membrane was examined [Othman and Kim, 2009]. The membrane exhibited no improvement over an unmodified γ-alumina membrane, showing Knudsen selectivity in both cases. The addition of Pd made the membranes more suitable for hydrogen and carbon dioxide separation.

Table 1.3 Summary of y-alumina membranes and α_{CO_2/N_2} values

Membrane	Permeation Temperature (°C)	α_{CO_2/N_2}	Reference
MgO/γ-alumina	25	1.1	Keizer et al., 1988
MgO/γ-alumina	20	1.0	Uhlhorn et al., 1989
Fe_2O_3/γ-alumina	25	1.68	Ma et al., 1992
Al_2O_3/γ-alumina	25	1.5	
CaO/γ-alumina	25	0.98	Cho et al., 1995
Silica/γ-alumina	25	1.4	
Silane coupled y-alumina	90	1.7	Hyun et al., 1996
Pd/γ-alumina	30	0.79	Othman and Kim, 2008

Based on the limited research and the poor separation factors shown in Table 1.3, it is clear that the mesoporous nature of γ-alumina membranes is too much to overcome. Even modification with materials known to attract and cause CO_2 to adsorb to the pore walls produced CO_2/N_2 permselectivities/separation factors no better than 1.7. Therefore, use of these membranes is not recommended for CO_2 and N_2 separation. However, alumina membranes will continue to play a vital role in the search for a CO_2 selective membrane. α-alumina remains a viable support material due do its high mechanical and chemical stability in harsh, high temperature environments. Plus, α-alumina supports are macroporous and offer little resistance to gas flow during separation, furthering their attractiveness as supports for microporous membranes. Mesoporous γ-alumina layers will continue to find use as intermediate layers between macroporous supports (i.e., α-alumina) and microporous layers for separation (i.e., carbons, silicas and zeolites).

1.3.2 Carbon molecular sieve (CMS) membranes

A considerable amount of work has been performed on carbon molecular sieve (CMS) membranes for CO_2 and N_2 separation. These membranes are made by the pyrolysis/carbonization of thermoset polymer precursors such as polyacrylonitriles (PAN), polyimides, phenolic resins, polyfurfuryl alcohol (PFA) and polyvinyl chloride (PVC) on porous substrates [Koresh and Sofer, 1983]. These particular types of polymers are used because they do not liquefy or soften during the pyrolysis process. This allows for the formation of well defined pore structures. Pyrolysis is the heating of these polymers to temperatures as high as 1000°C in an inert or vacuum environment to burn off everything except the elemental carbon matrix. The matrix that is left creates a network of pores by which the actual membrane is formed. In addition to the type of precursor used, precise control of the pore structure and morphology of the membrane can be achieved by adjusting the heating rate, pyrolysis temperature and atmosphere [Koresh and Sofer, 1983]. The ability to fabricate carbon membranes with a very controlled pore size and narrow pore size distribution make them good candidates for molecular sieving of gases with similar kinetic diameters, as is the case between CO_2 and N_2.

In the late 1990s, Kusakabe and Morooka were very active with research involving the fabrication of CMS membranes for CO_2 and N_2 separation and have published several papers on the topic. Early work focused on the formation of membranes by coating the surface of porous α-alumina tubular supports with a

polyamic film derived from 3,3',4,4'-byphenyltetracarboxylic dianhydride (BPDA) and 4,4'-oxydianline (ODA) [Hayashi et al., 1995]. The structures of these two polymers are shown in Figure 1.3.

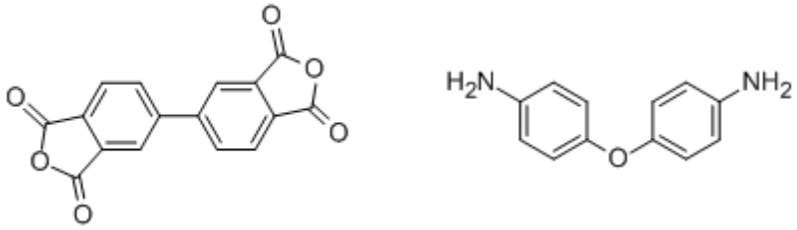

Figure 1.3 Structures of 3,3',4,4'-byphenyltetracarboxylic dianhydride (BPDA; left) and 4,4'-oxydianline (ODA; right)

The BPDA-ODA films were carbonized between 500 and 900°C. The best results were obtained from films pyrolyzed at temperatures over 600°C. CO_2 permeances at 30, 65 and 100°C were 5.0 $x10^{-8}$, 6.0$x10^{-8}$ and 7.0$x10^{-9}$ $mol \cdot m^{-2} \cdot s^{-1} \cdot Pa^{-1}$ for membranes pyrolyzed at 600°C. For membranes carbonized at 800°C, the CO_2 permeances dropped by about an order of magnitude to 2.0$x10^{-9}$, 4.0$x10^{-9}$ and 8.0$x10^{-9}$ $mol \cdot m^{-2} \cdot s^{-1} \cdot Pa^{-1}$ for the same respective temperatures. Table 1.4 summarizes the results obtained from the BPDA-ODA membranes carbonized at different temperatures.

Table 1.4 CO_2 permeances and α_{CO_2/N_2} permselectivities for BPDA-ODA carbon membranes

BPDA-ODA Carbonization Temperature (°C)	Permeation Temperature (°C)	CO_2 Permeance ($mol \cdot m^{-2} \cdot s^{-1} \cdot Pa^{-1}$)	α_{CO_2/N_2}	Reference
600	35	5.0×10^{-8}	30	Hayashi et al., 1995
600	100	7.0×10^{-8}	9	
700	35	4.0×10^{-8}	54	
700	100	9.0×10^{-8}	12	
800	35	2.0×10^{-9}	22	
800	100	9.0×10^{-9}	15	

It was theorized that transport of CO_2 through the CMS membranes was mainly controlled by the size distribution of micropores and not the total volume of such. Micropore size decreased as carbonization temperature increased which explains the reduction in CO_2 permeance at higher pyrolysis temperatures. The decrease in micropore size restricted entrance of N_2 into the pores, therefore explaining why permselectivity trended higher with increasing carbonization temperature.

Kusakabe and Morooka's group continued work with the BPDA-ODA precursor. To further optimize CO_2 permeation and CO_2/N_2 permselectivity, the CMS membranes were modified by CVD of carbon [Hayashi et al., 1997]. For an unmodified membrane (no CVD) at a permeation temperature of 35°C, the CO_2 permeance and CO_2/N_2 permselectivity were 3.0×10^{-9} $mol \cdot m^{-2} \cdot s^{-1} \cdot Pa^{-1}$ and 47 respectively. Upon modifying the membrane by CVD at 650°C, permselectivity increased to 73. The increase in permselectivity occurred by virtue of narrowing the pores with the carbon deposits formed during the CVD process. In separate work, the BPDA-ODA films were oxidized in a mixture of N_2 and O_2 up to 300°C

or in pure CO_2 at 800 or 900°C [Hayashi et al., 1997]. Oxidation in the high temperature CO_2 environments was detrimental because the pore size of the membranes could not be controlled. Better results were obtained for membranes oxidized at lower temperatures in the presence of oxygen. A fresh membrane carbonized at 700°C and oxidized in N_2/O_2 for 3 h at 300°C had a permeance of $4.0x10^{-7}$ $mol \cdot m^{-2} \cdot s^{-1} \cdot Pa^{-1}$ and permselectivity of about 8. The stability of the membranes was also tested by exposing them to air at 100°C for a period of up to 1 month. After the 1 month period, the membranes were subjected to several heat treatments. After those treatments, the membranes regained their original permeation and permselective properties.

Additional work was performed to continue investigating the effect of oxidation on the BPDA-ODA CMS membranes [Kusakabe et al., 1998]. The BPDA-ODA films were pyrolyzed at 700°C then oxidized for 3 h from 100 to 300°C. Oxidation was performed to increase the volume of micropores within the membrane, which from previous research was found to be the main factor that controls permselectivity. This action led to an increase in the CO_2 permeance at 35°C, but did not sacrifice CO_2/N_2 permselectivity (40) or selectivity (51). No difference was observed between using helium or argon as the sweep gas. Data obtained from membranes carbonized at 700°C then oxidized at 300°C is summarized in Table 1.5.

Table 1.5 Results for BPDA-ODA carbon membranes carbonized at 700℃ & oxidized at 300℃

Oxidation & Carbonization Temperature (°C)	Permeation Temp. (°C)	CO_2 Permeance ($mol \cdot m^{-2} \cdot s^{-1} \cdot Pa^{-1}$)	$\alpha CO_2/N_2$	Reference
Single gas permeation (He sweep)	35	$1.5x10^{-8}$	40	Kusakabe et al., 1998
	65	$2.7x10^{-8}$	28	
	100	$3.7x10^{-8}$	14	
Binary permeation (equimolar; He sweep)	35	$2.1x10^{-8}$	51	
	65	$3.1x10^{-8}$	30	
	100	$3.8x10^{-8}$	15	
Binary permeation (equimolar; Ar sweep)	35	$1.5x10^{-8}$	50	
	65	$2.6x10^{-8}$	29	
	100	$3.7x10^{-8}$	15	

Reasons for the lack of any significant difference between single and binary permeation were sought. It was proposed that these particular CMS membranes had 'slit-shaped' pores and because the pore diameter was less than the additive values of kinetic diameters of CO_2 and N_2 ($d_p < dN_2 + dCO_2$), the pores were too narrow for molecules to adsorb and concentrate within. Consequently, transport could only occur by movement of molecules along the width of the pore walls. This resulted in selectivity values that were only slightly higher than permselectivity. The particular mode of transport proposed in this work for the CMS membrane is shown in Figure 1.4.

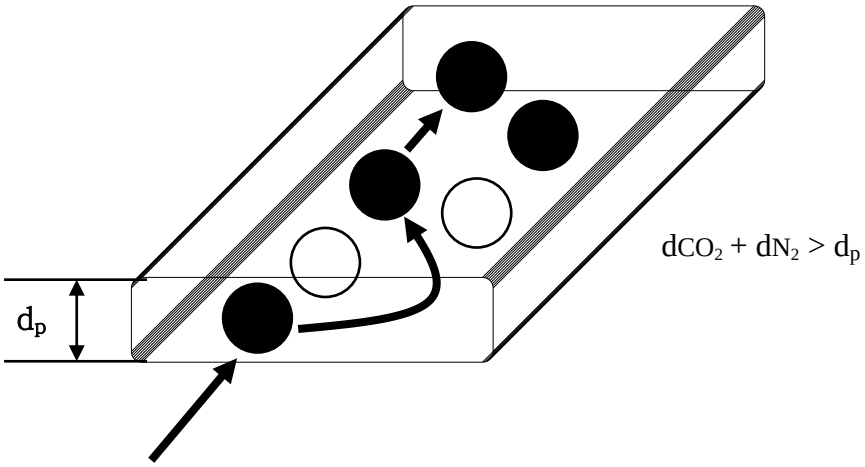

Figure 1.4 Proposed mechanism of CO_2 transport through 'slit-shaped' pores in some CMS membranes

Work on CMS membranes by the Kusakabe and Morooka group was extended to include use of BPDA-ODA polymer precursor with 2,4-diaminotoluene (DAT) [Yamamoto et al.,1997]. The structure of DAT can be seen in Figure 1.5.

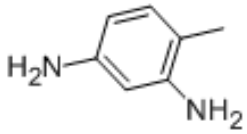

Figure 1.5 Structure and chemical formula of 2,4-diaminotoluene

Initially, the CO_2 permeance of the BPDA-ODA/DAT membrane was much lower than of that without DAT. Permeance was increased by oxidizing the membrane in air for 1 h at 400°C, followed by pyrolysis at 700°C. Under such conditions, this particular CMS membrane was able to produce CO_2 permeances of $2.0x10^{-8}$, $5.0x10^{-8}$ and $1.0x10^{-7}$ $mol \cdot m^{-2} \cdot s^{-1} \cdot Pa^{-1}$ with CO_2/N_2 permselectivities of 38, 10 and 5. The permeation temperatures were 35, 65 and 100°C

respectively. Additional CMS membranes were made from pyrolysis of condensed polynuclear aromatic (COPNA) compounds composed of pyrene, phenanthrene, and 1,4-benzenedimethanol from 400-1000°C [Kusakabe et al., 1998]. Unlike the BPDA-ODA membranes that contained only micropores, the COPNA membranes had both meso- and micropores. The CO_2/N_2 separation factor achieved from these membranes was about 35 at 30°C and 10 at 100°C. Despite the different pore structures between the COPNA and BDPA-ODA membranes, both precursors led to membranes with similar permeation properties. The compilation of data from this and previous work furthered the notion that micropores within CMS membranes are primarily responsible for the CO_2/N_2 permselectivities that are achieved.

Centeno and Fuertes have also engaged in several projects involving the use of CMS membranes for CO_2 and N_2 separation. A 13 wt% polyamic acid solution in N-methylpyrrolidone was coated on macroporous carbon supports [Fuertes and Centeno, 1998]. After drying, the membrane was imidized at 380°C then carbonized at 550°C. Imidization of the polymer created a polyimide with the structure BPDA-pPDA, as shown in Figure 1.6.

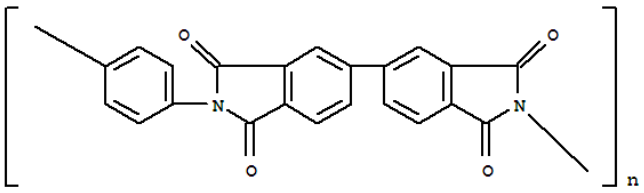

Figure 1.6 Chemical formula and structure of BPDA-pPDA

The permeance of CO_2 ($4.0x10^{-9}$ $mol \cdot m^{-2} \cdot s^{-1} \cdot Pa^{-1}$) did not change with increasing permeation temperature. This meant that the activation energy for CO_2 permeation was 0 $kJ \cdot mol^{-1}$. While an unusual result to some extent, it was believed that, while adsorption of CO_2 decreased at high temperatures, the diffusivity increased, thus corresponding to the lack of change in permeance. However, permeance of N_2 increased with increasing temperature. Due to this increase in N_2 permeance, the permselectivity at 25°C was 18.7, but fell to 5.8 at a permeation temperature of 150°C. The results are summarized in Table 1.6

Table 1.6 CO_2 permeance & permselectivities for BPDA-pPDA CMS membranes

Permeation Temperature (°C)	CO_2 Permeance ($mol \cdot m^{-2} \cdot s^{-1} \cdot Pa^{-1}$)	$\alpha CO_2/N_2$	Reference
25	$4.0x10^{-9}$	18.7	Fuertes and Centeno, 1998
50		13.5	
75		10.5	
100		8.5	
125		6.8	
150		5.8	

Continuing with the previous work, Fuertes and Centeno attempted multiple coatings of the BPDA-pPDA film to observe the effect of membrane thickness on the CO_2 permeation properties [Fuertes and Centeno, 1999]. Each coating was seen to increase the thickness of the membrane by 2 μm. For a single coating (2 μm), the CO_2 permeance was $1.19x10^{-8}$ $mol \cdot m^{-2} \cdot s^{-1} \cdot Pa^{-1}$ with a permselectivity of only 1.8 at 150°C. When the film thickness was 6 μm, permeance dropped to $1.4x10^{-9}$ $mol \cdot m^{-2} \cdot s^{-1} \cdot Pa^{-1}$, but the permselectivity at 150°C increased to 9.1. The permselective characteristics of CMS membranes prepared

using multiple coatings were better than the asymmetric membranes produced prior.

Research was extended to produce CMS membranes using commercially available polyetherimides (Figure 1.7) [Fuertes and Centeno, 1998].

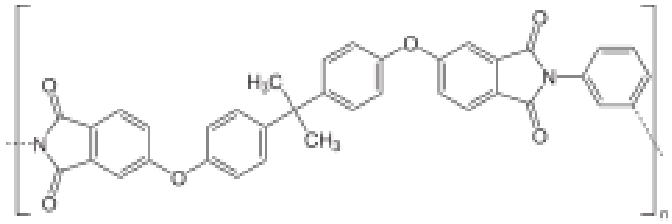

Figure 1.7 Structure and chemical formula for polyetherimide

The films were carbonized in a vacuum at temperatures up to 800°C. The 3 μm thick CMS membranes exhibited CO_2/N_2 permselectivities of 15, 14 and 9.1 at 25, 100 and 150°C. Carbon membranes were also produced using a phenolic resin [Centeno and Fuertes, 1999]. Rather than use an insert atmosphere, pyrolysis at 700°C was carried out under vacuum to produce nearly defect free membranes. The permselectivity of these membranes was as high as 19 at 25°C, but decreased to 8 at 150°C. For a gas mixture of 15% CO_2 and 85% N_2 (simulated flue gas), the separation factor was 45 and 10 at 25 and 150°C respectively. Comparison between the results from single gases and binary mixtures can be seen in Table 1.7.

Table 1.7 Permeation data for CMS membranes formed from carbonization of a phenolic resin

Single/Binary Permeation	Permeation Temp. (°C)	CO_2 Permeance ($mol \cdot m^{-2} \cdot s^{-1} \cdot Pa^{-1}$)	$\alpha CO_2/N_2$	Reference
Single gas permeation	25	$2.0x10^{-9}$	18.2	Centeno and Fuertes, 1999
	50	$2.86x10^{-9}$	16.8	
Binary gas permeation (15% CO_2, 85% N_2)	25	$1.95x10^{-9}$	44.3	
	50	$2.9x10^{-9}$	32.2	

It was believed that that the separation factors were much higher than the permselectivity because adsorbed CO_2 within the pores hindered the diffusion of N_2 into the micropores (0.42 nm) of the membrane. No such impediment occurred when pure N_2 was fed to the membrane.

The next step was to examine the permeation behavior of the membranes after coating the phenolic resin onto tubular supports rather than disks [Centeno and Fuertes, 2001]. The micropore size of the tubular CMS membranes formed with the phenolic resin was similar to that formed on the porous carbon support. A single coating of the phenolic resin produced a CMS membrane with a CO_2/N_2 permselectivity of 36.9 and 6.4 at 25 and 150°C. For the same temperatures, a three times coated membrane produced separation factors of 39.5 and 8.1, but lowered the CO_2 permeances. This proved that a single coating could produce defect-free CMS membranes on a tubular supports with the phenolic resin. It was later reported membranes from carbonized phenolic resins could be prepared in a single casting step by 1) coating the phenolic resin on the macroporous support 2)

carbonizing the film at 700°C and 3) oxidizing the film in air at 400°C [Fuertes, 2000].

Fuentes and Centeno have also produced CMS membranes using commercial polymers Allotherm 610-16 and Matrimid 5218 on carbon supports [Fuertes et al., 1999]. After imidization, the Allotherm 610-16 polymer becomes a compound known as Kapton. The structures of Matrimid 5218 and Kapton are shown in Figure 1.8.

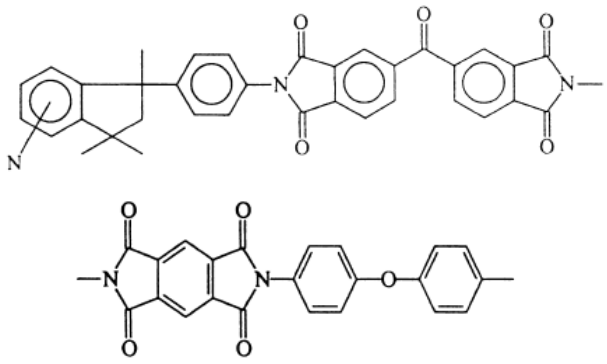

Figure 1.8 Structures and formulas of Matrimid 5218 (top) and Kapton (bottom)

Each film was heat treated from 450 to 700°C. Membranes made from both precursors exhibited molecular sieving properties. The membrane produced with Kapton and pyrolyzed at 650°C had a CO_2/N_2 permselectivity of 8.3, whereas the one made with Matrimid was 5 at room temperature. The permeance of the Kapton membranes was also much higher than the Matrimid CMS membranes. A comparison of the two polymers can be seen in Table 1.8

Table 1.8 Permeation properties of Kapton and Matrimid based CMS membranes

Permeation Temp. (°C)	Kapton		Matrimid		Ref.
	CO_2 Permeance ($mol \cdot m^{-2} \cdot s^{-1} \cdot Pa^{-1}$)	$\alpha CO_2/N_2$	CO_2 Permeance ($mol \cdot m^{-2} \cdot s^{-1} \cdot Pa^{-1}$)	$\alpha CO_2/N_2$	
25	$1.5x10^{-8}$	8.3	$4.0x10^{-10}$	5.0	Fuertes et al., 1999
50	$2.0x10^{-8}$	8.9	$5.0x10^{-10}$	5.6	
75	$2.0x10^{-8}$	8.0	$7.0x10^{-10}$	5.8	
100	$1.8x10^{-8}$	5.8	$8.0x10^{-10}$	5.3	
125	$1.6x10^{-8}$	4.6	$9.0x10^{-10}$	5.0	
150	$1.5x10^{-8}$	3.9	$9.0x10^{-10}$	4.3	

Finally, Fuertes and Centeno made CMS membranes by vacuum pyrolysis of poly(vinylidene chloride-co-vinyl chloride) from 500-1000°C [Centeno and Fuertes, 2000]. The film carbonized at 700°C was only 800 nm in thickness – the thinnest membrane produced throughout all of the research conducted by Fuertes and Centeno. The membrane had a CO_2 permeance of $6.0x10^{-9}$ $mol \cdot m^{-2} \cdot s^{-1} \cdot Pa^{-1}$ and CO_2/N_2 permselectivity of 18. At 150°C, the permeance increased to $9.0x10^{-9}$ $mol \cdot m^{-2} \cdot s^{-1} \cdot Pa^{-1}$ and CO_2/N_2 fell to 7. Preoxidizing the film at 200°C for 6 h improved the room temperature permselectivity (28) of the membrane, but at a cost of lowering the permeance ($9.0x10^{-10}$ $mol \cdot m^{-2} \cdot s^{-1} \cdot Pa^{-1}$).

Several other groups aside from Kusakabe/Morooka and Fuertes/Centeno have done work on CMS membranes for CO_2 separation. Shiflett and Foley prepared nanoporous carbon membranes using ultrasonic deposition of polyfurfuryl alcohol (PFA) on stainless steel supports [Shiflett and Foley, 2000]. The support was coated three times and heat treated at 150°C followed by an additional coat of the polymer precursor. Pyrolysis was carried out at 450°C. The membrane exhibited room temperature CO_2 and N_2 permeances of $1.87x10^{-10}$

and $1.24x10^{-10}$ $mol \cdot m^{-2} \cdot s^{-1} \cdot Pa^{-1}$ with a resulting in a permselectivity of 1.5. Suda and Haraya used a Kapton polyimide carbonized under different conditions (pyrolysis temperature, heating rate, heating atmosphere) to form CMS membranes [Suda and Haraya, 1997]. A summary of the conditions and CO_2/N_2 permselectivities obtained from the Kapton membranes at a permeation temperature of 35°C are shown in Table 1.9.

Table 1.9 Permselectivity at 35°C for Kapton membranes pyrolyzed under various conditions

Pyrolysis Conditions (Temp., Ramp Rate, Atmosphere)	$\alpha CO_2/N_2$	Reference
600°C, 10°C·min^{-1}, vacuum	22.2	Suda and Haraya, 1997
800°C, 10°C·min^{-1}, vacuum	42.2	
1000°C, 10°C·min^{-1}, vacuum	101	
950°C, 13.3°C·min^{-1}, Ar	82.7	
950°C, 4.5°C·min^{-1}, Ar	87.7	
950°C, 1.3°C·min^{-1}, Ar	122	

A Kapton membrane carbonized at 950°C in an argon atmosphere with a heating rate of 1.3°C·min^{-1} gave the best CO_2/N_2 permselectivity (122) at 35°C. The small pore size and narrow pore size distribution created by carbonizing at 950°C led to the formation of a membrane for which molecular sieving was the predominant transport mechanism.

Wang et al. fabricated supported carbon membranes using a furfuryl alcohol precursor by vapor deposition polymerization on γ/α-alumina or glass/α-alumina support tubes [Wang et al., 2000]. The tubes were pretreated with an acid catalyst and then exposed to furfuryl alcohol vapors at 90°C. Upon heating

the tubes to 200°C, the furfuryl alcohol within the pores became cross-linked to form polyfurfuryl alcohol (PFA). The resulting film was carbonized at 450, 525 or 600°C. This entire coating process was done twice to enhance the permeation properties of the membrane. Resulting CO_2 permeances were too low at temperatures of 450 and 525°C, hence subsequent membranes were carbonized at 600°C. Permselectivity of the CMS membrane on the γ/α-alumina support was 79.3 and 9.3 at 25 and 150°C respectively. For the glass/α-alumina support, the permselectivity values were 40.3 and 11.2 at the same respective temperatures. Low CO_2 permeance in all of the membranes was attributed to the deep penetration of the furfuryl alcohol vapor into the support, essentially plugging the pores. The results from work conducted by Wang et al. are summarized in Table 1.10.

Table 1.10 Affect of using γ-alumina or glass supports on PFA carbonized membranes

Permeation Temp. (°C)	CMS/γ-alumina		CMS/glass		Ref.
	CO_2 Permeance ($mol \cdot m^{-2} \cdot s^{-1} \cdot Pa^{-1}$)	$\alpha CO_2/N_2$	CO_2 Permeance ($mol \cdot m^{-2} \cdot s^{-1} \cdot Pa^{-1}$)	$\alpha CO_2/N_2$	
25	5.8×10^{-9}	79.3	2.7×10^{-9}	40.3	Wang et al., 2000
50	3.3×10^{-8}	9.3	2.9×10^{-9}	11.2	

400 nm thick CMS membranes were prepared by pyrolyzing lignocresol between 400 and 800°C [Kita et al., 2002]. The permeation characteristics of the membrane were found to be dependent on the pyrolysis temperature, for which the optimum was said to be 600°C. For a membrane carbonized at 600°C for 1 h,

the CO_2 permselectivity at 35°C was 36. Using the same membrane, a 20/80% CO_2 and N_2 mixture (simulated flue gas) produced a separation factor of 48. A membrane that was carbonized for 2 h at 600°C had a permselectivity of 40 and the separation factor of 45. The slight increase in separation factors over permselectivities indicated that nitrogen permeance was only slightly hindered by the selective adsorption of CO_2 within the pores of the membrane. This result was similar the results obtained for the 'slit shaped' pores in membranes made by Kusakabe and Morooka [Kusakabe et al., 1998].

Fuentes and Centeno were not the only research group to fabricate CMS membranes with Matrimid. Kiyono et al. also looked into the use of that particular precursor and compared its performance with 6FDA/BPDA-DAM [Kiyono et al., 2010]. 6FDA/BPDA-DAM was synthesized by the polycondensation reaction of 5,50-[2,2,2-trifluoro-1-(trifluoromethyl)ethylidene] bis-1,3-isobenzofurandione (6FDA) with 2,4,6-trimethyl-1,3-phenylene diamine (DAM) and 3,30,4,40-biphenyl tetracarboxylic dianhydride (BPDA) in a solution containing n-methylpyrrolidone (NMP). Pyrolysis was conducted at 550°C, with heating rates of 13.3°C·min^{-1} from room temperature to 250°C, then 3.85°C·min^{-1} from 250 to 535°C. From 535 to 550°C, the heating rate was kept very low at 0.25°C·min^{-1}. The membrane made from using Matrimid as the precursor produced a permselectivity of 16.7. In comparison, the CMS membrane formed

from pyrolysis of 6FDA/BPDA-DAM achieved a permselectivity of 35.1, but also showed a 7-fold increase in the permeance. The study found that the 6FDA/BPDA-DAM membrane had a more selective ultramicroporous structure than did the Matrimid membrane. In addition, 6FDA/BPDA-DAM was found have a higher sorption capacity for CO_2, hence providing better separation characteristics.

Some research has looked into the use of more exotic-type polymers or additives to increase the permeation properties of CMS membranes. Zhang et al. looked into the use of a new polymeric precursor, poly(phthalazinone ether sulfone) (PPES), to form carbon membranes [Zhang et al., 2009]. The structure of PPES is shown in Figure 1.9.

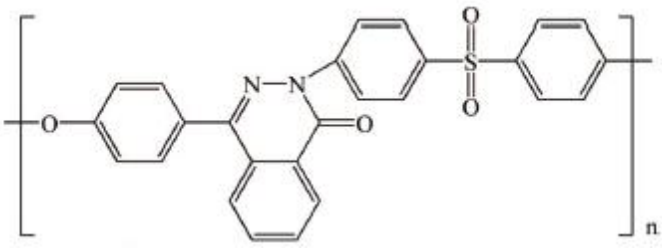

Figure 1.9 Structure chemical formula of poly(phthalazinoneethersulfone) (PPES)

During pyrolysis, the functional groups within the PPES gradually disappeared and formed a graphite-like structure. A membrane carbonized at 650°C exhibited a CO_2/N_2 permselectivity of 16.3, whereas the permselectivity of a membrane carbonized at 950°C was only 6.1. It was determined that, as the carbonization temperature increased, the degree of graphitization increased as well. Higher degrees of graphitization led to a denser carbon matrix, and therefore, lower

permeances. Lui et al. also examined the use of a novel polymer poly-(phthalazinone ether sulfone ketone) by thermostabilization in air at 400-500°C and carbonization at 650-850°C [Lui et al, 2008]. Results indicated that the most favorable thermostabilization temperature was 460°C. Therefore, all membranes were subject to such treatment. Membranes carbonized at 650, 750 and 850°C had CO_2/N_2 selectivities of 51.1, 74.1 and 93.1 at room temperature. The increasing permselectivity showed that the structure of the CMS membrane became more compact as carbonization temperature increased.

In a novel approach, CMS membranes impregnated with Ag^+ ions were produced using blends of P84 co-polyimide and a sulfonated poly(ether ether ketone) [Barsema et al., 2005]. $AgNO_3$ was used as the source for the Ag^+ ions. From previous work, it was believed that the addition of silver nanoparticles within the carbon matrix could create selective bypasses that would allow separation to occur via selective surface flow. For the CMS-Ag mixed-matrix membranes, an increase in the pyrolysis temperature was seen to increase CO_2/N_2 permselectivity. Ag^+ loading was also seen to have an effect on the permeation properties through the membrane, which can be viewed in Table 1.11.

Table 1.11 Affect of Ag^+ loading on CO_2/N_2 permselectivity at 25°C

Ag^+ content (wt %)	$\alpha CO_2/N_2$	Reference
0.0	1.2	Barsema et al., 2005
1.35	18.1	
2.46	35.5	
4.51	49.0	
6.21	65.3	

For a CMS membrane with no Ag (0 wt%), the separation factor was only 1.17 at 2 bar and 25°C. Conversely, for a membrane with 6.21 wt% Ag, the permselectivity was 65.3 and permeance was higher than the membrane without silver. These results confirmed the belief that the incorporation of the silver nanoparticles would, in fact, create selective bypasses within the membrane.

A few groups have looked into the separation properties of CMS hollow fiber membranes. Kusuki and coworkers made hollow fiber CMS membranes using a polyimide precursor [Kusuki et al., 1997]. Before treatment, the polymer films were dried in nitrogen at 270°C and then heat treated in air at 400°C. Afterwards, the membranes were pyrolyzed between 600 and 1000°C in a nitrogen atmosphere to produce the hollow fiber membranes. Hollow fiber membranes used after drying of just the polyimide film (no carbonization) displayed permeances of $2.5x10^{-8}$, $3.3x10^{-8}$ and $4.1x10^{-8}$ $mol \cdot m^{-2} \cdot s^{-1} \cdot Pa^{-1}$ at 50, 75 and 120°C. Comparatively, membranes carbonized at 700 and 850°C showed permeances of $4.0x10^{-8}$, $6.7x10^{-8}$, $9.0x10^{-8}$ and $1.8x10^{-9}$, $3.0x10^{-9}$, $5.0x10^{-9}$ $mol \cdot m^{-2} \cdot s^{-1} \cdot Pa^{-1}$ at the aforementioned permeation temperatures. At low permeation temperatures, the dried membrane (no carbonization) exhibited higher permselectivity than the membrane subjected to pyrolysis. CO_2/N_2 permselectivities at 120°C were better for the carbonized membranes. It was believed that the diffusion of CO_2 through the carbon membranes occurred through existing holes, but transport through the dried polyimide membrane occurred through the free space holes made by the thermal motion of the polymer

chains. CMS hollow fiber membranes were also prepared by using a polyamic acid [Ogawa and Nakano, 1999]. The effects of time, temperature and pH of the coagulant on the resulting CMS membranes were studied. Micropore formation and pore size were both found to be independent of gelation time. However, micropore volume was seen to increase as gelation temperature increased and pH decreased. The permselectivity of CO_2 over N_2 for a membrane with a gelation time of 6 h, pH of 9.4, and gelation temperature of 2°C was 230 at a permeation temperature of 25°C. Membranes prepared using the same gelation times and temperatures, but at pH values of 3 and 11, offered CO_2/N_2 values that were much lower at 28 and 5.

Some recent success with CMS membranes has been achieved using polyimide based pseudo-interpenetrating polymer networks (IPN) [Low and Chung, 2011]. IPNs can be used to tailor the structure of the polymer used, and therefore, also influences the final structure formed during carbonization. In the work, poly (2,3,5,6-phenylene-2,20-bis(3,4-carboxylphenyl) hexafluoropropane) diimide (6FDA–TMPDA) and the addition of different amounts of 2,6-bis(4-azidobenzylidene)-4 methylcyclohexanone (azide) were examined to produce high quality CMS membranes. A membrane formed by pyrolyzing just 6FDA–TMPDA at 550°C had a permselectivity of 24.6. No improvement in permselectivity for films pyrolyzed at 550°C was achieved when 10 or 30% azide was added to the precursor. However, CO_2 permeance of a membrane produced from 90/10% 6FDA–TMPDA/azide increased by about 35%. For 6FDA–

TMPDA/azide films pyrolyzed at 800°C, the CO_2/N_2 permselectivity increased to between 31.1 and 33.2 depending on the azide loading. The results show that the use of azide was a relative non-factor in terms of increasing permselectivity. However, it was seen that high azide loadings did cause a decrease in CO_2 permeance. Therefore, the addition of azide to 6FDA–TMPDA could be considered an unnecessary step in terms creating an effective membrane for CO_2/N_2 separation. It should be noted that the effect of the azide was more pronounced when separating carbon dioxide from methane.

Rather than use just homogeneous carbon membranes for CO_2 separation, Park and Lee [Park and Lee, 2005] decided to combine a continuous carbon matrix with a dispersed silica domain to fulfill this purpose. The addition of silica was believed to be one that would allow for improved permeation flux through the membrane without compromising selectivity. At the same time, the silica was also intended make the membrane more resistant to oxidation. For a membrane made from pyromellitic dianhydride (PMDA) as the polymer precursor with 10 wt% silica, the permselectivity was 35. Increasing the loading to 20% did not affect permselectivity, but did increase permeance by nearly 80%. An increase to 30 wt% silica in the carbon matrix caused a slight drop in CO_2/N_2 to 30.4, but increased permeance by 350% over the 10 wt% dispersed membrane. Even better results for both permeance and permselectivity were obtained by using ODA as the polymer precursor in conjunction with increasing dispersion of silica. The authors believed that the increase in gas permeability was mainly caused by

changing the silica network via the inclusion of DEDMS. At pyrolysis temperatures above 600°C, there is a redistribution of the -Si-O- and -Si-C- bonds. After redistribution, the silica that is derived from the co-condensation of both TEOS and DMDES is believed to be less porous than normal silica solely derived from TEOS. Consequently, permeance increased as the amount of DMDES increased.

The literature findings for CMS membranes indicate some effectiveness in separating CO_2 from N_2. Figure 1.10 depicts a Robeson-type plot that shows the relationship between CO_2 permeability and α_{CO_2/N_2}. In order to be a commercially viable option, a membrane should have high CO_2 permeance/permeability to go with a high α_{CO_2/N_2}. At this particular point in time, no reported CMS membrane fits the criteria. Those that are characterized by high CO_2/N_2 values are plagued by low permeability and vice versa. Furthermore, the scatter viewed in the figure leads to serious questions regarding the reproducibility of these particular membranes.

Figure 1.11 shows a plot of CO_2/N_2 dependency on permeation temperature. Clearly, CMS membranes are able to separate CO_2 from N_2 quite effectively at low temperatures. Within this region, surface diffusion and molecular sieving are the dominant transport mechanisms. However, as permeation temperature increases, α_{CO_2/N_2} values drop. The decrease in α_{CO_2/N_2} appears to be proportional to $1/T^{½}$. This indicates that Knudsen diffusion remains a key transport mechanism with these membranes in the higher temperature

region (T > 100°C). As mentioned prior, Knudsen diffusion is not an effective means of CO_2 separation from N_2. In order to produce better separation characteristics at high temperatures, the pore size and pore size distribution within the carbon structure needs to be to be further reduced to allow for increased impediment of N_2 molecules.

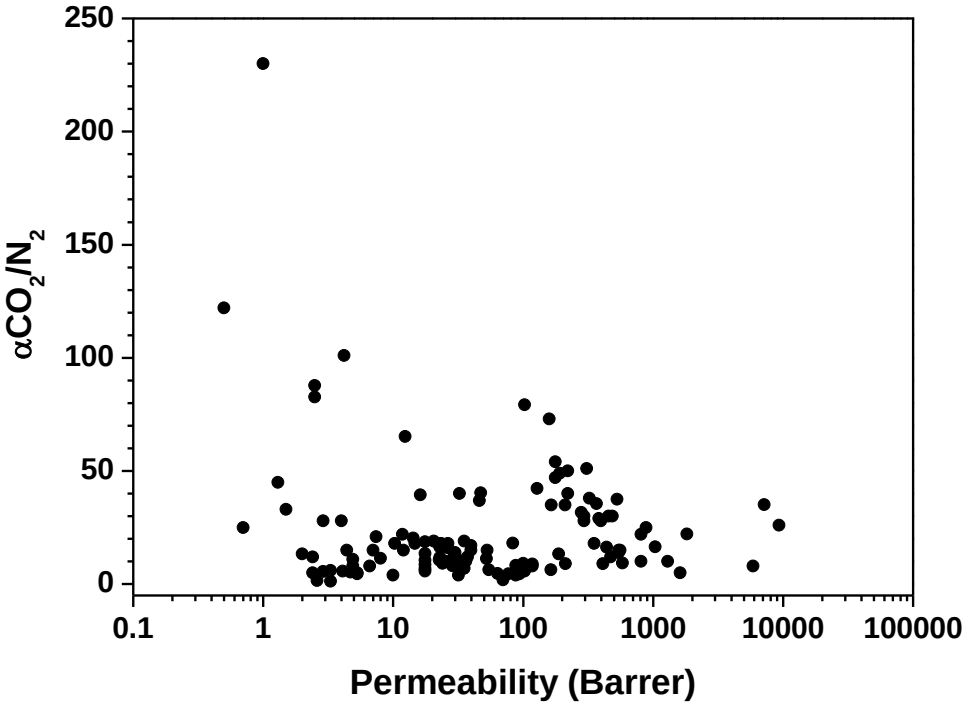

Figure 1.10 CO_2/N_2 Robeson plot for carbon molecular sieve membranes

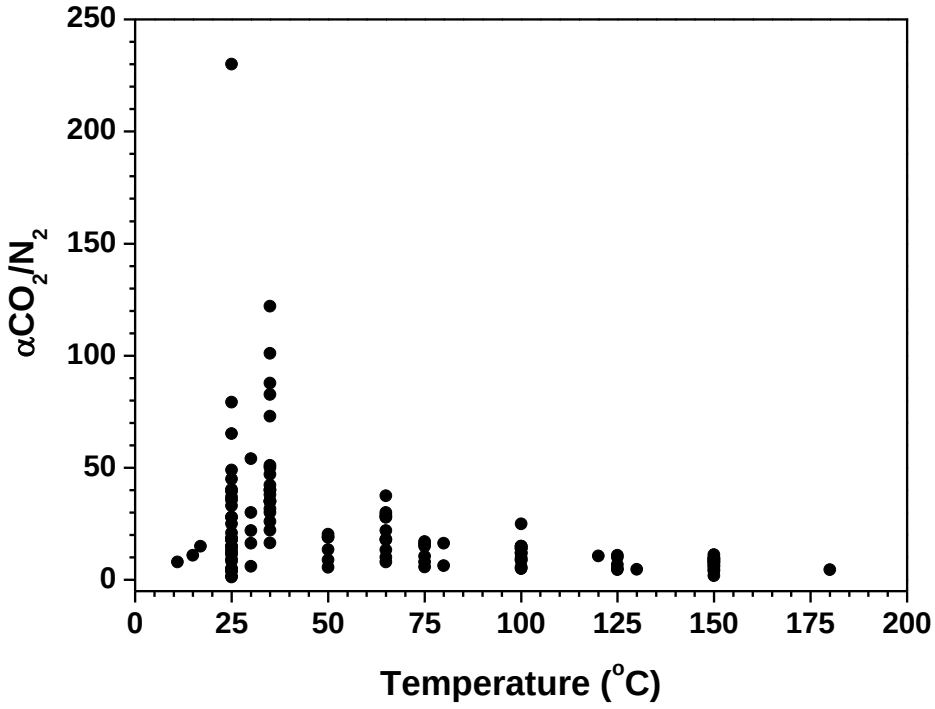

Figure 1.11 $\alpha CO_2/N_2$ dependency on permeation temperature for carbon membranes

1.3.3 Silica membranes

Similar to carbon molecular sieves, silica-based membranes can be produced with pore sizes on the order of 1 nm or less. This makes them particularly applicable for molecular sieving separations. Silica is a resourceful material because the structure can vary depending on the preparation method and conditions used to form the membrane. Furthermore, silica is not prone to undergo phase transitions or significant changes in pore structure and morphology at high temperatures or in oxidizing environments [Kusakabe et al., 1998]. This is unlike γ-alumina or some carbon membranes, which are prone to undergo structural changes at high temperatures or in oxidizing environments.

Microporous silica membranes are prepared by a number of different techniques. Most techniques involve the deposition of a silica layer onto a porous support by either the sol-gel method or via chemical vapor deposition (CVD) [Cooper and Lin, 2002]. Silica membranes as thin as tens of nanometers can be produce by these methods. Of the typical synthesis routes, the sol-gel technique is the most common. Tetraethyloxysilane (TEOS; sometimes referred to as tetraethylorthosilicate) is often used as the silica source for the membranes. The structure and chemical composition of TEOS is shown in Figure 1.12.

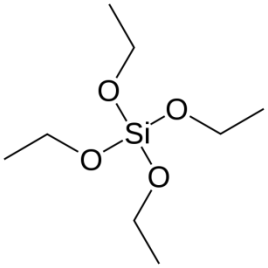

Figure 1.12 Structure and chemical compotation of tetraethoxysilane (TEOS).

Early efforts on the development of silica membranes for CO_2 and N_2 separation began in the late 1980s. Uhlhorn et al. used the sol-gel technique to produce microporous silica membranes on γ-alumina coated supports [Uhlhorn et al., 1989]. The silica membranes formed were only 30 nm thick on top of the γ-alumina layer. The membrane had a CO_2 permeance of 3.0×10^{-6} $mol \cdot m^{-2} \cdot s^{-1} \cdot Pa^{-1}$ and a CO_2/N_2 permselectivity of 15 at room temperature. An increase in upstream pressure led to increased permeances of CO_2 while N_2 permeance remained relatively unchanged. This observation confirmed that CO_2 permeated through the membrane via the surface diffusion mechanism. On the other hand, transport

of N_2 was governed by Knudsen diffusion; hence the lack of dependency on system pressure. Silica membranes were also produced by de Vos and Verweij via the sol-gel method using TEOS as the silica source [de Vos and Verweij, 1998]. The sol was dip-coated onto γ-alumina supported membranes and calcined at either 400 or 600°C. The resulting silica layer was only 30 nm thick. Permeance was measured as a function of temperature (25-200°C) and pressure (0.5-3 bar). For the silica membrane calcined at 400°C, permeance of CO_2 was only slightly dependent on the upstream pressure. The results are summarized in Table 1.12.

Table 1.12 CO_2 permeation characteristics for Si(400) membranes at 25 & 50°C

Pressure Difference (bar)	25°C		50°C		Reference
	CO_2 Permeance ($mol \cdot m^{-2} \cdot s^{-1} \cdot Pa^{-1}$)	$\alpha CO_2/N_2$	CO_2 Permeance ($mol \cdot m^{-2} \cdot s^{-1} \cdot Pa^{-1}$)	$\alpha CO_2/N_2$	
1.0	2.28×10^{-7}	22.8	2.76×10^{-7}	18.4	de Vos and Verweij, 1998
1.5	2.14×10^{-7}	21.4	2.65×10^{-7}	18.9	
2.0	2.06×10^{-7}	20.6	2.62×10^{-7}	20.2	
2.5	2.01×10^{-7}	22.3	2.61×10^{-7}	20.1	

The maximum CO_2/N_2 permselectivity was 22.8 at 25°C and a pressure difference of 1 bar. On the other hand, CO_2 permeance was found to be dependent on both temperature and pressure for the membrane calcined at 600°C. CO_2 permeance values were two orders of magnitude lower than that for membrane calcined at 400°C. N_2 permeance was undetectable. This was due to the denser structure formed upon calcination. The average pore size of the Si(600) membrane was believed to be just 0.36-0.38 nm, whereas the Si(400) had pores between 0.38 and 0.55 nm range. The kinetic diameter of nitrogen is 0.364 nm, hence explaining

why the permeance of N_2 was undetectable and why CO_2 permeance was low for the membrane calcined at 600°C. Later work involved the formation of a hydrophobic silica layer by adding methyltriethoxysilane (MTES; Figure 1.13) to the standard silica sol mixture [de Vos et al., 1999].

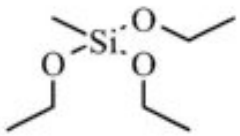

Figure 1.13 Structure & chemical compotation of methyltriethoxysilane (MTES).

Calcination was carried out at 400°C and produced a modified silica layer that was 60 nm thick – double that of the standard silica membrane in the previous work. The use of MTES made the membranes ten times more hydrophobic, but the separation characteristics were diminished. The CO_2 permeance values from the MTES modified silica membrane were double that of the previously used membranes, but the separation factors were much lower. The highest CO_2/N_2 permselectivity achieved was 1.92 at a temperature of 100°C and pressure differential of 0.5 bar. Permselectivity continued to decrease as both temperature and pressure difference increased. The hydrophobic nature of this membrane would make it more suitable for separation of gases that include water vapor, as the pores would not become blocked by the adsorption of water within. This could be of potential use in CO_2 separation from flue gas, as the mixture does contain some water vapor (~ 3%).

Instead of using TEOS, Moon et al. used only MTES as the silica source in their sol [Moon et al., 2005]. A defect free membrane that was 0.7 μm in thickness was produced by calcination at 300°C for 4 h. Permeation was examined as both a function of pressure and temperature. It was found that increases in the feed pressure led to increased permeances of CO_2, but decreased the separation factor. This was observed because the surface adsorption of CO_2 at low pressures occurs more readily than N_2. As a result, CO_2 adsorption in the pores blocked permeation of N_2. This effect becomes diminished at higher temperatures due to the lack of adsorbed CO_2. In addition, as temperature rose, CO_2 permeance decreased due to the diminished amount of CO_2 adsorbing within the pores. On the contrary, N_2 permeance increased slightly as temperature increased. These two occurrences led to a decrease in the separation factor with increasing temperature.

Kuraoka et al. produced asymmetric microporous silica xerogel membranes via the sol gel method [Kuraoka et al., 2000]. Porous alumina tubes with a mean pore size of 100 nm were coated 6 or 18 times with a silica sol. For a silica membrane coated 6 times, the CO_2 and N_2 permeances were 6.36×10^{-8} and 9.71×10^{-10} $mol \cdot m^{-2} \cdot s^{-1} \cdot Pa^{-1}$, resulting in a permselectivity of 66. On the other hand, the CO_2 and N_2 permeances for the 18 times coated membrane were 5.36×10^{-8} and 3.68×10^{-8} $mol \cdot m^{-2} \cdot s^{-1} \cdot Pa^{-1}$. In this case, the permselectivity was just 1.4. The poor separation characteristics of the 18 times dip coated silica membrane were attributed to the fact that the increased number of coatings led to

an increasingly thick silica layer. The increased thickness made the membrane more prone to the formation of defects, which becomes a defying factor as the number of coatings (i.e., thickness) increases.

Tsai et al. formed a novel dual-layer microporous silica membrane by the use of two different silica sols [Tsai et al., 2000]. To form the first layer, a "stock sol" having a pH of 4.7 with TEOS as the silica source was used. The 'standard sol' with a pH of 2.0 was used for the subsequent layer. The purpose of the (first) surfactant-templated silica layer was to improve the finish on top of the intermediate γ-alumina layer. Secondly, it was intended to prevent the top silica layer from penetrating the pores of the support. The intermediate silica layer had a pore size of about 1 nm, while the top silica layer had pores between 0.3 and 0.4 nm making this membrane an ideal candidate for separation via the molecular sieving mechanism. The combination of the two layers was believed to be only 30 nm thick. For a simulated reformate gas mixture (50% H_2, 34% N_2, 15% CO_2, 1% CO), the membrane had a CO_2 permeance of $3.4x10^{-8}$ $mol \cdot m^{-2} \cdot s^{-1} \cdot Pa^{-1}$ and a CO_2/N_2 separation factor of about 47 at 80°C. The results obtained show that this particular dual-layer type membrane could be very useful in molecular sieving applications, including CO_2 removal from flue gas.

Asaeda and Yamasaki used the hot coating method to produce silica membranes on porous α-alumina supports [Asaeda and Yamasaki, 2001]. Two different types of membranes were formed. One membrane was composed of a silica separating layer on top of intermediate silica layer. In the other case, the

intermediate layer consisted of both silica and zirconia. For both membranes, TEOS was used as the silica source. The resulting thickness of both membranes was 1 μm, which is rather large in comparison to most other silica membranes reviewed in literature. Both membranes are compared in Table 1.13.

Table 1.13 CO_2 permeation characteristics of silica/silica & silica/silica/zirconia membranes

Permeation Temp. (°C)	Silica/Silica		Silica/Silica/Zirconia		Ref.
	CO_2 Permeance ($mol \cdot m^{-2} \cdot s^{-1} \cdot Pa^{-1}$)	$\alpha CO_2/N_2$	CO_2 Permeance ($mol \cdot m^{-2} \cdot s^{-1} \cdot Pa^{-1}$)	$\alpha CO_2/N_2$	
35	$6.7x10^{-7}$	18.8	$8.9x10^{-7}$	25.0	Asaeda & Yamasaki, 2001
75	$5.6x10^{-7}$	15.6	$8.0x10^{-7}$	21.2	
100	$4.5x10^{-7}$	12.5	$7.6x10^{-7}$	18.9	
150	$4.2x10^{-7}$	11.9	$6.7x10^{-7}$	16.2	
200	$3.6x10^{-7}$	10.0	$4.5x10^{-7}$	10.5	
300	$2.7x10^{-7}$	7.5	$3.8x10^{-7}$	8.5	

For the membrane with just silica in the intermediate layer, the CO_2 permeance and permselectivity at 35°C was $6.7x10^{-6}$ $mol \cdot m^{-2} \cdot s^{-1} \cdot Pa^{-1}$ and 18.8. At 300°C, those values decreased to $2.7x10^{-7}$ $mol \cdot m^{-2} \cdot s^{-1} \cdot Pa^{-1}$ and 7.5. In the case when the silica-zirconia intermediate layer was involved, the permeance and selectivity were larger than the corresponding data obtained from the silica/silica membrane. For example, at 35°C, the CO_2 permeance was $8.9x10^{-7}$ with a $\alpha CO_2/N_2$ value of 25. The permeance was $3.8x10^{-7}$ $mol \cdot m^{-2} \cdot s^{-1} \cdot Pa^{-1}$ at 300°C with a permselectivity of 8.5. The membrane that included zirconia was very stable when used in humid and dry conditions, whereas the membrane without zirconia was stable only in dry environments. These membranes were believed to have performed well, especially at high temperatures, due to the fact that adsorption of carbon dioxide

was high within the silica layers that were created. The relatively high permselectivities achieved at 300°C make this membrane a potential candidate for high temperature CO_2 separation.

Kang et al. modified γ-alumina membranes with an average pore size of 2.2 nm by coating them with a layer of microporous silica [Kang et al., 1999]. Colloidal silica sols were used to establish the layer of silica. Calcination to form the silica layers was conducted between 200 and 400°C. For the silica/γ-alumina membrane heat treated at 200°C, a CO_2 permeance of 4.9×10^{-7} $mol \cdot m^{-2} \cdot s^{-1} \cdot Pa^{-1}$ and permselectivity of 1.69 was obtained. A subsequent coating of silica and heat treatment at 200°C decreased permeance slightly, but caused the permselectivity to increase to 2.13. Singular coatings at higher calcination temperatures did not improve permselectivity. It was deemed that both Knudsen and surface diffusion were the governing transport mechanisms through this particular membrane.

Xomeritakis et al. prepared microporous silica membranes with the sole purpose of testing them under flue gas conditions [Xomeritakis et al., 2007]. Pure silica, nickel-doped silica and aminosilicate membranes were derived via the sol-gel method. Binary separation of CO_2 and N_2 was carried out at several relative humidities. For aluminosilicate membranes, CO_2 permeance was very low and decreased with increasing relative humidity. For pure silica membranes, separation factors between 50 and 80 could be achieved at a permeation temperature of 25°C and feed mixture of 10/90% CO_2/N_2. Table 1.14 shows the results obtained from several different membranes.

Table 1.14 CO_2 permeance & separation factor for 10/90% CO_2/N_2 for a pure silica membrane

Membrane	CO_2 Permeance ($mol \cdot m^{-2} \cdot s^{-1} \cdot Pa^{-1}$)	$\alpha CO_2/N_2$	Reference
1	$1.9x10^{-7}$	52.7	Xomeritakis et al., 2007
2	$1.0x10^{-7}$	48.6	
3	$1.5x10^{-7}$	78.4	
4	$1.2x10^{-7}$	57.0	
5	$1.8x10^{-7}$	44.5	
6	$1.6x10^{-7}$	59.7	

The low permeance was attributed to the fact that the pore size and porosity were difficult to control with the inclusion of the amino groups within the silica framework. Increased doping of the silica membrane with nickel was seen to improve the separation characteristics. Several membranes with a Ni:Si ratio of 0.1 had separation factors of around 20 for a 10/90% CO_2/N_2 mixture at 25°C. This indicated the relative reproducibility of this particular type of membrane. When the Ni/Si ratio was doubled, the separation factor increased to 92 under the same permeation conditions. The results are tabulated in Table 1.15.

Table 1.15 Permeance & separation factor for Ni-doped silica membranes (10/90% CO_2/N_2)

Ni:Si ratio	CO_2 Permeance ($mol \cdot m^{-2} \cdot s^{-1} \cdot Pa^{-1}$)	$\alpha CO_2/N_2$	Reference
0.1	$3/3x10^{-7}$	21.9	Xomeritakis et al., 2007
	$2.3x10^{-7}$	19.2	
	$3.6x10^{-7}$	16.4	
	$4.3x10^{-7}$	21.7	
0.2	$4.3x10^{-8}$	92.0	

Sakamoto et al. [Sakamoto et al., 2007] produced silica membranes via both the sol-gel and hydrothermal synthesis methods. Membranes formed via the hydrothermal synthesis method produced a silica layer that was 200 nm thick. The layer of silica formed by the sol-gel method was much thicker (500 nm). Measurements were taken for a 20/80% gas mixture of CO_2 and N_2. The membrane formed via hydrothermal synthesis had a CO_2 permeance of $1.0x10^{-7}$ $mol \cdot m^{-2} \cdot s^{-1} \cdot Pa^{-1}$ with a separation factor identical to Knudsen selectivity at 25°C. Under the same permeation conditions, the sol-gel derived silica membrane a permeance about 3 times lower, but selectivity was the same. Both membranes were amine-functionalized and the permeation properties for the same gas mixture were examined at 100°C. The addition of the amines caused the thickness of the hydrothermal silica membrane to increase to 2 μm. No changed was observed for the sol-gel derived membrane. For the amine-modified silica membrane formed by hydrothermal synthesis, a CO_2 permeance of $4.7x10^{-10}$ $mol \cdot m^{-2} \cdot s^{-1} \cdot Pa^{-1}$ separation factor of 50 was obtained. Although the permeance was low, the separation factor was rather high for the given temperature. However, as good as that is, better results were obtained for the sol-gel derived silica membrane after amine functionalization. The permeance of CO_2 through this membrane was nearly twice as good as the prior membrane at $1.0x10^{-9}$ $mol \cdot m^{-2} \cdot s^{-1} \cdot Pa^{-1}$. The major difference between the two was the selectivity, which increased 16-fold to 800. It should be noted that the selectivity of the amine modified sol-gel silica membrane decreased dramatically after 100°C, approaching Knudsen selectivity

near a temperature of 150°C. The superior results obtained from the sol-gel modified membrane were believed to be a result of the thinner, denser separation layer formed during synthesis. The high selectivity values are believed to be the result of repeated adsorption and desorption of CO_2 on the amino-groups while nearly hindering all N_2 transport.

Okubo and Inoue prepared silica membranes by vaporization of TEOS on tubular porous glass substrates [Okubo and Inoue, 1989]. The TEOS vapor that penetrated into the pores of the membrane was subsequently decomposed at 200°C in an oxygen environment to form the silica membrane. The transport mechanism through the porous glass substrate was deemed to be Knudsen diffusion. Upon modification with silica, the mechanism began to shift towards micropore/activated diffusion. However, both the CO_2 permeance (8.0×10^{-10} $mol \cdot m^{-2} \cdot s^{-1} \cdot Pa^{-1}$) and permselectivity (1.6) were quite low at a permeation temperature of 60°C. Sea and Lee produced a silica membrane on a porous γ-alumina supported membrane [Sea and Lee, 2001]. After coating the α-alumina support with a boehmite sol to create the γ-alumina layer, the support was subjected to CVD of TEOS at 600°C to form the silica membrane. Forced cross-flow was employed during CVD to produce better plugging within the mesopores of the support. At a permeation temperature of 250°C, the CO_2 permeance was 3.9×10^{-8} $mol \cdot m^{-2} \cdot s^{-1} \cdot Pa^{-1}$. The permselectivity at this temperature was 4.7. Interestingly enough, upon raising the temperature to 450°C, the CO_2 permeance (4.0×10^{-8} $mol \cdot m^{-2} \cdot s^{-1} \cdot Pa^{-1}$) and permselectivity (4.9) remained relatively

unchanged. The authors explained this result by claiming that the surface diffusion mechanism continued to play a prominent role in separation, even at the increased temperatures.

Gu and Oyama showed that thermally stable microporous silica membranes can be prepared by the high temperature CVD method [Gu and Oyama, 2007]. The pore size of the synthesized membranes was 0.3 nm and the membranes exhibited CO_2 and N_2 permeances of $3.0x10^{-10}$ and $1.25x10^{-10}$ $mol \cdot m^{-2} \cdot s^{-1} \cdot Pa^{-1}$ respectively at 600°C with a CO_2/N_2 permselectivity of only 2.4. The permselectivity achieved is quite high considering the temperature at which the measurements were taken. The high permselectivity is likely a result of the very small pore size of this particular silica membrane. Cuffe et al. prepared microporous silica membranes by high temperature, subatmospheric CVD of silica on microporous Vycor glass membranes [Cuffe et al., 2006]. These membranes were reported to have CO_2/N_2 selectivities of 36 and 75 at 600°C for CVD temperatures of 670 and 600°C respectively. However, CO_2 permeances were on the order of 10^{-10}-10^{-11} $mol \cdot m^{-2} \cdot s^{-1} \cdot Pa^{-1}$, which is far too low to be considered economical for any process involving membranes for CO_2 removal. It was observed that a selectivity of 275 was achieved at 600°C when the CVD temperature was decreased to 500°C, but again, the permeance was on the order of 10^{-12} $mol \cdot m^{-2} \cdot s^{-1} \cdot Pa^{-1}$. While the permselectivity achieved in Cuffe's work is encouraging, the low values for CO_2 permeance leave much to be desired.

Nitodas et al. produced microporous silica membranes using TEOS and ozone (O_3) as the precursors [Nitodas et al., 2008]. Silica was deposited onto γ-alumina supported tubes via the CVD method. Prior to deposition, the support had a CO_2 permeance of 5.77×10^{-8} $mol \cdot m^{-2} \cdot s^{-1} \cdot Pa^{-1}$ and a permselectivity of 0.82, showing that Knudsen diffusion was the governing mechanism for transport through the support. For a silica membrane formed during 1 h of CVD, the CO_2 permeance dropped to 1.24×10^{-8} $mol \cdot m^{-2} \cdot s^{-1} \cdot Pa^{-1}$, but no improvement in permselectivity was achieved. A membrane formed during 9 h of CVD modification had a CO_2 permeance that dropped to 1.10×10^{-10} $mol \cdot m^{-2} \cdot s^{-1} \cdot Pa^{-1}$, but again, no improvement in CO_2/N_2 was observed. Based on the results, it was determined that the membrane was mainly permeable to hydrogen only. The CVD process decreased the pore size too much, thus hindering the transport of larger gases including CO_2 and N_2.

Along with using the sol-gel and CVD methods, silica membranes can also be produced by pyrolysis of silane compounds. Li and Hwang used this method to produce silica membranes on Vycor glass tubes [Li and Hwang, 1991]. To form the silica layer, chlorosilanes were hydrolyzed to form the corresponding silanol. The silanol was then dehydrated, after which point, polymerization took place. After *in situ* polymerization, pyrolysis was carried out between 300 and 530°C for 4-48 h in oxygen, nitrogen or helium at various flow rates. The silane polymer used to form the membrane contained both –Si–C– and –Si–O– bonds. The weaker –Si–C– bonds are broken first, hence leaving behind a network that

consists of –Si–O– bonds within the silica membrane. CO_2 permselectivity was about 12 at room temperature and decreased with increasing temperature up to 200°C. The authors suggested that permeance through the membrane was governed by the activated diffusion mechanism. In later work, Li and Hwang later formed membranes by polymerizing trichloromethylsilane and pyrolyzing the resulting polymer at high temperatures [Li and Hwang, 1992]. Permeation of the corresponding silica membranes was observed between 25 and 680°C. The permselectivity results are summarized in Table 1.16 below.

Table 1.16 CO_2/N_2 permselectivity as function temperature for a pyrolyzed silica membrane

Permeation Temperature (°C)	$\alpha CO_2/N_2$	Reference
25	2.3	Li and Hwang, 1992
50	1.77	
100	1.75	
200	1.71	
300	1.55	
400	1.46	
500	1.41	
600	1.31	
680	1.25	

Although the pyrolyzed silica membrane appeared to remain thermally stable even at the highest recorded temperatures, separation with this membrane was not effective. The table clearly shows that the permselectivities begin trending towards a value of 0.80. However, despite the trend that indicates a transition towards Knudsen diffusion, the authors concluded that better methods to seal the

membranes at high temperatures were required in order to obtain reliable data at such temperatures.

Way and Roberts [Way and Roberts, 1992] and Ma and co-workers [Shelekhin et al., 1992] studied CO_2 permeation and separation through microporous silica hollow fiber membranes prepared by PPG (commercially purchased). The membranes consisted of hollow fibers that had inner and outer diameters of 22 and 32 μm, resulting in a wall thickness of 10 μm. The length of the fibers was 13.5 cm. Unlike carbon hollow fibers, these particular fibers exhibited good flexibility and were easy to handle. At 30°C, the hollow fiber silica membrane had a CO_2/N_2 selectivity of 34. Permeance increased with increasing temperature, but at a cost of decreased permselectivity, which fell to 6.8 at a system temperature of 250°C. The permeation fluxes of CO_2 were somewhat low due to the large wall thickness of the hollow silica fibers. Hassan et al. also used PPG silica hollow fiber membranes for carbon dioxide and nitrogen separation and showed similar results when compared to those of Ma and coworkers [Hassan et al., 1995].

In addition to the work done on carbon membranes, the Kusakabe and Morooka group also investigated the use of silica membranes for CO_2 separation [Kusakabe et al., 1999]. The membranes were prepared using TEOS with octyltriethoxysilane (C8TES), dodecyltriethoxysilane (C12TES) or octadecyltriethoxysilane (C18TES) as the silica source. The chemical formulas structures of C8TES, C12TES and C18TES are shown in Figure 1.14.

Octyltriethoxysilane (C8TES)

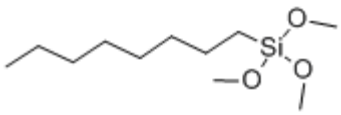

Dodecyltriethoxysilane (C12TES)

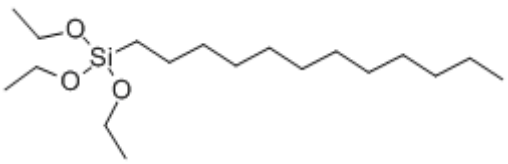

Octadecyltriethoxysilane (C18TES)

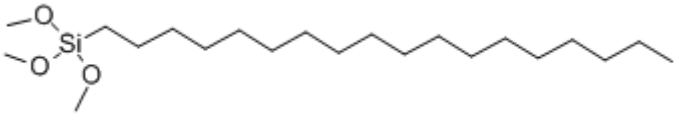

Figure 1.14 Chemical formulas and structures for octyltriethoxysilane (C8TES), dodecyltriethoxysilane (C12TES) and octadecyltriethoxysilane (C18TES)

The use of the different silica precursors in the sols led to the formation of membranes with different pore sizes. The large alkyl substituents in C18TES led to the formation of mesopores. As a result, the structure was not able to withstand shrinkage during calcination. Hence, transport and subsequent separation through the TEOS/C18TES silica derived membrane was controlled by Knudsen diffusion. On the other hand, crack-free silica membranes were formed with the TEOS/C8TES and TEOS/C12TES sols. For the C8TES membrane, an $[H_2O]/[C8TES+TEOS]$ ratio of 4 gave high permeances but poor α_{CO_2/N_2} values. When the ratio was decreased to 1, the permeances were lower, but with greatly improved permselectivities. Slightly lower permselectivities were observed for the membrane formed from the TEOS and C12TES mixture. The group also investigated the effect of using different silica sources during CVD on the permeation properties of the membrane. In the work, TEOS,

phenyltriethoxysilane (PTES) and diphenyldiethoxysilane (DPDES) were used as the silica sources (Figure 1.15) during CVD [Sea et al., 1997].

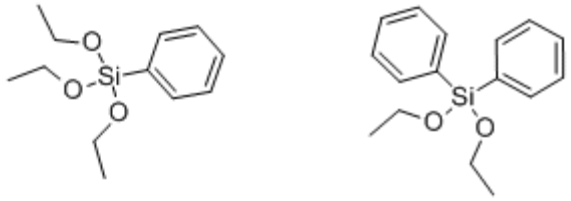

Figure 1.15 Structures phenyltriethoxysilane (PTES) & diphenyldiethoxysilane (DPDES)

The results obtained from silica membranes derived from the three different precursors are shown in Table 1.17.

Table 1.17 CO_2 permeation characteristics of TEOS, PTES and DPDES silica membranes

Precursor	Permeation Temperature (°C)	CO_2 Permeance ($mol \cdot m^{-2} \cdot s^{-1} \cdot Pa^{-1}$)	$\alpha CO_2/N_2$	Reference
TEOS	30	$3.6x10^{-10}$	0.72	Sea et al., 1997
	200	$3.3x10^{-10}$	0.66	
PTES	30	$8.0x10^{-9}$	5.0	
	200	$1.0x10^{-8}$	5.9	
DPDES	30	$8.1x10^{-8}$	8.9	
	200	$3.3x10^{-9}$	4.2	

Permeances achieved with the TEOS derived membrane were low, on the order of 10^{-10} $mol \cdot m^{-2} \cdot s^{-1} \cdot Pa^{-1}$ with permselectivities less than Knudsen. PTES derived silica membranes had permeances that were an order of magnitude higher at 10^{-9} $mol \cdot m^{-2} \cdot s^{-1} \cdot Pa^{-1}$ with CO_2/N_2 permselectivities 5 and 5.9 at 30 and 200°C. The best performance was achieved with the DPDES silica membrane, which gave permeances on the order of 10^{-8} $mol \cdot m^{-2} \cdot s^{-1} \cdot Pa^{-1}$ and CO_2/N_2 values of 8.9 and 4.2

at 30 and 200°C. It was explained that the DPDES membrane gave the best separation performance because the entire membrane was completely microporous whereas the other two had some aspects of mesoporosity. Seeing as how the DPDES membrane gave the best performance of the three, further measurements were taken to compare the results of single and binary gas permeation. The results are summarized in Table 1.18.

Table 1.18 Single and binary component permeation through DPDES silica membrane (S = single, B = binary component separation)

Permeation Temp. (°C)	Helium Sweep		Argon Sweep		Ref.
	CO_2 Permeance ($mol \cdot m^{-2} \cdot s^{-1} \cdot Pa^{-1}$)	$\alpha CO_2/N_2$	CO_2 Permeance ($mol \cdot m^{-2} \cdot s^{-1} \cdot Pa^{-1}$)	$\alpha CO_2/N_2$	
30 (S)	8.1×10^{-8}	8.9	2.1×10^{-8}	0.98	Sea et al., 1997
200 (S)	3.3×10^{-8}	4.2	1.9×10^{-8}	0.85	
30 (B)	1.4×10^{-8}	1.4	2.3×10^{-8}	1.1	
200 (B)	1.5×10^{-8}	1.5	2.1×10^{-8}	0.97	

The permselectivities of CO_2 at 30 and 200°C suggest that the DPDES membrane is controlled by surface diffusion. However, the selectivities achieved during binary separation were unexpectedly low. The belief was that the DPDES membrane could contain three different kinds of pores: M_S pores which are completely impermeable to CO_2 and N_2; M_M pores which are permeable to both CO_2 and N_2; and M_K pores that belong to the Knudsen regime. For the DPDES membrane, only M_M pores are of any concern. Within these pores, diffusion is rate-limited by the slowest moving component, N_2. As a consequence, the permeation characteristics for binary mixtures produced lower permeances and separation factors than seen during single component permeation.

Figure 1.16 depicts the Robeson-type plot that shows the relationship between CO_2 permeability and α_{CO_2/N_2} for the silica membranes discussed in this review. At first sight, it is noticeable that silica membranes, unlike polymers, have no upper bound region in the Robeson-type plot. The figure also shows that silica membranes have very high permeabilities. This results from the fact that the membranes are rather thin. Specifically, several synthesis methods were shown to produce silica membranes that were only tens to hundreds of nanometers thick. In comparison, carbons and zeolites are often in the 1-10 micron range, and therefore have decreased permeabilities by virtue of lower permeances. The selectivities, permselectivities and separation factors derived from these membranes are low because of the difficulty in producing completely defect-free membranes. In order to become a viable separation option, α values will need to be increased by several factors while maintaining the already high permeabilities. Figure 1.17 shows a plot of CO_2/N_2 dependency on permeation temperature through silica membranes. Like CMS membranes, silica membranes show good separation characteristics near room temperature. However, as permeation temperature increases, so do the $\alpha_{CO2/N2}$ values. Again, the drop appears to be proportional to $1/T^{½}$ which means that Knudsen diffusion becomes a key transport mechanism at high temperature.

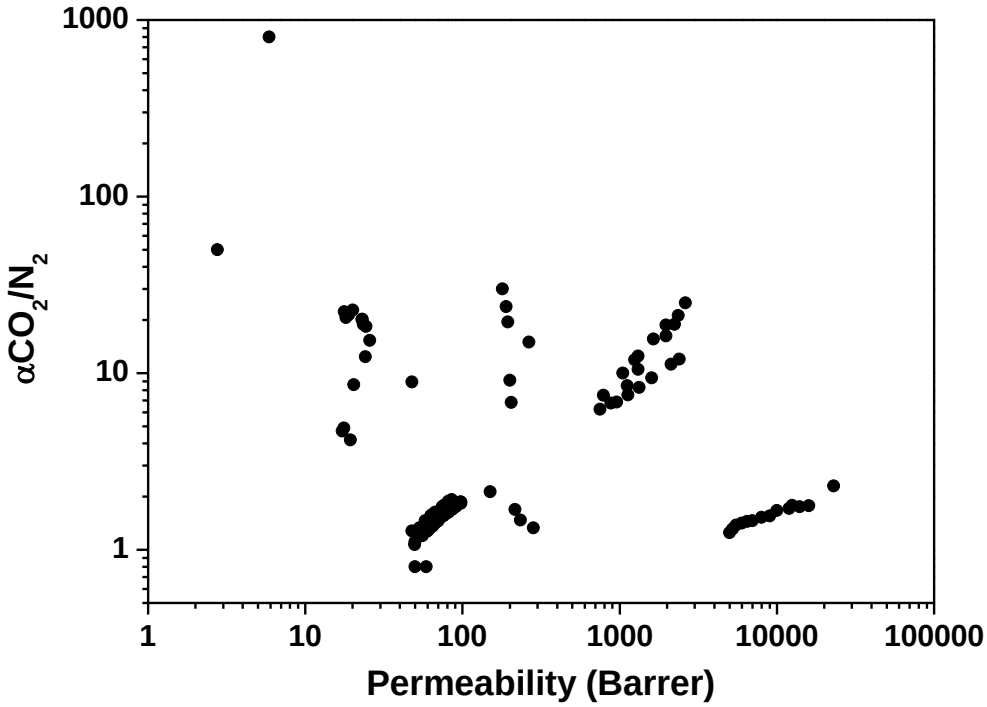

Figure 1.16 CO_2/N_2 Robeson plot for silica membranes

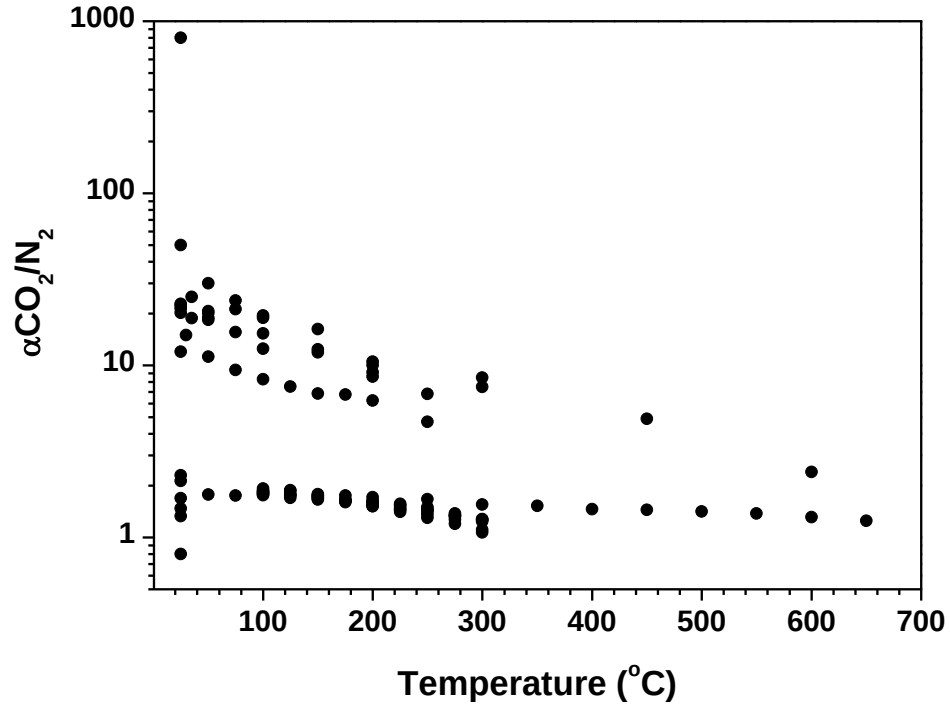

Figure 1.17 α_{CO_2/N_2} dependency on permeation temperature for silica membranes.

1.3.4 Zeolite membranes

Zeolites are another type of material that is commonly used for inorganic membranes because they exhibit exceptional thermal and chemical stability. Zeolites are crystalline aluminosilicates that are composed of different pore connectivities resulting from various connections of TO_4 tetrahedrals (T = Si or Al) [Lin et al., 2002]. There are nearly 200 different families of zeolite frameworks that have been documented [Baerlocher & McCusker, 2011]. Structures vary based on several factors, but are mainly a result of the Si/Al ratio used and synthesis route taken (i.e., hydrothermal synthesis, secondary growth etc.). The combination of molecular sieving capabilities and unique adsorption

characteristics make these zeolites particular useful for separation of CO_2. These membranes can be further tailored for CO_2 separation by addition of cations within the structure via ion-exchange. This is especially true in Y-type and ZSM-5 zeolites.

Of all the zeolites examined for separation of CO_2 and N_2, Y-type is one of the most common. Y-type zeolites belong to the faujasite family of zeolite structures. The structure (Figure 1.18) and characteristics (Table 1.19) of Y-type zeolite are given as indicated [Baerlocher & McCusker, 2011].

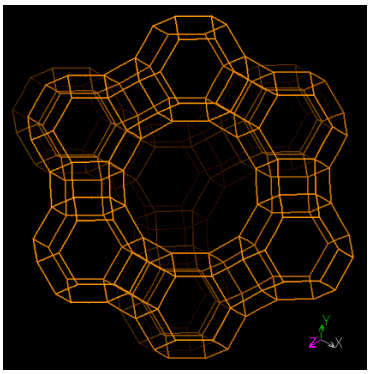

Figure 1.18 Structure of Y-type zeolite

Table 1.19 Characteristics of Y-type zeolite

Space Group	Fd-3m
Cell Parameters	a = b = c = 24.345Å
	$\alpha = \beta = \gamma = 90°$
Cell Volume	14428.77Å^3
Ring Sizes (# of T atoms)	12, 6, 4
Viewing Plane	[111]

These zeolites are characterized by having rather large apertures (pore openings), and is made with Si/Al ratios ranging from 1.5 to 3.0.

As was the case for both carbon and silica membranes, Kusakabe and Morooka have done a considerable amount of research on Y-type zeolite membranes for CO_2 and N_2 separation [Kusakabe et al., 1997]. Y-type zeolite membranes were formed on the outer surface of a tubular α-alumina support by hydrothermal synthesis at 90°C for 6, 12 or 24 h. These membranes will be respectively referred to as A, B and C. Permeance measurements were conducted between 30 and 130°C. Membranes A and B exhibited CO_2 permeances on the order of 10^{-7} $mol \cdot m^{-2} \cdot s^{-1} \cdot Pa^{-1}$ with a CO_2/N_2 selectivity ranging from 20-100 at 30°C. The selectivity decreased to 8-15 at a permeation temperature of 130°C. Membrane C showed a CO_2 permeance that ranged between 3.0×10^{-7} and 9.0×10^{-7} $mol \cdot m^{-2} \cdot s^{-1} \cdot Pa^{-1}$ and a CO_2/N_2 selectivity of 50-75 at 30°C. CO_2 permeance was nearly identical regardless of whether or not a single or binary gas mixture was used. The similarity between single and binary mixtures was due to the pore-size controlled adsorption of CO_2 that led to a narrowing of the pores within the zeolite structure. As such, N_2 was obstructed from permeating through the membrane. Work was extended to determine the permeation properties of ion-exchanged Y-type zeolite membranes [Kusakabe et al., 1998]. Here, Li^+, Na^+ and K^+ ions were incorporated into the zeolite matrix in the hopes of increasing CO_2 affinity within the pores. The zeolite membranes were placed into solutions of LiCl, KCl, $MgCl_2$, $CaCl_2$ or $BaCl_2$ to accomplish the necessary cation exchange. The LiY zeolite membrane gave the highest CO_2 permeance (2.0×10^{-6} $mol \cdot m^{-2} \cdot s^{-1} \cdot Pa^{-1}$) but also the lowest separation factor (3.5). The best overall separation

characteristics were achieved with the KY zeolite membrane, which had a rather high permeance of $1.4x10^{-6}$ $mol \cdot m^{-2} \cdot s^{-1} \cdot Pa^{-1}$ and a separation factor of 30.3. The results for all of the ion-exchanged membranes at a permeation temperature of 40°C are shown in Table 1.20.

Table 1.20 Permeation properties of ion-exchanged (Li^+, Na^+, K^+, Mg^{2+}, Ca^{2+}, Ba^{2+}) zeolites

Precursor	CO_2 Permeance ($mol \cdot m^{-2} \cdot s^{-1} \cdot Pa^{-1}$)	$\alpha CO_2/N_2$	Reference
LiCl	$2.0x10^{-6}$	3.5	Kusakabe et al., 1998
NaCl	$1.3x10^{-6}$	19.6	
KCl	$1.4x10^{-7}$	30.3	
$MgCl_2$	$3.3x10^{-7}$	20.5	
$CaCl_2$	$5.0x10^{-7}$	11.8	
$BaCl_2$	$9.0x10^{-7}$	23.7	

In the same set of work, NaX zeolite membranes were formed by decreasing the Si/Al ratio of the starting solution. Si/Al ratios[4] of 1.22, 1.54 and 2.18 were investigated. Overall, the membranes exhibited lower CO_2 permeances but higher selectivities than the NaY-type membranes.

Kusakabe continued work with ion-exchanged NaY-type zeolite membranes produced via hydrothermal synthesis [Kusakabe et al., 1999]. In addition to producing NaY zeolite membranes, additional membranes were ion-exchanged with Li^+ and K^+. The zeolite layers formed in this study were said to be 3 μm thick. Single and binary gas permeations experiments were carried out at 35°C. Although permeance depended on the sample being tested, CO_2/N_2

[4] The Si/Al ratio of 1.22 forms the X-type zeolite membrane

selectivity and permselectivity depended on the type of ion present in the zeolite matrix ($K^+ > Na^+ > Li^+$). For the KY zeolite membrane, the single and binary separation factors were 9.1 and 47.6 respectively. For the NaY membrane, α_{CO_2/N_2} was similar to that of the KY membrane at 8.9; however, the binary separation factor, 30.0, was quite a bit lower. The Li^+ exchanged membrane had the lowest single (3.1) and binary (9.9) α_{CO_2/N_2} of all the membranes observed. The increase in α_{CO_2/N_2} for binary gas mixtures shows that the selective adsorption of CO_2 within the ion-exchanged pores of the Y-type zeolite membranes effectively blocks permeation of N_2.

Additional work was conducted on the incorporation of different alkali metal cations using solutions of KCl, RbCl or CsCl [Hasagawa et al., 2001]. These membranes were compared to the standard NaY zeolite membrane. The degrees of ion exchange were 62%, 40% and 32% for K^+, Rb^+ and Cs^+ respectively. Permeation behavior of the membranes was investigated at 35°C for both single and binary gas mixtures of CO_2 and N_2. Membrane performance increased in the order of $Rb^+ = K^+ > Cs^+ > Na^+$. The inclusion of Rb^+, Cs^+ and Na^+ did not have a drastic effect on the permeance, but it did cause the separation factors to nearly double in comparison to the NaY zeolite membrane. For the NaY zeolite membrane, a binary separation factor of 19 was obtained. However, inclusion of K^+, Rb^+ and Cs^+ caused the separation factors to increase to 39, 40 and 34 respectively. These results are summarized in Table 1.21.

Table 1.21 $\alpha CO_2/N_2$ selectivities and permselectivities for Na^+, K^+, Rb^+ and Cs^+ Y-type zeolites

Cation	Single component	Binary component	Reference
	$\alpha CO_2/N_2$	$\alpha CO_2/N_2$	
Na	5.4	19	Hasagawa et al., 2001
K (62%)	5.6	39	
Rb (40%)	3.2	40	
Cs (32%)	2.2	34	

Investigations on the effect of Si/Al ratios in zeolite membranes continued [Hasagawa, 2002]. This time, NaY and NaX membranes were compared. For the NaY membrane (Si/Al = 1.54), a CO_2 permeance of $1.4x10^{-6}$ $mol \cdot m^{-2} \cdot s^{-1} \cdot Pa^{-1}$ was obtained. Single and binary values of $\alpha CO_2/N_2$ were 6 and 30 respectively. When the Si/Al ratio was decreased to 1.26 and 1.16 (NaX-type zeolites), the CO_2 permeance dropped slightly, but the binary separation factor increased by more than a factor of two. The incorporation of Rb^+ into the X-type membranes caused an increase in the permeance of both CO_2 and N_2. No improvement was seen for $\alpha CO_2/N_2$. Rb^+ and K^+ were then ion-exchanged into Y-type zeolite membranes. The Rb^+ exchanged Y-type membrane exhibited a permeance of around $8.0x10^{-7}$ $mol \cdot m^{-2} \cdot s^{-1} \cdot Pa^{-1}$ with separation factors between 65 and 90. The KY membrane exhibited CO_2 permeances from $8.0\text{-}14.0x10^{-7}$ $mol \cdot m^{-2} \cdot s^{-1} \cdot Pa^{-1}$ and separation factors from 65-105. The increased selectivities from the K^+ and Rb^+ ion-exchanged membranes indicate that the addition of the cations decreases the pore size of the zeolite ever so slightly, but at the same time, causes a significant

increase in the adsorption of CO_2 within the pores. As a result, higher permeance and selectivities were achieved.

Gu et al. produced defect-free NaY-type zeolite membranes and investigated CO_2 and N_2 separation in both dry and humid atmospheres [Gu et al., 2005]. For the humidified mixture, the permeance of both CO_2 and N_2 increased with temperature, with a maximum selectivity occurring at 140°C. The increase in permeance of both components at high temperatures occurs as a result of water desorption, which leads to easier diffusion of the components. With that said, both the CO_2 permeance and selectivities of the humid mixture are very low. Transport of CO_2 could only occur through the intercrystalline gaps in the membrane because the zeolitic pores were blocked with adsorbed water. As one might expect, CO_2 permeance and selectivities with the dry gas mixture were higher than that of the moistened system. For dry CO_2 and N_2, the membrane exhibited a CO_2/N_2 selectivity of about 31.2 with a permeance of about 2.1×10^{-8} $mol \cdot m^{-2} \cdot s^{-1} \cdot Pa^{-1}$. In this instance, CO_2 acts in a similar fashion to water in the humid system. The zeolitic pores become blocked with the adsorbed CO_2 molecules, hence N_2 can only permeate through the intercrystalline gaps. This explains why the CO_2 permeance and CO_2/N_2 are greater for the dry system than in the system that contains water vapor.

Recent success using ultrathin Y-type zeolite membranes was achieved by Verweij and coworkers [White et al., 2010]. The characteristics of zeolite layers grown both slowly (days) and rapidly (hours) were examined. Rapidly grown

membranes had zeolite layers close to 2 μm thick. The slowly grown zeolite layer showed a composite structure having a dense layer with a thickness of 350-600 nm covered by a rather thick and very porous layer (25 μm). The rapidly grown zeolite membrane had a low CO_2 permeance of $2.9x10^{-9}$ $mol \cdot m^{-2} \cdot s^{-1} \cdot Pa^{-1}$ and high permselectivity of at least 550 at 30°C. Similar values for permeance and permselectivity were obtained at 130°C with the same membrane. The thinner but denser Y-type zeolite membrane exhibited slightly higher permeances than the aforementioned membrane. Permselectivities from the thinner membrane were 503 and 41 at 30 and 130°C respectively. The permselectivity value of 41 at 130°C is especially promising and shows that ultrathin Y-type zeolites may be potential suitors for high temperature CO_2 separation from flue gas.

Along with Y-type zeolite membranes, ZSM-5 membranes have also been investigated at length for this particular application. ZSM-5 is part of the MFI family of zeolites. The structure of ZSM-5 and other MFI-type zeolites is shown in Figure 1.19, while the characteristics of the material are described in Table 1.22 [Baerlocher & McCusker, 2011].

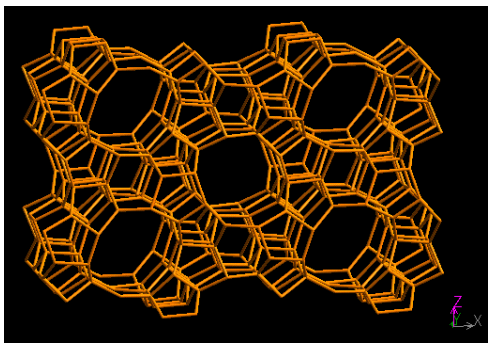

Figure 1.19 Structure of ZSM-5 zeolite

Table 1.22 Characteristics of ZSM-5 zeolite

Space Group	Pnma
Cell Parameters	a = 20.090Å b = 19.739Å c = 13.124Å
	$\alpha = \beta = \gamma = 90°$
Cell Volume	5211.28Å^3
Ring Sizes (# of T atoms)	10, 6, 5, 4
Viewing Plane	[010]

Kusakabe et al. investigated the production of ZSM-5 membranes via hydrothermal synthesis on porous α-alumina supports [Kusakabe et al., 1996]. Fine silica powder was used as the silica source while the template was tetrapropylammoniumhydroxide and bromide. Calcination of the membrane was carried out at either 400 or 550°C. This particular synthesis route produced a membrane with three distinct layers. The top layer consisted of a polycrystalline zeolite layer, while the intermediate layer was a mixture of zeolite deposits and α-alumina particles. The base layer consisted of zeolitic deposits within the pores of the support. Permeation measurements were conducted at 30, 60 and 100°C. The membranes calcined at 540°C had higher permeances, but slightly lower permselectivities. For permeation at 100°C, the membrane calcined at 540°C had a permeance of 2.0×10^{-7} $mol \cdot m^{-2} \cdot s^{-1} \cdot Pa^{-1}$ and a permselectivity of about 6. In comparison, the membrane calcined at 400°C had a permeance of just 6.0×10^{-9} $mol \cdot m^{-2} \cdot s^{-1} \cdot Pa^{-1}$ and only a slightly higher permselectivity (8.7). Lovallo et al. also synthesized ZSM-5 membranes, but unlike Kusakabe, synthesized the membranes on disks, rather than tubes [Lovallo et al., 1998]. During permeation

experiments, a significant difference in CO_2 permeance was observed as the amount of CO_2 in the feed increased. This observation was further pronounced at higher temperatures. As expected, the separation factor increased at first, then decreased as temperature rose. The decrease was due to limited CO_2 sorption within the zeolite membrane in the higher temperature regime. With that said, the membrane still exhibited good separation characteristics at moderately high temperatures. For example, at a permeation temperature of 180°C and feed composition containing 60% CO_2, the membrane had a CO_2 permeance of about $2.0x10^{-8}$ $mol \cdot m^{-2} \cdot s^{-1} \cdot Pa^{-1}$ and a selectivity of about 20.

Hyun et al. synthesized ZSM-5 zeolite membranes and evaluated their ability to separate CO_2 and N_2 [Hyun et al., 1999]. Two different membrane synthesis routes were taken to determine the effect each had on the permeation properties of the membranes. In one case, the ZSM-5 membranes were prepared by a dip-coating hydrothermal treatment (DH). The other membrane was subjected to a pressurized coating hydrothermal treatment (PH). From SEM images, it appeared that the DH-ZSM-5 membranes were about 2-3 μm thick. PH-ZSM-5 membranes appeared to be 10 times thicker. For the DH membrane, CO_2 permeance increased as temperature rose. N_2 permeance decreased initially and finally leveled out at high temperature. The maximum separation factor achieved was just 2.5 at 120°C. The membrane formed by the PH method had a maximum separation factor of 9 at room temperature. However, CO_2 permeances from this membrane were lower because of the thicker zeolite layer created by the

PH method. The separation factors for both membranes were higher than the permselectivities. As has been the case in several other works chronicled in this review, the higher separation factors relative to the permselectivities are a result of the adsorption of CO_2 and subsequent pore blockage, effectively keeping N_2 from permeating as easily as it would during single gas permeation.

Similar to the work done with ion-exchanged Y-type zeolite membranes, Aoki et al. performed ion-exchange with ZSM-5 zeolite membranes having Si/Al ratios of 25 and 600 [Aoki et al., 2000]. Chloride solutions containing NH_4^+, Na^+, Cs^+, K^+, Ba^{2+} and Ca^{2+} were used for the ion exchange portion of the study. CO_2 permeances for the ion-exchanged and Si/Al(600) membrane were low. The highest CO_2 permeance achieved was from the H-ZSM-5 (ion-exchanged with NH_4^+) which was 8.5×10^{-8} $mol \cdot m^{-2} \cdot s^{-1} \cdot Pa^{-1}$ with a permselectivity of about 2 at 50°C. Similar values for α_{CO_2/N_2} have also been reported by others [Bernal et al., 2004]. For the membranes formed using a Si/Al ratio of 25, the highest permeances were obtained from the Na^+ and NH_4^+ ion-exchanged membranes. For permeation of single gases with the Si/Al(25) membranes, CO_2 permeance increased in the order of $NH_4^+ = Na^+ > Cs^+ > Ca^{2+} > Ba^{2+} > K^+$. The order shown happens to correspond with decreasing in cation size, with Cs^+ being the lone exception.

Shin et al. reported on the modification of ZSM-5 zeolite membranes by coating them with a polymeric silica sol [Shin et al., 2005]. The use of the polymeric sol was to minimize gas permeation through the intercrystalline gaps

created in the zeolite structure. At 25°C, the membrane had a CO_2 permeance of $3.6x10^{-8}$ $mol \cdot m^{-2} \cdot s^{-1} \cdot Pa^{-1}$ and a permselectivity of 54.3. Upon increasing the temperature to 100°C, permselectivity fell to 14.9, while CO_2 permeance increased to $1.25x10^{-7}$ $mol \cdot m^{-2} \cdot s^{-1} \cdot Pa^{-1}$. Unlike the results obtained from Gu et al., moisture had a negligible effect on the separation factor. Overall, the CO_2 permeation through the membranes developed by Shin et al. was believed to be controlled by both the adsorption/surface diffusion mechanisms in conjunction with activated micropore diffusion. Transport of nitrogen was governed by only micropore diffusion.

Silicalite membranes also fall into the MFI family of zeolites. In a silicalite membrane, the Si/Al ratio is essentially infinite – that is, there is no aluminum added to the synthesis solution. Bakker et al. produced silicalite-1 membranes on stainless steel supports [Bakker et al., 1997]. The support was 3 mm thick and was covered with smooth metal wool having a thickness between 50 and 150 μm. After synthesis, the zeolite membrane was formed on the smooth surface after calcination at 400°C. The resulting silicalite layer had a thickness between 50 and 60 μm. A maximum permselectivity of 2.4 was achieved at 30°C with the membrane. The corresponding CO_2 permeance was $3.2x10^{-7}$ $mol \cdot m^{-2} \cdot s^{-1} \cdot Pa^{-1}$. When the permeation temperature was raised to 400°C, CO_2 permeance decreased to $1.3x10^{-7}$ $mol \cdot m^{-2} \cdot s^{-1} \cdot Pa^{-1}$ and permselectivity was just 1.4. The authors came to the conclusion that the silicalite-1 membrane operated under two different diffusion mechanisms. At low temperatures, adsorption was a key

factor. In this regime, diffusion takes place by mass transport of the adsorbing species. However, at high temperature, little to no adsorption takes place. Here, diffusion of gases is defined by gas translational diffusion. Additional work was conducted to verify the existence of two different diffusion mechanisms. It was verified that permeance through the silicalite-1 membrane is controlled by the two diffusion mechanisms initially presumed [van den Broeke et al., 1999]. It was also shown that the separation factor would be nearly identical to the permselectivity if the gas mixture contained two weakly adsorbing species (i.e., N_2 and CH_4) [van den Broeke et al., 1999]. However, for the case when one of the components is an adsorbing gas (i.e., CO_2), permeation of the non-adsorbing species would be reduced for a binary mixture.

In an effort to enhance the properties of a silicalite-1 membrane, Wirawan modified the membranes by impregnating them with calcium via use of a calcium nitrate solution [Wirawan, 2010]. Prior to impregnation, the membranes exhibited very high permeances ($1.3x10^{-5}$ $mol \cdot m^{-2} \cdot s^{-1} \cdot Pa^{-1}$), but the permselectivities were very low (1.0). After modification, the permeance of the membranes dropped by an order of magnitude, but the separation factors doubled due to the addition of Ca sites in the zeolite.

Another type of zeolite membrane that has been researched for CO_2 and N_2 separation is SAPO-34 (silicoaluminophosphate). A structural view of this particular zeolite is given in Figure 1.20. The cell parameters, angles and other characteristics are presented in Table 1.23 [Baerlocher & McCusker, 2011].

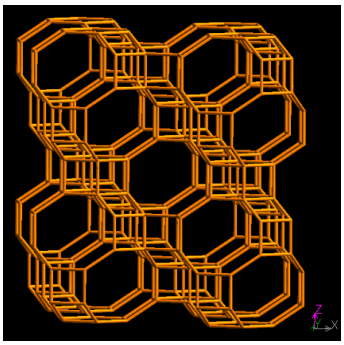

Figure 1.20 Structure of SAPO-34 zeolites

Table 1.23 Characteristics of SAPO-34 zeolites

Space Group	R-3m
Cell Parameters	a = b = 13.675Å c = 11.919Å
	α = β = 90° γ = 120°
Cell Volume	2391.59Å^3
Ring Sizes (# of T atoms)	8, 6, 4
Viewing Plane	[010]

Poshusta et al. prepared such membranes via in-situ synthesis on porous α-alumina support tubes [Poshusta et al., 1998]. For single gas permeation at a feed pressure of 270 kPa (ΔP = 138 kPa), N_2 permeance was relatively constant from 27-200°C. On the other hand, CO_2 permeance dropped from $2.4x10^{-8}$ $mol \cdot m^{-2} \cdot s^{-1} \cdot Pa^{-1}$at 27°C to about $1.0x10^{-8}$ $mol \cdot m^{-2} \cdot s^{-1} \cdot Pa^{-1}$ at 200°C. This resulted in a permselectivity decrease from 6.0 to 2.0. Another study by Poshusta et al. was conducted using a slightly different synthesis procedure to make the SAPO-34 membranes [Poshusta et al., 2000]. Here, the crystallization rate was reduced by increasing the synthesis temperature from 175 to 185°C and decreasing the synthesis time from 24 to 20 h. For a membrane subjected to up and downstream

pressures of 270 kPa and 138 kPa respectively, permeance varied from $6.0x10^{-8}$ $mol \cdot m^{-2} \cdot s^{-1} \cdot Pa^{-1}$ at 30°C to $1.5x10^{-8}$ $mol \cdot m^{-2} \cdot s^{-1} \cdot Pa^{-1}$at 200°C. The corresponding separation factors were 5 and 1.9. For binary gas mixtures, the ideal selectivity at the same temperatures was 16-20 and 2.5-2.8 respectively.

Li and Fan produced SAPO-34 membranes by using multiple templates and reductions in the crystallization time [Li and Fan, 2010]. For a 50/50 mixture of CO_2/N_2 at 22°C, a permeance of $1.2x10^{-6}$ $mol \cdot m^{-2} \cdot s^{-1} \cdot Pa^{-1}$ and a separation factor of 32 were achieved. Upon raising the temperature to 200°C, the permeance and separation factor dropped to $2.5x10^{-7}$ $mol \cdot m^{-2} \cdot s^{-1} \cdot Pa^{-1}$ and 6.0. During the tests, the aforementioned membrane was subjected to up and downstream pressures of 240 and 102 kPa respectively. CO_2 permeance increased upon creating a vacuum on the downstream side of the membrane by virtue of increasing the driving force. Permeance of CO_2 and N_2 was identical for single gas and binary gas mixtures. Addition of 8% water to the feed had no effect on CO_2 and N_2 permeance over the long term, as the separation factor remained at 10 for more than 40 h. From the results, the authors concluded that the selectivity of the SAPO-34 membranes could be further improved by post-treatment of the membrane to further reduce the SAPO pores to below that of the kinetic diameter of N_2. This would allow for the membrane to separate based on molecular size of the permeating components.

Venna and Carreon [Venna and Carreon, 2011] recently examined the separation characteristics of amino-functionalized SAPO-34 zeolite membranes.

Ethylenediamine (ED) was used to functionalize the membranes with amine groups. Permeation measurements were conducted at 22°C and at a feed pressure of 138 kPa. For a non-functionalized SAPO-34 membrane, a CO_2 permeance of $1.1x10^{-7}$ $mol \cdot m^{-2} \cdot s^{-1} \cdot Pa^{-1}$and selectivity of 29 was achieved. Optimal performance was found when 0.33 mmol of ED was used during synthesis. In this scenario, a CO_2 permeance of $2.0x10^{-7}$ $mol \cdot m^{-2} \cdot s^{-1} \cdot Pa^{-1}$ and selectivity of 39 was obtained. Loading with 8.32 mmol of ED produced a membrane with nearly identical permeance but a selectivity that decreased by more than half.

The last type of membrane that has been extensively studied for CO_2 separation is an A-type zeolite, which is shown in Figure 1.21 along with the various characteristics in Table 1.24 [Baerlocher & McCusker, 2011].

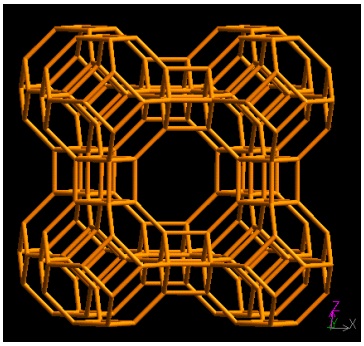

Figure 1.21 Structure of A-type zeolite

Table 1.24 Characteristics of A-type zeolite

Space Group	Pm-3m
Cell Parameters	a = b = c = 11.919Å
	$\alpha = \beta = \gamma = 90°$
Cell Volume	1693.24Å^3
Ring Sizes (# of T atoms)	8, 6, 4
Viewing Plane	[100]

The Kusakabe/Morooka group has also investigated A-type zeolites for CO_2 separation [Aoki et al., 1998]. A-type zeolite membranes fabricated after 5 h of synthesis are denoted as Membranes A and B. The membrane synthesized for 4 h was labeled Membrane C. Membrane A exhibited a CO_2 permeance of $1.0x10^{-8}$ mol·m^{-2}·s^{-1}·Pa^{-1} at 35°C. However, the N_2 permeance was identical to that of CO_2, giving a poor CO_2/N_2 permselectivity of only 1.0. Membrane B showed remarkable resistance to changes in permeance with increasing temperature, as the permeance remained constant at $2.0x10^{-9}$ mol·m^{-2}·s^{-1}·Pa^{-1} from 35-300°C. Membrane C showed similar behavior to that of Membrane B between 35 and 100°C. However, the poor permselectivities achieved in this work, none of which exceeded 2, led the authors to conclude that membrane reproducibility is the key to the success of using such membranes (i.e., zeolites) for practical applications. Although Membrane A and B were made under identical conditions, the permeation results from each varied quite dramatically. The removal of non-zeolitic pores would be critical in making these membranes viable candidates for CO_2 separation. Later work was conducted to determine the effect of water on CO_2 permeation through A-type zeolite membranes [Aoki et al.,

2000]. For single gas permeation, the CO_2 permeance was roughly $3.5x10^{-10}$ $mol \cdot m^{-2} \cdot s^{-1} \cdot Pa^{-1}$ from 30-200°C. CO_2/N_2 permselectivities in this case were 0.7, which is actually less than Knudsen selectivity. When water was included in the feed, the CO_2 and N_2 permeance actually increased. In this scenario, the CO_2 permeance was found to be $2.5x10^{-9}$ $mol \cdot m^{-2} \cdot s^{-1} \cdot Pa^{-1}$ with a permselectivity of about 1.7 for the same range of temperatures. The explanation given for the increased permeance of CO_2 in the presence of water was due to the fact that carbon dioxide has an affinity for water. This affinity makes it possible for CO_2 molecules to become entrained within the pores along with the water molecules. Because water moves through the membrane with a higher permeation flux, the CO_2 moves with it leading to higher permeances than observed during single gas permeation.

Finally, Zhou et al. looked into the formation of a NaA zeolite and carbon nanocomposite thin film for CO_2 and N_2 separation [Zhou et al., 2007]. To form this composite membrane, nanosized zeolites were synthesized and added to a novolak-type phenolic resin solution. The solution was dip-coated onto tubular α-alumina supports and pyrolyzed in N_2 at 600°C for 2 h. The resulting film was estimated to be 1-2 μm thick from SEM images. Before coating with the composite film, the support had a CO_2 permeance of $6.5x10^{-5}$ $mol \cdot m^{-2} \cdot s^{-1} \cdot Pa^{-1}$ and a separation factor of just 1.0. After coating the film on the support, CO_2 permeance dropped to $3.4x10^{-7}$ $mol \cdot m^{-2} \cdot s^{-1} \cdot Pa^{-1}$, but the separation factor

increased six-fold. Additional work would be required with this particular type of membrane to make it a useful candidate for CO_2 removal from flue gas.

A Robeson-type plot for zeolite membranes intended for CO_2 and N_2 separation is shown in Figure 1.22. Like the case for silica membranes, no upper bound region can be distinguished in the figure. Furthermore, of the three major categories of microporous membranes discussed (carbons, silicas and zeolites), zeolites seem to have the best combination of permeability and separation factors. In fact, a good portion of the zeolite membranes reviewed have permeabilities ranging from 10,000 to 100,000 Barrer and corresponding α_{CO_2/N_2} values as high as 550. Furthermore, the data appears to be less scattered than that for carbon and silica membranes indicating the relative reproducibility of zeolite membranes. However, high separation factors are generally achieved for zeolites only when binary mixtures of CO_2 and N_2 are used due to the very good sorption characteristics of CO_2 within the pores of these materials that helps block permeation of N_2. Figure 1.23 shows the temperature dependence of α_{CO_2/N_2} in zeolite membranes. Like carbon and silica membranes, zeolites also suffer from decreasing α values as temperature increases. At room temperature, the values for CO_2/N_2 were as high as 550, but as the temperature approached 200°C, the values decreased closer to that of which is predicted by Knudsen diffusion. The decrease of CO_2/N_2 in accordance with temperature seems to be, once again, proportional to $1/T^{½}$. To achieve better selectivity, either zeolites with smaller apertures will need to be used or the characteristics of the membrane will need to

be tailored to allow for greater adsorption of CO_2 under high temperature conditions.

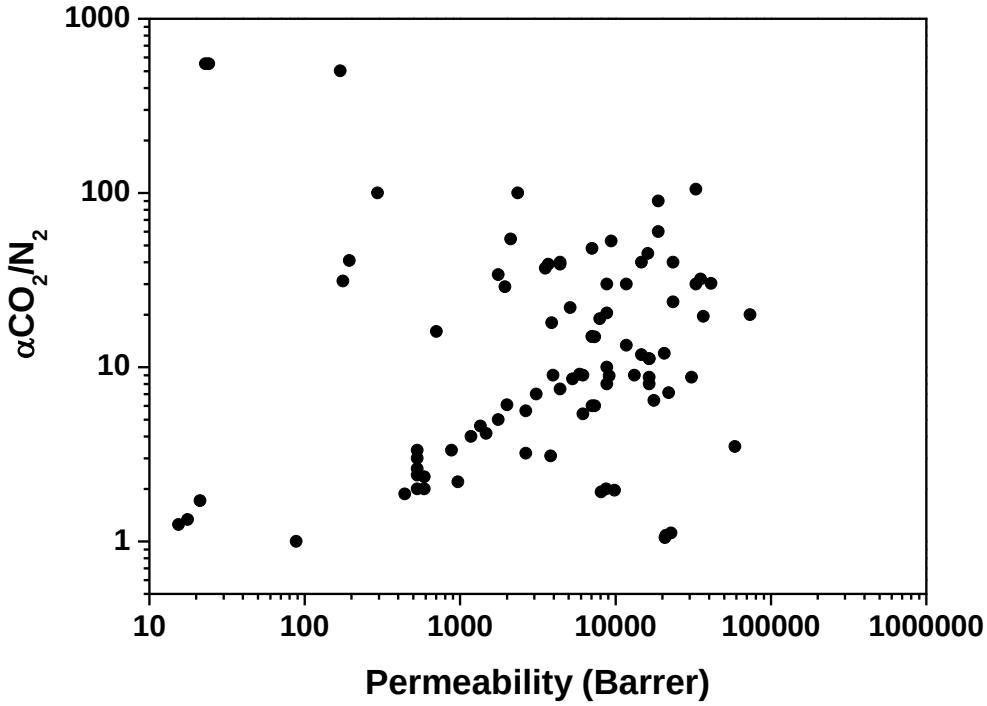

Figure 1.22 CO_2/N_2 Robeson plot for zeolite membranes

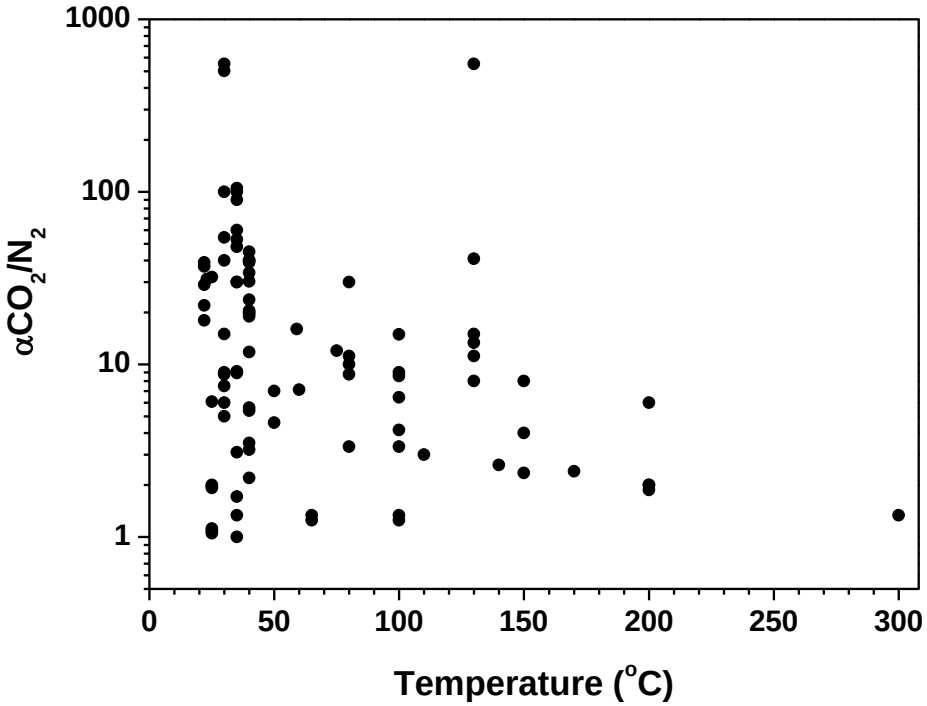

Figure 1.23 CO_2/N_2 dependency on permeation temperature for zeolite membranes.

1.4 Concluding remarks on microporous membranes

As one looks at the timeline pertaining to the microporous membranes, it is quite amazing to see the strides that have been made in such a short period of time. Early efforts using γ-alumina membranes showed little effectiveness in separating CO_2 and N_2. In fact, CO_2/N_2 permselectivities with these membranes rarely exceeded 2. Fast forward to present times in which some researchers have shown the ability to obtain α_{CO_2/N_2} values with microporous membranes as high as 275 [Cuffe et al., 2006] and 550 [White et al., 2010].

The decision regarding which type of inorganic membrane to use for CO_2 and N_2 separation will vary based on several factors. However, considering all of

the factors in play, the one of greatest concern is the temperature at which permeation takes place. For low temperature separation, zeolite membranes, specifically ion-exchanged X and Y-types appear to offer the best combination of permeance/permeability and selectivity. This has been confirmed by computer simulations conducted by Krishna and van Baten who looked at several microporous membranes and found Y-type zeolites to be among the best candidates for this purpose [Krishna and van Baten, 2010]. Furthermore, the selectivity obtained from zeolites is enhanced when binary gas mixtures are used. This makes them ideal candidates for low temperature, in situ removal of CO_2 from flue gas. However, this is not to say that carbon or silica membranes have no role in future research. The high selectivities/permselectivities achieved by carbon membranes would make them ideal candidates for this purpose if the CO_2 permeances could be increased by just an order or magnitude or two. Similarly, if the selectivity of silica membranes could be enhanced while maintaining the already high permeabilities obtained from these membranes, they would become prime candidate as well.

With that said, all three types of microporous membranes discussed are not recommended for use at high temperatures. It has been well documented within this review that these microporous membranes operate within two separate diffusion regimes. At low temperature, the separation characteristics are good as a result of selective surface adsorption and diffusion of CO_2 and subsequent blockage of N_2. At high temperature, the diffusion mechanism shifts due to the

lack of adsorption of CO_2 within the pores of all the membranes discussed. The shift from adsorption controlled to gas translational diffusion causes the separation factors to decrease dramatically towards Knudsen selectivity. As a result, new means of high temperature separation are being sought that have both high permeation fluxes and selectivities.

1.5 Research objectives and significance

1.5.1 Background information

In 2003, Lin and coworkers proposed a unique CO_2 sorption mechanism on lithium zirconate. In the proposed mechanism, lithium zirconate ($LiZrO_3$) could separate CO_2 at high temperatures via the formation of two electrolytic species, Li_2CO_3 and ZrO_2 [Ida and Lin, 2003]. Work was later extended towards the use of modified lithium zirconates for CO_2 sorption [Ida et al., 2004]. Additional work with this mechanism was also investigated by Kawamura et al. [Kawamura et al., 2005] and Nair et al. [Nair et al., 2009] for CO_2 separation and sorption by lithium zirconate and similar materials. The proposed mechanism led to the development of inorganic dual-phase membranes for CO_2 separation.

Initially, Chung et al. looked into CO_2 and N_2 separation using a metallic dual-phase membrane [Chung et al., 2005]. The membrane combined an electron conducting metal phase with an ion conducting molten carbonate phase – hence the term, dual-phase membrane. Separation is based on the premise that CO_2 will react with O_2 in the presence of an electron source (metallic support) to form a carbonate ion ($CO_3^{=}$), which can then diffuse through the molten carbonate phase

to achieve separation. Theoretically, this should lead to an infinite separation factor since N_2 cannot ionize and pass through the membrane. From 450-750°C, single gas permeance of N_2 and CO_2 was less than $5.0x10^{-9}$ $mol \cdot m^{-2} \cdot s^{-1} \cdot Pa^{-1}$. However, once oxygen was introduced with CO_2, permeance went up by about a factor of three to nearly $2.5x10^{-8}$ $mol \cdot m^{-2} \cdot s^{-1} \cdot Pa^{-1}$ at 650°C with a permselectivity of 17. This result validated the proposed mechanism for separation. However, over time at high temperatures, the metal support began to form insulating lithium iron oxides on the surface, thus causing a decrease in electron flow. This, in turn, inhibited formation of $CO_3^{=}$ and led to a rapid decrease in CO_2 permeance.

This dissertation will present a systematic study towards the improvement of the dual-phase membrane. This work will discuss the use of a support composed of a more oxidation resistant, ceramic-like perovskite material, $La_{0.6}Sr_{0.4}Co_{0.8}Fe_{0.2}O_{3-\delta}$ (LSCF. Unlike the metallic dual-phase membrane, the ceramic dual-phase membrane does not require electrons to form $CO_3^{=}$. Here, oxygen ions ($O^{=}$) within the support react with CO_2 to form $CO_3^{=}$:

$$CO_2 + O^{=} \leftrightarrow CO_3^{=} \qquad (1.C)$$

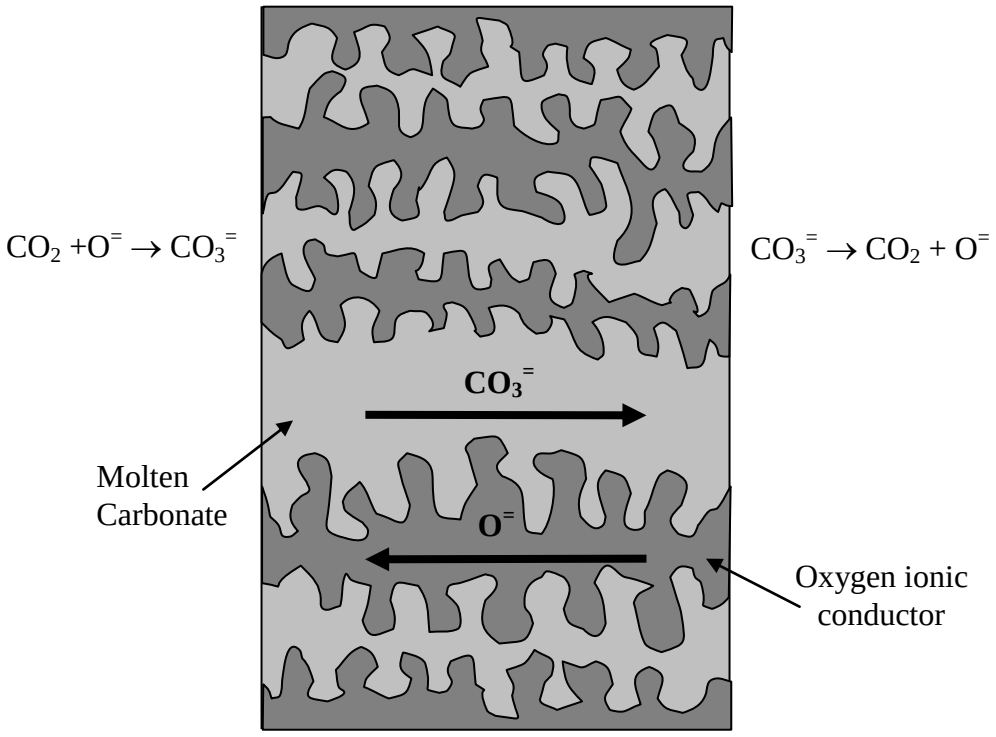

Figure 1.24 Pictorial representation of the concept of the ceramic-carbonate dual-phase membrane for CO_2 separation

In addition to being more stable than its metallic predecessor, another advantage of using a material that conducts oxygen ions for the support is that it eliminates the need for oxygen in the feed. This allows for separation of pure CO_2 on the downstream side of the membrane.

1.5.2 Objective 1

The initial objective of this work was to prove the concept of the carbonate-ceramic dual-phase membrane. To begin, LSCF powders were synthesized via the liquid citrate method. The powders were processed such that they could be formed into disk-shaped membranes that are porous in nature. These porous membranes were then infiltrated with a molten carbonate mixture to

form the dual-phase membrane. The membranes were be characterized by room temperature permeance measurements and X-ray diffraction techniques before and after infiltration. Furthermore, thermogravimetric analysis and differential scanning calorimetry (TGA-DSC) were conducted to evaluate the high temperature CO_2 sorption characteristics of the supports used in this study. High temperature CO_2 permeation measurements were carried out from 700-900°C in 50°C increments. During high temperature permeation, a 50/50% mixture of CO_2 and Ar was fed to the upstream surface of the membrane. Ar was used as a replacement for N_2 to allow for greater ease in measuring the gas with the GC used. In addition to studying the temperature effect, several membrane thicknesses (3.0, 1.5, 0.75 and 0.38 mm) were also studied to determine the effect of reducing thickness on CO_2 permeation flux. The results obtained from these experiments have been compiled and compared to that predicted by a theoretical high temperature permeation model.

1.5.3 Objective 2

To fully understand the permeation mechanism that leads to separation through the dual-phase membrane, it was necessary to look into all of the factors that may be in play during permeation. In objective 1, the effects of temperature and membrane thickness were studied at length. For each experiment performed in objective 1, the upstream partial pressure remained constant at 0.50 atm. In order to determine the effect of partial pressure on permeation, additional experiments were conducted in which temperature, thickness and partial pressure

were all varied. In this work, permeation was studied at 750, 800 and 850°C for membrane thicknesses of 1.5 and 0.75 mm while varying CO_2 partial pressures from 0 to 1 atm. The results obtained from this study will be key in determining whether or not the theoretical model developed from work conducted in objective 1 needs to be adjusted.

1.5.4 Objective 3

The final objective in this work was to demonstrate the use of the dual-phase membrane as a membrane reactor. Viable separation with this membrane at high temperatures would produce streams of warm, highly concentrated CO_2 that could be used as a chemical feedstock for the synthesis of syngas (H_2 + CO). In this study, the dual-phase membrane was used in conjunction with a catalyst in three different reaction configurations 1) a blank system with no catalyst, 2) addition of a LSCF combustion catalyst and 3) use of a 10% Ni/γ-alumina reforming catalyst. The influence of operating temperature (750-850°C), sweep gas flow rate (10-50 $mL \cdot min^{-1}$) and methane concentration of the sweep gas (10-50%) on the total CO_2 flux, H_2 production rate, H_2:CO ratio, and CO_2 and CH_4 conversions were measured to determine the effect each has on syngas production.

Chapter 2

CARBONATE-CERAMIC DUAL-PHASE MEMBRANE FOR CARBON DIOXIDE SEPARATION

2.1 Introduction

Information presented in Chapter 1 discussed how the majority of carbon dioxide emissions are a result of flue gas that is released from coal burning power plants. However, separation of CO_2 from flue gas is difficult because CO_2 (0.33 nm) and N_2 (0.364 nm) have similar kinetic diameters and temperatures of the gas can reach temperatures as high as 1000°C. Although early efforts on development of microporous inorganic membranes for CO_2 separation using silica [Kuroka et al., 2000; Yoshioka et al., 2001; Kim et al., 2004], zeolite [Kusakabe et al., 1997; Lovallo et al., 1998; Poshusta et al., 2000] and carbon membranes [Katsaros et al., 1997; Fuertes et al., 1999; Vu et al., 2002] showed some promise, data presented in Chapter 1 proved that these membranes are still incapable of separating CO_2 at high temperature.

Based on the current status, it can be inferred that microporous inorganic membranes for CO_2 separation either suffer from poor selectivity, permeance or both at high temperatures. Lin and coworkers have focused on the use of dense, dual-phase membranes for separation of CO_2 at high temperatures. Original work using a metallic dual-phase membrane was particular promising, but the formation of insulating iron oxides on the surface at high temperatures rendered the membranes useless over time. To improve the high temperature stability of

the dual-phase membrane and eliminate the need for O_2 in the feed stream, the use of a ceramic-like perovskite material, $La_{0.6}Sr_{0.4}Co_{0.8}Fe_{0.2}O_{3-\delta}$ (LSCF) was proposed for use as the support. This material has been well studied as a mixed conductor (electrons and oxygen ions). In fact, it has been shown to have particularly high electronic and ionic conductivities [Teraoka et al., 1988; Xu et al., 2004; Xu et al., 2004].

A pictorial representation of the ceramic-carbonate dual-phase membrane and the proposed mechanism for CO_2 separation was shown in Chapter 1, Figure 1.24. Oxygen ions ($O^{=}$) within the support (solid oxide phase) react with CO_2 (gas phase) in the feed stream to form $CO_3^{=}$, as shown:

$$CO_2 + O^{=} \leftrightarrow CO_3^{=} \qquad (2.B)$$

The $CO_3^{=}$ ion is mobile in the molten carbon (liquid) phase. Separation is believed to be driven by the partial pressure gradient of CO_2 between the up and downstream sides of the membrane. Upon reaching the downstream side, pure CO_2 is released and the charged oxygen ions remain in the solid phase. Moreover, the nature of the ceramic material should provide greater chemical stability than was observed from the stainless steel dual-phase membrane. The objective of this paper is to report the synthesis, characterization and CO_2 permeation properties of the new ceramic-carbonate dual-phase membrane for high temperature CO_2 separation for a specific range of temperatures and membrane thicknesses.

2.2 Experimental

2.2.1 Preparation of porous and dense $La_{0.6}Sr_{0.4}Co_{0.8}Fe_{0.2}O_{3-\delta}$ membranes

$La_{0.6}Sr_{0.4}Co_{0.8}Fe_{0.2}O_{3-\delta}$ (LSCF) powder was synthesized via the liquid citrate method according to the procedure described by Yin and Lin [Yin and Lin, 2007]. Reagent grade nitrate metal precursors $La(NO_3)_3 \cdot 6H_2O$, $Sr(NO_3)_2$, $Co(NO_3)_3$ and $Fe(NO_3)_3$ were weighed out according to the specific composition for a 0.05 mol basis of LSCF powder. The dried gel was self ignited at 400°C in air to remove the majority of the organic compounds. The self ignited powder was ground with a mortar and pestle to produce a finer powder. The ground powder was placed into a crucible and calcined at 600°C in air for 20 hours. Following calcination, 15 g of LSCF powder was reground and mixed with 1 mL of 3 wt% polyvinyl alcohol (PVA) solution to bind the powder during pressing. The powder was placed into a 30 mm stainless steel mold and pressed to 160 MPa for five minutes in a Carver hydraulic press. The green disks were sintered in air for 24 h at 900°C and 1200°C ($2°C \cdot min^{-1}$ ramp rates) to produce porous and dense LSCF supports respectively.

2.2.2 Synthesis and characterization of porous and dense LSCF supports

The average pore size (radius) and pore size distribution of the support sintered at 900°C were measured by helium permeation [Chang et al., 1994] and mercury porosimetry (Porosimetry Pascal 140). Helium permeance of the support prior to and after infiltration was obtained from a permeation setup and used to determine the mean pore size of the supports [Chung et al., 2005]. The phase

structure of the LSCF powder, support and infiltrated membrane was characterized by X-ray diffraction (XRD) (Bruker AXS, D8 Focus Diffractometer, CuKα). Theromogravimetric analysis and differential scanning calorimetry (TGA-DSC) was carried out on LSCF powder using a TA Instruments SDT Q-600 to examine the stability of the support in high P_{CO_2} (0.9998 atm) and low P_{CO_2} (~ 10^{-4} atm) atmospheres. The oxygen partial pressure (P_{O_2}) in both cases was approximately 10^{-4} atm. Total electrical conductivity measurements for porous and dense LSCF supports were obtained at low oxygen partial pressure ($P_{O_2} = 10^{-4}$ atm) from 400-900°C using the four-point DC method as described by Wei and Lin [Wei and Lin, 2008]. Scanning electron microscopy (SEM) imaging (FEI Nova 200) was performed to confirm the porous and dense nature of the supports before and after infiltration respectively.

2.2.3 Synthesis and characterization of the dual-phase membrane

Sintered LSCF supports were infiltrated with molten carbonate to obtain the dual-phase membrane. Direct infiltration of the supports was performed according to the procedure developed by Chung et al. [Chung et al., 2005]. Lithium (Li), sodium (Na), and potassium (K) carbonates from Fisher Scientific (Li_2CO_3, 99.2%; Na_2CO_3, 99.9%; K_2CO_3, 99.8%) were mixed in 42.5/32.5/25 mole percent ratio and heated to 520°C in a vertical tube furnace. The supports were preheated above the molten carbonate mixture in the furnace for 20 minutes. The support was then lowered into the molten carbonate, such that only the bottom of the support was in contact with the molten liquid. The support was

held in place for twenty minutes to allow for the molten carbonate to soak into the membrane via capillary action. The membrane was slowly removed from the furnace to avoid thermal shock of the support. After the dual-phase membrane had cooled, residual carbonates were removed from the contact surface with Struers 500-grit SiC polishing paper by lightly polishing the contact surface between the support and molten carbonate.

2.2.4 High temperature CO_2 permeation measurements

High temperature CO_2 permeation measurements were conducted using the high temperature setup shown in Figure 2.1.

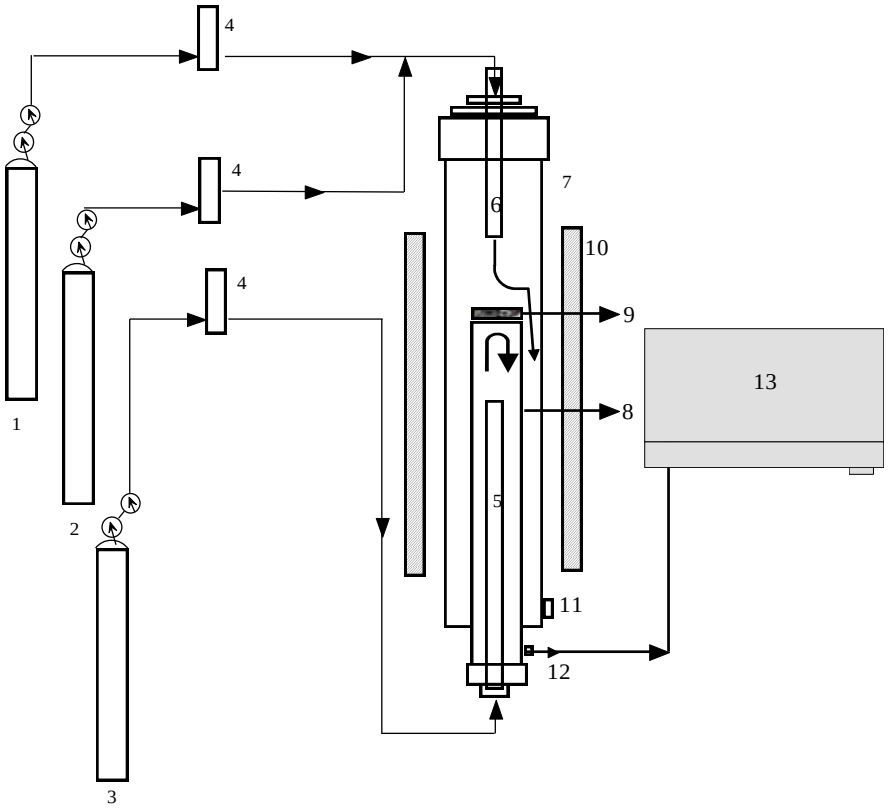

Figure 2.1 Schematic of the high temperature CO2 permeation set up. 1) CO_2 cylinder, 2) Argon cylinder, 3) Helium cylinder, 4) Mass flow controllers, 5) Sweep/purge tube, 6) Feed tube, 7) Outer tube, 8) Inner tube, 9) Dual-phase membrane, 10) Furnace, 11) Permeate, 12) Retentate, 13) GC

The dual-phase membranes were sealed to the inner alumina tube (2.54 cm OD) by creating a paste composed of a mixture of ground, sintered (900°C) LSCF powder (40 wt%), ground Pyrex™ beaker glass (50%), sodium aluminum oxide ($Al_2O_3 \cdot Na_2O$; 10%) and water [Qi et al., 2001]. The system was completely sealed inside a 3.8 cm OD alumna tube and heated at a rate of $1°C \cdot min^{-1}$ to 900°C to allow for the seal to soften and set. Gases were delivered to the up and downstream sides of the membrane by connecting mass flow controllers to 1 cm

OD alumina tubes. Each tube was placed about 3 cm away from the membrane on both sides. During heating and permeation, the feed side consisted of 50 $mL \cdot min^{-1}$ each of CO_2 and Ar, while He flowed on the sweep side at a rate of 100 $mL \cdot min^{-1}$. The flow rates were controlled by MKS Instruments mass flow controllers. All gases used were of industrial grade quality. Argon was used to check for leaks in place of nitrogen in the event that experiments with O_2 were ever conducted in the future. This was done because N_2 and O_2 peaks can overlap in the GC. Argon was viewed as an acceptable substitute because it is inert and is similar in kinetic diameter to N_2, thus making it possible to use CO_2/Ar selectivities in the place of CO_2/N_2.

The system was allowed to remain at 900°C for one hour to reach steady state and to allow the seal to set. CO_2 permeation measurements were taken, starting at 900°C and working downwards to 700°C in 50°C increments. Once the desired temperature was reached, one hour was given to allow the system to attain steady state prior to data collection. The permeate and retentate flow rates were measured using a bubble flow meter, while the gas composition of the permeate was measured using a HP 5890 Series II gas chromatograph, equipped with a TCD detector and an Alltech's Hayesep DB 100/120 column (30' x 1/8" x 0.85" SS). Helium was used as the carrier gas for the GC. Error associated with permeation measurements was found to be $\pm$ 5.6%.

2.3 Results and discussion

2.3.1 Mixed-conductivity of LSCF and its interaction with molten carbonate

The XRD patterns of the LSCF powder after calcination, support after sintering and the dual-phase membrane after infiltration are shown in Figure 2.2. The XRD pattern of the calcined powder confirms that LSCF was properly synthesized via the liquid citrate method. The XRD pattern becomes further pronounced after sintering of the powder (in support form) at 900°C, showing a fully developed perovskite-like structure (indicated by •) [Yuan et al., 2006]. The pattern of the non-contact side of the membrane after infiltration shows peaks indicative of molten carbonate at 2θ values of 29.4 and 37.3° (indicated by *). Both the feed and sweep sides of the membrane show the presence of molten carbonate after high temperature permeation experiments, although the peaks have lower relative intensities than that shown in the fresh membrane. The feed and sweep sides of the membrane also show the presence of new peaks at roughly 26 and 43°, with an additional peak on the sweep side at 63° (indicated by +). The results show that, while the calcination temperature is not high enough to remove all of the impurities (i.e., $SrCO_3$, $CoCO_3$), the sintering temperature is high enough to burn out most of them. XRD analysis of the support indicates that the structure of LSCF is rhombohedral, with lattice constants of 5.49 and 13.40Å for *a* and *c* respectively with a cell volume is 350.66$Å^3$. The XRD patterns show that LSCF begins to develop the desired structure after calcination at 600°C, but it is the sintering step where the material fully develops. The analysis confirms that

the powder and supports synthesized in this manner are of the desired perovskite structure and possess the characteristics essential for the dual-phase membrane, as well as showing that the membrane can be properly synthesized via the direct infiltration method. After high temperature permeation, the feed side shows a stronger molten carbonate peak than the sweep side, probably due to the high partial pressure of CO_2 (0.5 atm) on that side during permeation. The presence of CO_2 helps prevent decomposition of the carbonate mixture. The additional peaks on the feed and sweep side at 26 and 43° are likely due to strontium carbonate formation. Although unknown at this time, the additional peak on the sweep side at 63°could be from lithium cobaltite ($LiCoO_2$). It is possible that this reaction can occur on the sweep side due to the lower partial pressures (~ 0 atm) of CO_2 present, causing some of the lithium carbonate in the mixture to decompose and react with the support. Additional studies will be required to determine the exact nature of the new peaks formed and their effect on permeation behavior.

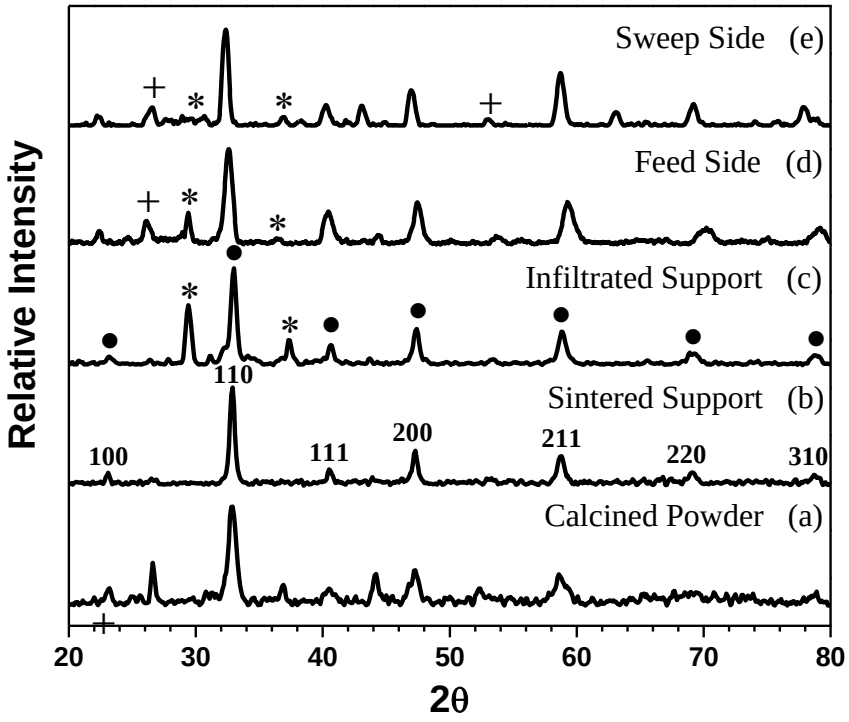

Figure 2.2 XRD patterns of a) LSCF powder after calcination, b) a sintered support, b) the non-contact side of the dual-phase membrane after infiltration, c) feed side and e) sweep side of a dual-phase membrane after a high temperature permeation experiment.

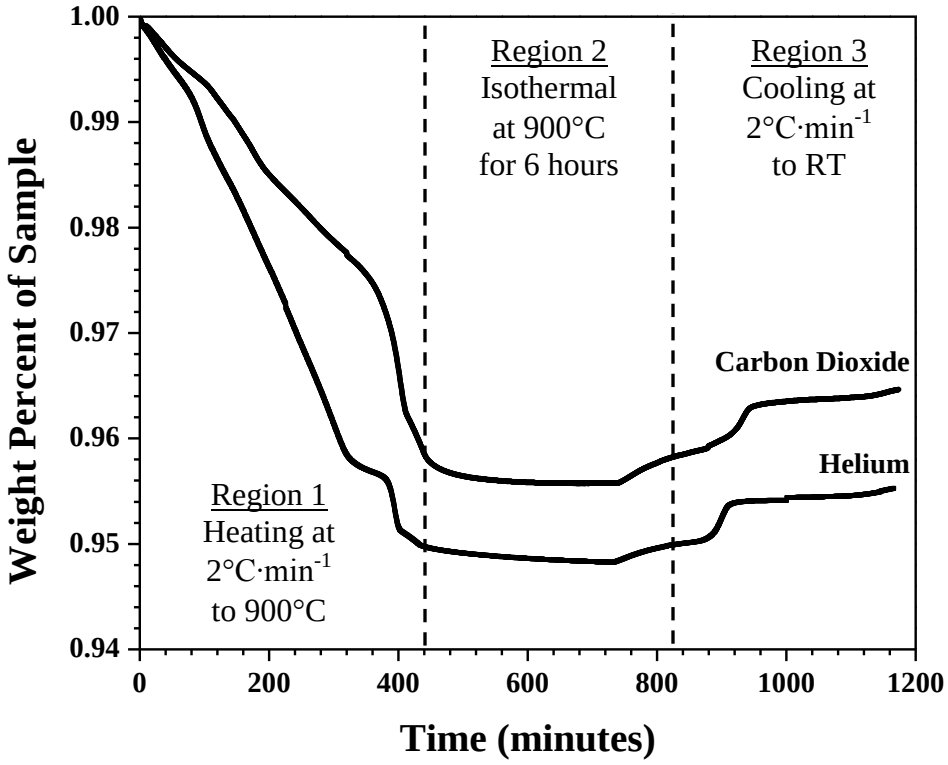

Figure 2.3 Thermogravimetric analysis of LSCF powder in high P_{CO_2} and low P_{CO_2} (helium) environments

Figure 2.3 shows the results of TGA analysis conducted to verify the stability of LSCF powder in high P_{CO_2} and low P_{CO_2} environments. Both samples of LSCF powder experienced a weight loss as temperature increased to 900°C. Upon reaching 900°C, the weight of both samples reached a steady value. The sample exposed to He (low P_{CO_2}) experienced a 0.007% greater weight loss. Finally, during cooling, there is a slight and nearly identical weight increase seen in both samples. The weight decrease with increasing temperature is due to the loss of lattice oxygen (O_o^x) upon formation of gaseous oxygen, as described by Sammells and Mundschau [Sammells and Mundschau, 2006]:

$$2Fe_{Fe}^{\ x} + O_o^{\ x} \xrightarrow{heat} \tfrac{1}{2}O_{2\,(g)} + V_o^{\bullet\bullet} + 2Fe_{Fe}^{\ '} \qquad (2.C)$$

where $O_o^{\ x}$ represents lattice oxygen and $V_o^{\bullet\bullet}$ are oxygen vacancies. The slight weight gain seen during cooling in both samples occurs as a result of oxygen recombination from oxygen impurities in the gases used.

From start to finish, the weight loss was less for the sample heated in CO_2, indicating an interaction between the LSCF powder and the environment. This occurs because CO_2 can participate in the oxygen surface exchange reaction with LSCF. It is this interaction between CO_2 and LSCF that leads to a slight deviation between the weights of the samples. With some LSCF-like materials, surface modification of LSCF does not occur while being heated in CO_2 environments, but can take place upon cooling from high temperatures in CO_2 and H_2O containing atmospheres [Benson et al., 1999]. In some perovskite compounds, strontium (Sr) and cobalt (Co) can react to form carbonates with CO_2 at high temperatures [Sammells and Mundschau, 2006]. The formation of these carbonates on the membrane surface would reduce the ionic conductivity of the material at the reaction interface, hence limiting the rate of formation of $CO_3^{=}$. However, because both trends in the figure are the same, it can be inferred that there was a lack of carbonate formation on the surface of the sample heated in CO_2, and the difference can be attributed solely to the participation of CO_2 in the surface exchange reaction. Therefore, it can be concluded that the LSCF powder used in this study is stable in low P_{CO_2} and high P_{CO_2} environments.

Figure 2.4a and b show plots of helium permeance (F; $mols \cdot m^{-2} \cdot s^{-1} \cdot Pa^{-1}$) versus average pressure (P_{avg}; kPa) and mercury porosimetry results of the porous LSCF support respectively.

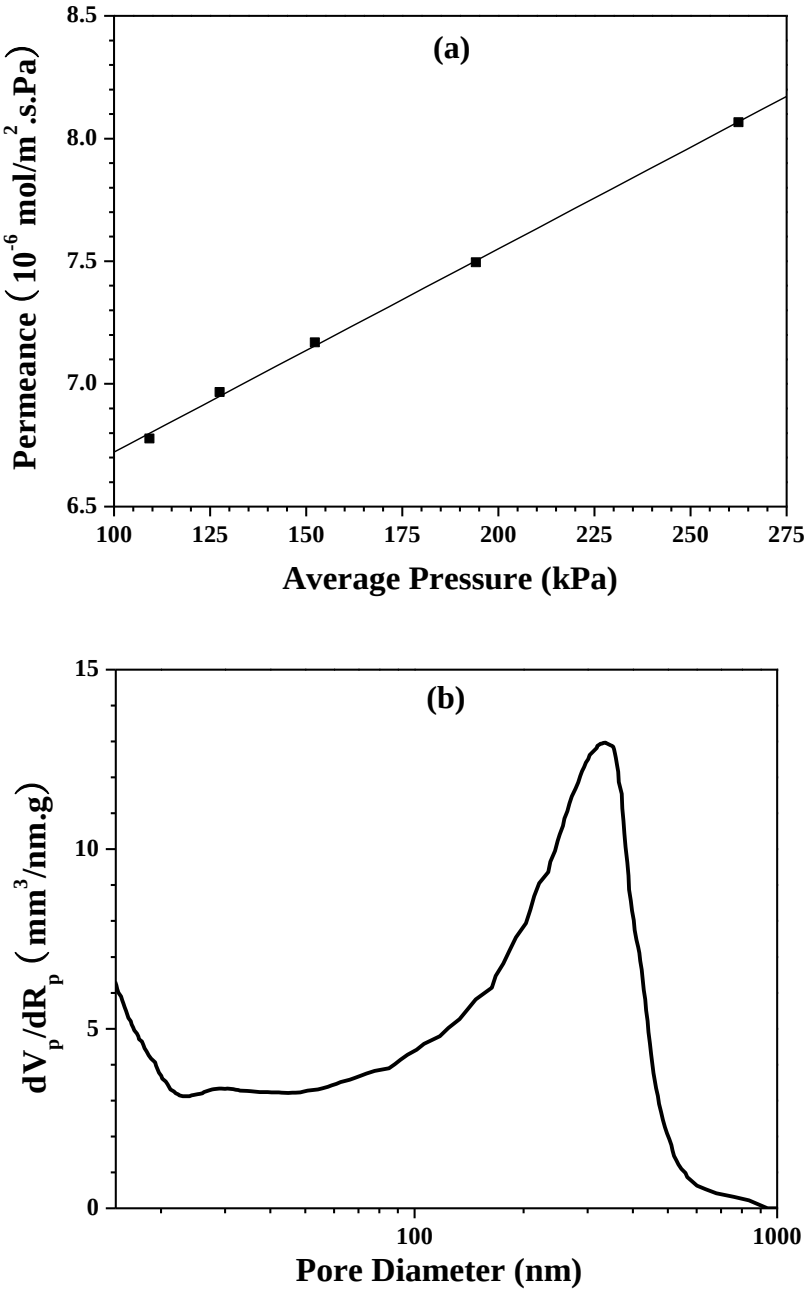

Figure 2.4 (a) Steady state helium permeance versus average pressure of LSCF support also used to determine the average pore radius of the support. (b) Mercury porosimetry measurement of a LSCF support that was used to determine the average pore radius of the support

Helium permeance of the porous LSCF supports was found to be on the order of 10^{-6} mols·m^{-2}·s^{-1}·Pa^{-1}. Permeation data in Figure 2.4a can be described by the following equations considering the Knudsen and viscous flow [Way and Roberts, 1992; Leenaars et al., 1984]:

$$\frac{F}{L} = \alpha + \beta P_{avg} \tag{2.1}$$

with the intercept and slope related to the pore structure and helium properties as:

$$\alpha = 1.06\left(\frac{\varepsilon}{\tau}\right)\frac{r_p}{L\sqrt{RTM_w}} \tag{2.2}$$

$$\beta = 0.125\left(\frac{\varepsilon}{\tau}\right)\frac{r_p{}^2}{L\mu RT} \tag{2.3}$$

where L is the thickness (m) of the membrane, P_{avg} is the average pressure (Pa) between the up and downstream sides of the membrane, μ is the viscosity (Pa·s) of He at room temperature, ε and τ represent the porosity and tortuosity factor of the support, R is the gas constant (8.314 (m^3·Pa·mol^{-1}·K^{-1}), T is the temperature (K) and M_w is the molecular (g·mol^{-1}) weight of He. The regressed values of the slope and intercept for data in Figure 2.4a are given in Table 2.1.

Table 2.1 Helium permeation data and pore structure of LSCF support

α	from steady state He permeation data ($mol \cdot m^{-2} \cdot s^{-1} \cdot Pa^{-1}$)	$5.89 \cdot 10^{-6}$
β	from steady state He permeation data ($mol \cdot m^{-2} \cdot s^{-1} \cdot Pa^{-2}$)	$8.28 \cdot 10^{-12}$
L	Support thickness (m)	$1.5 \cdot 10^{-3}$
M_W	molecular weight of He ($kg \cdot mol^{-1}$)	$4.00 \cdot 10^{-3}$
T	steady state temperature (K)	298
μ	Viscosity of He at steady state temperature (Pa·s)	$1.99 \cdot 10^{-5}$
R	ideal gas constant ($m^3 \cdot Pa \cdot mol^{-1} \cdot K^{-1}$)	8.314
r_p	pore radius of LSCF6482 support (m)	$1.82 \cdot 10^{-7}$
ε/τ	Porosity/Tortuosity	0.145

From the values in Table 2.1, the pore radius and the ratio of porosity/tortuosity factor (ε/τ) were obtained by using Equations 2.2 and 2.3. Those results are also given in Table 2.1. As shown, the LSCF supports have an average pore radius of 182 nm and porosity/tortuosity factor of 0.145.

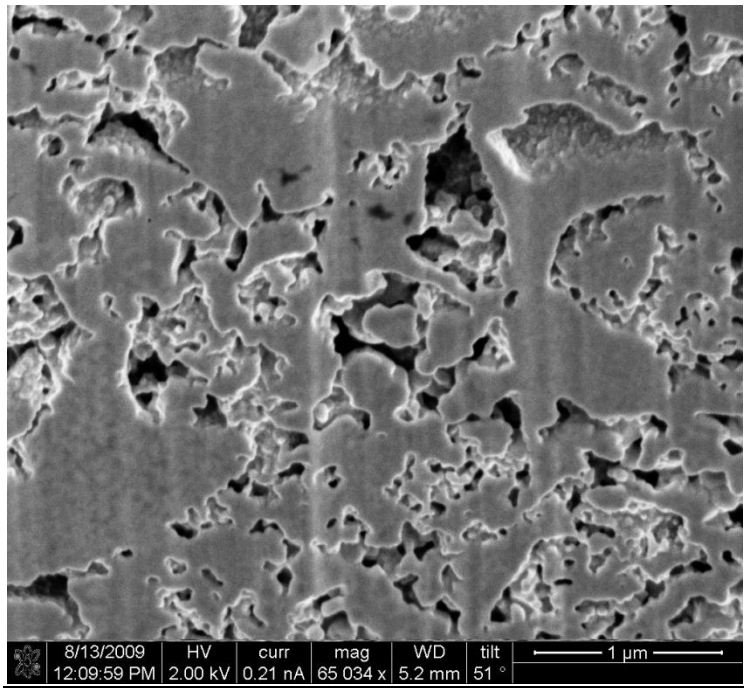

Figure 2.5 SEM image of a cross section of LSCF support before infiltration with molten carbonate

The mercury porosimetry results suggest that the pore radius distribution of the supports spans a wide range, as indicated by mercury porosimetry. Figure 2.5 shows an SEM micrograph of the support. The SEM image shows presence of a wide pore size distribution, but with several pore radii in the 175 nm range. All three methods (helium permeation, mercury porosimetry and SEM imaging) confirm the highly porous nature of the LSCF support with average pore radii of roughly 180 nm. The LSCF support remains porous for two main reasons – the presence of impurities in the pre-sintered powder and the influence of sintering temperature. First, after calcination at 600°C, the powder begins to adopt the desired perovskite structure, but the powder shows the presence of strontium carbonate ($SrCO_3$, $2\theta = 26°$) impurities, as is seen in the XRD pattern. During

sintering of the green disk, these impurities are burnt out, leaving large porous gaps within the support. The removal of these impurities accounts for a considerable fraction of the large pores and porosity seen in the mercury porosimetry data and SEM image. Secondly, the supports are sintered well below the densification temperature for this material, which is about 1200°C [Xu et al., 2004], thus keeping the highly porous nature of the support intact.

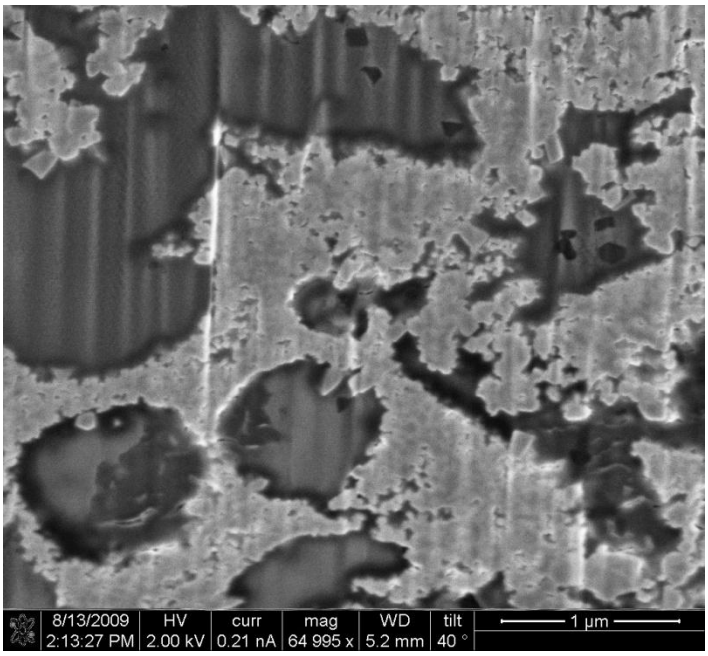

Figure 2.6 SEM image of a cross section of a LSCF support after infiltration with molten carbonate

Figure 2.6 is an SEM image of the cross section of a support after infiltration with molten carbonate. A discernable change is observed between the porous support in Figure 2.5 and an infiltrated support in Figure 2.6. The darker regions in Figure 2.6 are composed of molten carbonate while the light regions represent the electron conducting LSCF phase. It was observed that the entire

depth of the support showed carbonate infiltration. After infiltration, the supports increased in weight by 33%. The observed weight increase suggests that molten carbonate takes up 42% of the volume within the support. This value corresponds quite well with the percentage (~ 40%) of molten carbonate visible in Figure 2.6. EDS analysis of the infiltrated support indicates the presence of Na and K throughout the entire cross section of the dual-phase membrane. Helium permeance of the infiltrated support was below 10^{-10} mols·m^{-2}·s^{-1}·Pa^{-1} (the lower limit of the permeation setup). These results all confirm that molten carbonate can be directly infiltrated into the pores of the LSCF support via capillary action. The fact that the supports are fully infiltrated means that CO_2 can only permeate through molten carbonate via the $CO_3^{=}$ ion at high temperatures.

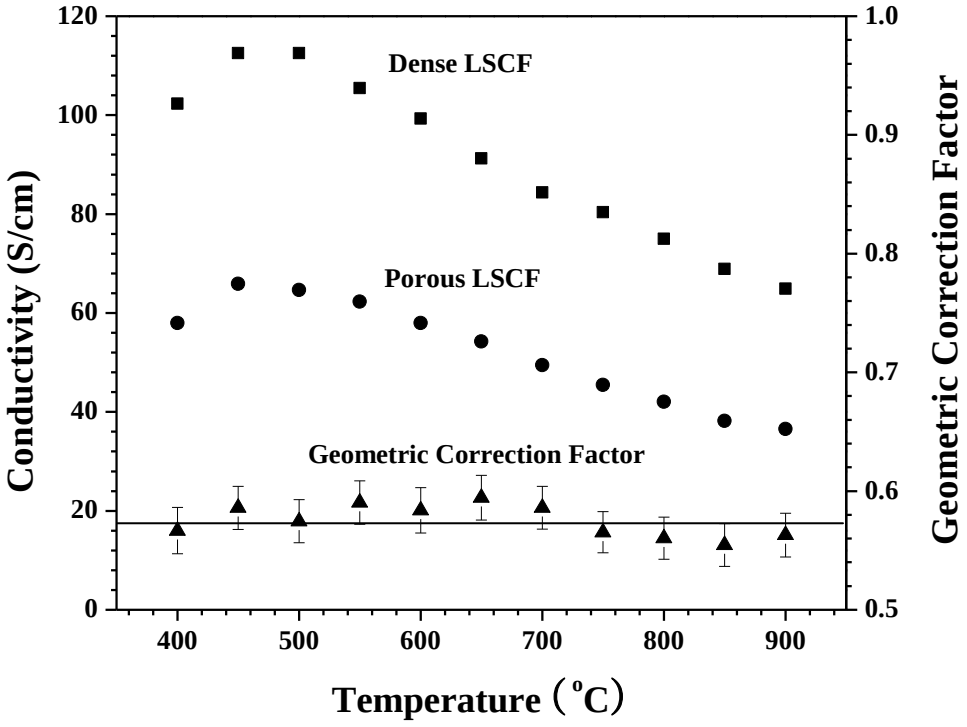

Figure 2.7 Four-point DC total conductivity of a dense and porous LSCF support.

Figure 2.7 shows the total electrical conductivity of both the porous and dense LSCF supports as a function of temperature. The total conductivity trend, which reaches a maximum at 500°C then decreases linearly as temperature increases, resembles data that has been reported for LSCF [Wang et al., 2003; Xu et al., 2004]. The negative temperature dependence of total conductivity at temperatures greater than 500°C is due to the decrease in electronic carrier concentration. The ratio of the electrical conductivity for the porous support to that for the dense support, referred to as the geometric correction factor (ϕ), at different temperatures is plotted in Figure 2.7. The values for ϕ are seen to be around 0.57. This geometric correction factor is related to the transport of oxygen ions in porous supports, which is essential in predicting the CO_2 permeation flux through the dual-phase membrane, as to be discussed next.

Table 2.2 CO_2 permeation characteristics of membranes of different thicknesses

Thickness (mm)	Permeance at 900°C (10^{-8} mol·m^{-2}·s^{-1}·Pa^{-1})	Activation Energy (kJ·mol^{-1})
3.00	2.01	86.4
1.50	3.73	87.7
0.75	4.63	89.6*
0.375	4.77	89.9*

* Apparent activation energy (bulk diffusion no longer rate limiting)

2.3.2 CO_2 permeation through LSCF/molten carbonate dual-phase membrane

Figure 2.8a shows CO_2 permeation as a function of temperature for several thicknesses of the LSCF-carbonate dual-phase membrane. The results of the high temperature permeation experiments are also summarized in Table 2.2. At 900°C,

the CO_2 permeance was observed to be on the order of at least 10^{-8} mols·m^{-2}·s^{-1}·Pa^{-1} for each of the different membrane thicknesses. Highest permeances of 2.01, 3.73, 4.63 and $4.77 \cdot 10^{-8}$ mol·m^{-2}·s^{-1}·Pa^{-1} were obtained for membrane thicknesses of 3.0, 1.5, 0.75 and 0.375 mm respectively at 900°C. Previous work dealt with the use of solid-solid interaction between the electrolytic species to separate CO_2. Values of permeance are higher here because the carbonate mixture was molten (liquid), quicker transport of $CO_3^{=}$. In addition, LSCF has a larger ionic conductivity than those materials previous examined providing for quicker transport of the ionic species through the membrane [Kawamura et al., 2005; Yamaguchi et al., 2007]. A plot of activation energy is shown in Figure 8b. The activation energy of the LSCF/molten carbonate dual-phase membrane was calculated to be between 86.4 and 89.9 kJ·mol^{-1}, depending on the thickness of the membrane. The decreasing rate of improved permeance and the slight increase in activation energy both indicate that the surface reaction becomes a factor as thickness decreased.

Based on transport mechanism proposed, only CO_2 is permeable through the carbonate phase of the membrane. Since Ar was mixed with CO_2 in the feed, detection of Ar in the permeate side would indicate selectivity of the membrane or possible leakage. No Ar in the permeate stream could be detected by GC. Based on the detection limit of the GC used in the work, the CO_2/Ar separation factor for the dual-phase membrane is above 225 for the 0.375 mm thick membrane at

900°C. Since Ar and N_2 are comparable in size, it is safe to assume that the CO_2/N_2 selectivity for the dual phase membrane is above 225 as well.

Lin and co-workers recently published models for CO_2 permeation through dual-phase membranes using mixed-conducting supports [Rui et al., 2009]. For CO_2 permeation through the LSCF-carbonate dual-phase membrane in the absence of oxygen, the oxygen ion conductivity for LSCF is much smaller than that of carbonate ions in molten carbonate. Using this simplification, the following oxygen permeation equation can be obtained from Equation 25 from reference [Rui et al., 2009]:

$$F_{CO_2} = -\left(\frac{\varepsilon}{\tau}\right)_{MC} \frac{RT\phi\sigma_i}{4(P'_{CO_2} - P''_{CO_2})F^2 L} \ln\left(\frac{P''_{CO_2}}{P'_{CO_2}}\right) \qquad (2.4)$$

In Equation 2.4, ε is the porosity and τ is the tortuosity factor for the LSCF support. Since the support pores are filled with carbonate, these two properties represent transport of the carbonate ion in the molten carbonate phase. The value of ε/τ was measured to be 0.145 (see Table 2.1). Furthermore, ϕ is the geometric correction factor for solid phase of the porous LSCF support. Physically, it represents the ratio of the relative cross-sectional area of the solid phase to the solid tortuosity for oxygen ion transport in the solid skeleton of the porous LSCF support. As was discussed previously, the value of ϕ was measured to be 0.57. P'CO_2 and P"CO_2 are carbon dioxide partial pressures (Pa) in the feed and permeate, and L is the membrane thickness (m). P'CO_2 is 5.07×10^4Pa and P"CO_2 was measured experimentally for each permeation data point and is listed in Table

2.3. Finally, σ_i is oxygen ionic conductivity in the CO_2 atmosphere for permeation experiments ($PO_2 = 10^{-4}$ atm in the present study).

Oxygen ionic conductivity for different LSCF compounds can be obtained from the following equation [Teraoka et al., 1988]:

$$\sigma_i = \frac{(zq)^2 C_v D_v}{kT} \tag{2.5}$$

where z is the charge of the conducting ion, q is the charge of an electron (1.69×10^{-19} C), C_v is the concentration of vacancies (cm^{-3}), D_v is the diffusivity of oxygen vacancies ($cm^2 \cdot s^{-1}$), and k is Boltzmann's constant (1.38×10^{-23} $m^2 \cdot kg \cdot s^{-2} \cdot K^{-1}$). The diffusivity, D_v, of oxygen vacancies in $LaCoO_3$ perovskite materials was evaluated using the following equation [Ishigaki et al., 1984]:

$$D_v = 1.59 \cdot 10^{-2} e^{\left(\frac{-E_a}{RT}\right)} \tag{2.6}$$

where activation energy for oxygen vacancy diffusion, E_a is 72.3 $kJ \cdot mol^{-1}$. To determine the concentration of vacancies, C_v, the oxygen nonstoichiometry (δ) of the material had to be considered. Values for δ were found based on work by Wang et al., which described the nonstoichiometry of LSCF as a function of temperature and P_{O_2} [Wang et al., 2003]. The number of vacancies was calculated by relating the number of oxygen atoms per cm^3 of LSCF to the nonstoichiometry of the material at various temperatures and P_{O_2}. Table 2.4 summarizes the ionic conductivity of LSCF from 700-900°C calculated from Equation 2.5. The value calculated for the oxygen ion conductivity of the LSCF at

900°C is 0.17 $S \cdot cm^{-1}$, which is reasonably close to the reported experimental value of 0.20 $S \cdot cm^{-1}$ at 900°C [Teraoka et al., 1991].

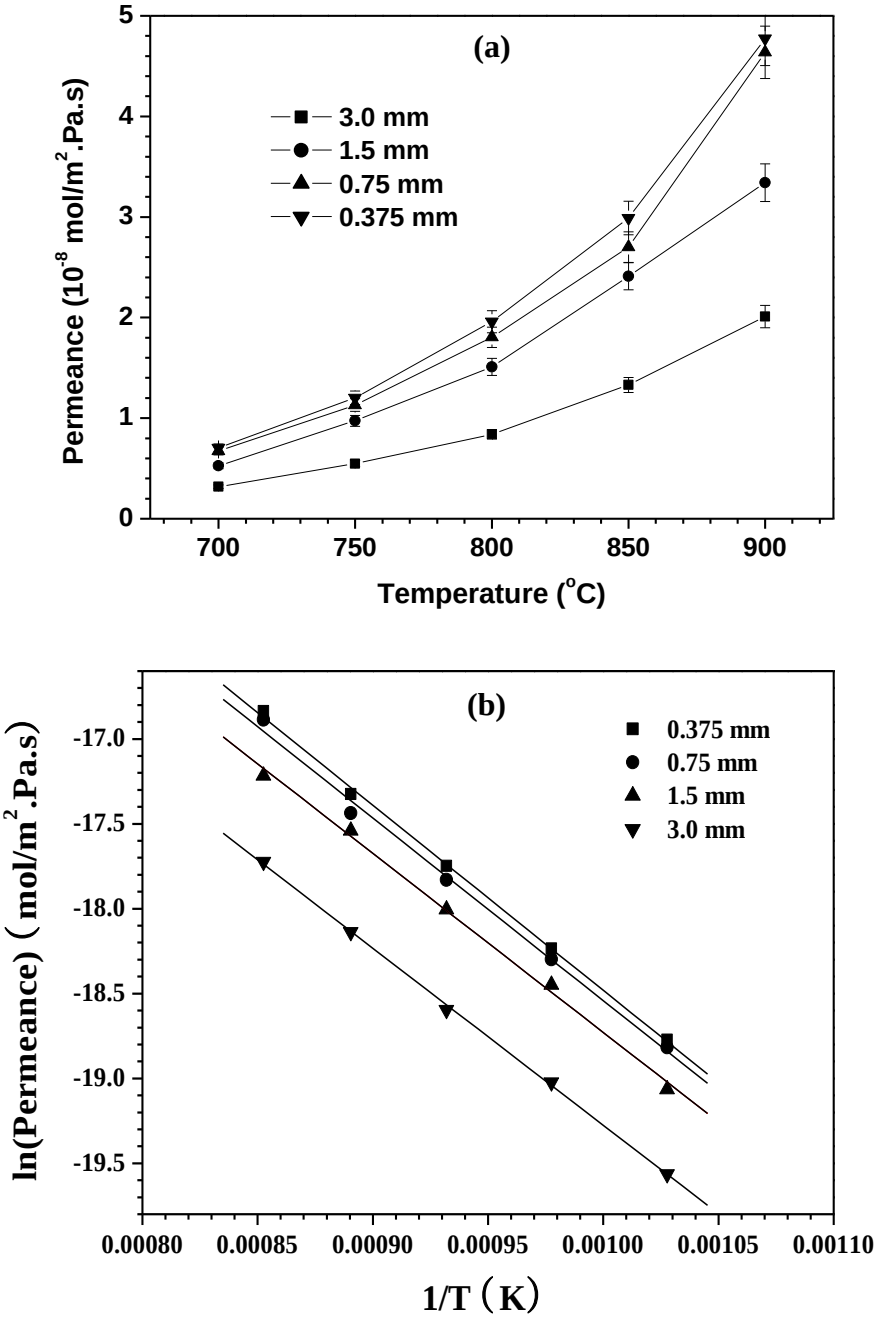

Figure 2.8 (a) High temperature CO_2 permeance of the dual-phase membrane for various membrane thicknesses as a function of temperature. (b) Arrhenius plot of the dual-phase membrane for various membrane thicknesses

.

Table 2.3 Downstream CO_2 partial pressures for 1.5 and 3.0 mm thick membranes

Temperature (°C)	P''CO_2 3.0 mm* membrane (Pa)	P''CO_2 1.5 mm** membrane (Pa)
900	37.1	52.8
850	63.7	91.0
800	97.4	138.7
750	153.8	219.8
700	265.2	378.9

* Permeation Area: 1.410 cm^3
** Permeation Area: 1.330 cm^3

Table 2.4 Oxygen ionic conductivity data for LSCF at different temperatures

Temperature (°C)	Theoretical ($S \cdot cm^{-1}$)
700	0.024
750	0.043
800	0.072
850	0.114
900	0.173

CO_2 permeation fluxes are calculated by Equation 2.5 for two of the LSCF-carbonate dual phase membranes (1.5 and 3.0 mm). The calculated fluxes are compared with experimental data in Figure 2.9. As shown, the model agrees well with the experimental data for the thicker membranes. This confirms that CO_2 permeates ionically through the molten carbonate phase. Furthermore, it shows that permeation through the LSCF-carbonate membrane is controlled by oxygen ionic conducting in the LSCF phase. It also shows that the structure for

the carbonate phase and solid LSCF phase can be reliably characterized by helium permeation and electrical conductivity measurements. Predicted CO_2 fluxes for the thinner membranes (0.75 and 0.375 mm) do not agree with the experimental data, indicating the influence of surface reaction kinetics on the permeation mechanism as membrane thickness decreases.

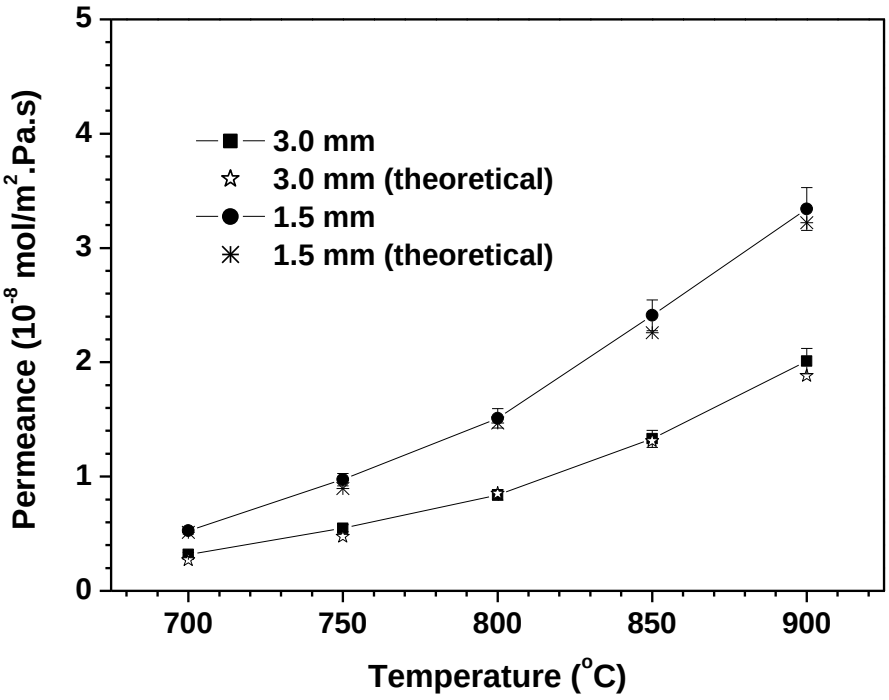

Figure 2.9 Comparison of the high temperature theoretical model and actual permeance of CO2 through the LSCF dual-phase membrane for thicknesses of 1.5 and 3.0 mm.

2.4 Conclusions

Gas-tight dual-phase membranes composed of porous $La_{0.6}Sr_{0.4}Co_{0.8}Fe_{0.2}O_{3-\delta}$ supports infiltrated with a Li/Na/K molten carbonate phase can be prepared by the direct infiltration method. Molten carbonate fills entire

pores of the LSCF support. CO_2 permeation through the dual-phase membranes can be measured using a high temperature permeation setup and a glass-ceramic seal. High temperature permeation experiments show CO_2 permeances of 2.01, 3.73, 4.63 and $4.77 \cdot 10^{-8}$ $mol \cdot m^{-2} \cdot s^{-1} \cdot Pa^{-1}$ for dual-phase membranes with thicknesses of 3.0, 1.5, 0.75 and 0.375 mm respectively at 900°C. The structure of the pore and solid phase of LSCF support can be respectively characterized by helium permeation and electrical conductivity measurements. The experimental CO_2 permeation data can be well predicted by a theoretical permeation model developed in previous work. The model considers oxygen ion conduction in the solid phase of the LSCF support as the rate-limiting step in high temperature CO_2 permeation. The agreement of experimental and model permeance data at different temperatures confirms the CO_2 permeation mechanism through the dual phase membrane, showing that it is controlled by oxygen ion conductivity in the solid skeleton of the LSCF support.

Chapter 3

CARBON DIOXIDE PERMEATION THROUGH CARBONATE-CERAMIC DUAL-PHASE MEMBRANES

3.1 Introduction

Results presented in Chapter 2 showed that the dual-phase membrane is a viable method for high temperature CO_2 separation. Several LSCF dual-phase membranes of varying thicknesses were examined from 700-900°C with an equimolar feed mixture of CO_2/Ar at a total feed pressure of 1 atm. CO_2 permeances of 2.01, 3.73, 4.63 and $4.77 \cdot 10^{-8}$ $mol \cdot m^{-2} \cdot s^{-1} \cdot Pa^{-1}$ were obtained for membrane thicknesses of 3.0, 1.5, 0.75 and 0.375 mm respectively at 900°C. The permeances obtained correspond to fluxes ranging from 0.186 to 0.322 $mL \cdot min^{-1} \cdot cm^{-2}$. The CO_2/Ar separation factor for the dual-phase membrane was greater than 225 for the 0.375 mm thick membrane. The membrane was able to successfully separate CO_2 without the need for oxygen in the feed while remaining chemically stable at high temperatures [Anderson and Lin, 2010].

Rui et al. recently published a model for CO_2 permeation through dual-phase membranes using mixed-conducting supports [Rui et al., 2009]:

$$F_{CO_2} = -\left(\frac{\varepsilon}{\tau}\right)_{MC} \frac{RT\gamma\sigma_i}{4(P'_{CO_2} - P''_{CO_2})F^2 L} \ln\left(\frac{P''_{CO_2}}{P'_{CO_2}}\right) \qquad (3.1)$$

From the model, it is seen that several variables can affect permeation at high temperature. The objective of this work is complete additional experiments with the LSCF dual-phase membrane to further understand transport of CO_2 through

the membrane. Temperature and thickness effects have already been studied [Anderson and Lin, 2010]. However, the effect of the CO_2 pressure gradient is unknown. In this work, results obtained from varying both upstream and downstream partial pressure of CO_2 on the permeation flux have been investigated at length.

3.2 Experimental

3.2.1 Preparation/characterization of LSCF dual-phase membranes

$La_{0.6}Sr_{0.4}Co_{0.8}Fe_{0.2}O_{3-\delta}$ (LSCF) powder was synthesized via the liquid citrate method [Anderson and Lin, 2010]. Two different dual-phase membrane thicknesses were studied in this work: 0.75 and 1.5 mm. To form the 1.5 mm thick LSCF supports, 2.75 g of the powder and binder mixture was placed into a 30 mm stainless steel mold and compressed to 160 MPa for five minutes in a Carver hydraulic press. Similarly, 1.4 g of the mixture was used to make 0.75 mm thick supports. The thinner supports were also pressed to 160 MPa. The green disks were sintered in air for 24 h at 900°C (2°C·min^{-1} ramp rates) to produce mechanically stable, porous supports with the appropriate thickness and pore size. Sintered LSCF supports were infiltrated with the same molten carbonate mixture and procedure discussed in the previous study of the LSCF dual-phase membrane [Anderson and Lin, 2010].

Theromogravimetric analysis and differential scanning calorimetry (TGA-DSC) was carried out on sections of infiltrated LSCF supports (3 mm x 3 mm x 1.5 mm) using a TA Instruments SDT Q-600 instrument to examine the CO_2

sorption characteristics of the dual-phase membrane. In the initial set of experiments, several samples were heated 850°C at 1°C·min^{-1} in varying CO_2 partial pressures ranging from 0 to 1 atm. The total flow rate of gas in the machine was kept constant at 100 mL·min^{-1} and balanced with N_2. Upon reaching 850°C, the system was kept isothermal for a period of 6 h and then cooled to room temperature at 5°C·min^{-1}. In the second experiment, a dual-phase membrane sample was heated to 850°C at 1°C·min^{-1} in 25% CO_2 and 75% N_2 (total flow rate = 100 mL·min^{-1}). Upon reaching 850°C, the system temperature was maintained at such conditions for a period of 12 h. The composition of gas entering the system was changed to 100% N_2 (100 mL·min^{-1}) for a period of 24 h. Finally, the composition of the gas entering the TGA was switched once more to 25% CO_2 and 75% N_2 to examine the sorption characteristics of the sample for one final 12 h period. At the conclusion of the experiment, the sample was cooled to room temperature at 5°C·min^{-1}.

3.2.2 High temperature CO_2 flux measurements at various partial pressures

High temperature CO_2 flux measurements were conducted using the high temperature setup, measurement devices (GC, bubble flow mater, mass flow controllers) and sealing procedure described in a previous study [Qi et al, 2001; Anderson and Lin, 2010]. Error associated with permeation measurements was found to be $\pm$ 5.6%. The primary goal of this work was to determine the effect of CO_2 partial pressures (feed and sweep sides) on flux through the carbonate-

ceramic dual-phase membrane. To measure this effect, three different cases were investigated.

The first case examined was when the partial pressure of CO_2 in the feed was greater than the equilibrium partial pressure (P_{eq}) of the molten carbonate mixture. Here, the permeation apparatus was heated to 850°C at 1°C·min^{-1} in 5% CO_2 and 95% N_2. A total flow rate of 100 mL·min^{-1} and pressure of 1 atm was maintained on the feed side while the downstream portion of the membrane was constantly swept with 100 mL·min^{-1} of He. Measurements were taken at feed compositions of 5%, 25%, 50%, 75% and 95% CO_2 with the balance accounted for by N_2. After each change in feed composition, 2 h was given for the system to reach steady state. Flux measurements were also collected at 750 and 800°C for the same range of partial pressures. In these two instances, the system was heated to 850°C initially to allow the seal to set and was then cooled at 1°C·min^{-1} to the desired permeation temperature. After reaching the desired temperature, the system was allowed to remain for 1 h before data collection.

The second case investigated was when the P_{CO_2} in the feed stream was below the P_{eq} of the molten carbonate mixture. The heating conditions, as well as the feed and sweep flow rates were identical to the previous case. Measurements were taken starting with a feed composition of 5% CO_2, then decreased to 4%, 3%, 2%, 1%, 0.5% and 0%. In each case, N_2 was used to balance the feed at 100 mL·min^{-1}. Measurements were taken every 2 h and done only at 850°C for this particular case.

The downstream CO_2 partial pressure was regulated to determine the effect on membrane performance. The system was heated to 850°C in 25% CO_2 and 75% N_2. This particular feed composition was kept constant for the duration of the experiment. The total feed rate was 100 $mL \cdot min^{-1}$. During heating, the membrane was swept with 10 $mL \cdot min^{-1}$ of helium on the downstream side. The system was allowed to remain at 850°C for 1 h to reach steady state and allow the seal to set. Permeation measurements were taken, starting at a He sweep rate of 10 $mL \cdot min^{-1}$ and working upward to 300 $mL \cdot min^{-1}$ in predetermined increments. After taking a measurement at each specific sweep rate, the flow rate was increased and 2 h were given for the system to attain steady state before collecting the next set of data.

The last test involved examining the long term performance and stability of the dual-phase membrane. The system was heated to 850°C in 25% CO_2 and 75% N_2, while maintaining a total flow rate on the feed side of 100 $mL \cdot min^{-1}$ and feed pressure of 1 atm. The feed composition was kept constant for the duration of the experiment and the downstream side was constantly swept with 100 $mL \cdot min^{-1}$ of He. The system was allowed to remain at 850°C and the aforementioned conditions for 1 h to reach steady state and allow the seal to set. Flux measurements were taken over a span of 100 hours to determine the long term stability and permeation characteristics of the LSCF dual-phase membrane. After the stability test, the phase structure of the membrane was characterized by X-ray diffraction (XRD) (Bruker AXS, D8 Focus Diffractometer, CuKα).

3.3 Results and discussion

3.3.1 Performance below molten carbonate equilibrium partial pressure

Prior to this work, the effect of CO_2 partial pressure on transport through the dual-phase membrane had been unknown. Previous work detailed the permeation properties of the membrane at a single upstream partial pressure (0.50 atm) [Anderson and Lin, 2010]. In this work, CO_2 partial pressures ranging from 0 to 0.95 atm were studied. Figure 3.1 shows the CO_2 flux when a 1.5 mm membrane was exposed to upstream carbon dioxide partial pressures ranging from 0 to 0.95 atm at 850°C. Specific interest was paid to partial pressures at or below 0.05 atm. From the figure, it is observed that there is a steep decrease in the CO_2 flux from 0.154 $mL \cdot cm^{-2} \cdot min^{-1}$ at a partial pressure of 0.05 atm to 0.027 $mL \cdot cm^{-2} \cdot min^{-1}$ at 0 atm. Due to the lack of a driving force, there should have been no measureable flux at an upstream P_{CO_2} of 0 atm. However, that was not observed in this instance. At partial pressures above 0.05 atm, the flux is relatively constant. This observation with be discussed at length in the following section.

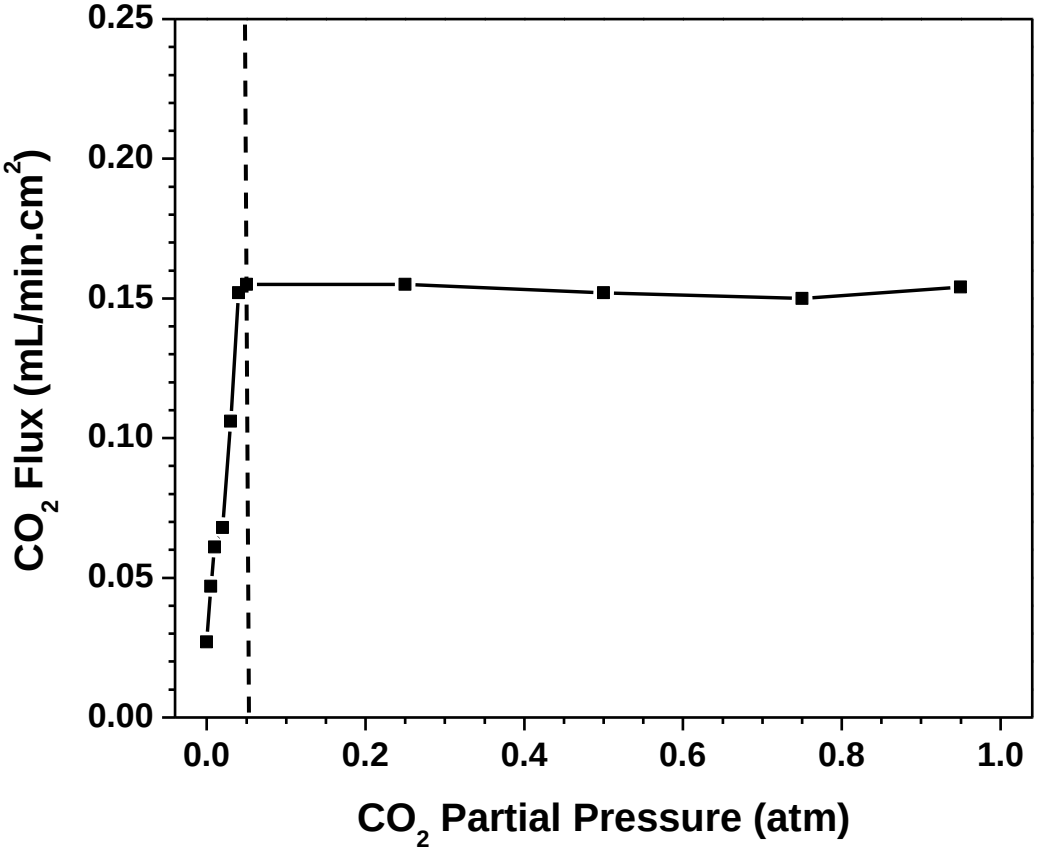

Figure 3.1 CO_2 flux for a 1.5 mm thick LSCF dual-phase membrane at 850℃ at various feed pressures ranging from 0 atm to as high as 0.95 atm. The dotted line represents the equilibrium partial pressure of the molten carbonate mixture.

CO_2 detected in the permeate at partial pressures below 0.05 atm is not an actual flux measurement, rather, it is attributed to the transient decomposition of the molten carbonate mixture. The equilibrium CO_2 partial pressure (P_{eq}) of this particular mixture can be calculated from the following equation [Janz et al., 1979]:

$$p(atm) = 0.0013 \cdot 10^{\left(-\frac{630057}{T(K)}+7.22\right)} \qquad (3.1)$$

Table 3.1 shows the P_{eq} of the 42.5/32.5/35% Li/Na/K molten carbonate mixture at the various permeation temperatures studied.

Table 3.1 Equilibrium partial pressures of the 42.5/32.5/25% Li/Na/K molten carbonate mixture

Temperature (°C)	Molten Carbonate Equilibrium Partial Pressure (atm)
750	0.015
800	0.029
850	0.053

The P_{eq} of the molten carbonate mixture at 850°C is 0.053 atm. At CO_2 partial pressures below this value, the molten carbonate in the membrane decomposes into the corresponding metal oxides (M_2O) and carbon dioxide:

$$M_2CO_3 \xrightarrow{P_{CO_2} < P_{eq}} M_2O + CO_2 \qquad (3.B)$$

where M = Li, Na or K.

Decomposition provides a reasonable explanation for the detection of CO_2 in the permeate in Figure 3.1 despite being at an upstream P_{CO_2} of 0 atm.

The propensity of molten carbonate to decompose at low partial pressures brought forth the question of whether or not the dual-phase membrane could be regenerated after being left in low P_{CO_2} atmospheres for a long period of time. Figure 3.2 shows the results of a TGA-DSC test performed on a 3 mm x 3 mm x 1.5 mm membrane sample to determine the behavior of the membrane after being exposed to high and low P_{CO_2} at high temperatures. In region I, the sample was heated to 850°C at 1°C·min^{-1} in a stream containing CO_2 at a partial pressure of

0.25 atm. Here, the sample shows continuous sorption of CO_2 after passing the melting point of the molten carbonate mixture (397°C) and onwards to 850°C. In region II, the dual-phase membrane sample remained isothermal at 850°C for a period of 12 h, during which CO_2 sorption continued until nearly leveling out towards the end of the time frame. Region III shows that the sample experienced a rapid weight loss after being exposed to a P_{CO_2} of 0 atm. Even after 24 h, the sample continued to lose weight in the absence of carbon dioxide. Weight loss is observed as a result of decomposition and subsequent release of CO_2 by the molten carbonate. Finally, during the recovery process in region IV, CO_2 was reintroduced to the sample at a partial pressure of 0.25 atm. CO_2 reacts rapidly with the metal oxides (M_2O) created during decomposition to reform molten carbonate (M_2CO_3). However, the sample was never able to fully recover to its original state observed in region 1. This leads to the conclusion that the performance of the dual-phase membrane could be hindered if the membrane was kept below the P_{eq} for a long period of time.

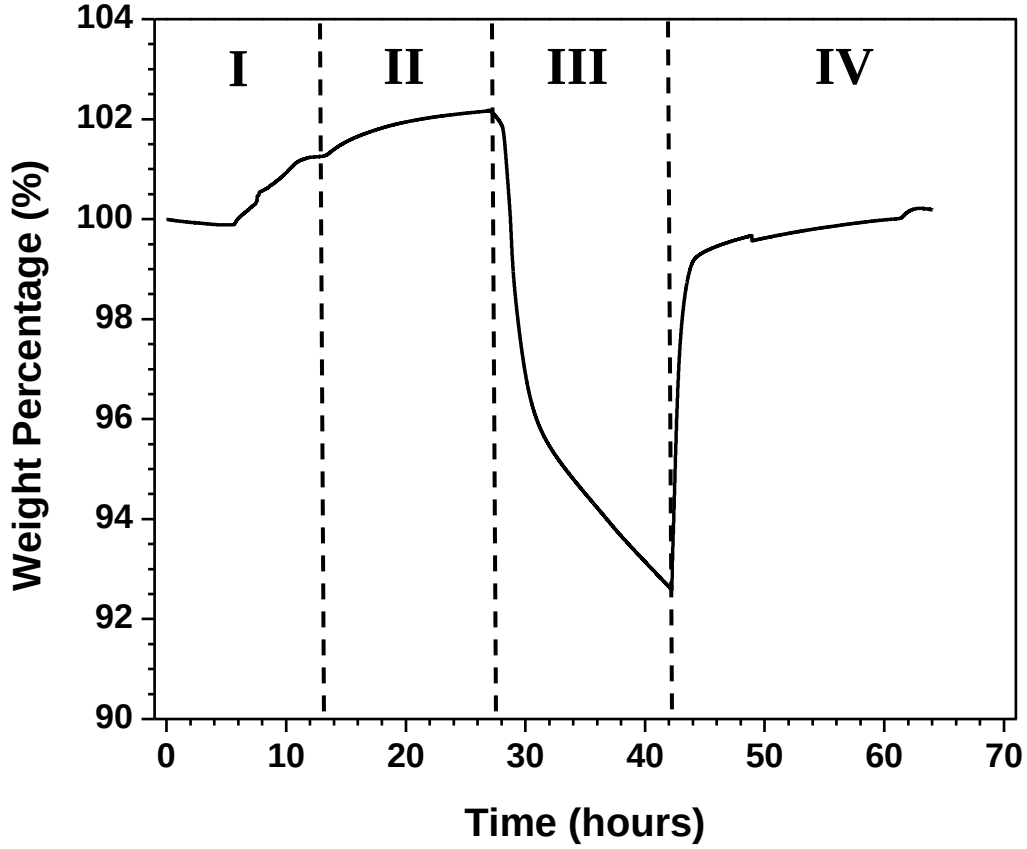

Figure 3.2 Long term TGA data of a section of a dual-phase membrane exposed to different CO_2 partial pressures at 850℃.

Although Figure 3.2 showed that the dual-phase membrane would be unlikely to recover fully from being left in a low P_{CO_2} environment, it was still desired to examine the behavior of a membrane system under such conditions. Towards this, an experiment was conducted to determine the recovery behavior of the LSCF dual-phase membrane after being exposed to high and low partial pressures of CO_2. The results are portrayed in Figure 3.3. The membrane was given ample time to reach equilibrium at 850°C with a feed mixture consisting of 25% CO_2 and 75% N_2 at a total pressure of 1 atm. After reaching 850°C, several

measurements were taken to determine the flux, which was calculated to be 0.150 $mL \cdot cm^{-2} \cdot min^{-1}$ (region I).

After 1 h of data collection, pure nitrogen was fed to the upstream side of the membrane (region II). It can be seen that there is a rapid decrease in the flux after removing CO_2 from the feed stream. This rapid decrease corresponds to the asymptotic weight decrease seen in region III of Figure 3.2. After a period of 5 h, the mole fraction of CO_2 in the permeate reached a pseudo steady state value of about 0.036 $mL \cdot cm^{-2} \cdot min^{-1}$. It should be noted that the leakage rate of N_2 measured in the permeate grew over time when CO_2 was not present in the feed. Leakage results from long term decomposition of molten carbonate, leading to release of CO_2. The release of CO_2 from within the pores leads to the formation of defects. The introduction of defects likely creates small pockets of porosity that can allow nitrogen to permeate through the otherwise dense membrane.

Region III shows the behavior of the membrane after reintroducing 25% CO_2 to the upstream surface. The membrane recovers rapidly, reaching a steady state CO_2 flux of 0.158 $mL \cdot cm^{-2} \cdot min^{-1}$ within about 1 h. The rapid increase in CO_2 flux observed in Figure 3.3, which represents the reaction of CO_2 and M_2O to produce molten carbonate, corresponds quite well with the data presented in region IV of Figure 3.2. The aforementioned nitrogen leak did decrease in magnitude, hence showing that most of the metal oxides formed during composition reacted with CO_2 to form molten carbonate. This filled a majority of the defects. However, not all defects were filled and, therefore, a minor N_2 leak

remained. This is an indication that full recovery of the membrane is not possible, at least over short periods of time, thus confirming the behavior observed in region IV of Figure 3.2.

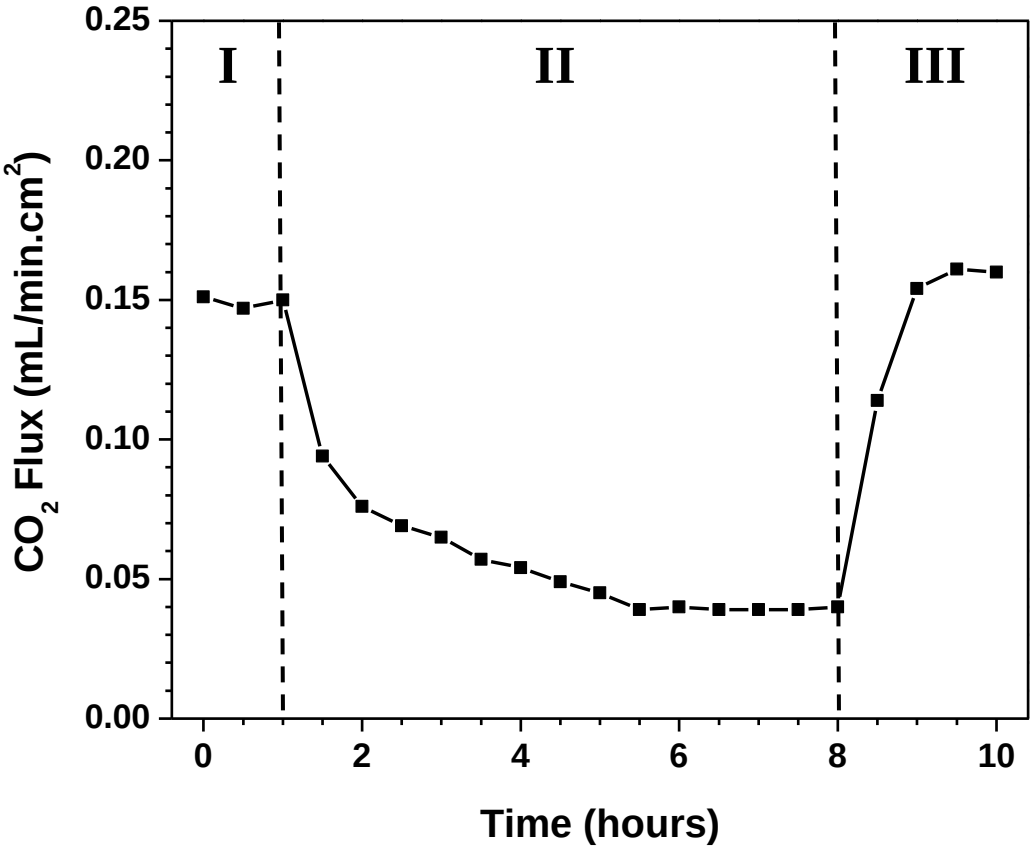

Figure 3.3 CO_2 flux through a 1.5 mm thick LSCF dual-phase membrane at 850℃ after being exposed to partial pressures of CO_2 above and below the equilibrium partial pressure of the molten carbonate

3.3.2 Performance above molten carbonate equilibrium partial pressure

Figures 3.4 and 3.5 show the CO_2 flux through the LSCF dual-phase membrane as a function of CO_2 partial pressure. The figures detail the results obtained from 1.5 and 0.75 mm thick dual-phase membranes respectively at 750,

800 and 850°C. The figures shows that, within the P_{CO_2} range of 0.05-0.95 atm, the high temperature CO_2 flux remains relatively constant for both membrane thicknesses. For the 1.5 mm thick membrane, average CO_2 fluxes of 0.053, 0.081 and 0.151 $mL \cdot cm^{-2} \cdot min^{-1}$ were observed at 750, 800 and 850°C respectively. Likewise, CO_2 fluxes of 0.067, 0.098 and 0.176 $mL \cdot cm^{-2} \cdot min^{-1}$ were obtained for the 0.75 mm thick dual-phase membrane at the same respective temperatures and range of partial pressures. The average fluxes obtained from both figures are summarized in Table 3.2, while Table 3.3 shows a comparison between data collected from this work with that at a P_{CO_2} of 0.50 atm in previous work [Anderson and Lin, 2010]. Data in the table indicates that the values obtained in this work at a partial pressure of 0.50 atm are reasonably close to previously reported results at the same P_{CO_2}. The minor differences in each case can be attributed to slight adjustments made to the permeation setup.

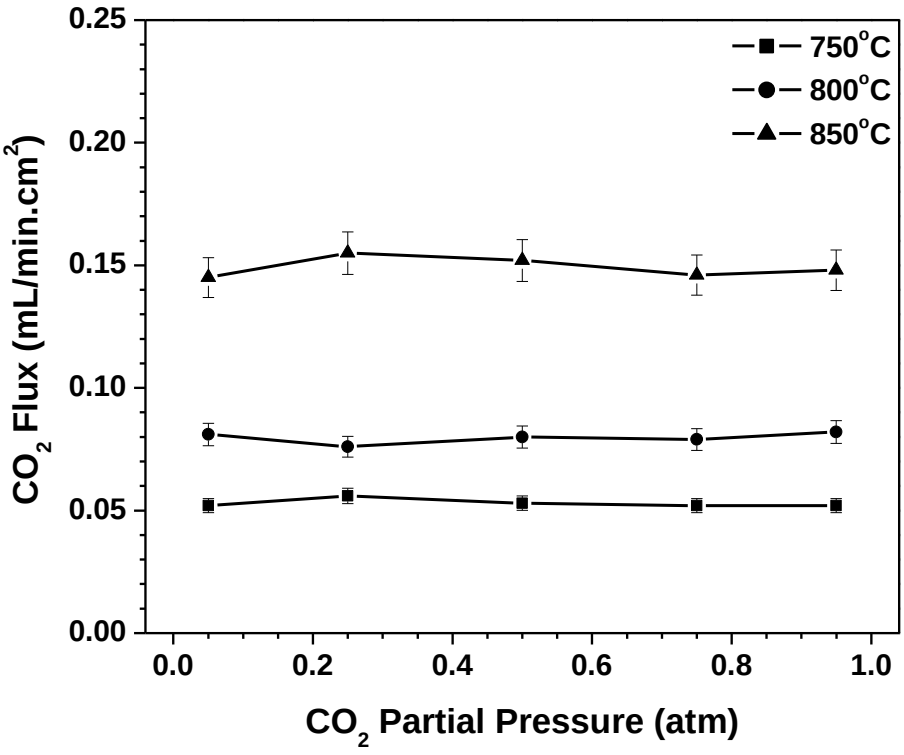

Figure 3.4 High temperature CO_2 flux at various carbon dioxide feed partial pressures ($0.05 \leq P_{CO_2} \leq 0.95$ atm) for a 1.5 mm thick LSCF dual-phase membrane at 750, 800 and 850℃

.

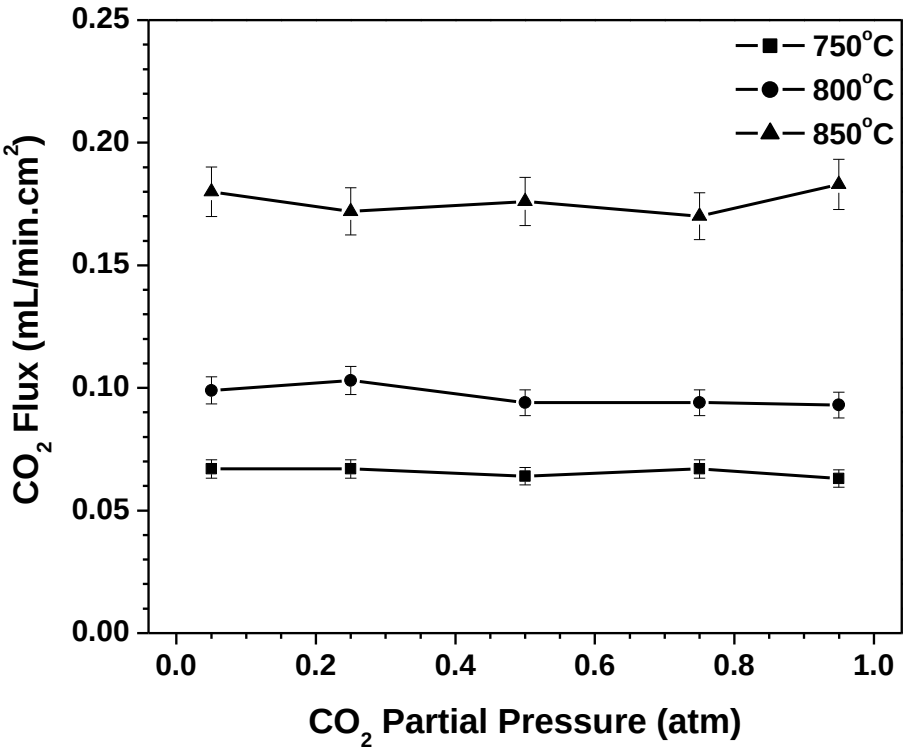

Figure 3.5 High temperature CO_2 flux at various carbon dioxide feed partial pressures (0.05 atm $\leq P_{CO_2} \leq$ 0.95 atm) for a 0.75 mm thick LSCF dual-phase membrane at 750, 800 and 850℃

.

Table 3.2 Average CO_2 Flux in the P_{CO_2} range of 0.05-0.95 atm from Figures 3.4 and 3.5

Thickness (mm)	Temperature (°C)	CO_2 Flux ($mL \cdot cm^{-2} \cdot min^{-1}$)
1.5	750	0.053
	800	0.081
	850	0.151
0.75	750	0.067
	800	0.098
	850	0.176

Table 3.3 Comparison of CO_2 flux in this work versus previous work [Anderson and Lin, 2010]

Temperature (°C)	1.5 mm Flux ($mL \cdot cm^{-2} \cdot min^{-1}$)		0.75 mm Flux ($mL \cdot cm^{-2} \cdot min^{-1}$)	
	Previous Work	This Work	Previous Work	This Work
750	0.063	0.053	0.076	0.067
800	0.099	0.081	0.121	0.098
850	0.162	0.151	0.181	0.176

The fact that both membranes in Figures 3.4 and 3.5 showed a seemingly constant flux throughout the entire range of CO_2 partial pressures was an unexpected result. It was previously believed that the partial pressure gradient of carbon dioxide (ΔP_{CO_2}) was a driving force for permeation. Clearly, that is not the case here as these results prove contrary to that belief.

Further investigations were conducted to explain the results depicted in Figures 3.4 and 3.5. Figure 3.6 shows the high temperature CO_2 sorption characteristics of the dual-phase membrane. Several 3 mm x 3 mm x 1.5 mm thick LSCF support were individually infiltrated and placed into the TGA-DSC

apparatus at various CO_2 partial pressures. In region I, each sample was heated to 850°C at 1°C·min^{-1}. In this region, the samples experienced little to no weight gain until reaching 400°C (6 h). This temperature corresponds to the melting point of the molten carbonate mixture [Janz et al., 1979]. Prior to this temperature, the molten carbonate within the membrane is in its solid form and therefore, not likely to absorb $CO_3^{=}$ - at least not at noticeable rate. Once the molten carbonate had melted, $CO_3^{=}$ was easily absorbed into the molten liquid, hence explaining the sudden weight increases observed for the samples heated in 1%, 5%, 10%, 50% and 100% CO_2. As expected, no such weight increase was observed for the sample heated in 0% CO_2, as the $CO_3^{=}$ ion would not be formed in such a case.

The sample heated in pure nitrogen (0% CO_2) begins to experience weight loss after 9 hours, which corresponds to a system temperature of about 550°C. At this point, the equilibrium partial pressure, although low at approximately 4x10^{-4} atm, is substantial enough for decomposition of molten carbonate to initiate. Therefore, the weight loss is attributed to the loss of CO_2 from the molten carbonate. The sample heated in 1% CO_2 increased in weight until reaching roughly 725°C (11 h), then experienced a rapid weight decrease as temperature increased towards 850°C. At 725°C, the decomposition partial pressure of molten carbonate is about 0.01 atm, thus explaining why the sample experienced a weight gain up to that particular point and subsequent weight loss thereafter. These results further confirm the CO_2 detected in the permeate at feed CO_2 partial

pressures below P_{eq} is the result of the decomposition of molten carbonate on the downstream side of the membrane. All of the samples shown in Figure 3.6 that were heated at or above the P_{eq} of molten carbonate at 850°C showed similar weight gains over the span of the experiment. The data in Figure 3.6 can be further dissected to justify the constant flux values for the dual-phase membrane shown in Figures 3.4 and 3.5. By examining the weight loss and/or gain of the samples in Figure 3.6, an isotherm for CO_2 sorption into the dual-phase membrane could be established.

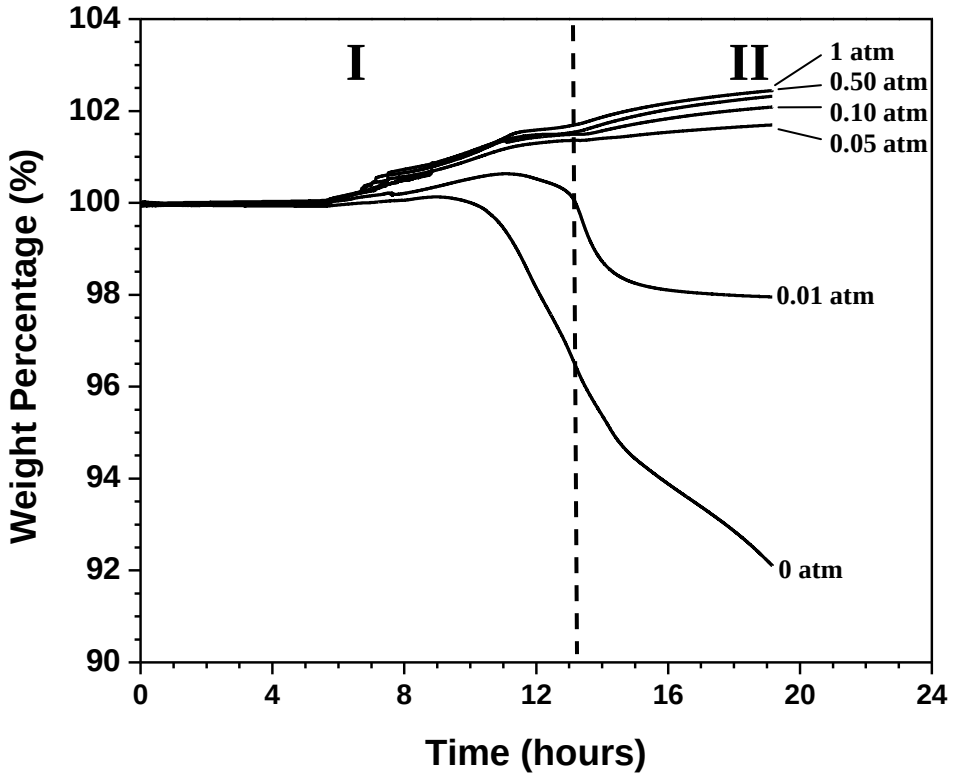

Figure 3.6 Thermogravimetric data of sections of an LSCF dual-phase membrane exposed to different CO_2 partial pressures and heated to 850℃ for a period of 6 h

The amount of CO_2 absorbed was taken from region II in Figure 3.6 using the weight gain or loss experienced by each sample upon completion of the experiment. From this data, Figure 3.7 was created to show the number of mol of CO_2 absorbed per g of dual-phase membrane as a function of CO_2 partial pressure. The dotted line shown in the figure represents the equilibrium partial pressure of the molten carbonate mixture at 850°C. The plot shows that for P_{CO_2} < 0.05 atm, the membrane does not uptake CO_2; rather, it loses CO_2 as a result of the decomposition of molten carbonate, which is evident due to the negative CO_2 sorption values. The sorption of CO_2 by the membrane follows that of a step function. There appears to be no sorption until reaching the equilibrium partial pressure, after which point, sorption is relatively constant at about $5x10^{-4}$ mol $CO_2 \cdot g^{-1}$ membrane. This step-like behavior was reported previously for uptake of CO_2 using lithium zirconate (Li_2ZrO_3). Ida and coworkers found that there was no sorption of carbon dioxide into the Li_2ZrO_3 powder below the equilibrium partial pressure of the material [Ida et al., 2004]. Constant sorption of CO_2 was observed at pressures above $P_{eq,}$ which is identical to the phenomena observed in the present work. Comparison of Figures 3.1 and 3.7 show the same type of behavior, thus leading credence to the belief that CO_2 partial pressure is not a driving force for permeation through the dual-phase membrane.

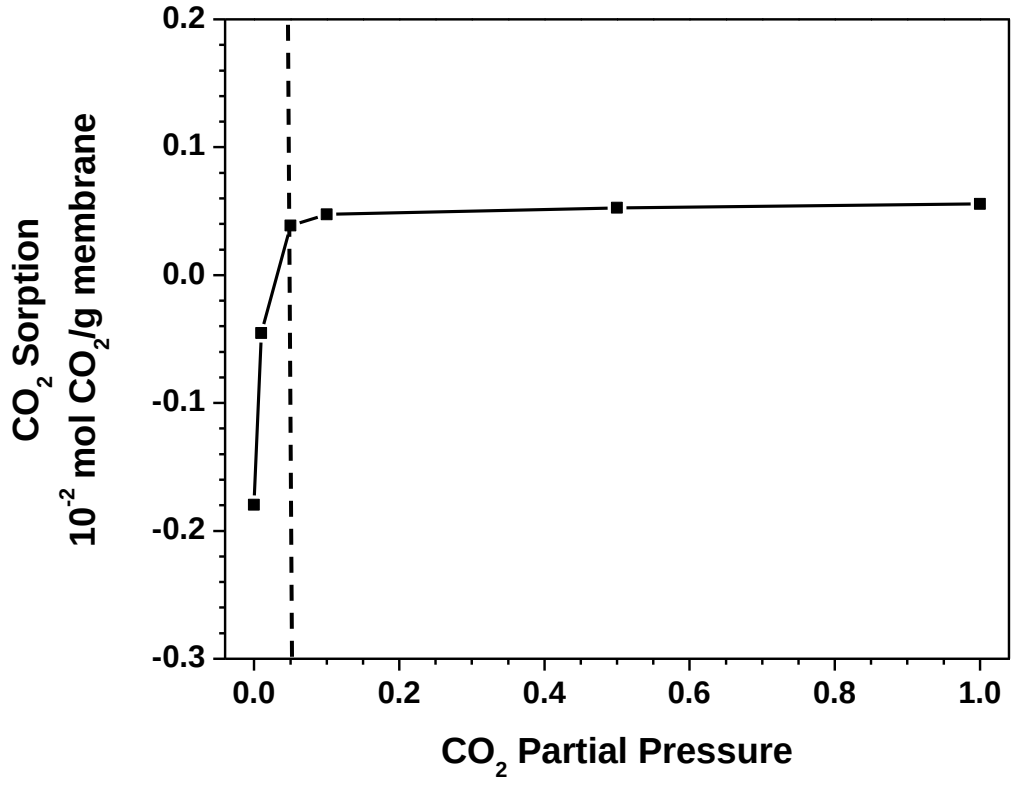

Figure 3.7 CO_2 sorption isotherm at 850℃ for the LSCF dual-phase membrane as a function of CO_2 partial pressure.

The data and figures shown prior all indicate that the sorption of CO_2 is constant as long as the upstream partial pressure is above the equilibrium partial pressure the of molten carbonate. This means that the partial pressure gradient of CO_2 has little or no influence on flux. It was desired to understand whether the same held true for the downstream partial pressure of CO_2. Figure 3.8 shows the CO_2 flux through the LSCF dual-phase membrane as a function of increasing helium sweep rate. Increasing the sweep rate effectively decreases the mole fraction of CO_2 on the downstream side of the membrane. Here, the upstream CO_2 partial pressure is 0.25 atm. Table 3.4 shows the mole fraction of CO_2 on the

downstream side at the corresponding sweep rate. The figure shows that CO_2 permeation increases ever so slightly as the helium sweep rate increases. Although the mole fraction decreases by a factor of more than 26, the CO_2 flux increases from 0.130 to just 0.141 $mL \cdot cm^{-2} \cdot min^{-1}$ from sweep rates of 10 to 300 $mL \cdot min^{-1}$. Error bars indicate that the flux is constant within the calculated range of errors. This is further confirmation that the partial pressure gradient of CO_2 has either very little or no bearing on permeation through the membrane.

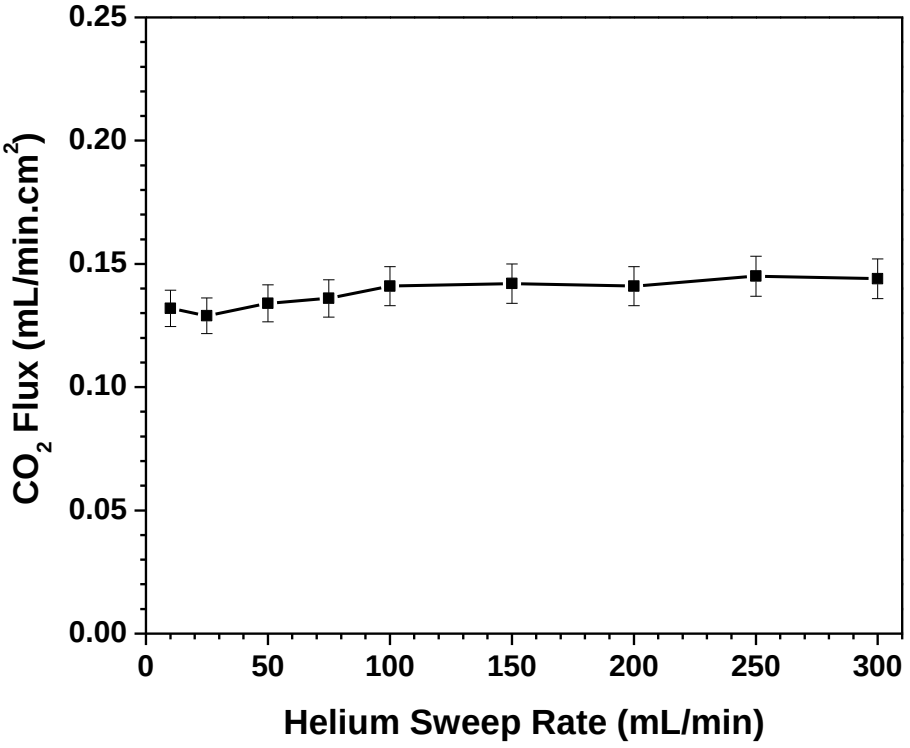

Figure 3.8 High temperature CO_2 flux for a 1.5 mm thick dual-phase membrane at various helium sweep rates

Table 3.4 Helium sweep rate & corresponding CO_2 mole fraction in the permeate

Helium Sweep Rate ($mL \cdot min^{-1}$)	CO_2 Mole Fraction
10	0.0131
25	0.0051
50	0.0027
75	0.0018
100	0.0014
150	0.0009
200	0.0007
250	0.0006
300	0.0005

3.3.3 Modeling CO_2 permeation through the dual-phase membrane

In order to explain and further understand the results presented in this study, the model used to predict high temperature CO_2 permeation through the dual-phase membrane was revisited [Rui et al., 2009]. In non-oxygen, carbon dioxide containing atmospheres, the two charged species within the dual-phase membrane are $CO_3^{=}$ and $O^{=}$, which are denoted as 1 and 2 respectively. Under steady state conditions, the particle fluxes (J_i) of these two charges species can be represented by the following two equations:

$$J_1 = -\frac{\sigma_1}{z_1^{\,2}F}\left(\nabla\mu_1 + z_1 F\nabla\phi_1\right) \tag{3.3}$$

$$J_2 = -\frac{\gamma\sigma_2}{z_2^{\,2}F}\left(\nabla\mu_2 + z_2 F\nabla\phi_2\right) \tag{3.4}$$

where σ_i is conductivity, z_i is the charge, F is Faraday's constant, $\nabla\mu_i$ is the chemical potential and $\nabla\phi_i$ is the electrical potential each species. Here, the charge of both species, z_1 and z_2 is equal to -2. A geometric factor (γ) has been

added to Equation 3.4 to account for support porosity. Since there is no external current for the dual-phase membrane (no wires, etc.), the charge within the system remains balanced at all times:

$$z_1 J_1 + z_2 J_2 = 0 \tag{3.5}$$

Combination of Equations 3.3-3.5 provides the particle flux for the $CO_3^{=}$ ion:

$$J_1 = -\frac{\gamma \sigma_1 \sigma_2}{(\sigma_1 + \sigma_2) z_1^{\,2} F^2} \left(\nabla \mu_1 - \frac{z_1}{z_2} \nabla \mu_2 \right) \tag{3.6}$$

The assumption that local equilibrium holds here, as is the case for oxygen permeation in mixed conducting membranes, cannot be used. The chemical potential ($\nabla \mu_i$) can be correlated to the concentration of the charge species by:

$$\nabla \mu_i = \frac{RT}{C_i} f_i \nabla C_i \tag{3.7}$$

where R is the gas constant, T is temperature, C_i is concentration of species *i* and f_i is the thermodynamic coefficient. The thermodynamic coefficient is defined as:

$$f_i = \frac{\partial \ln a_i}{\partial \ln C_i} \tag{3.8}$$

Combining Equations 3.6-3.8 gives the following expression:

$$J_{CO_2} = -\frac{\gamma \sigma_1 \sigma_2 RT}{(\sigma_1 + \sigma_2) z_1^{\,2} F^2} \left(\frac{f_1}{C_1} \nabla C_1 - \frac{z_1}{z_2} \frac{f_2}{C_2} \nabla C_2 \right) \tag{3.9}$$

Equation 3.9 can be further simplified with a few reasonable assumptions. First, the ionic conductivity of molten carbonate is much greater than the ionic conductivity of oxygen ions in the solid phase ($\sigma_1 >> \sigma_2$). Secondly, the

concentration of $CO_3^{=}$ (C_1 in Equation 3.9) and M^+ ions in the molten carbonate phase are both very high and essentially constant throughout the cross section of the membrane. The concentration can be determined from the density (ρ_{MC}) and molecular weight (M_{MC}) of the molten carbonate mixture:

$$C_{CO_3^{=}} = C_1 = \frac{\rho_{MC}}{M_{MC}} \tag{3.10}$$

Using the relationship shown in Equation 3.10 and the assumptions stated prior, Equation 3.9 can be simplified to:

$$J_{CO_2} = -\frac{\gamma RTf_2}{z_1 z_2 F^2}\left(\frac{\sigma_2}{C_2}\nabla C_2\right) \tag{3.11}$$

Based on Einstein's relation, which assumes that diffusivity is independent of pressure, the conductivity of oxygen ions can be described by:

$$\sigma_2 = \frac{C_2}{C_2^0}\sigma_2^0 \tag{3.12}$$

where superscript "0" indicates oxygen ion conductivity under the standard conditions. Standard conditions could refer to the conductivity in an oxygen-free atmosphere (P_{O_2} = 0 atm) or in an oxygen containing atmosphere (P_{O_2} = 1 atm). Inserting Equation 3.12 into 3.11 gives:

$$J_{CO_2} = -\frac{\gamma RT\sigma_2^o f_2}{z_1 z_2 F^2 C_2^o}\nabla C_2 \tag{3.13}$$

To simplify matters further, it is assumed that this system follows ideal thermodynamic behavior; therefore, the value of f_2 is assumed to be 1.

Integration of Equation 3.13 over the entire membrane thickness from Z = 0 to L gives:

$$J_{CO_2} = \frac{\gamma RT\sigma_2^o}{z_1 z_2 F^2 L}\left[\frac{C_{2,I}}{C_2^o} - \frac{C_{2,II}}{C_2^0}\right] \tag{3.14}$$

where L is the membrane thickness and $C_{2,I}$ and $C_{2,II}$ are oxygen vacancy concentration in solid oxide phase on the upstream and downstream surface respectively. Equation 3.13 is the general flux model of the dual-phase membrane with the following qualifications: (1) the conductivity of the molten carbonate is much larger than oxygen ion conductivity in the solid phase and (2) the metal oxide phase follows ideal behavior with a thermodynamic factor (f) approximately equal to 1.

Determining the values for $C_{2,I}$ and $C_{2,II}$ is not a straight forward process. The CO_2 permeation flux can be correlated to P'_{CO_2} and P''_{CO_2} if the equilibrium oxygen vacancy concentration in the solid phase can be correlated to P_{CO_2} in the gas phase. This entails being able to solve an equilibrium problem involving a three phase system, similar to the one shown in Figure 3.9. However, this particular type of three-phase system involving defect reactions has not been addressed before and would require more experimental and modeling efforts. This requirement is beyond the scope of this study and will be dealt with in future work.

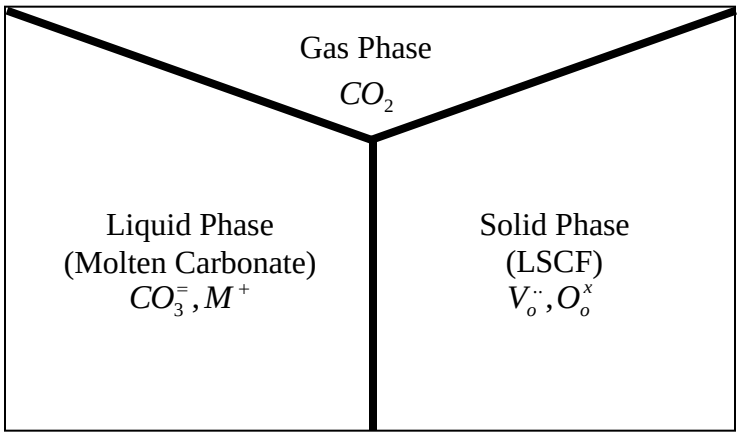

Figure 3.9 Visual depiction of a typical three-phase system between the gas phase, liquid phase and solid phase in the carbonate-ceramic dual-phase membrane

3.3.4 Long term performance and stability of the dual-phase membrane

The final issue to examine with this work was the long term performance of the LSCF dual-phase membrane. Figure 3.10 shows the results gathered from a 100 h long stability test with the LSCF dual-phase membrane and the average daily flux is tabulated in Table 3.5. The feed side was exposed to a 25% CO_2 and 75% N_2 mixture, while the sweep side was exposed to 100% helium. Both the feed and sweep side flow rates were maintained at 100 mL·min^{-1} and kept at 1 atm total pressure. The figure and table both show that the high temperature CO_2 flux is relatively constant over the 100 h time span, thus showing long term stability, in terms of performance, of the membrane. The slight increase observed on days 4 and 5 can likely be attributed to the fact that there was a slight leak through the seal, and calculations to account for the leak caused the values to be somewhat

higher than what was likely observed. However, within the observed error range, flux appears to be relatively constant.

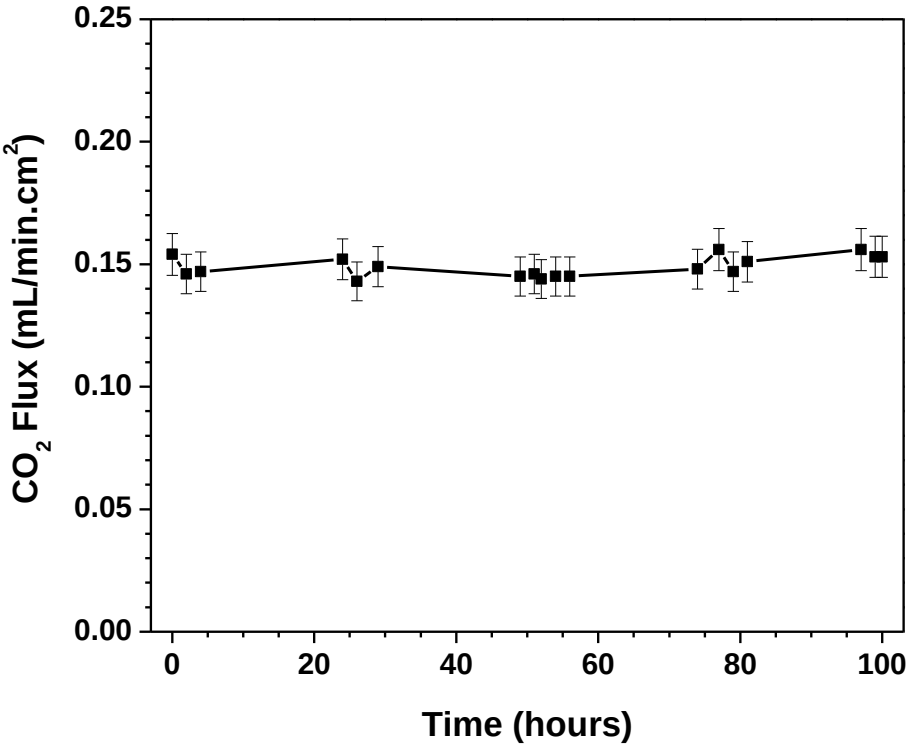

Figure 3.10 Long term (100 h) high temperature CO_2 flux for a 1.5 mm thick dual-phase membrane at 850℃.

Table 3.5 Average daily CO_2 flux of the dual-phase membrane over 100 hr

Day	CO_2 Flux ($mL \cdot cm^{-2} \cdot min^{-1}$)
1	0.149
2	0.148
3	0.145
4	0.150
5	0.154

After the 100 h test, both the feed and sweep sides of the membrane were characterized by XRD, the results of which are shown in Figure 3.11. The figure

also includes patterns of a sintered and infiltrated support for comparison sake. Slight shifts in 2θ from one sample to the next result from using membrane and not powder samples. The feed side XRD pattern shows very little change from that of the infiltrated support, in terms of both the perovskite structure of the support and the pronounced molten carbonate peaks. The unchanged nature of the pattern indicates that the side exposed to high P_{CO_2} remains relatively stable at high temperatures for long periods of time. However, it should be noted that there was a discernable change in the color of the membrane from black at the beginning of the experiment to brick red after completion. On the other hand, the sweep side pattern does show distinct differences from the sintered and infiltrated patterns. Most notably, the perovskite pattern of the support shows signs of being almost nonexistent. However, the there is some semblance of the molten carbonate peaks within the pattern, indicating that decomposition on the sweep side was limited. This leads credibility to the idea that, as long as there are $CO_3^{=}$ ions available on the upstream surface, molten carbonate does not decompose on either side of the membrane.

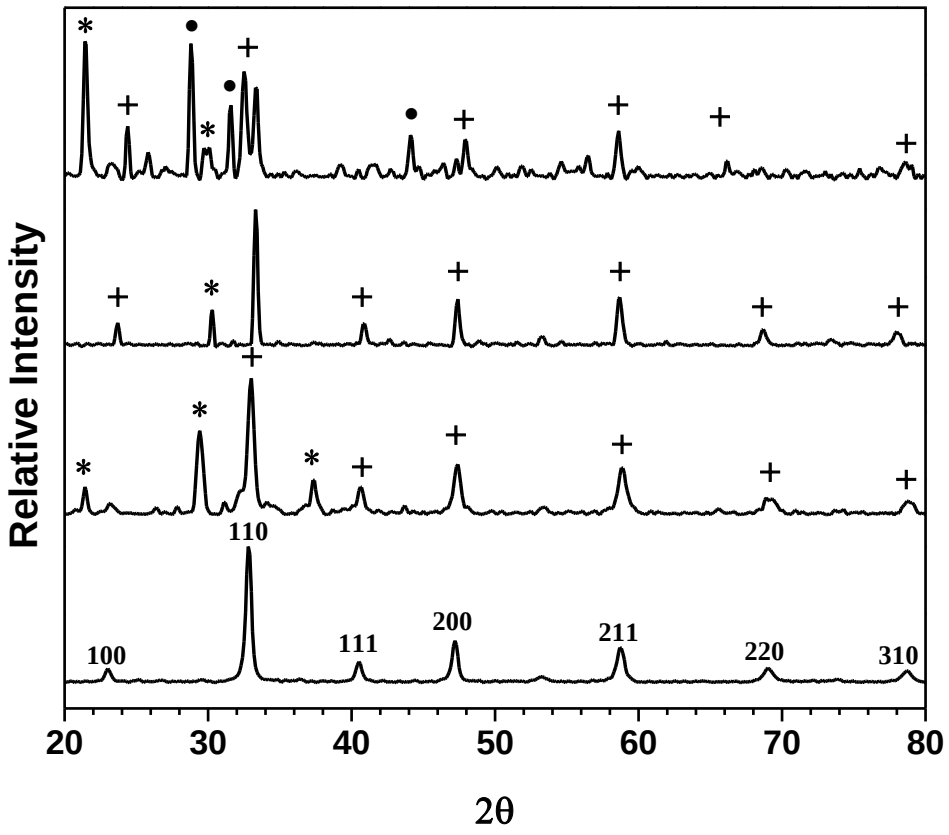

*Figure 3.11 XRD patterns for LSCF dual-phase membrane samples exposed to high and low P_{CO_2} for 100 h at 850℃ (+, * and • indicates diffraction peaks for perovskite, carbonate and unknown structures respectively).*

3.4 Conclusions

LSCF supports were successfully synthesized by pressing and sintering powder prepared by the liquid citrate method. Dual-phase membranes were successfully infiltrated with a eutectic Li/Na/K molten carbonate mixture by the direct infiltration method. Data collected showed that CO_2 measured in the permeate below the equilibrium partial pressure was caused by thermal decomposition and ensuing release of CO_2 by the molten carbonate mixture.

Leaving the dual-phase membrane in environments below the CO_2 equilibrium partial pressure was found to be a detriment to performance, as decomposition caused partially irreversible defect creation within the pores of the membrane.

For a 1.5 mm thick membrane, the CO_2 flux was seen to be 0.056, 0.081 and 0.152 $mL \cdot cm^{-2} \cdot min^{-1}$ at 750, 800 and 850°C respectively for CO_2 partial pressures ranging from 0.05 to 0.95 atm. Likewise, a membrane with a thickness of 0.75 mm showed fluxes of 0.065, 0.094 and 0.174 $mL \cdot cm^{-2} \cdot min^{-1}$ at the same respective temperatures and partial pressures. Based on TGA-DSC data, it was found that CO_2 sorption into the dual-phase membrane was relatively constant at $5x10^{-4}$ mol $CO_2 \cdot g^{-1}$ Membrane. The constant sorption of CO_2 at pressures above P_{eq} provided an explanation for the constant fluxes observed. Furthermore, downstream partial pressure was also found to have a negligible effect on CO_2 flux. A 100 h long experiment at a P_{CO_2} of 0.25 atm showed that the LSCF dual-phase membrane had a nearly constant CO_2 flux of 0.149 $mL \cdot cm^{-2} \cdot min^{-1}$ for the duration of the experiment. Lastly, the model used to predict permeation in pervious works was revisited to investigate potential reasons to account for the lack of driving force provided by the CO_2 partial pressure gradient. It was determined that the equilibrium oxygen vacancy concentration in the solid phase must be correlated to partial pressure of carbonate dioxide in the gas phase. To solve this, a complicated three-phase system involving the gas, liquid and solid phases involved in permeation will be addressed in future work.

Chapter 4

CARBON DIOXIDE SEPARATION AND DRY REFORMING OF METHANE FOR SYNTHESIS OF SYNGAS BY A DUAL-PHASE MEMBRANE REACTOR

4.1 Introduction

Chapters 2 and 3 showed that the dual-phase membrane is a viable method to separate CO_2 at high temperatures. However, questions remain as to what is the most effective way to deal with the CO_2 once it has been separated. Sequestration is one option that has been researched at length, and can be accomplished by various methods, including terrestrial (plant life) or oceanic sequestration, underground injection or storage as mineral carbonates (i.e., $CaCO_3$).

Although sequestration is a popular post separation option, it is not the only one. Streams of warm, highly concentrated CO_2 can also be used as a feedstock for chemical synthesis of syngas. Syngas is a mixture of hydrogen (H_2) and carbon monoxide (CO) that can be used to make a number of important chemical products including ethylene, ethylene glycol, various alcohols and diesel fuel [Prahbu and Oyama, 2000]. It can also be used in the production of synthetic gasoline, in ammonia plants for fertilizer production [Pompeo et al., 2005] and in the Fischer-Tropsch process to synthesize liquid fuels [Shao et al., 2001; Tong et al., 2002; Bouwmeester, 2003]. Production can be accomplished via a number of different reaction pathways which are discussed as follows.

Steam reforming of methane (CH_4) is the process that is almost exclusively used to produce syngas commercially [Pompeo et al., 2005]. Here, CH_4 reacts with water vapor to form the H_2/CO gas mixture, as shown:

$$CH_4 + H_2O(v) \leftrightarrow CO + 3H_2 \qquad (4.A)$$

There are several negative aspects for using Reaction A for syngas production. First, the reaction is endothermic (ΔH^0_{298} = 206 kJ·mol^{-1}) and must be carried out at high temperature, thus requiring substantial energy and capital investment to sustain a high throughput process [Balachandran et al., 1997; Dong et al., 2001; Luo et al., 2010]. Furthermore, the H_2:CO ratio produced in the reaction is 3:1. Synthesis of many fuels, especially those via the Fischer-Tropsch process, all require that the H_2:CO ratio is as close to 1 as possible for maximum efficiency [Wang et al., 2003; Luo et al., 2010]. Lastly, the failure to remove sulfur containing compounds in the methane stream can poison the catalysts in the packed bed and lead to lower reaction conversions over time.

Another method that can be used to produce syngas is by the direct partial oxidation of methane. Here, methane reacts with O_2 to form the syngas mixture:

$$CH_4 + \tfrac{1}{2}O_2 \leftrightarrow CO + 2H_2 \qquad (4.B)$$

Direct partial oxidation is mildly exothermic (ΔH^0_{298} = -36 kJ·mol^{-1}) and produces H_2 and CO in a ratio of 2:1. Although the H_2:CO ratio is closer to the desired figure for methanol and Fischer-Tropsch synthesis, the reaction scheme is not without drawbacks. The major disadvantage centers on the reactivity of H_2 and CO with oxygen. Both products can be further oxidized to make CO_2 and H_2O.

Therefore, this particular method is only suitable for reactors with extremely small residence times [Balachandran et al., 1995; Balachandran et al., 1997; Dong et al., 2001; Ikeguchi et al., 2005]. Additionally, due to the formation of CO_2 and H_2O during direct partial oxidation, it is thought that the actual mechanism of syngas production occurs via the combustion (C; ΔH^0_{298} = -802 kJ·mol^{-1}) and reforming (D; ΔH^0_{298} = 247 kJ·mol^{-1}) reaction mechanisms:

$$CH_4 + O_2 \leftrightarrow CO_2 + 2H_2O \quad (4.C)$$

$$CH_4 + CO_2 \leftrightarrow 2CO + 2H_2 \quad (4.D)$$

A major drawback of Reaction C is that it requires a feed stream of pure oxygen into the system [Dong et al., 2001; Wang et al., 2003]. For this reason, a cryogenic oxygen plant would be required. This would increase costs dramatically [Rostrupnielsen and Hansen, 1993]. Moreover, this particular process would have to be designed to avoid against the occurrence of hot spots and potential reactor runaway, as Reaction C is very exothermic.

The dry reforming reaction shown in Reaction D produces a H_2:CO ratio of 1:1 which is highly suitable for liquid fuel synthesis. Using this reaction to produce syngas would eliminate the need for a feed stream of pure oxygen and all of the shortcomings that accompany Reaction C. In addition, unlike Reaction A-C, the dry reforming reaction uses two greenhouse gases, CO_2 and CH_4, to create a valuable chemical feedstock [Rostrup-Nielsen, 1994]. Several potential side reactions accompany the dry reforming reaction, including the reverse water gas shift reaction [Lemoniodu et al., 1998], the methane cracking reaction [Hou et al.,

2003] and the Boudouard reaction [Juan-Juan et al., 2004]. Another downside is the fact that catalysts used are prone to carbon deposition from the methane cracking and Boudouard reactions as a result of the lower H to C ratio in the reaction [Edwards and Maitra, 1995]. Yet, despite these undesirable characteristics, Reaction D remains a viable method for syngas production.

Several groups have studied the use of membrane reactors to enhance the production of syngas via the dry reforming reaction. Prabhu et al. compared the dry reforming of methane in a simple plug flow reactor and in another that contained a hydrogen selective membrane [Prabhu et al., 1999]. The addition of a Vycor glass membrane to the reactor resulted in methane conversions above thermodynamic equilibrium. The high methane conversion was attributed to the preferential removal of H_2 by the membrane, thus driving equilibrium in favor of the products. Prabhu and Oyama continued work on the use of H_2 selective membranes by modifying a Vycor glass membrane with silica and using an alumina supported Ruthenium catalyst [Prabhu and Oyama, 2000]. Once again, CH_4 conversions above thermodynamic equilibrium were achieved. Gallucci and co-workers used porous tubular palladium-silver membranes selective to H_2 in conjunction with an alumina supported Ni catalyst [Gallucci et al., 2008]. The porous membranes were found to offer higher CO_2 and CH_4 conversions of 20.6 and 17.41%. In the absence of a membrane, the corresponding conversions were just 14.0 and 8.4%. Finally, Bosko et al. performed the dry reforming reaction in membrane reactors using Pd and Ad-Ag composite membranes [Bosko et al.,

2010]. Electroless plating was used to coat the Pd and Pg-Ag films on NaA modified porous stainless steel supports. With these membranes, a methane conversion of 80% was made possible at 450°C.

This paper reports on an experimental study regarding the use of carbonate-ceramic dual-phase membranes as membrane reactors in conjunction with the dry reforming reaction for carbon dioxide capture and synthesis of syngas. Membrane reactor experiments were conducted using three different system arrangements. In one case, the dry reforming reaction was performed with the dual-phase membrane in the absence of a catalyst on the downstream side of the membrane. In the two other instances, a LSCF combustion catalyst and a 10 wt% Ni/γ-alumina reforming catalyst were packed on the downstream side to help drive reaction in the forward direction. The effect of temperature (750-850°C), sweep rate (10-50 $mL \cdot min^{-1}$) and methane concentration (10-50%) on CO_2 flux, H_2 production rate, H_2:CO ratio and CO_2 and CH_4 conversions were investigated.

4.2 Experimental

4.2.1 Synthesis of the LSCF-carbonate dual-phase membranes

$La_{0.6}Sr_{0.4}Co_{0.8}Fe_{0.2}O_{3-\delta}$ (LSCF) powder was synthesized via the liquid citrate method according to the procedure described Anderson and Lin [Anderson and Lin, 2010]. The thickness of LSCF supports prepared was 1.5 mm. To form the supports of that thickness, 3.0 g of the LSCF powder and PVA binder mixture was placed into a 30 mm stainless steel mold and pressed to 160 MPa for five minutes in a Carver hydraulic press. The green disks were sintered in air for 24 h

at 900°C (2°C·min^{-1} ramping rates) to produce mechanically stable, porous supports with the appropriate pore size. The porous supports were infiltrated the 42.5/32.5/25 mol % $Li_2CO_3/Na_2CO_3/K_2CO_3$ molten carbonate mixture to obtain dense dual-phase membranes via the direct infiltration method [Chung et al., 2005; Anderson and Lin, 2010]. Helium permeance measurements were performed to confirm that the infiltrated membranes were dense at room temperature.

4.2.2 Synthesis of the LSCF and 10% Ni/γ-alumina catalysts

The same composition of powder ($La_{0.6}Sr_{0.4}Co_{0.8}Fe_{0.2}O_{3-\delta}$) used to prepare the supports for the dual-phase membrane was used for the LSCF combustion catalyst. As such, the same method was used to make catalyst powder [Anderson and Lin, 2010]. After calcination at 600°C, the powder was reground with a mortar and pestle and then sintered for 24 h at 900°C (ramp rate = 2°C·min^{-1}). To further decrease the particle size, the powder was placed into a Teflon tumbler and mixed with ethanol. The tumbler was filled with three parts ethanol to one part powder by weight to form a slurry. Zirconia balls of 2 and 5 mm in diameter were added to the tumbler and the resulting slurry was ball milled for 48 h. After ball milling, the ethanol was evaporated from the slurry and the remnants were reground for use as the catalyst in the dry reforming experiments.

To synthesize the 10% (by wt.) Ni/γ-alumina reforming catalyst, appropriate amounts of $Ni(NO_3)_2 \cdot 6H_2O$ (Alfa Aesar, 98%) and γ-alumina (Alfa Aesar) were obtained. Pellets of γ-alumina were ground with a mortar and pestle

and then separated with a #80 sieve. Sieving was done to assure that all of particles used for the catalyst were less than 180 μm in size. The $Ni(NO_3)_2 \cdot 6H_2O$ and sieved γ-alumina were mixed with deionized water at room temperature. The solution was then heated to 80°C and mixed thoroughly to allow for the Ni to coat the γ-alumina particles. The temperature of the slurry was raised to 120°C and left overnight to allow all of the water to evaporate. The remnants were ground with a mortar and pestle and then calcined for 4 h at 700°C (Ramp rate = $5°C \cdot min^{-1}$). The calcined material was then reduced in a 10% H_2/He gas mixture for 6 h at 600°C to activate the catalyst. After reducing the catalyst, the powder was ground one last time. Both catalysts and used membranes were characterized by X-Ray Diffraction in the 2θ range of 20° to 80° with a step size of 0.05°/s using a Bruker D8 Focus Diffractometer (Cu Kα = 1.54 Å). The supports and infiltrated membranes were characterized by room temperature helium permeation measurements. Nitrogen porosimetry experiments on both catalysts were carried out at liquid nitrogen temperature (77K) using a Micromeretics ASAP 2020 to determine the average pore size and surface areas.

4.2.3 High temperature CO_2 separation and membrane reactor measurements

High temperature CO_2 flux measurements were conducted using a similar high temperature setup to the one described in previous work [Anderson and Lin, 2010]. A schematic of the setup is shown in Figure 4.1 to illustrate placement of the catalyst within the system. The dual-phase membranes were sealed to the inner alumina tube (2.54 cm OD) by creating a paste composed of a mixture of

ground, sintered LSCF powder (40 wt%), ground Pyrex™ beaker glass (50%), sodium aluminum oxide (Alumina·Na_2O; 10%) and water [Qi et al, 2001]. A stainless 2.50 cm OD stainless steel ring was placed on top of the membrane. Appropriate amounts of LSCF (1.0 g) and Ni/γ-alumina (0.6 g) catalyst were added into the ring to form a consistent bed height of 3 mm.

The catalyst and membrane system were sealed inside a 3.8 cm OD alumina tube and heated at a rate of 1°C·min^{-1} to 850°C to allow for the seal to soften and set. Gases were delivered to the up and downstream sides of the membrane by connecting mass flow controllers to 1 cm OD alumina tubes. Each tube was placed about 3 cm away from the membrane on both sides. The composition (25% CO_2, 75% N_2) and flow rate (100 mL·min^{-1}) of the feed stream were kept constant throughout this entire study. The composition and flow rate of the downstream (sweep) gases varied depending on the experiment being conducted. For each of the scheduled experiments, the permeate and retentate flow rates were measured using a bubble flow meter, while the gas composition of the permeate was determined by running gas samples through a gas chromatographer (Agilent, 6890N) with a packed column (2836PC, Alltech) and a TCD detector. Error associated with permeation measurements was found to be $\pm$ 5.6%.

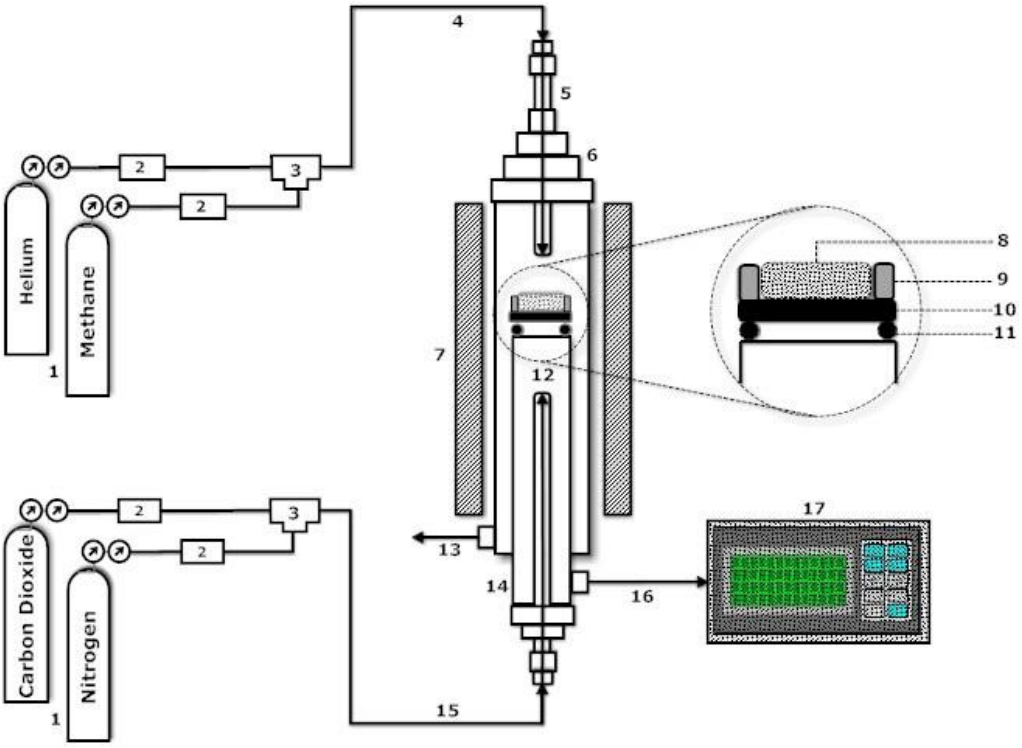

Figure 4.1 Schematic of the high temperature CO_2 permeation and synthesis of syngas set up used in this work. 1) Gas cylinders, 2) Mass flow controllers, 3) Gas mixing tees, 4) Feed line, 5) Feed tube, 6) Outer tube, 7) Furnace, 8) Catalyst, 9) Stainless steel ring, 10) Dual-phase membrane, 11) Ceramic seal, 12) Sweep tube, 13) Retentate, 14) Inner tube, 15) Sweep line, 16) Purge gas, 17) Gas chromatograph.

4.3 Results and discussion

4.3.1 Properties of the LSCF-carbonate dual-phase membrane and catalysts

Prior to using the LSCF dual-phase membrane for CO_2 separation and as a membrane reactor for the dry reforming reaction, the support and infiltrated membranes were characterized. Previous helium permeation experiments showed that LSCF supports had a room temperature permeance on the order of 10^{-6}

$mol \cdot m^{-2} \cdot s^{-1} \cdot Pa^{-1}$ with an average pore diameter of 365 nm. This result was further confirmed via mercury porosimetry and SEM, both of which indicated a similar average pore size for the support [Anderson and Lin, 2010]. After infiltration, the room temperature helium permeance of the dual-phase membrane decreased by four orders of magnitude to 10^{-10} $mol \cdot m^{-2} \cdot s^{-1} \cdot Pa^{-1}$, approaching the measuring capability limit of the permeation setup. Complete infiltration of the support was also confirmed via SEM imaging [Anderson and Lin, 2010]. The drastic drop in permeance between the support and dual-phase membrane indicated that molten carbonate completely infiltrated the tortuous pores via capillary action to form a dense membrane. This is a stringent requirement towards producing a selective membrane at high temperature, as formation of a gas tight membrane ensures that only CO_2 will permeate at high temperatures.

XRD patterns of the LSCF support and infiltrated membrane are shown in Figure 4.2. The pattern of the sintered support confirms that LSCF was properly synthesized via the citrate method, as the peaks and indices match that which has been reported previously by Wang et al. [Wang et al., 2003]. Supports synthesized in this manner are of the desired perovskite structure and possess the characteristics essential for the dual-phase membrane. The XRD pattern of the non-contact side of the membrane after infiltration shows peaks indicative of molten carbonate at 2θ values of 21.9, 29.4 and 37.3° in Figure 4.2. The presence of the molten carbonate peaks on the non-contact side confirms complete infiltration throughout the entire thickness of the membrane.

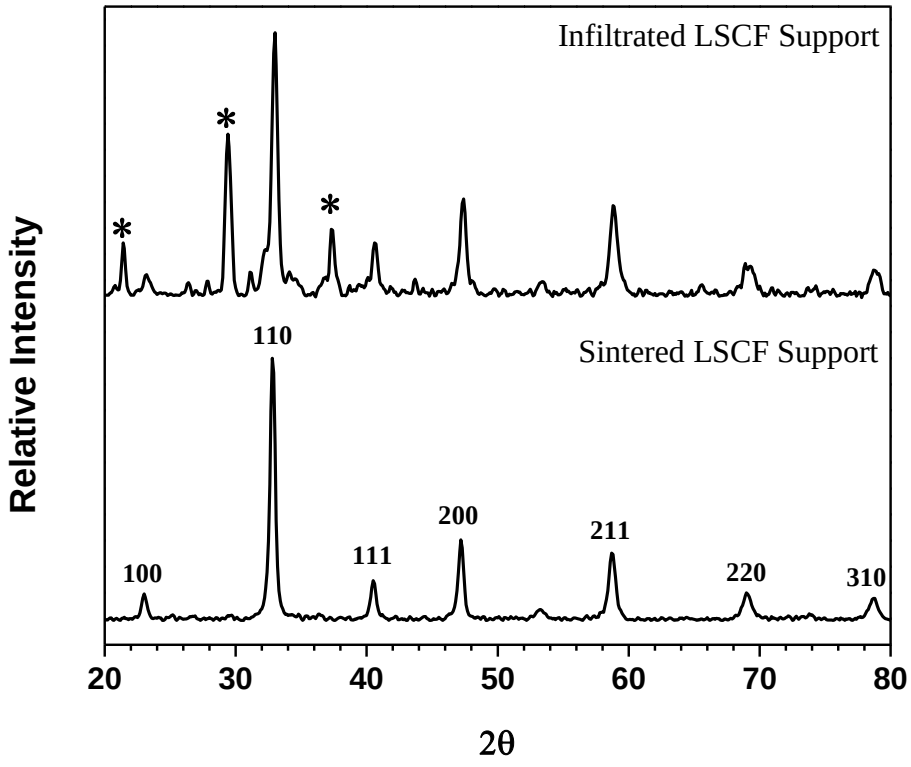

Figure 4.2 XRD patterns of a sintered LSCF support and carbonate infiltrated membrane (indicates diffraction peak for carbonate). The perovskite peaks for the LSCF material are indexed.*

Three different membrane reactor systems used to synthesize syngas by dry reforming of CO_2 and CH_4 were studied in this work. The first system dealt with a membrane reactor that contained no catalyst on the downstream side. This configuration was conceived to determine whether or not the surface of the dual-phase membrane could serve as a vehicle to drive the dry reforming reaction. For the two other arrangements, catalysts were packed on the downstream side of the membrane, as previously indicated in Figure 4.1.

Some studies point toward the effectiveness of perovskite powders as catalysts for use in reactions involving the conversion of methane to syngas [Choudhary et al., 1996; Choudhary et al., 1999]. Towards this, the first type of catalyst studied in this work was a LSCF catalyst with the composition $La_{0.6}Sr_{0.4}Co_{0.8}Fe_{0.2}O_{3-\delta}$. This catalyst is the same composition of powder that was used to make supports for the dual-phase membranes. Figure 4.3a shows the nitrogen sorption isotherms for the catalyst. The figure depicts a Type II isotherm. This particular isotherm is indicative of materials with a wide distribution of pore sizes. This is confirmed by the wide pore size distribution shown in the inset of Figure 4.3a. Here, monolayer adsorption is observed at low relative pressures of N_2. Multilayer adsorption begins to occur towards saturation at a relative pressure (P/P_o) of 0.90. The catalyst is characterized as having a very low BET surface area of 2.85 $m^2 \cdot g^{-1}$ with a wide pore size distribution. To maintain a consistency for the catalyst beds in this study, all tests were done using a bed height of 3 mm. For the LSCF catalyst tests, 1.0 g of catalyst was necessary to achieve this height.

The second catalyst used in this study was a 10% (by weight) Ni/γ-alumina powder. This particular material has been shown to be effective in reforming reactions such as the one at the center of this work. Therefore, this catalyst will often be referred to as the reforming catalyst. The nitrogen sorption isotherms are plotted in Figure 4.3b. The isotherm resembles a Type IV isotherm with a hysteresis that appears at a relative pressure of 0.80, indicative of a

material having fairly large mesopores. The relatively flat region within the figure suggests that there is formation of a monolayer within the pores of the mesoporous catalyst. However, the major difference here is that there is finite multi-layer formation of the adsorbate that corresponds to complete filling of the pores inside the catalyst near a relative pressure of unity, unlike the indefinite filling of pores in the Type II isotherm seen for the LSCF catalyst. This is common in materials with mesopores, which are clearly present based on the pore size distribution for the material, which is shown in the inset of Figure 4.3b. From the results, it was determined that the catalyst has a BET surface area of 154.0 $m^2 \cdot g^{-1}$. This value is consistent with previously reported results [Gonclaves et al., 2006]. To achieve a 3 mm bed height with this catalyst, 0.6 g of material was required.

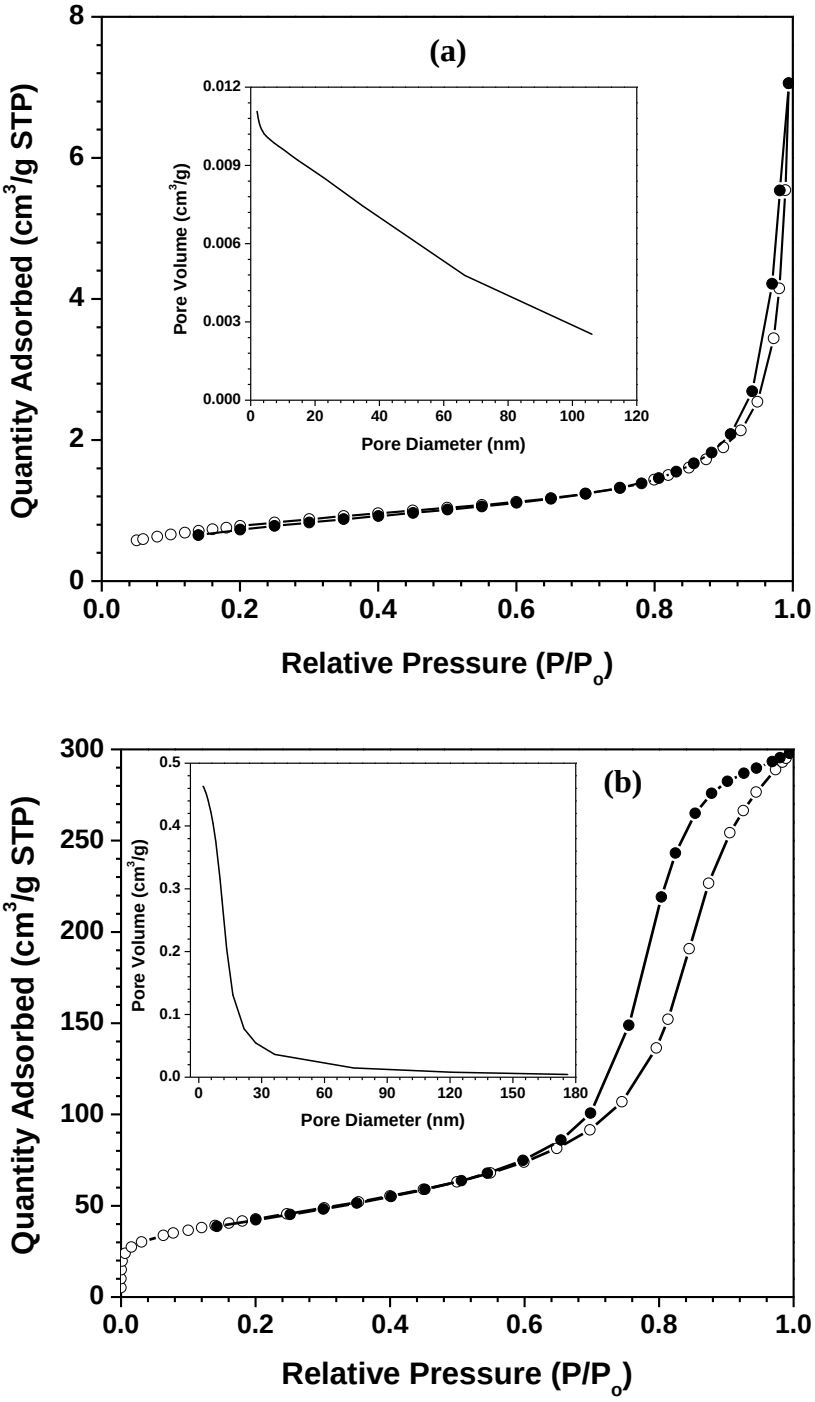

Figure 4.3 Nitrogen adsorption and desorption isotherms at 77K for a) LSCF catalyst, b) Ni/γ-alumina catalyst Absorption ○; Desorption ●. The insets in the figures show the pore size distribution for each respective catalyst.

4.3.2 Carbonate-LSCF dual-phase membrane performance with reducing sweep

Some work has been done on CO_2 permeation through dual-phase membranes using inert sweeps on the downstream side of the membrane [Anderson and Lin, 2010]. However, the high temperature permeation behavior of the membranes using a reducing (methane) sweep has not been studied prior to this work. In order to determine the total flux of CO_2 through the membrane, it was necessary to know both the amount of CO_2 consumed and unconsumed during the dry reforming reaction. Unconsumed CO_2 could be determined by analyzing the peak area of CO_2 from the GC software. The amount of CO_2 consumed by the reaction was dependent on the production rates ($Q_{PR(H_2)}$) of H_2 or CO. For every two mol of H_2 and CO produced, one mol of CO_2 was consumed. The following equation was used to determine the total CO_2 flux that permeated through the membrane in each of the experiments conducted:

$$J_{CO_2} = J_{CO_2}(unconsumed) + \frac{Q_{PR(H_2)}}{2} \qquad (4.1)$$

H_2 and CO are supposed to be produced in a 1:1 ratio during the dry reforming reaction, so the production rate of either species could can be used to calculate the total CO_2 flux in the above equation. In this study, H_2 was chosen due to the greater accuracy in measuring the production rate via the GC.

Measurements were taken from the system that contained no catalyst on the downstream side. This particular arrangement will be referred to as the 'blank system.' Other systems used in this study involved either the use of the LSCF or Ni/γ-alumina catalysts. When running experiments dealing with changes in

methane percentage, the sweep rate (10 $mL \cdot min^{-1}$) and temperature (850°C) were held constant throughout data collection. Similar actions were taken during experiments dealing with changes in sweep rates (methane percentage: 50%; temperature: 850°C) and temperature (methane percentage: 50%; sweep rate: 10 $mL \cdot min^{-1}$). A summary of the variables and constants for each experiment are summarized in Table 4.1.

Table 4.1 Summary of experimental variables and constants in dry reforming experiments

Variable (range)	Constants (value)	
Methane Percentage (10-50%)	Sweep Rate (10 $mL \cdot min^{-1}$)	Temperature (850°C)
Sweep Rate (10-50 $mL \cdot min^{-1}$)	Methane Percentage (50%)	Temperature (850°C)
Temperature (750-850°C)	Methane Percentage (50%)	Sweep Rate (10 $mL \cdot min^{-1}$)

The dependency of CO_2 permeation upon changing the methane percentage (10-50%) and sweep rate (10-50 $mL \cdot min^{-1}$) is shown in Figures 4.4a and b. The figures indicate that neither a change in the concentration of methane in the sweep from 10 to 50% nor a change in the sweep rate from 10 to 50 $mL \cdot min^{-1}$ have any noticeable effect on CO_2 flux. In both figures, the values for CO_2 flux remained at or around 0.165 $mL \cdot min^{-1} \cdot cm^{-2}$ for each adjustment made to either system. The flux measured with the reducing methane sweep compares rather closely to the CO_2 flux obtained from a dual-phase membrane of identical

thickness when an inert sweep gas was used (0.163 $mL \cdot min^{-1} \cdot cm^{-2}$) [Anderson and Lin, 2010].

Figures 4.5a and b describe the temperature dependency on CO_2 permeation and the corresponding activation energy respectively. In Figure 4.5a, CO_2 flux increases with increasing temperature due to the fact that the ionic conductivity of the support also increases [Teraoka et al., 1988]. At the lowest system temperature, the average CO_2 flux with the reducing sweep was 0.061 $mL \cdot min^{-1} \cdot cm^{-2}$. The CO_2 flux obtained using an inert sweep gas was 0.068 $mL \cdot min^{-1} \cdot cm^{-2}$. At 850°C, the average CO_2 flux was 0.171 $mL \cdot min^{-1} \cdot cm^{-2}$. This value is marginally higher than the 0.163 $mL \cdot min^{-1} \cdot cm^{-2}$ CO_2 flux measured at the same temperature with a helium sweep [Anderson and Lin, 2010]. The higher value could be a result of carbon monoxide production via dry reforming and subsequent reaction with oxygen impurities from the cylinders used. However, hydrogen, which was also produced in large quantities during this experiment, is also very reactive with O_2 yet no H_2O was detected at any time during these experiments. Nevertheless, despite the slight variations, the results obtained in each of the three systems with a reducing sweep are quite comparable to previously recorded data obtained with a helium sweep.

Figure 4.5b shows the Arrhenius plot used to calculate the activation for CO_2 permeation. The activation energies were similar, with an average between the three of about 99.3 $kJ \cdot mol^{-1}$. This particular value is about 12-13% higher than the activation energies calculated using an inert sweep. The activation

energy shows that CO_2 flux has a strong dependency on temperature. Furthermore, the activation energy is still similar to that for oxygen vacancy diffusion in LSCF materials.

The similarity in CO_2 flux values between the reducing and inert gases signifies that the inclusion of methane in the sweep gas does not radically influence permeation. Due to the infancy of work on the dual-phase membrane, the exact reason for this is not clearly understood at this time. However, it is possible that the use of industrial grade quality gases containing oxygen impurities may be part of the reason. These cylinders contain oxygen at an approximate partial pressure of about 10^{-4} atm. Past studies have shown that the permeation through the dual-phase membrane is controlled by oxygen ion conductivity [Anderson and Lin, 2010]. The oxygen partial pressure difference between the up and downstream side of the membrane may not be large enough to create an increase in the ionic conductivity of support. However, one could argue that the production of CO and H_2 would eliminate most or all of the oxygen impurities present on the downstream side by reacting to form CO_2 and/or H_2O. Such occurrences could cause the partial pressure of oxygen on the downstream side to be much lower than 10^{-4} atm. Perhaps there are other reasons for the observed permeation behavior. Further studies regarding the CO_2 permeation mechanism maybe produce more insight towards understanding what system parameters are most likely to affect and optimize permeation.

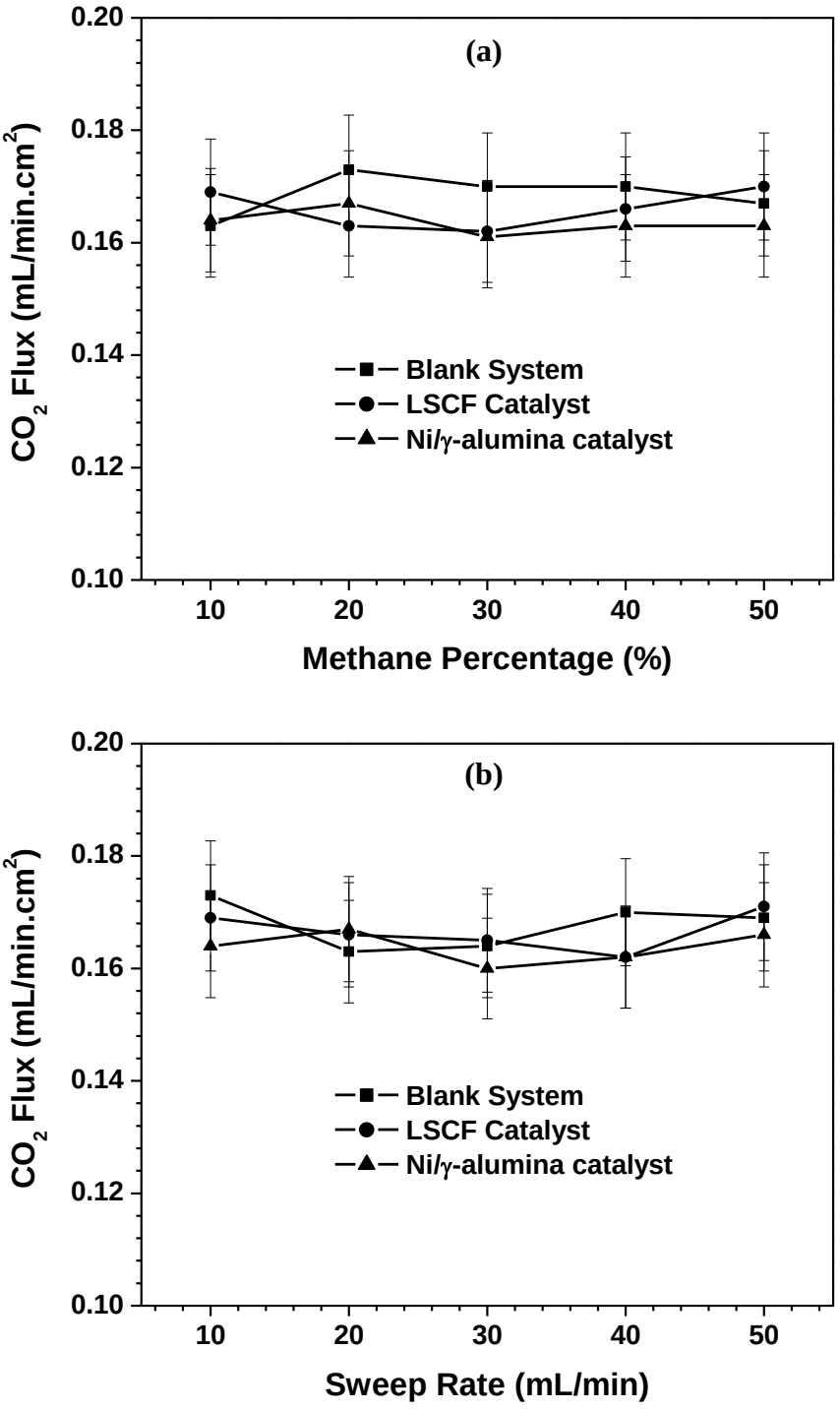

Figure 4.4 Total CO_2 flux dependency on changing the (a) Methane percentage and (b) Sweep rate.

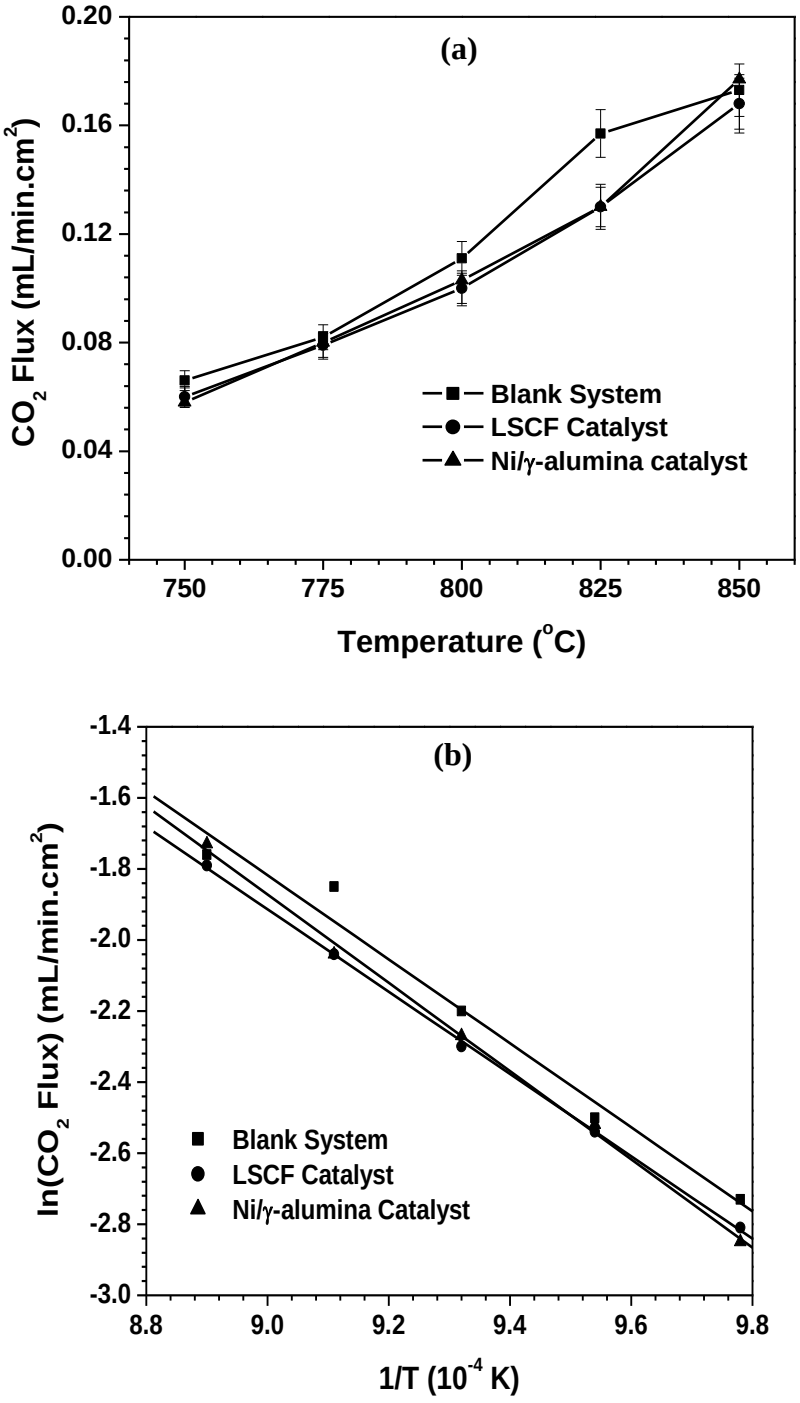

Figure 4.5 (a) Total CO_2 flux dependency on system temperature; (b) shows a plot of the activation energy for CO_2 permeation obtained from Figure 4.5a for the blank system, LSCF and Ni/γ-alumina catalysts

4.3.3 Dry reforming of methane for syngas production

Several aspects of the dry reforming reaction were monitored throughout the course of this study. For each experiment, the production of hydrogen (PR_{H_2}) and carbon monoxide were determined from GC peak areas with integration software. Here, hydrogen production ($mL \cdot min^{-1} \cdot cm^{-2}$) and H_2:CO ratio are reported. Conversion of both CO_2 and CH_4 are also presented in the figures that follow. The conversion of each was calculated using the products of the dry reforming reaction. To determine the overall conversion of carbon dioxide, the total CO_2 flux calculated from Equation 4.1 was required. As per Reaction D, the amount of H_2 produced is twice that of the amount of CO_2 consumed. Therefore, CO_2 conversion was determined by using the following equation:

$$CO_2 \ Conversion \ (\%) = \left(\frac{\frac{1}{2} Q_{PR(H_2)}}{J_{CO_2}} \right) \times 100 \qquad (4.2)$$

Where $Q_{PH(H_2)}$ is the production rate of hydrogen ($mL \cdot min^{-1} \cdot cm^{-2}$) and J_{CO_2} is the total CO_2 flux ($mL \cdot min^{-1} \cdot cm^{-2}$) calculated from Equation 4.1.

The amount of methane in the sweep gas was known at all times. During the dry reforming reaction, for each H_2 molecule produced, one CH_4 is consumed. Therefore, by knowing the amount of methane fed into the system by the mass flow controller, the dual-phase membrane area and the hydrogen production rate, it was possible to determine the conversion of CH_4:

$$CH_4\ Conversion\ (\%) = \left(\frac{\frac{1}{2} Q_{PR(H_2)}}{\frac{F_{CH_4}}{A}} \right) \times 100 \qquad (4.3)$$

where $Q_{PR(H_2)}$ is the production rate of H_2, F_{CH_4} is the flow rate of methane into the system and A is the area (cm^2) of the dual-phase membrane. Overall carbon balances into and out of the systems showed no noticeable accumulation within the system. Therefore, it was determined that coke formation on the catalysts was negligible during the time frame in which experiments were conducted.

Figures 4.6a and b show the rate of H_2 production and H_2 to CO when the methane percentage of the sweep gas was changed from 10-50%. The sweep rate and temperature of the system were held constant at 10 $mL \cdot min^{-1}$ and 850°C respectively. Each figure presents details the results obtained for all three of the different catalytic systems (blank system, LSCF catalyst, Ni/γ-alumina catalyst) studied in this work. Figure 4.6a shows that the production rate of H_2 increases in all three of the systems as methane percentage in the sweep was increased, reaching maximum H_2 production at a methane concentration of 50%. However, a drastic difference in the production rates can be observed between using the Ni/γ-alumina reforming catalyst and the LSCF combustion catalyst or blank system. With the reforming catalyst and a methane sweep concentration of 50%, the production rate of H_2 was 0.274 $mL \cdot min^{-1} \cdot cm^{-2}$. In comparison, the rate of production of H_2 is just 0.083 and 0.092 $mL \cdot min^{-1} \cdot cm^{-2}$ for the blank and combustion catalyst systems under the same experimental conditions.

The H_2 to CO ratios in Figure 4.6b indicate that, for the most part, the production of H_2 and CO is carried out at a 1:1 ratio. As mentioned prior, one of the desirable aspects of the dry reforming reaction is a production ratio of H_2 and CO in unity. However, from the figure, it can be seen that, at low methane percentages, some of the ratios are somewhat lower than one. For instance, the H_2:CO ratio at a methane percentage of 10% for the blank system is 0.797. However, despite the disparity from unity, the ratio calculated in this case is somewhat misleading. The values obtained for the production rates of H_2 and CO each are relatively close at 0.0059 and 0.0074 $mL \cdot min^{-1} \cdot cm^{-2}$, respectively. Calculating the ratios using such low, yet similar flux values leaves open the possibility for large disparities from unity, as is seen in this particular case. It should also be noted that the production rate of CO could be slightly higher than H_2 because CO and O_2 share the same retention time in the packed column installed in the GC used for this work. Gas tight syringes are used to collect samples from the permeate, and although minimal, air does find its way into the syringe. Even though this occurrence is accounted for in the calculations of the CO production rate, it is possible that slightly larger amounts of air leak into the syringe on occasion and lead to slightly higher CO areas. Such instances would lead to H_2 to CO ratios of less than unity, particular in cases with low production rates.

Figures 4.7a and b reveal the conversion percentages of CO_2 and CH_4 respectively as methane percentage in the sweep increases. From the figures, it is

clearly noticeable that conversion of both species increases as methane concentration rises, with one exception. As methane concentration increases in the Ni/γ-alumina system, conversion of CH_4 drops. This can be explained by looking back at Equation 4.3. The area normalized flow rate of methane into the system at 10% is low and increases by an order of magnitude at 50%. However, while H_2 production increases with CH_4 concentration from 10-50%, it remains of the same order of magnitude. This explains the drop in CH_4 conversion as concentration increases. Another issue to point out is the glaring difference in the magnitude at which the species are converted to syngas. Take for instance the system configuration with the Ni/γ-alumina catalyst at a methane percentage of 50%. In this case, conversion of CO_2 is 84.1%. Methane conversion is just 7.3%. The discrepancy comes from the fact that, in this study, the limiting reactant is CO_2. In comparison, methane is present in great excess. CO_2 fluxes through the membrane are on the order of 10^{-1} $mL \cdot min^{-1} \cdot cm^{-2}$, whereas, the area normalized methane rates are on the order of 10^{1} $mL \cdot min^{-1} \cdot cm^{-2}$. Therefore, CO_2 conversion is higher than methane conversion.

The highest conversions of CO_2 were achieved when methane concentration was 50%. Carbon dioxide conversion with the LSCF combustion catalyst and blank system are low, never breaching 32%. The probability that CO_2 and CH_4 will interact on the surface of membrane or within the catalyst bed increase at higher methane concentration. However, the low surface area of the LSCF catalyst provides no obvious improvement in comparison to the blank

system. A catalyst with much higher area and activity would be more suitable for this type of system which was confirmed by the addition of the Ni/γ-alumina catalyst.

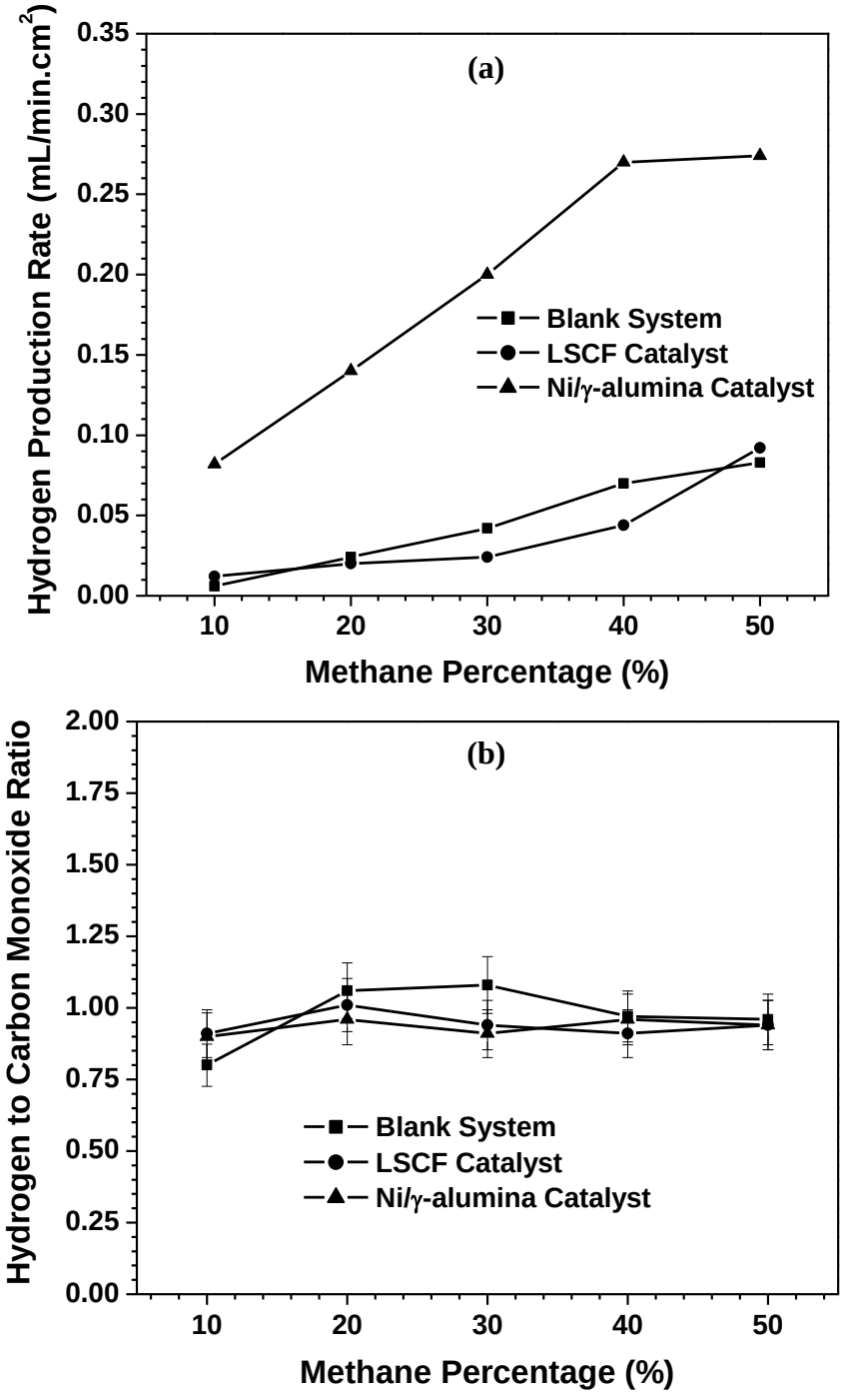

Figure 4.6 Production of syngas dependency on methane percentage in the sweep gas on (a) Hydrogen production rate and (b) the hydrogen to carbon monoxide ratio.

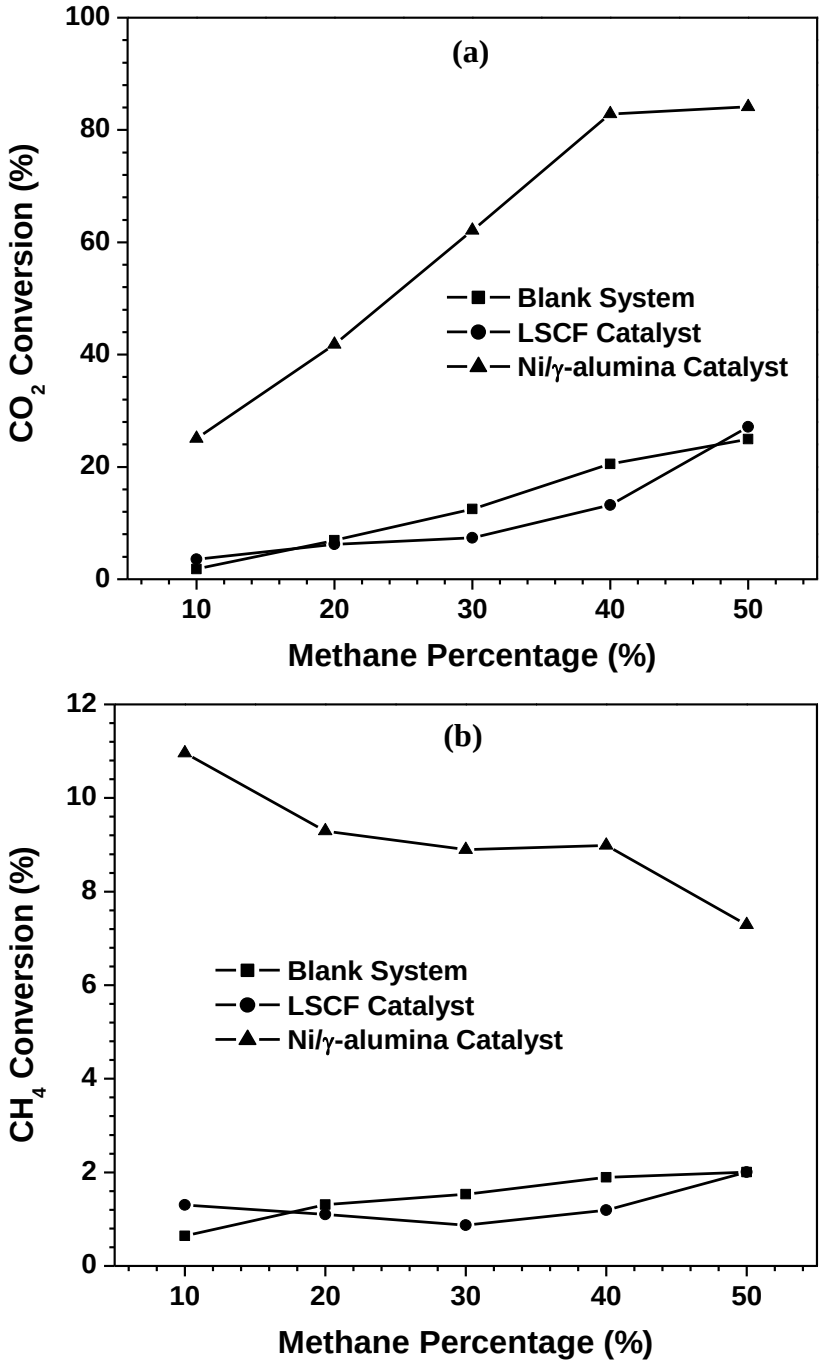

Figure 4.7 (a) CO_2 conversion and (b) CH_4 conversion for changes in methane percentage within the sweep gas and constant temperature (850℃) and sweep rate (10 mL·min^{-1})

The next system parameter that was studied was the sweep rate used on the downstream side of the membrane. Figures 4.8a and b show the rate of H_2 production when the methane percentage and sweep rate on the downstream side of the dual-phase membrane was increased from 10 to 50% and 10 to 50 $mL \cdot min^{-1}$ respectively for the blank system, and the LSCF and Ni- alumina catalysts. For this particular set of experiments, the methane concentration in the sweep and temperature of the system were held constant at 50% and 850°C, respectively. In Figure 4.8a, the production of syngas is maximized in the Ni/γ-alumina catalyst system at a sweep rate of 10 $mL \cdot min^{-1}$. Here, the H_2 production rate is 0.289 $mL \cdot min^{-1} \cdot cm^{-2}$. Conversely, for a sweep rate of 50 $mL \cdot min^{-1}$, the production rate drops by about 40% to 0.184 $mL \cdot min^{-1} \cdot cm^{-2}$. Even at low sweep rates, the production of H_2 using the LSCF catalyst or blank system never reaches a rate greater than 0.110 $mL \cdot min^{-1} \cdot cm^{-2}$. Figure 4.8b shows the H_2:CO ratio achieved with increasing sweep flow rate on the downstream side of the membrane. As was the case in Figure 4.6b, the general trend here indicates that the ratio of products is about 1, regardless of whether or not the sweep rate is low or high.

Figure 4.9a shows that as sweep rate increases, CO_2 conversion decreases for each of the systems in this study. The CO_2 conversions achieved a sweep rate of 10 $mL \cdot min^{-1}$ for the blank system, LSCF and Ni/γ-alumina catalysts were 31.2, 31.9 and 88.3% respectively. In comparison, for an increase in sweep rate to 50 $mL \cdot min^{-1}$, the conversions decreased to 11.4, 14.7 and 55.4%. The same general trend for methane conversion is depicted in Figure 4.9b. For instance, the

conversion of CH_4 is roughly 7.2% in the Ni/γ-alumina system at a sweep rate of 10 $mL \cdot min^{-1}$. However, the conversion drops to less than 0.60% when the sweep rate is increased by a factor of 5. While the values are for the Ni/γ-alumina system are low, the conversion rates are even lower in the LSCF catalyst and blank systems at roughly 0.15%. The decrease in syngas production with increase sweep rate can be ascribed to the fact that the reactants (CH_4 and CO_2) are swept away from the surface of the membrane or from within the catalyst bed at a faster rate. The increase in sweep rate leads to lower residence times. The low residence time does not allow for the dry reforming reaction to take place [Akin and Lin, 2004]. Again, the conversion of CO_2 and CH_4 to syngas is very low as a result of the very low surface areas for reaction for the LSCF catalyst and blank system. The use of the reforming catalyst was the only method by which syngas was produced in reasonable amounts.

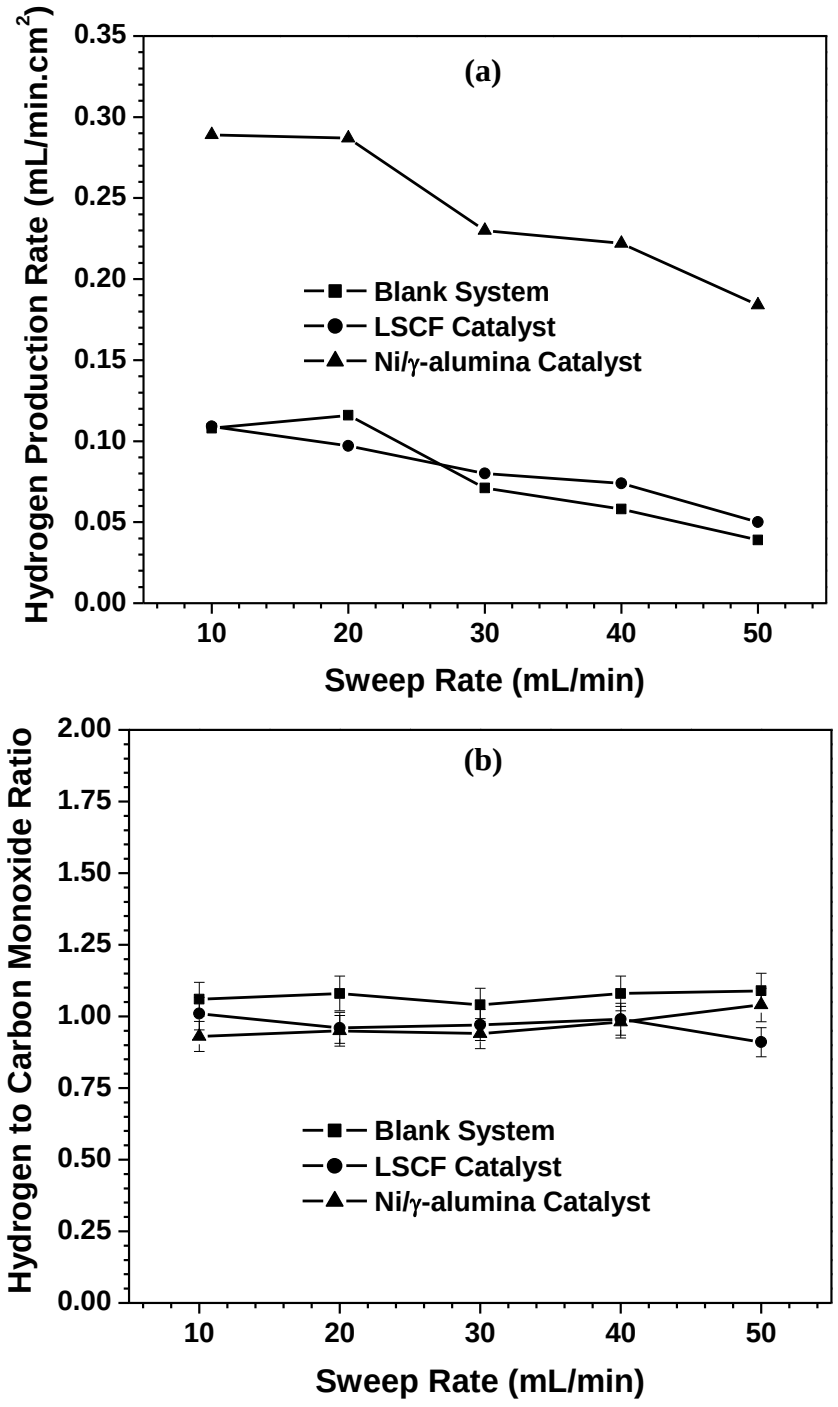

Figure 4.8 Production of syngas dependency on sweep flow rate on (a) Hydrogen production rate and (b) the hydrogen to carbon monoxide ratio.

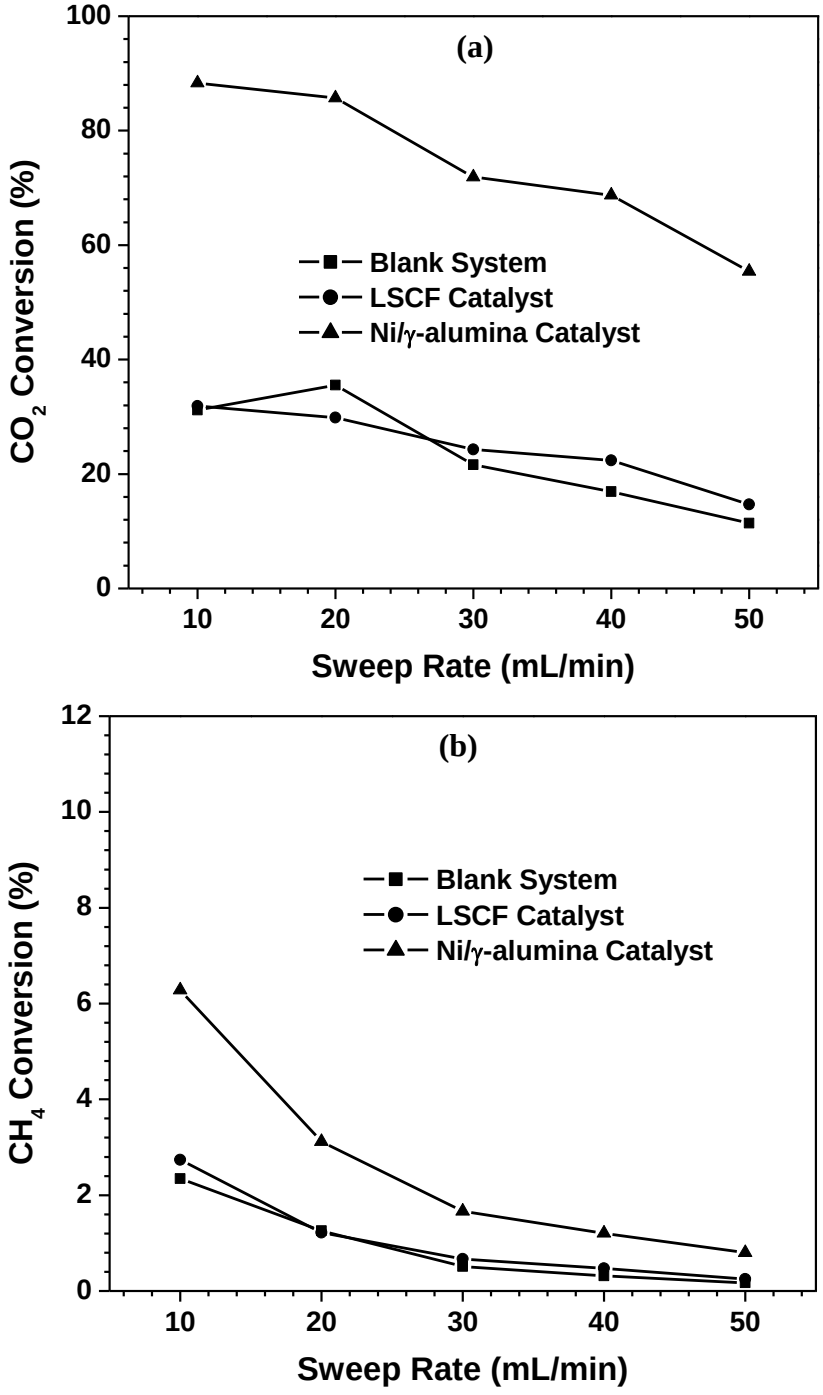

Figure 4.9 (a) CO_2 conversion and (b) CH_4 conversion for changes in sweep flow rate at constant temperature (850℃) and methane percentage (50%).

The final system parameter investigated was the effect of system temperature on the production of syngas. Figures 4.10a and b show the rate of H_2 production and H_2 to CO ratio for temperatures ranging from 750-850°C. For this portion of the study, the methane percentage in the sweep and the sweep rate were held constant at 50% and 10 $mL \cdot min^{-1}$ respectively. As Figure 4.10a clearly shows, the production of hydrogen is greatly enhanced at high temperatures. Furthermore, the addition of the Ni/γ-alumina catalyst in conjunction with higher system temperatures further increases the production of H_2. At 850°C, the production rate of H_2 is 0.100 and 0.109 $mL \cdot min^{-1} \cdot cm^{-2}$ for the LSCF catalyst and blank systems. For the same conditions in the Ni/γ-alumina system, the production of H_2 is more than triple at 0.330 $mL \cdot min^{-1} \cdot cm^{-2}$. However, the profound effect of the Ni/γ-alumina catalyst is less pronounced at lower temperatures. For instance, the H_2 production rate for the blank system is 0.020 $mL \cdot min^{-1} \cdot cm^{-2}$ at 750°C. At the same temperature, the rate is marginally higher at 0.027 $mL \cdot min^{-1} \cdot cm^{-2}$ for the Ni/γ-alumina catalyst.

As was the cases in Figures 4.6b and 4.8b, the H_2 to CO ratio shown in Figure 4.10b for changes in system temperature is relatively close to 1 throughout the entire range of temperatures tested. However, there is one small exception which occurs for the LSCF catalyst at 750°C in which the H_2:CO ratio is 0.77. However, this is not a result of drastically different production rates, but rather low values that result in greater disparity when calculating the H_2:CO ratio. The production of H_2 and CO for this particular data point are relatively close at

0.0056 and 0.0076 $mL \cdot min^{-1} \cdot cm^{-2}$ respectively. The same explanation given earlier for the disparity in the ratio from what is expected holds true here as well. Using such low, yet similar fluxes causes somewhat misleading values for the H_2:CO ratios.

The conversion of CO_2 and CH_4 decrease as temperature decreases, as presented in Figures 4.11a and b. Similar to the other experiments performed in this work, the maximum CO_2 and CH_4 conversions were experienced when using the dual-phase membrane in conjunction with the Ni/γ-alumina catalyst. At 850°C, the conversions in this case were 93.3 and 7.2% respectively. Drastic drops in the conversions of both gases occur at 750°C, decreasing to 23.1% for CO_2 and 0.58% for CH_4. Similar characteristics were observed for the LSCF catalyst and blank systems. Despite the presence of the LSCF combustion catalyst, little to no improvement was achieved in comparison to the results obtained for the blank system.

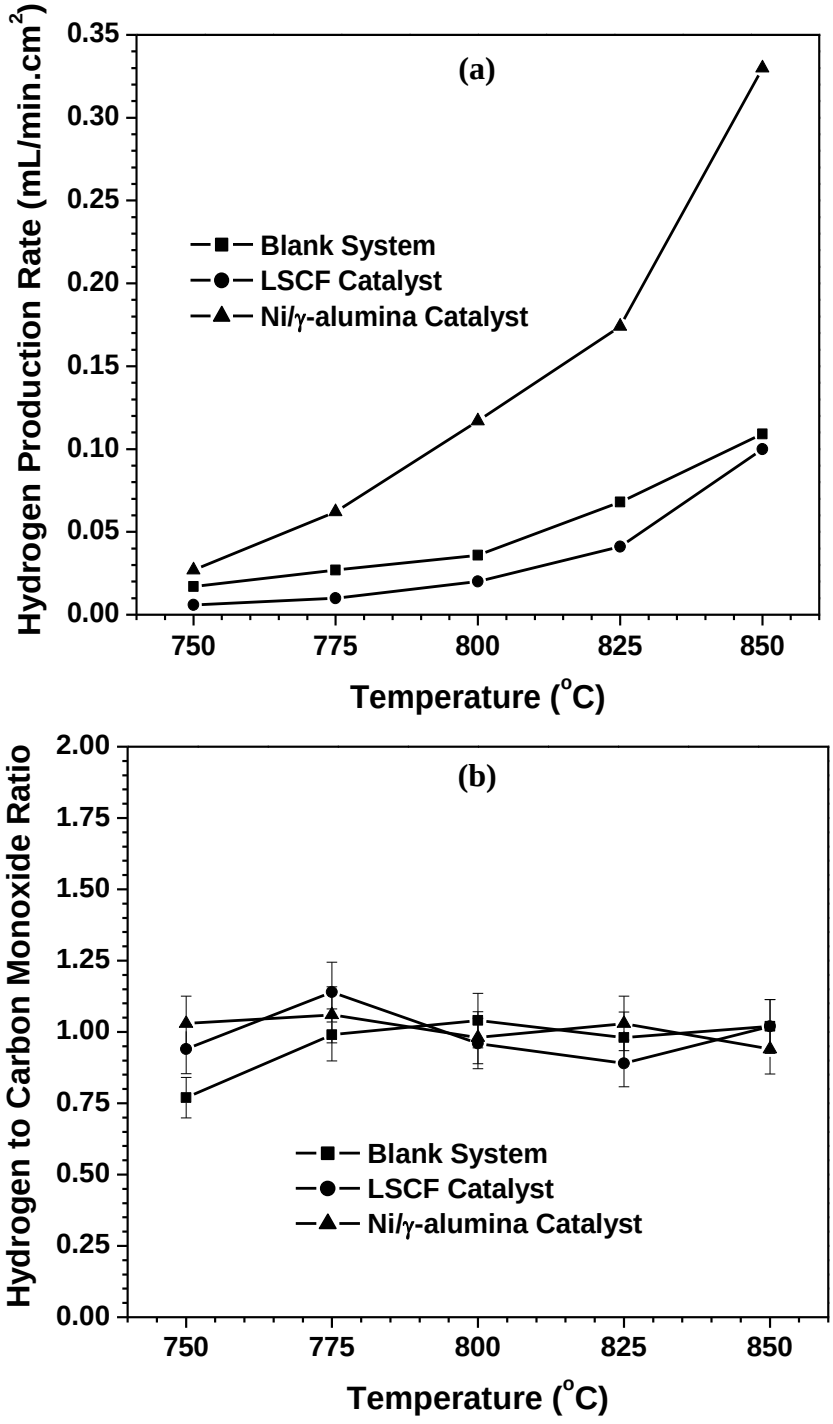

Figure 4.10 Production of syngas dependency on temperature on (a) Hydrogen production rate and (b) the hydrogen to carbon monoxide ratio.

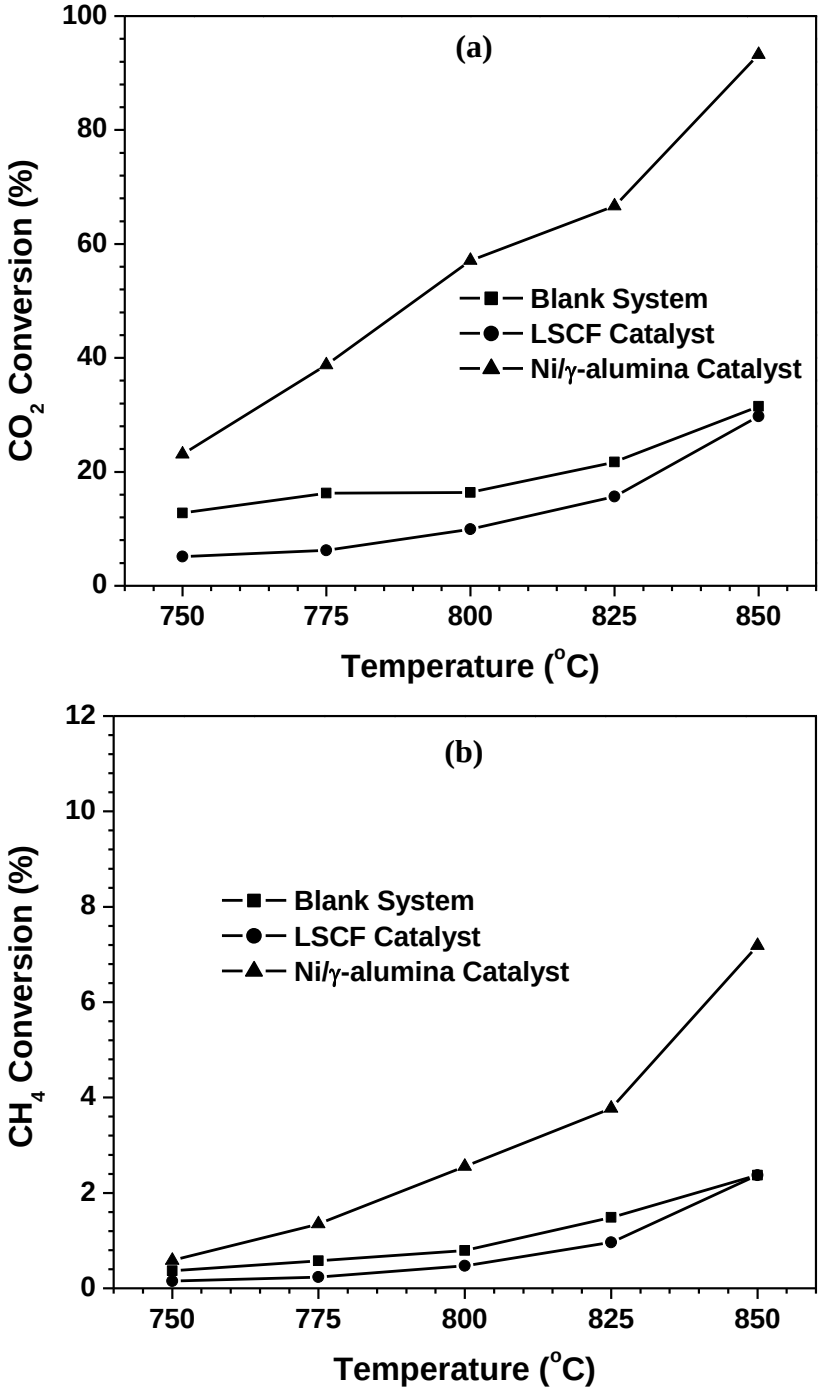

Figure 4.11 (a) CO_2 conversion and (b) CH_4 conversion for changes in system temperature at constant methane percentage (50%) and sweep rate (10 mL·min^{-1}).

4.3.4 Comparison of the three membrane reactor systems and membrane stability

The nine experiments conducted in this study were all designed to share one point in common for comparison sake. These points represent the perceived optimum (i.e., favorable) conditions for syngas production, which are high methane percentage (50%), low sweep rate (10 $mL \cdot min^{-1}$) and high temperature (850°C). The three points in common have been averaged and summarized in the table below.

Table 4.2 Summary of Data Obtained from Figures 4.4-4.11

Catalyst	CO_2 Flux ($mL \cdot min^{-1} \cdot cm^{-2}$)	H_2 Production Rate ($mL \cdot min^{-1} \cdot cm^{-2}$)	H_2:CO	CO_2 Conv. (%)	CH_4 Conv. (%)
Blank (none)	0.171	0.100	0.92	29.2	2.2
LSCF	0.169	0.097	0.99	29.5	2.4
Ni/γ-alumina	0.168	0.298	1.01	88.5	8.1

From Table 4.2, it can be inferred that the addition of either catalyst had no affect on CO_2 permeation through the membrane. In terms of syngas production, the addition of the LSCF catalyst did nothing to improve performance. While it was believed that the blank system would provide the poorest results, it was unexpected to see the blank system and LSCF catalyst perform so similarly. The lack of improvement observed for the use of the LSCF catalyst in this study is ascribed to the fact that the LSCF catalyst does not have a very high surface area. Furthermore, perovskite-type catalysts like LSCF are more suitable for combustion reactions rather than reforming reactions due to the presence of oxygen ions within and on the surface of the material [Zawadzki and

Trawczyński, 2010]. In addition, it took 1.0 g of catalyst to create a bed height of 3 mm for the LSCF catalyst. In comparison, it took only 0.6 g for the Ni/γ-alumina catalyst. The more densely packed bed, and hence lower void volumes, could have limited the flow of gases within the bed and also contributed to the low reactivity within the system. For these reasons, the results gathered from using the LSCF catalyst are no better than those obtained when using just the surface of the membrane to enhance the reaction.

The use of the mesoporous Ni/γ-alumina catalyst led to high conversions in each of the cases involved in this work. Pompeo et al. and Lui et al. reported similar results for conversions of CO_2 via dry reforming at elevated temperatures [Lui et al., 2002; Pompeo et al., 2007]. Haag et al. also demonstrated that the calculated equilibrium conversion of CO_2 in dry reforming reactions is greater than 90% at temperatures above 850°C [Haag et al., 2007]. At that temperature, the conversion of CO_2 was near or above 90% for each case in this work. On the other hand, Haag also demonstrated that CO_2 conversion at 750°C was in the 80% range. In this work, CO_2 conversion at that temperature was only 38% at 750°C with the Ni/γ-alumina catalyst. The lack of conversion at the lower system temperature can possibly be attributed to less than optimal conditions (tube placement with regards to the catalyst beds) within the permeation setup.

It should be noted that the loading of Ni was kept low at 10% to limit deactivation of the catalyst. Ni based catalysts with a loading above 10 wt.% metal have been shown to be prone to deactivation as a result of carbon

deposition. XRD analysis performed on both the Ni/γ-alumina and LSCF catalysts before and after the reactions showed no discernable change in the patterns, hence pointing towards, at the very least, the short term capabilities of using the systems described in this work. Arena et al. [Arena et al., 1996] indicated that the presence of these alkali earth metals within catalysts could improve the catalytic stability and activity of various materials. The molten carbonate used to infiltrate the membrane contains lithium, sodium and potassium – all alkali earth metals, which possibly help stability the catalysts, hence explaining the short term stability that was observed.

XRD results obtained from analysis of the LSCF dual-phase membrane after performing a dry reforming experiment with the Ni/γ-alumina reforming catalyst are shown in Figure 4.12 in order to compare the characteristics of untarnished membranes. For the most part, it appears that the perovskite structure of the support remains relatively unchanged. However, there are noticeable differences in the appearance, or lack thereof, of the molten carbonate peaks. For the feed side, the dominant peak indicating the presence of molten carbonate at 29.4° is less intense than that of a freshly infiltrated membrane. Furthermore, the minor peak indicating the presence of molten carbonate at 37.3° is not visible in the pattern. The results for the sweep side XRD pattern of the membrane are vice versa. Whereas there was a peak at 29.4° for the feed side, the peak is absent on the sweep side pattern. However, unlike the feed side, the molten carbonate peak at 37.3° is present. Although these changes are somewhat peculiar and not

completely understood, the results are likely linked to the decomposition partial pressure of molten carbonate mixture used in this work. The feed side is consistently at a feed CO_2 at a partial pressure of 0.25 atm. This is well above the decomposition partial pressure the molten carbonate within the membrane. However, the CO_2 partial pressure on the sweep side is below the decomposition partial pressure. Furthermore, there is the inclusion of an additional peak at approximately 46.0°. This peak may correspond to a metal oxide formed during the decomposition reaction of molten carbonate. Future studies involving the chemical stability of the dual-phase membrane will be conducted to better understand the reactive behavior of the support in various high temperature atmospheres

Due to sealing issues, long term performance tests could not be attempted. However, if long term experiments are to be carried out in the future, catalysts capable of withstanding the harsh conditions present during the dry reforming reaction for a long period of time would likely be necessary. Pomepo et al. described the use of a α-alumina supported Ni catalyst that was modified with zirconia (ZrO_2) to improve long term stability and activity [Pomepo et al., 2005]. Cerium IV Oxide could also be used, as it has been shown to increase the effectiveness of Ni-alumina based catalysts [Laosiripojana et al., 2005].

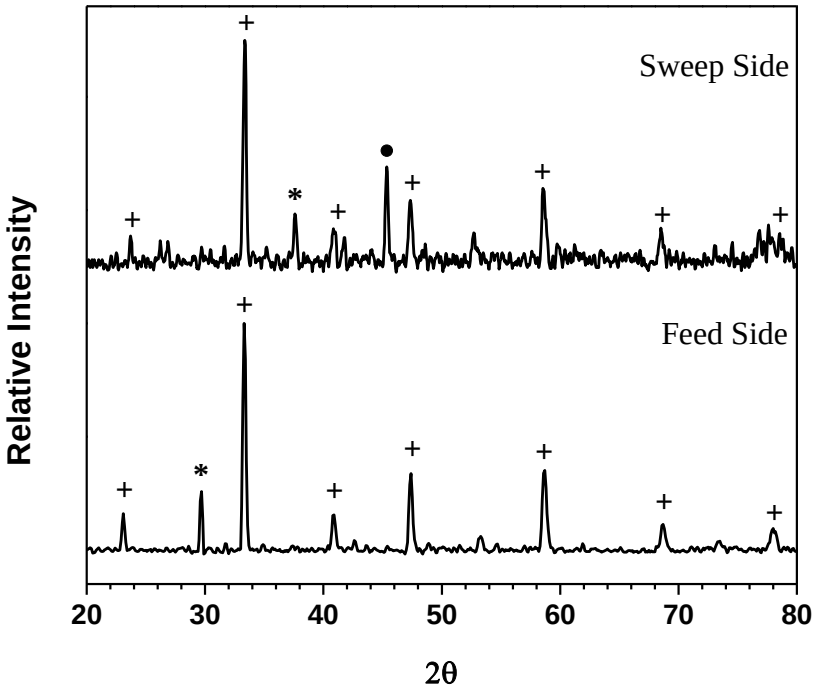

*Figure 4.12 XRD patterns of the feed and sweep side of a LSCF-carbonate dual-phase membrane after the dry reforming reaction using the Ni/γ-alumina catalyst (+, * and • indicates diffraction peaks for perovskite, carbonate and unknown structures respectively).*

4.4 Conclusion

The use of the dual-phase membrane to produce syngas via the dry reforming reaction was examined using three different system configurations: 1) a blank system with no catalyst present on the downstream side of the membrane; 2) addition of a LSCF combustion catalyst; and 3) use of a 10% Ni/γ-alumina reforming catalyst. The performance, in terms of syngas production, increased in the order of blank system < LSCF combustion catalyst < Ni/γ-alumina reforming catalyst. In fact, the use of the LSCF combustion catalyst provided no

improvement in syngas production in comparison to the blank membrane system due to the catalyst's low activity and surface area in comparison to the reforming catalyst.

CO_2 flux measured with a reducing sweep closely resembled that of which was observed for an inert sweep in previous work. The average activation energy for CO_2 permeation from 750-850°C was 99.3 $kJ \cdot mol^{-1}$, or 12% higher than the activation energy using an inert sweep. The conversion of CO_2 and CH_4 to syngas increased in the order of blank system < LSCF combustion catalyst < Ni/γ-alumina reforming catalyst. Optimum conditions for using the dual-phase membrane to convert permeated CO_2 to syngas were identified to be high temperature (850°C), low sweep gas flow rate (10 $mL \cdot min^{-1}$) and high methane concentration (50%) using the Ni/γ-alumina reforming catalyst. Under such conditions, the average production rate of H_2 was 0.298 $mL \cdot min^{-1} \cdot cm^{-2}$ with a H_2:CO ratio of 1.01, while the conversions of CO_2 and CH_4 was found to be 88.5 and 8.1% respectively.

Chapter 5

SUMMARY AND RECOMMENDATIONS

5.1 Summary

It has been established that conventional microporous membranes are incapable of achieving separation of CO_2 and N_2 at high temperatures. The research presented in this dissertation was focused on the fundamental study of a novel carbonate-ceramic dual-phase membrane for high temperature CO_2 separation. The permeation mechanism through the carbonate-ceramic dual-phase membrane, which involves a reaction between CO_2 (gas phase) and $O^{=}$ (solid phase) to form $CO_3^{=}$, would allow for separation of CO_2 at temperatures above 500°C.

Towards this, a carbonate-ceramic dual-phase membrane was synthesized from porous $La_{0.6}Sr_{0.4}Co_{0.8}Fe_{0.2}O_{3-\delta}$ (LSCF) supports and infiltrated with a mixture of molten carbonate ($Li_2CO_3/Na_2CO_3/K_2CO_3$). The first objective of the work (Chapter 2) was to prove the concept of the dual-phase membrane and show that the membrane, could in fact, separate CO_2 at high temperature. Another goal of the work was to determine the key factors that govern separation. Within the study, the effect of membrane thickness and temperature were studied. CO_2 flux was found to increase with rising temperature. For example, a 1.5 mm thick membrane exhibited a CO_2 permeation flux of 0.039 $mL \cdot min^{-1}cm^{-2}$ at 700°C. For the same membrane, the flux increased more than 7-fold to 0.282 $mL \cdot min^{-1}cm^{-2}$ at 900°C. In additional work, it was found that decreasing membrane thickness

from 3.0 to 0.375 mm led to higher permeation fluxes at 900°C, ranging from 0.186 to 0.322 $mL \cdot min^{-1} \cdot cm^{-2}$ respectively. A CO_2/Ar separation factor of at least 225 was achieved at 900°C for the 0.375 mm thick membrane. The activation energy for permeation through these membranes was calculated to be 86.4 – 89.9 $kJ \cdot mol^{-1}$, which corresponds to the energy required for oxygen vacancy conduction within LSCF-type perovskites. This correlation indicates that oxygen ion conduction is the rate limiting factor during permeation. A theoretical model was developed to determine the major factors that govern CO_2 permeation through the dual-phase membrane. The key factors were identified to be ionic conductivity of the support material, membrane thickness, system temperature and the CO_2 partial pressures of the up and downstream sides of the membrane.

The influence of the up and downstream CO_2 partial pressure on carbon dioxide permeation flux through the LSCF dual-phase membrane was addressed in Chapter 3. For CO_2 partial pressures below 0.05 atm, the dual-phase membrane exhibited transient decomposition of the eutectic molten carbon mixture. The decomposition of the molten carbonate led to the formation of Knudsen-sized defects within the pores of the support. For CO_2 partial pressures above 0.05 atm, the membranes exhibited a relatively constant permeation fluxes for all temperatures tested. For a 1.5 mm thick membrane, CO_2 flux was found to be 0.056, 0.081 and 0.152 $mL \cdot cm^{-2} \cdot min^{-1}$ at 750, 800 and 850°C respectively for all upstream CO_2 partial pressures above 0.05 atm. Similarly, a 0.75 mm thick membrane exhibited CO_2 fluxes of 0.065, 0.094 and 0.174 $mL \cdot cm^{-2} \cdot min^{-1}$ at the

same respective temperatures and range of partial pressures. The model used to predict permeation in pervious works was revisited. It was determined that the equilibrium oxygen vacancy concentration in the solid phase must be correlated to partial pressure of carbon dioxide in the gas phase in order to accurately predict permeation.

The third and final objective of this work was to demonstrate the feasibility of using the dual-phase membrane as a membrane reactor. Separation at high temperatures would produce streams of warm, highly concentrated CO_2 that could be used as a chemical feedstock for the synthesis of syngas (H_2 + CO). In this work, three different reaction configurations were examined: 1) a blank system with no catalyst, 2) addition of a LSCF combustion catalyst and 3) use of a 10% Ni/γ-alumina reforming catalyst. All of these were used in conjunction with the dual-phase membrane. The influence of operating temperature (750-850°C), sweep gas flow rate (10-50 $mL \cdot min^{-1}$) and methane concentration of the sweep gas (10-50%) on the total CO_2 flux, H_2 production rate, H_2:CO ratio, and CO_2 and CH_4 conversions were measured.

In terms of syngas production, performance increased in the order of blank system < LSCF combustion catalyst < Ni/γ-alumina reforming catalyst. Optimum conditions for CO_2 permeation and syngas production were identified to be high temperature (850°C), low sweep gas flow rate (10 $mL \cdot min^{-1}$) and high methane concentration (50%) using the Ni/γ-alumina catalyst. Under the aforementioned conditions, the average production rate of H_2 was 0.298 $mL \cdot min^{-1} \cdot cm^{-2}$ with a

H_2:CO ratio of 1.01. Conversions of CO_2 and CH_4 were 88.5 and 8.1% respectively.

5.2 Recommendations

Based on the experimental and theoretical studies in this dissertation, several recommendations are suggested for future research. These suggestions are discussed as follows..

5.2.1 Choice of supports with different geometries and higher ionic conductivities

Results throughout this work have indicated that the ionic conductivity of the support is the limiting factor for CO_2 permeation through the dual-phase membrane. With that being the case, it stands to reason that using a material with a higher ionic conductivity should provide higher CO_2 permeation fluxes. The ionic conductivity of LSCF is on the order of 0.1 $S \cdot cm^{-1}$ [Teraoka et al., 1991]. While this value is considered to be somewhat large, some bismuth-related materials have ionic conductivities that are reportedly an order of magnitude greater (i.e., 1-2 $S \cdot cm^{-1}$). Use of these materials as the support could lead to the same order of magnitude increases in permeation fluxes. However, the material that is chosen should remain chemically stable in both high temperature CO_2 containing environments and with the molten carbonate mixture.

One potential material being studied in the Membrane and Energy Laboratory for this purpose is the use of a CO_2 tolerant perovskite with the formula $La_{0.85}Ce_{0.1}Ga_{0.3}Fe_{0.65}Al_{0.05}O_{3-\delta}$ (LCGFA) [Dong et al., 2009]. Porous supports have been prepared from this material, and molten carbonate can be

easily infiltrated into the pores of these supports. Preliminary measurements with the LCGFA dual-phase membrane have shown that the material is capable of achieving separation within the temperature range of 700-900°C. The values achieved are about 25% lower than those of the LSCF dual-phase membrane, but if the material proves to have a higher chemical stability, then it may be a better candidate for this particular membrane. With that said, additional research is necessary to confirm that the material is more stable than the LSCF predecessor.

Finally, the geometry of the membranes can be improved to enhance separation. The work presented in this dissertation only deals with membranes having a disk-like geometry that are relatively thick (0.375-3.0 mm) in nature. This particular geometry, while easy to construct, limits the permeation area to 1-2 cm^2. In order to increase the permeation area, tubular supports are recommended for future research. Presently, tubes with an inner diameter of 1 cm and length of 5 cm are being developed. This would increase the permeation area to about 15 cm^2. However, fabrication of tubes with LSCF powder and subsequent infiltration is not a trivial matter. Utmost care must be taken in order to develop the tubes. Furthermore, thinner membranes are predicted to induce higher permeation fluxes, but synthesis of thin, defect free membranes and infiltration of such is a difficult problem to tackle. Combination of all three improvements 1) combination of a macroporous tubular support 2) development of a thin dual-phase layer and 3) using a material that has a high ionic

conductivity would ultimately lead to a membrane with superior high temperature separation characteristics.

5.2.2 Molten carbonate mixtures with low melting points and low equilibrium CO_2 partial pressures

The components of the molten carbonate mixture used in this study are Li_2CO_3, Na_2CO_3 and K_2CO_3. Individually, these components have melting points above 800°C. When mixed in the appropriate amounts (42.5/32.5/25 mol%), the carbonates form a eutectic mixture that melts at 397°C. Another attractive characteristic of this particular mixture is the high ionic conductivity (~ 1-2 S·cm-1) towards $CO_3^{=}$. However, at high temperatures (850°C+) and low partial pressures of carbon dioxide, the mixture has a tendency to decompose into CO_2 and the corresponding metal oxides (M_2O, where M = Li, Na, K). Decomposition of molten carbonate within the membrane leads to the formation of defects, hence allowing N_2 (and other unwanted gases) to permeate. To sidestep this particular issue, it is recommended that other molten carbonate mixtures be investigated. In choosing a new type of molten carbonate, it should continue to have a high conductivity and a low melting point, but remain stable in low P_{CO_2} environments at high temperature. Several combinations of Li/Na/K carbonates have been studied, and the characteristics of these have been reported by Janz et al. [Janz et al., 1979]. Potential candidates for use in the dual-phase membrane could be selected based on the aforementioned findings.

5.2.3 Development of better sealing techniques

At present, a ceramic-like seal composed of the parent powder (i.e., LSCF), Pyrex beaker glass and $Al_2O_3 \cdot Na_2O$ is used to seal the dual-phase membranes at high temperature. During permeation experiments, the seal is able to withstand the high temperature environments for about 48 hours, meaning the seal remains relatively leak free during this period. However, during longer experiments ($t > 48$ hours), the seal begins to break down. As a result, leakage of both CO_2 and N_2 becomes a concern. In order to circumvent this issue, additional sealing materials should be investigated. Gold and silver seals have been used for sealing at high temperature due to their low melting points and relative inertness. However, the melting points of those two materials are too high for use as seals for the current dual-phase membrane. A soft metal alloy with a melting temperature somewhere near 900°C having noble metal qualities would be an ideal candidate for this purpose. Literature research should be conducted to determine suitable materials for this purpose.

REFERENCES

Aaron, D., & Tsouris, C. (2005). Separation of CO_2 from flue gas: A review. *Separation and Purification Technology*, 40, 321-348.

Akin, F. T. & Lin, Y. S. (2004). Oxygen permeation through oxygen ionic or mixed-conducting ceramic membranes with chemical reactions. *Journal of Membrane Science*, 231, 133-146.

Anderson, M., & Lin, Y. S. (2010). Carbonate-ceramic dual-phase membrane for carbon dioxide separation. *Journal of Membrane Science*, 357, 122-129.

Aoki, K., Kusakabe, K., & Morooka, S. (1998) Gas permeation properties of A-type zeolite formed on porous substrate by hydrothermal synthesis. *Journal of Membrane Science*, 141, 197-205.

Aoki, K., Kusakabe, K., & Morooka, S. (2000). Separation of gases with an A-type zeolite membrane. *Industrial and Engineering Chemistry Research*, 39, 2245-2,251.

Aoki, K., Tuan, V. A., Falconer, J. L., & Noble, R. D. (2000). Gas permeation properties of ion- exchanged ZSM-5 zeolite membranes. *Microporous and Mesoporous Materials*, 39, 485-492.

Arena, F., Frusteri, F., & Parmaliana, A. (1999). Alkali promotion of Ni/MgO catalysts. *Applied Catalyst A: General*, 145, 127-140.

Asaeda, M., & Yamasaki, S. (2001). Separation of inorganic/organic gas mixtures by porous silica membranes. *Separation and Purification Technology*, 25, 151-159.

Baerlocher, C., & McCusker, L. B. (2001). Database of zeolite structures: http://www.iza-structure.org/databases/.

Bakker, W. J. W., van den Broeke, L. J. P., Kapteijn, F., & Moulijn, J. A. (1997). Temperature dependence of one-component permeation through a silicalite-1 membrane. *AIChE Journal*, 43, 2203-2214.

Balachandran, U., Dusek, J. T., Maiya, P. S., Ma, B., Mieville, R. L., Kleefisch, M. S., & Udovich, C. A. (1997). Ceramic membrane reactor for converting methane to syngas. *Catalysis Today*, 36, 265-272.

Balachandran, U., Dusek, J. T., Mieville, R. L., Poeppel, R. B., Kleefisch, M. S., Pei, S., Kobylinski, T. P., Udovich, C. A., & Bose, A. C. (1995). Dense ceramic membranes for partial oxidation of methane to syngas. *Applied Catalysis A: General*, 133, 19-29.

Barsema, J. N., van der Vegt, N. F. A., Koops, G. H., & Wessling, M. (2005). Ag-functionalized carbon molecular-sieve membranes based on polyelectrolyte/polyimide blend precursors. *Advanced Functional Materials*, 15, 69-75.

Benson, S. J., Waller, D., & Kilner, A. J. (1999). Degradation of $La_{0.6}Sr_{0.4}Fe_{0.8}Co_{0.2}O_{3-\delta}$ in carbon dioxide and water atmospheres. *Journal of the Electrochemical Society*, 146, 1305-1309.

Bernal, M. P., Coronas, J., Menendez, M., & Santamarıa, J. (2004) Separation of CO_2/N_2 mixtures using MFI-type zeolite membranes. *AIChE Journal*, 50, 127-135.

Bhave, R. R. (1991). Inorganic membranes: Synthesis, characteristics and applications. New York: Van Nostrand Reinhold.

Biedenkopf, P., Bischoff, M. M., & Wochner, T. (2000). Corrosion phenomena of alloys and electrode materials in molten carbonate fuel cells. *Materials and Corrosion*, 146, 287-302.

Bosko, M. L., Munera, J. F., Lombardo, E. A., & Cornaglia, L. M. (2010). Dry reforming of methane in membrane reactors using Pd and Pd-Ag composite membranes on a NaA modified porous stainless steel support. *Journal of Membrane Science*, 364, 17-26.

Bouwmeester, H. J. M. (2003). Dense ceramic membranes for methane conversion. *Catalysis Today*, 82, 141-150.

Burggraaf, A. J. (1999). Single gas permeation of thin zeolite (MFI) membranes: Theory and analysis of experimental observations. *Journal of Membrane Science*. 155, 45-65.

Centeno, T. A., & Fuertes, A. B. (1999). Supported carbon molecular sieve membranes based on a phenolic resin. *Journal of Membrane Science*, 160, 201-211.

Centeno, T. A., & Fuertes, A. B. (2000). Carbon molecular sieve gas separation membranes based on poly(vinylidene chloride-co-vinyl chloride). *Carbon*, 38, 1067-1073.

Centeno, T. A., & Fuertes, A. B. (2001). Carbon molecular sieve membranes derived from a phenolic resin supported on porous ceramic tubes. *Separation and Purification Technology*, 25, 379-384.

Chang, C.-H., Gopalan, R., & Lin, Y. S. (1994). A comparative study on thermal and hydrothermal stability of alumina, titania and zirconia membranes. *Journal of Membrane Science*, 91, 27-45.

Cho, Y.-K., Han, K., & Lee, K.-H. (1995). Separation of CO_2 by modified γ-alumina membranes at high temperature. *Journal of Membrane Science*, 104, 219-230.

Choudhary, V. R., Uphade, B. S., & Belhekar, A. A. (1996). Oxidative conversion of methane to syngas over $LaNiO_3$ perovskite with or without simultaneous steam and CO_2 reforming reactions: Influence of partial substitution of La and Ni. *Journal of Catalysis*, 163, 312-318.

Choudhary, V. R., Uphade, B. S., & Pataskar, S. G. (1999). Low temperature complete combustion of methane over Ag-doped $LaFeO_3$ and $LaFe_{0.5}Co_{0.5}O_3$ perovskite oxide catalysts. *Fuel*, 78, 919-921.

Chung, S. J., Park, J. H, Li, D., Ida, J.-I., Kumakiri, I., & Lin, Y. S. (2005). Dual-phase metal carbonate membrane for high-temperature carbon dioxide separation. *Industrial and Engineering Chemistry Research*, 44, 7999-8006.

Cooper, C. A., & Lin, Y. S. (2002). Microstructural and gas separation properties of CVD modified mesoporous g-alumina membranes. *Journal of Membrane Science*, 195, 35-50.

Cuffe, L., MacElroy, J. M. D., Tacke, M., Kozachok, M., & Mooney, D. A. (2006). The development of nanoporous membranes for separation of carbon dioxide at high temperatures. *Journal of Membrane Science*, 272, 6-10.

de Vos, R. M., & Verweij, H. (1998). Improved performance of silica membranes for gas separation. *Journal of Membrane Science*, 143, 37-51.

de Vos, R. M., Maier. W. F., & Verweij, H. (1999). Hydrophobic silica membranes for gas separation. *Journal of Membrane Science*, 158 (1999) 277-288.

Do, D. D. (1998). Adsorption analysis: Equilibrium and kinetics. London: Imperial Press.

Dong, H., Shao, Z., Xiong, G., Tong, J., Sheng, S., & Yang, W. (2001). Investigation on POM reaction in a new perovskite membrane reactor. *Catalysis Today*, 67, 3-13.

Dong, H., Zhang, G., Lui, Z., Zhong, Z., Jin, W., & Xu., N. (2009). CO_2-tollerant mixed conducting oxide for catalytic membrane reactor. *Journal of Membrane Science*, 340, 141-147.

Draper, E. L., & Leer, S. F. (2000). Research and development needs for the sequestration of carbon dioxide as part of a carbon management strategy. Washington, D.C.: The National Coal Council.

Edwards, J. H., & Maitra A. M. (1995). The chemistry of methane reforming with carbon dioxide and its current and potential applications. *Fuel Processing Technology*, 42, 269-289.

Figueroa, J. D., Fout, T., Plasynski, S., McIlvried, H., & Srivastava, R. D. (2008). Advances in CO_2 capture technology – The U.S. Department of Energy's carbon sequestration program. *International Journal of Greenhouse Gas Control*, 2, 9-20.

Fuentes, A. B., & Centeno, T. A. (1998). Preparation of supported asymmetric carbon molecular sieve membranes. *Journal of Membrane Science*, 144, 105-111.

Fuentes, A. B., & Centeno, T. A. (1999). Preparation of supported carbon molecular sieve membranes. *Carbon*, 37, 679-684.

Fuertes, A. B. (2000). Adsorption-selective carbon membrane for gas separation. *Journal of Membrane Science*, 177, 9-16.

Fuertes, A. B., & Centeno, T. A. (1998). Carbon molecular sieve membranes from polyetherimide. *Microporous and Mesoporous Materials*, 26, 23-26.

Fuertes, A. B., Nevskaia, D. M., & Centeno, T. A. (1999). Carbon composite membranes from Matrimid® and Kapton® polyimides for gas separation. *Microporous and Mesoporous Materials*, 33, 115-125.

Gallucci, F., Toshi, S., & Basile, A. (2008). Pd-Ag tubular membrane reactors for methane dry reforming: A reactive method for CO_2 consumption and H_2 production. *Journal of Membrane Science*, 317, 96-105.

Goncalves, G., Lenzi, M. K., Santos, O. A. A., & Jorge, L. M. M. (2006). Preparation and characterization of nickel based catalysts on silica, alumina and titania obtained via the sol-gel method. *Journal of Non-Crystalline Solids*, 352, 3697-3704.

Gu, X., Dong, J., & Nenoff, T. M. (2005). Synthesis of defect-free FAU-type zeolite membranes and separation for dry and moist CO_2/N_2 mixtures. *Industrial and Engineering Chemistry Research*, 44, 937-944.

Gu, Y., & Oyama, S. T. (2007). Ultrathin, hydrogen-selective silica membranes deposited on alumina-graded structures prepared from size-controlled boehmite sols. *Journal of Membrane Science*, 306, 216-227.

Gu, Y., & Oyama, S. T. (2007). High molecular permeance in a poreless ceramic membrane. *Advanced Materials*, 19, 1636-1640.

Haag, S., Burgard, M., & Ernst, B. (2007). Beneficial effects of the use of a nickel membrane reactor for the dry reforming of methane: Comparison with thermodynamic equilibrium. *Journal of Catalysis*, 252, 190-204.

Hasegawa, Y., Tanaka, T., Watanabe, K., Jeong, B.-H., Kusakabe, K., & Morooka, S. (2002). Separation of CO_2-CH_4 and CO_2-N_2 systems using ion-exchanged zeolite membranes with different Si/Al ratios. *Korean Journal of Chemical Engineering*, 19, 309-313.

Hasegawa, Y., Watanabe, K., Kusakabe, K, & Morooka, S. (2001). The separation of CO_2 using Y-type zeolite membranes ion-exchanged with alkali metal cations. *Separation and Purification Technology*, 22-23, 319-325.

Hassan, M. H., Way, J. D., Thoen, P. M., & Dillon, A. C. (1995). Single component and mixed gas transport in a silica hollow fiber membrane. *Journal of Membrane Science*, 104, 27-42.

Hayashi, J.-I., Mizuta, H., Yamamoto, M., Kusakabe, K., & Morooka, S. (1997). Pore size control of carbonized BPDA-pp'ODA polyimide membrane by chemical vapor deposition of carbon. *Journal of Membrane Science*, 124, 243-251.

Hayashi, J.-I., Yamamoto, M., Kusakabe, K., & Morooka, S. (1995). Simultaneous improvement of permeance and permselectivity of 3,3',4,4'-biphenyltetracarboxylic dianhydride-4,4'-oxydianiline polyimide membrane by carbonization. *Industrial and Engineering Chemistry Research*, 34, 4364-4370.

Hayashi, J.-I., Yamamoto, M., Kusakabe, K., & Morooka, S. (1997). Effect of oxidation on gas permeation of carbon molecular sieving membranes based on BPDA-pp'ODA polyimide. *Industrial and Engineering Chemistry Research*, 36, 2134-2140.

Hou, Z., Yokota, O., Tanaka, T., & Yashima, T. (2003). Characterization of Ca-promoted Ni/α-Al_2O_3 catalyst for CH_4 reforming with CO_2. *Applied Catalysis A: General*, 253, 381-387.

Hsieh, H. P. (1996). Inorganic membranes for separation and reaction. Amsterdam: Elsevier.

Hyun, S. H., Jo, S. Y., & Kang, B. S. (1996). Surface modification of g-alumina membranes by silane coupling for CO_2 separation. *Journal of Membrane Science*, 120, 197-206.

Hyun, S. H., Song, J. K., Kwak, B. I., Kim, J. H., & Hong, S. A. (1999). Synthesis of ZSM-5 zeolite composite membranes for CO_2 separation. *Journal of Materials Science*, 34, 3096-3105.

Ida, J.-I., & Lin, Y. S. (2003). Mechanism of high temperature CO_2 sorption on lithium zirconate. *Environmental Science and Technology*, 37, 1999-2004.

Ida, J.-I., Xiong, R., & Lin, Y. S. (2004). Synthesis and CO_2 sorption properties of pure and modified lithium zirconate. *Separation and Purification Technology*, 36, 41-51.

Ikeguchi, M., Mimura, T., Sekine, Y., Kikuchi, E., & Matsukata, M. (2005). Reaction and oxygen permeation studies in $Sm_{0.4}Ba_{0.6}Fe_{0.8}Co_{0.2}O_{3-\delta}$ membrane reactor for partial oxidation of methane to syngas. *Applied Catalysis A: General*, 290, 212-220.

Indermühle, A., Stocker, T. F., Joos, F., Fischer, H., Smith, H. J., Wahlen, M., Deck, B., Mastroianni, D., Tschumi, J., Blunier, T., Meyer & R., Stauffer, B. (1999). Holocene carbon-cycle dynamics based on CO_2 trapped in ice at Taylor Dome, Antarctica. *Nature*, 398, 121-126.

Ishigaki, T., Yamauchi, S., Mizusaki, J., Fueki, K., & Tamura, H. (1984). Tracer diffusion coefficient of oxide ions in $LaCoO_3$ single crystal. *Journal of Solid State Chemistry*, 54. 100-107.

Janz, G. J., Allen, C. B., Bansal, N. P., Murphy, R. M., & Tomkins, R. P. T. (1979). Physical properties data compilations relevant to energy storage; Molten salts: Data on single and multi component salt system. NIST standard reference database standard NSRDS-NBS.61, Part 2. Washington, D.C.: National Bureau of Standards.

Juan-Juan, J., Román-Martínez, M. C., Illán-Gómez, M. J. (2004). Catalytic activity and characterization of Ni/Al_2O_3 and NiK/Al_2O_3 catalysts for CO_2 methane reforming. *Applied Catalysis A: General*, 264, 169-174.

Kang, B. S., & Hyun, S. H. (1999). g-alumina composite membranes modified with microporous silica for CO_2 separation. *Journal of Materials Science*, 34, 1391-1398.

Kanniche, M., Gros-Bonnivard, R., Jaud, P., Valle-Marcos, J., Amann, J.-M., & Bouallou, C. (2010). Pre-combustion, post-combustion and oxy-combustion in thermal power plan for CO_2 capture. *Applied Thermal Engineering*, 30, 53–62.

Kapteijn, F., Bakker, W. J. W., van de Graaf, J., Zheng, G., Boppe., J., & Moulijn, J. A. (1995). Permeation and separation behaviour of a silicalite-1 membrane. *Catalysis Today*, 25, 213-218.

Katsaros, F. K., Steriotis, T. A., Stubos, A. K., Mitropoulos, A., Kanellopoulos, N. K., & Tennison, S. (1997). High pressure gas permeability of microporous carbon membranes, *Microporous Materials*, 8, 171-176.

Kawamura, H., Yamaguchi, T., Nair, B. N., Nakagawa, K., & Nakao, S.-I. (2005). Dual-ion conducting lithium zirconate-based membranes for high temperature CO_2 separation, *Journal of Chemical Engineering of Japan*, 38, 322-328.

Keizer, K., Uhlhorn, R. J. R., Van vuren, R. J., & Burggraaf, A. J. (1988). Gas separation mechanisms in microporous γ-alumina membranes. *Journal of Membrane Science* 39, 285-300.

Kim S., Ida, J., Guliants, V. V., & Lin, Y. S. (2004). Functionalized mesoporous silica membrane for the separation of carbon dioxide. *International Journal of Environmental Technology and Management*, 4, 21-31.

Kita, H., Nanbu, K., Hamano, T., Yoshino, M., Okamoto, K.-I., & Funaoka, M. (2002). Carbon molecular sieving membranes derived from lignin-based materials. *Journal of Polymers and the Environment*, 10, 69-75.

Kiyono, M., Williams, P. J., & Koros, W. J. (2010). Effect of polymer precursors on carbon molecular sieve structure and separation performance properties. *Carbon*, 48, 4432-4441.

Koresh, J. E., & Sofer, A. (1983). Molecular sieve carbon permselective membrane. Part 1. Presentation of a new device for gas mixture separation. *Separation and Purification Technology*, 18, 723-734.

Krishna, R., & van Baten, J. M. (2010). In silico screening of zeolite membranes for CO_2 capture. *Journal of Membrane Science*, 360, 323–333.

Krishna, R., Vlugt, T. J. H., & Smit, B. (1999). Influence of isotherm inflection on diffusion in silicalite, *Chemical Engineering Science*, 54, 1751-1757.

Kuraoka, K., Nubo, N., & Yazawa, T. (2000). Microporous silica xerogel membrane with high selectivity and high permeance for carbon dioxide separation. *Journal of Sol-Gel Science and Technology*, 19, 515-518.

Kusakabe, K., Gohgi, S., & Morooka, S. (1998). Carbon molecular sieving membranes derived from condensed polynuclear aromatic (COPNA) resins for gas separations. *Industrial and Engineering Chemistry Research*, 37, 4262-4266.

Kusakabe, K., Kuroda, T., & Morooka, S. (1998). Separation of carbon dioxide from nitrogen using ion-exchanged faujasite-type zeolite membranes formed on porous support tubes. *Journal of Membrane Science*, 148, 13-23.

Kusakabe, K., Kuroda, T., Murata, A., & Morooka, S. (1997). Formation of a Y-type zeolite membrane on a porous α-alumina tube for gas separation. *Industrial and Engineering Chemistry Research*, 36, 649-655.

Kusakabe, K., Kuroda, T., Uchino, K., Hasegawa, Y., & Morooka, S. (1999). Gas permeation properties of ion-exchanged faujasite-type zeolite membranes. *AIChE Journal*, 45, 1220-1226.

Kusakabe, K., Li, Z. Y., Maeda, M., & Morooka, S. (1995). Preparation of supported composite membrane by pyrolysis of polycarbosilane for gas separation at high temperature. *Journal of Membrane Science*, 103, 175-180.

Kusakabe, K., Sakamoto, S., Saie, T., & Morooka, S. (1999). Pore structure of silica membranes formed by a sol-gel technique using tetraethoxysilane and alkyltriethoxysilanes. *Separation and Purification Technology*, 16, 139-146.

Kusakabe, K., Yamamoto, M., & Morooka, S. (1998). Gas permeation and micropore structure of carbon molecular sieving membranes modified by oxidation. *Journal of Membrane Science*, 149, 59-67.

Kusakabe, K., Yoneshige, S., Murata, A., & Morooka, S. (1996). Morphology and gas permeance of ZSM-5 type zeolite membrane formed on a porous α-alumina support tube. *Journal of Membrane Science*, 116, 39-46.

Kusuki, Y., Shimazaki, H., Tanihara, N., Nakanishi, S., & Yoshinaga, T. (1997). Gas permeation properties and characterization of asymmetric carbon membranes prepared by pyrolyzing asymmetric polyimide hollow fiber membrane. *Journal of Membrane Science*, 134, 245-253.

Laosiripojana, N., Sutthisripok, W., & Assabumrungrat, S. (2005). Synthesis gas production from dry reforming of methane over CeO_2 doped Ni/Al_2O_3: Influence of doping ceria on the resistance toward carbon formation. *Chemical Engineering Journal*, 112, 13-22.

Leenaars, A. F. M., Keizer, K., & Burggraaf, A. J. (1984). Microstructural investigations on non-supported membranes, *Journal of Materials Science*, 19, 1077-1088.

Lemoniodu, A. A., Goula, M. A., Vasalos, I. A. (1998). Carbon dioxide reforming of methane over 5 wt.% nickel calcium aluminate catalysts – effect of preparation method. *Catalysis Today*. 46, 175-183.

Li, D., & Hwang, S.-T. (1991). Preparation and characterization of silicon based inorganic membrane for gas separation. *Journal of Membrane Science*, 59, 331-352.

Li, D., & Hwang, S.-T. (1992). Gas separation by silicon based inorganic membrane at high temperature. *Journal of Membrane Science*, 66, 119-127.

Li, S., & Fan, C. Q. (2010). High-flux SAPO-34 membrane for CO_2/N_2 Separation. *Industrial and Engineering Chemistry Research*, 49, 4399-4404.

Li, Y., Rui, Z., Xia, C., Anderson, M., & Lin, Y. S. (2009). Performance of ionic-conducting ceramic/carbonate composite material as solid oxide fuel cell electrolyte and CO_2 permeation membrane. *Catalysis Today*, 148, 303-309.

Lin, Y. S., & Burggraaf, A J. (1993). Experimental studies on pore size change of porous ceramic membranes after modification. *Journal of Membrane Science*, 79, 65-82.

Lin, Y. S., Kumakiri, I., Nair, B. N., & Alsyouri, H. (2002). Microporous inorganic membranes. *Separation and Purification Technology*, 31, 229-379.

Liu, B. S., Gao, L. Z., & Au, C. T. (2002). Preparation, characterization and application of catalytic NaA membrane for CH_4/CO_2 reforming to syngas. *Applied Catalysis A: General*, 235, 193-206.

Liu, S., Wang, T., Liu, Q., Zhang, S., Zhao, Z., & Liang, C. (2008). Gas permeation properties of carbon molecular sieve membranes derived from novel poly(phthalazinone ether sulfone ketone). *Industrial and Engineering Chemistry Research*, 47, 876-880.

Lovallo, M. C., Gouzinis, A., & Tsapatsis, M. (1998). Synthesis and characterization of oriented MFI membranes prepared by secondary growth. *AIChE Journal*., 44, 1903-1913.

Low, B. T., and Chung, T. S. (2001). Carbon molecular sieve membranes derived from pseudo-interpenetrating polymer networks for gas separation and carbon capture. *Carbon*, 49, 2104-2112.

Luo, H., Wei, Y., Jiang, H., Yuan, W., Lv, Y., Caro, J., & Wang, H. (2010). Performance of a ceramic membrane reactor with high oxygen flux Ta-containing perovskite for the partial oxidation of methane to syngas. *Journal of Membrane Science*, 350, 154-160.

Ma, Y. H., Becker, Y. L., Moser, W. R., & Dixon, A. G. (1992). Effect of catalyst impregnation on the transport properties of porous alumina membranes. *Key Engineering Materials*, 61-62, 337-346.

Merkel, T. C., Lin, H., Wei, X., & Baker, R. (2010). Power plant post-combustion carbon dioxide capture: An opportunity for membranes, *Journal of Membrane Science*, 359, 126-139.

Moon, J.-H., Park, Y.-J, Kim, M.-B., Hyun, S.-H., Lee, C.-H. (2005). Permeation and separation of a carbon dioxide/nitrogen mixture in a methyltriethoxysilane templating silica/?-alumina composite membrane. *Journal of Membrane Science*, 250, 195-205.

Nair., B. N., Burwood, R. P., Goh, V. J., Nakagawa, K., & Yamaguchi, T. (2009). Lithium based ceramic materials and membranes for high temperature CO_2 separation. *Progress in Materials Science*, 54, 511-541.

Nitodas, S. F., Favvas, E. P., Romanos, G. E., Papadopoulou, M. A., Mitropoulos, A. C., & Kanellopoulos, N. K. (2008). Development and characterization of silica-based membranes for hydrogen separation. *Journal of Porous Materials*, 15, 551-557.

Noble, R. D., & Stern, S. A. (1995). Membrane separation technology: Principles and applications. Amsterdam: Elsevier.

Ogawa, M., & Nakano, Y. (1999). Gas permeation through carbonized hollow fiber membranes prepared by gel modification of polyamic acid. *Journal of Membrane Science*, 162, 189-198.

Okubo, T., & Inoue, H. (1989). Single gas permeation through porous glass modified tetraethoxysilane. *AIChE Journal*, 35, 845-848.

Othman, M. R., and Kim, J. (2008). Permeation characteristics of H_2, N_2 and CO_2 in a binary mixture across meso-porous Al_2O_3 and Pd-Al_2O_3 asymmetric composites. *Microporous and Mesoporous Materials*, 112, 403-410.

Park, H. B., & Lee, Y. M. (2005). Fabrication and characterization of nanoporous carbon/silica membranes. *Advanced Materials*, 17, 477-483.

Plasynski, S. I., Litynski, J. T., McIlvried, H. G., & Srivastava, R. D. (2009). Progress and new developments in carbon capture and storage. *Critical Reviews in Plant Science*, 28, 123-138.

Pompeo, F., Nichio, N. N., Souza, M. M. V. M., Cesar, D. V., Ferretti, O. A. & Schmal, M. (2007). Study of Ni and Pt catalysts supported on α-Al_2O_3 and ZrO_2 applied in methane reforming with CO_2. *Applied Catalysis A: General*, 316, 175-183.

Poshusta, J. C., Tuan, V. A., Falconer, J. L.,& Noble, R. D. (1998). Synthesis and permeation properties of SAPO-34 tubular membranes. *Industrial and Engineering Chemistry Research*, 37, 3924-3929.

Poshusta, J. C., Tuan, V. A., Pape, E. A., Noble, R. D., & Falconer, J. L. (2000). Separation of light gas mixtures using SAPO-34 membranes. *AIChE Journal*, 46, 779-789.

Powell, C. E., Qiao. G. G., (2006). Polymeric CO_2/N_2 gas separation membranes for the capture of carbon dioxide from power plant flue gases. *Journal of Membrane Science*, 279, 1-49.

Prabhu, A. K., Radhakrishnan, R., & Oyama, S. T. (1999). Supported nickel catalysts for carbon dioxide reforming of methane in plug flow membrane reactors. *Applied Catalysis A: General*, 183, 241-252.

Qi, X., Akin, F. T., & Lin, Y. S. (2001). Ceramic–glass composite high temperature seals for dense ionic-conducting ceramic membranes. *Journal of Membrane Science*, 193, 185-193.

Rostrup-Nielsen, J. R. (1994). Aspects of CO_2-reforming of methane. *Studies in Surface Science and Catalysis*, 81, 25-41.

Rostrupnielsen, J. R., & Hansen, J. H. B. (1993). CO_2-reforming of methane over transition metals. *Journal of Catalysis*, 1, 38-49.

Rui, Z., Anderson, M., Lin, Y. S., & Li, Y., (2009). Modeling and analysis of carbon dioxide permeation through ceramic-carbonate dual-phase membranes, *Journal of Membrane Science*, 345, 110-118.

Sakamoto, Y., Nagata, K., Yogo, K., & Yamada., K. (2007). Preparation and CO_2 separation properties of amine-modified mesoporous silica membranes. *Microporous and Mesoporous Materials*, 101, 303-311.

Sammells, A., & Mundschau, M. (2006). Nonporous inorganic membranes for chemical processing. Weinheim: Wiley-VCH.

Scholes, C. A., Smith, K. H., Kentish, S. E., & Stevens, G. W. (2010). CO_2 capture from pre-combustion processes – Strategies for membrane gas separation. *International Journal of Greenhouse Gas Control*, 4, 739-755.

Sea, B., & Lee, K.-H. (2001). Molecular sieve silica membrane synthesized in mesoporous g-alumina layer. *Bulletin of the Korean Chemical Society*, 22, 1400-1402.

Sea, B.-K., Kusakabe, K., & Morooka, S. (1997). Pore size control and gas permeation kinetics of silica membranes by pyrolysis of phenyl-substituted ethoxysilanes with cross-flow through a porous support wall. *Journal of Membrane Science*, 130, 41-52.

Shao, Z., Xiong, G., Dong, H., Yang, W., & Lin, L. (2001). Synthesis, oxygen permeation study and membrane performance of a $Ba_{0.5}Sr_{0.5}Co_{0.8}Fe_{0.2}O_{3-\delta}$ oxygen-permeable dense ceramic reactor for partial oxidation of methane to syngas. *Separation and Purification Technology*, 25, 97-116.

Shelekhin, A. B., Dixon, A. G., & Ma, Y. H. (1992). Adsorption, permeation, and diffusion of gases in microporous membranes. II. Permeation of gases in microporous glass membranes. *Journal of Membrane Science*, 75, 233-244.

Shiflett, M. B., & Foley, H. C. (2000). On the preparation of supported nanoporous carbon membranes. *Journal of Membrane Science*, 179, 275-282.

Shin, D. W., Hyun, S. H., Cho, C. H., & Han, M. H. (2005). Synthesis and CO_2/N_2 gas permeation characteristics on ZSM-5 zeolite membranes. *Microporous and Mesoporous Materials*, 85, 313-323.

Solomon, S., Qin, D., Manning, M., Chen, Z., Marquis, M., Averyt, K. B., Tignor, M., & Miller, H. L. (2007). Climate Change 2007: Contribution of Working Group I to the Fourth Assessment Report of the Intergovernmental Panel on Climate Change: IPCC. Cambridge, United Kingdon and New York, USA: Cambridge University Press.

Suda, H., & Haraya, K. (1997). Gas permeation through micropores of carbon molecular sieve membranes derived from Kapton polyimide. *Journal of Physical Chemistry B*, 101, 3988-3994.

Teraoka, Y., Nobunaga, T., Okamoto, K., Miura, N., & Yamazoe, N. (1991). Influence of constituent metal cations in substituted $LaCoO_3$ on mixed conductivity and oxygen permeability. Solid State Ionics, 48, 207-212.

Teraoka, Y., Zhang, H. M., Okamoto, K., & Yamazoe, N. (1988). Mixed ionic-electronic conductivity of $La_{1-x}Sr_xCo_{1-y}Fe_yO_{3-\delta}$ perovskite-type oxides. *Materials Research Bulletin*, 23, 51-58.

Tong, J., Yang, W., Cai, R., Zhu, B., & Lin, L. (2002). Novel and ideal zirconium-based dense membrane reactors for partial oxidation of methane to syngas. *Catalysis Letters*, 78, 129-137.

Tsai, C.-Y., Tam, S.-Y, Lu, Y., & Brinker, C. J. (2000). Dual-layer asymmetric microporous silica membranes. *Journal of Membrane Science*, 169, 255-268.

Uhlhorn, R. J. R., Huis In't Veld, M. H. B. J., Keizer, K., & Burggraaf, A. J. (1989). High permselectivities of microporous silica-modified γ-alumina membranes. *Journal of Materials Science* Letters, 8, 1135-1138.

Uhlhorn, R. J. R., Keizer, K., & Burggraaf, A. J. (1989). Gas and surface diffusion in modified γ-alumina systems. *Journal of Membrane Science*, 46, 225-241.

van de Graaf, J. M., Kapteijn, F., & Moulijn, J. A. (1999). Modeling permeation of binary mixtures through zeolite membranes. *AIChE Journal*, 45, 497-511.

van den Broeke, L. J. P., Bakker, W. J. W., Kapteijn, F., & Moulijn, J. A. (1999). Transport and separation properties of a silicalite-1 membrane-I. Operating conditions. *Chemical Engineering Science*, 54, 245-258.

van den Broeke, L. P. J., Kapteijn, F., & Moulijn, J. A. (1999). Transport and separation properties of a silicalite-1 membrane-II. Variable separation factors. *Chemical Engineering Science*, 54, 259-269.

Venna, S. R., & Carreon, M. A. (2011). Amino-functionalized SAPO-34 membranes for CO_2/CH_4 and CO_2/N_2 separation. *Langmuir*, 27, 2888-2894.

Vu, D. Q., & Koros, W. J. (2002). High pressure CO_2/CH_4 separation using carbon molecular sieve hollow fiber membranes. *Industrial and Engineering Chemistry Research*, 41, 367-380.

Wade, J. L., Lackner, K. S., & West, A. C. (2007). Transport model for a high temperature, mixed conducting CO_2 separation membrane. *Solid State Ionics*, 178, 1530-1540.

Wade, J. L., Lee, C., West, A. C., & Lackner, K. S. (2011). Composite electrolyte membranes for high temperature CO_2 separation. *Journal of Membrane Science*, 369, 20-29.

Wang, H., Cong, Y., & Yang, W. (2003). Investigation on the partial oxidation of methane to syngas in a tubular $Ba_{0.5}Sr_{0.5}Co_{0.8}Fe_{0.2}O_{3-\delta}$ membrane reactor. *Catalysis Today*, 82, 157-166.

Wang, H., Zhang, L., & Gavalas, G. R. (2000). Preparation of supported carbon membranes from furfuryl alcohol by vapor deposition polymerization. *Journal of Membrane Science*, 177, 25-31.

Wang, S., Katsuki, M., Dokiya, M., & Hashimoto, T. (2003). High temperature properties of $La_{0.6}Sr_{0.4}Co_{0.8}Fe_{0.2}O_{3-\delta}$ phase structure and electrical conductivity. *Solid State Ionics*, 159, 71-78.

Way, J. D., & Roberts, D. L. (1992). Hollow fiber inorganic membranes for gas separations. *Separation and Purification Technology*, 27, 29-41.

Wei, X., & Lin, Y. S. (2008). Protonic and electronic conductivities of terbium doped strontium cerates. *Solid State Ionics*, 178, 1804-1810.

White, J. C., Dutta, P. K., Shqau, K., & Verweij, H. (2010). Synthesis of ultrathin zeolite Y membranes and their application for separation of carbon dioxide and nitrogen gases. *Langmuir*, 26, 10287-10293.

Wirawan, S. K. Single gas permeation through a modified silicalite-1 membrane. (2010). *AIChE Journal*, 10, 35-44.2

Xiao, J., & Wei, J. (1992). Diffusion mechanism of hydrocarbons in zeolites—I. Analysis of experimental observations. *Chemical Engineering Science*, 47, 1143-1159.

Xiao, J., & Wei, J. (1992). Diffusion mechanism of hydrocarbons in zeolites—I. Theory. *Chemical Engineering Science*, 47, 1123-1141.

Xomeritakis, G., Liu, N. G., Chen, Z., Jiang, Y.-B., Kohn, R., Johnson, P. E., Tsai, C.-Y., Shah, P. B., Khalil, S., Singh, S., & Brinker. C. J. (2007). Anodic alumina supported dual-layer microporous silica membranes. *Journal of Membrane Science*, 287, 157-161.

Xu, Q., Huang, D.-P., Chen, W., Lee, J.-H., Kim, B.-H., Wang, H., & Yuan, R.-Z. (2004). Influence of sintering temperature on microstructure and mixed electronic-ionic conduction properties of perovskite-type $La_{0.6}Sr_{0.4}Co_{0.8}Fe_{0.2}O_{3-\delta}$ ceramics. *Ceramics International*, 30, 429-433.

Xu, Q., Huang, D.-P., Chen, W., Lee, J.-H., Wang, H., & Yuan, R.-Z. Citrate method synthesis, characterization and mixed electronic-ionic conduction properties of $La_{0.6}Sr_{0.4}Co_{0.8}Fe_{0.2}O_{3-\delta}$ perovskite-type oxides. *Scripta Materialia*, 50, 165-170.

Yamaguchi, T., Niitsuma, T., Nair, B. N., & Nakagawa, K. (2007). Lithium silicate based membranes for high temperature CO_2 separation, *Journal of Membrane Science*, 294, 16-21.

Yamamoto, M., Kusakabe, K., Hayashi, J.-I., & Morooka, S. (1997). Carbon molecular sieve membrane formed by oxidative carbonization of a copolyimide film coated on a porous support tube. *Journal of Membrane Science*, 133, 195-205.

Yang, R. T. (1987). Gas separation and adsorption processes. Boston: Butterworths.

Yin, Q., & Lin, Y. S. (2007). Beneficial effect of order–disorder phase transition on oxygen sorption properties of perovskite-type oxides. *Solid State Ionics*, 178, 83-89.

Yoshioka, T., Nakanishi, E., Tsuru, T., & Asaeda, M. (2001). Experimental studies of gas permeation through microporous silica membranes. *AIChE Journal*, 57, 2052-2063.

Yuan, W., Hu, X., & Li, L. (2006). Preparation and characterization of single-phase perovskite $La_{0.6}Sr_{0.4}Co_{0.8}Fe_{0.2}O_{3-\delta}$. *Journal of Natural Gas Chemistry*, 15, 58-62.

Zawadzki, M., & Trawczyński, J. (2010). Synthesis, characterization and catalytic performance of LSCF perovskite for VOC combustion. *Catalysis Today*, doi:10.1016/j.cattod.2010.10.070.

Zhang, B., Shen, G., Wu, Y., Wang, T., Qiu, J., Xu, T., & Fu, C. (2009). Preparation and characterization of carbon membranes derived from poly(phthalazinone ether sulfone) for gas separation. *Industrial and Engineering Chemistry Research*, 48, 2886-2890.

Zhou, Z., Yang, J., Zhang, Y., Chang, L., Sun, W., & Wang, J. (2007). NaA zeolite/carbon nanocomposite thin films with high permeance for CO_2/N_2 separation. *Separation and Purification Technology*, 55, 392-395.

APPENDIX A

SYNTHESIS OF LANTHANUM STRONTIUM COBALT IRON OXIDE (LSCF) POWDER

1. To synthesize $La_xSr_{1-x}Co_yFe_{1-y}O_{3-\delta}$ powder, weight out the appropriate amount of nitrate metal precursors (shown in Table A.1) for 0.05 mol of product. This procedure details the production of LSCF powder in a 6:4:8:2 ratio. 50% excess citric acid is added with the nitrate metal precursors to ensure complete reaction. When weighing out chemicals, be sure to wear gloves, safety glasses, a lab coat, and a dust mask.

Table A.1 Constituents of $La_xSr_{1-x}Co_yFe_{1-y}O_{3-\delta}$ (6:4:8:2)

Material	Weight (g)
$La(NO_3)_3.6H_2O$	12.993
$Sr\ (NO_3)_2$	4.2362
$CO(NO_3)_3.6H_2O$	11.6416
$Fe(NO_3)_3.9H_2O$	4.0400
Citric Acid	38.5240

2. Dissolve the nitrate metal precursors and citric acid in 1000 mL of de-ionized water. Use a 1.5 or 2 L beaker.
3. Be sure that the ventilation system in the hood is working before proceeding any further. To commence the polymerization process, heat the solution on the hot plate to about 105^oC. Place a glass cover over the beaker to limit evaporation of water. Leave the solution at this temperature for about 4 hours.
4. Increase the temperature of the solution to 110^oC and remove the glass cover to promote a higher rate of evaporation. This is known as the condensation process and will last for at least 3-4 hours (if not more), depending on the temperature and amount of water added at the start of the process.
5. At the end of condensation process, a brownish/red, viscous gel-like substance should be obtained. To prevent the gel from burning, check the material

periodically and decrease heat or remove the beaker from the hotplate if necessary. Note: This step in the process will emit NO_x fumes into the hood. Be sure that the hood is ventilated properly and that the hood doors are closed to prevent the emission of these gases into the lab.

6. After getting a gel-like substance, remove it from the hotplate and place the beaker in furnace at 110°C for 24 hours. This will allow the gel to dry. Keep in mind that when you dry the material in the oven or furnace, it will rise quite a bit. So for the first hour of drying, continue to monitor the beaker every 5 minutes to ensure that it does not escape the beaker and make a mess.
7. After drying, self-ignition of the organic materials is performed at 400^{o}C for around 2 hours. Remove the material from the beaker and grind it for about 5 minutes to produce a powder. Perform grinding in a well ventilated space. Always wear gloves, safety glasses, and a dust mask along with your lab coat when grinding, as small particles from the mortar can be emitted as a result of vigorous grinding. Place the ground powder is a crucible for higher temperature treatments.
8. After self-ignition, calcination of the powder is performed at 600^{o}C for 5 hours or more if desired. Heating conditions for this set are listed in Table A.2.

Table A.2 Heating condition for calcination of LSCF powder

Temp. range [^{o}C]	50-600^{o}C	600^{o}C	600-50^{o}C
Time [hrs.]	10	20	10
Ramping Rate [^{o}C / hr.]	60	0	- 60

9. After calcination at 600°C, the material is removed from the crucible and placed into a mortar and ground for at least 20 minutes to arrive at a very fine powder. Safety precautions discussed in step 7 of this procedure for grinding should be followed here as well. The powder can then be pressed into disks and sintered to produce LSCF membranes or further processed to produce a combustion catalyst.

APPENDIX B

SYNTHESIS OF LANTHANUM STRONTIUM COBALT IRON OXIDE (LSCF) MEMBRANES

1. To prepare LSCF perovskite type membranes, LSCF powder is required. Please see the procedure in APPENDIX A on how to produce LSCF powder.
2. Before pressing the LSCF powder into disks, it is important to make sure that the powder has been ground for the appropriate amount of time. Normal grinding time is at 20-25 minutes. If regrinding is necessary, wear gloves, safety glasses, and a dust mask along with your lab coat, as small particles from the mortar can be emitted as a result of vigorous grinding
3. After grinding, the material is placed into the chosen mold. This procedure is specifically written for a stainless steel die-mold with a diameter of 2.921 cm (1.15 in).
4. Place approximately 3.5g of ground LSCF powder in the mold. Add 4-5 drops of 3 wt% PVA binder if necessary. Tap the sides of the mold to evenly distribute the powder. Be sure to wear safety glasses, gloves and a dusk mask throughout the entire pressing process to prevent inhalation of powder.
5. Put the mold in the hydraulic press. Close the safety door on the press and increase the load on the powder to 5000 lbs for about 1 minute. After this time, increase to load to 20,000 lbs and keep it at this value for about 5 more minutes.
6. Take the mold out of the press and carefully remove the pressed LSCF disk. The membrane should have some mechanical strength and not fall apart after removal.
7. After you have finished pressing all the disks, be sure to thoroughly clean the

molds so future use by other group members does not result in contamination of their sample(s).

8. The porosity of the membranes will depend on the temperature at which sintering takes place. Dense membranes are sintered at higher temperatures (i.e., 1200^{o}C) while porous membranes are sintered around 900^{o}C. When programming the furnace, make sure you know what type of membrane you are making.
9. When programming the furnace for sintering, the ramping rate to the target temperature should be 2^{o}C/min.
10. Program the furnace to remain at the target temperature for 24 hours. Finally, set the ramping rate for cooling to 2^{o}C/min and end the program once the furnace has cooled back down to 50^{o}C

APPENDIX C

DIRECT INFILTRATION OF MOLTEN CARBONATE IN LANTHANUM STRONTIUM COBALT IRON OXIDE (LSCF) MEMBRANES

1. The LSCF membranes can be infiltrated with molten carbonate to form the LSCF-carbonate dual-phase membrane. This process can be dangerous and should be done with the utmost care. To begin, molten carbonate should be placed into one of the crucible cups. The cup should be placed into the vertical tube furnace and heated to 500°C.
2. Always wear a lab coat and a protective face shield when working with the molten carbonate. It is best to use high temperature gloves for this purpose.
3. At 500°C, the molten carbonate will be a very hot liquid. As such, it is prone to spill if one bumps the vertical furnace hard enough. Spilling of the hot liquid could start a fire if spilled on paper, or burn you or another lab member. Therefore, you should do your best to keep from bumping the furnace and causing such incidents.
4. Suspend your membrane about 1-2 cm above the molten carbonate. Allow the membrane to preheat for 10-20 min.
5. Slowly raise the crucible using the designed apparatus at the bottom of the furnace. Once the liquid barely touches the bottom surface of the membrane, let it remain for 15 min. A good sign that infiltration is complete is when the top surface of the membrane has a shiny look to it.
6. Lower the molten carbonate until it is about 1-2 cm below the membrane. Slowly remove the membrane from the furnace. Removing too fast can cause thermal shock which can cause the membrane to break.
7. Allow the membrane to cool to room temperature

8. Remove any excess carbonates with SiC polishing paper.

APPENDIX D

HIGH TEMPERATURE TOTAL CONDUCTIVITY MEASUREMENT

1. Starting with a membrane (in disk form), grind it until you have a ceramic rectangle with dimensions about 2×10×16 mm. Four short silver wires (with 2-3 cm long ends) were wrapped around the sample and further adhered by a silver conductive paint.
2. The sample is loaded into the quartz tube and the four wires are connected to the silver wires within the system. The two outer wires on the bar are to be connected to the Potentiostat (Radiometer AIS, PG2O1). This device provides a direct electrical current through the sample bar. The inner wires are connected to a digital multimeter (Protek, B-845) which allows for measurement of the voltage drop in the bar.
3. Heat the system to 900^{o}C with a temperature ramping rate of 5^{o}C/min in air. This allows the silver wires on the bar to soften and, hence, provides better contact with the surface.
4. Introduce the gas or gases into the system (if necessary), under which the conductivity will be measured.
5. Set the internal voltage of Potentiostat at 0 mV, and keep at standby mode to wait for steady state of the sample in the gas flow.
6. When both the display of the Potentiostat E (free) and the multimeter voltage are zero at standby mode, measurements can be started. Usually it takes 3 hours to reach steady state conditions in a new gas environment and 30 minutes at a new temperature.

7. For measurements, set the Potentiostat in operation mode with the voltage of 100 mV. Note the current on the Potentiostat and the voltage value on the multimeter. The electrical resistance R of the inner section of the sample can be calculated using these two values (R = V/I). Using the length (L), width (w) and thickness (t), total conductivity σ can be calculated by the equation: σ = L/(wtR).

APPENDIX E

SEALING DUAL-PHASE MEMBRANES FOR HIGH TEMPERATURE PERMEATION

1. To seal the dual-phase membrane, a ceramic-based seal is necessary. The seal consists of the parent material (i.e., if you have an LSCF dual-phase membrane, use LSCF powder), ground Pyrex beaker glass and sodium aluminum oxide ($Al_2O_3 \cdot Na_2O$).
2. The parent powder (in this case, LSCF), should be sintered beforehand to the highest temperature that permeation experiments will be conducted. For example, if experiments will be conducted at 900°C, the powder should be sintered prior to use in the seal at the same temperature. Furthermore, to produce better seals, ball milling of the powder is recommended to reduce the particle size.
3. Mix 0.4 g LSCF powder (or whatever powder the membrane is composed of), 0.5 g of ground breaker glass and 0.10 g $Al_2O_3 \cdot Na_2O$. Grind the materials together using a mortar and pestle until the powders are well mixed and very fine.
4. Place the powder into a petri dish and add water one drop at a time. While adding water, continually mix it in with the powder. Keep adding water until the paste reaches a "ketchup-like" consistency.
5. Before sealing the membrane, ensure that it is smooth on the side which will be in contact with the seal. Use SiC grinding paper to smooth the surface. Also make sure that the ceramic tube that the membrane will be sealed to is also smoothed.

6. Spread a thin layer (1 mm thick) of the sealing paste on the ceramic tube and gently place the membrane on top. Firmly press down to ensure a tight seal is created with the paste between the ceramic tube and the membrane.
7. Apply paste to the outer portion of the tube/membrane interface to further enhance the seal.
8. Leave the seal to dry for at least 1 hour at room temperature.
9. After the seal has dried, gently remove any excess paste on the edges with SiC grinding paper. If necessary, another coat of the seal can be applied at this point.
10. Install this inner tube carefully into the permeation apparatus.
11. Heat the system to 900°C to allow the seal to set. Wait for 1 hour to search steady state. Use the GC to check for leakage through the seal. If no leaked persists, then a successful sealing has been obtained.
12. If a leak is present, try heating the system to a slightly higher temperature (i.e., 910°C) to see if the seal softens and sets at that temperature. Continue this method until achieving a good seal. If not achieved by 950°C, then it is best to shut the experiment down, as the seal is unlikely to improve from this point on.

APPENDIX F

SYNTHESIS OF NICKEL BASED REFORMING CATALYST

1. To prepare the nickel (Ni) based reforming catalyst by the wet-impregnation method, weigh out appropriate amounts of $Ni(NO_3)_2 \cdot 6H_2O$ and γ-Al_2O_3.
2. To produce 0.0172 mol of the 10% Ni/γ-alumina catalyst (by weight), 5.055 g of $Ni(NO_3)_2 \cdot 6H_2O$ and 9.0 g of γ-Al_2O_3 were weighed out, respectively.
3. The γ-Al_2O_3 material was used as a support for nickel. The material came in pellet form, hence it needed to be ground with a mortar and pestle before use. To produce a fine catalyst, the alumina powder was sieved with a #80 sieve. This would ensure that all particles used during wet-impregnation were 180 μm or less.
4. The sieved alumina powder and $Ni(NO_3)_2 \cdot 6H_2O$ were dissolved in 25 ml of de-ionized water by vigorous stirring.
5. Heat the solution on a hot plate to 80°C to allow the excess water to evaporate.
6. Dry the resulting slurry at 110-120°C for 24 hours.
7. After drying, grind the dried sample with a mortar and pestle for 10 minutes.
8. Once the material has been completely reground, calcine the powder sample for 4 hours at 700°C (ramp rate = 5°C/min).
9. Remove the powder from the furnace and grind it once more. Place the powder in an elongated crucible and into a tube furnace for reduction. Reduce the sample in a 10% H_2/He gas mixture for 6 hours at 600°C (ramp rate = 5°C/min). After reduction, the catalyst should be grey in color. If areas of green/blue remain, continue reduction for an additional 6 hours.

APPENDIX G

SYNTHESIS OF LANTHANUM STRONTIUM COBALT IRON OXIDE (LSCF) COMBUSTION CATALYST

1. To synthesize $La_{0.6}Sr_{0.4}Co_{0.8}Fe_{0.2}O_{3-\delta}$ powder for use as a combustion catalyst, the same procedure used to produce the powder in APPENDIX A should be followed.
2. After the power has been calcined at 600C, it should be ground and then sintered at 900°C for 24 hours. Use ramp rates of 2°C/min.
3. After sintering, the powder should be transferred to the Teflon tumbler. Up to 25% of powder will be lost in the extraction process, so keep that in mind when deciding how much powder to place in the tumbler. After adding the powder, mix in ethanol or isopropyl alcohol. Add enough of the liquid to create slurry.
4. Add zirconia balls to the tumbler. To produce the smallest particles possible, use the smallest zirconia balls available.
5. Seal the tumbler tightly and ball mill for 24-48 hours.
6. After ball milling, remove as much of the slurry as possible from the tumbler. This is a messy and painstaking process. Use excess ethanol or isopropyl alcohol to help remove the slurry.
7. Transfer the liquid/powder mixture to a breaker and heat at 60-70°C until all of the solvent has evaporated.
8. Remove the dried powder from the beaker and grind it once more. The powder is now ready for use as the combustion catalyst.

APPENDIX H

STEADY STATE HELIUM PERMEATION

1. Make sure that the helium cylinder (2) or whatever gas you plant to use is properly attached and the pressure is set to no higher than 40 psi. Note: The numbers in ( ) refer to locations in Figure H.1
2. Put the membrane in the permeation cell (7). Be sure to tighten the cell such that the o-rings within seal the membrane properly. However, sealing too tight can also cause the membrane to break, so find the correct balance between the two.
3. Close valve B fully and open valves A and C fully.
4. Check for leakage of the gas at all tube connections. This can be done by using a soap solution (or Snoop) and placing a few drops at each point of connection. If no bubbles form, there is no significant leak.
5. Set the mass flow controller to the appropriate flow rate. A13 α-alumina membranes will require high flow rates (100 mL/min). A15 and A16 α-alumina membranes use lower flow rates (10-20 mL/min).
6. Flip the switch on the pressure sensor (5) to the up position marked as 2 on the box. This reading tells us the ΔP (gauge pressure difference) across the membrane. If this reading is below 2.5 psi, continue to step 7. If the value shown is above 2.5 psi, skip to step 19.
7. The position marked 1 on the pressure sensor (5) gives the gauge upstream pressure (P_h)
8. Let the system equilibrate for about an hour or until there is no noticeable change in the system's conditions for an extended period of time.

9. Measure the flow rate of helium in the system three times with a bubble flow meter (8).
10. Record ΔP and P_h.
11. Close valve C ten turns and repeat steps 8-10.
12. Close valve C one turn and repeat steps 8-10.
13. Close valve C one turn and repeat steps 8-10.
14. Close valve C one-half turn and repeat steps 8-10.
15. Close valve C one-half turn and repeat steps 8-10.
16. Close valve C one-quarter turn and repeat steps 8-10.
17. Close valve C one-quarter turn and repeat steps 8-10.
18. When you are done, turn the helium cylinder (2) off and remove the membrane from the permeation cell.
19. Open valves A and B to vent the system so the pressure sensor will not be damaged (especially important for those testing membranes with a small pore size).
20. After venting, close valve A, then do the same to valve B.
21. Set the mass flow controller to channel 1 and set the value to 20%.
22. Let the system equilibrate for about an hour or until there is no noticeable change in the system's conditions for an extended period of time.
23. Measure the flow rate of helium in the system THREE times with a bubble flow meter (8)

24. Measure ΔP and P_h by flipping from position 1 to position 2 on the pressure sensor (5).
25. Repeat steps 22-24 with the mass flow controller on channel 1 for values of 40%, 60%, 80% and 100%.
26. When you are done, turn the helium cylinder (2) off and remove the membrane from the permeation cell.

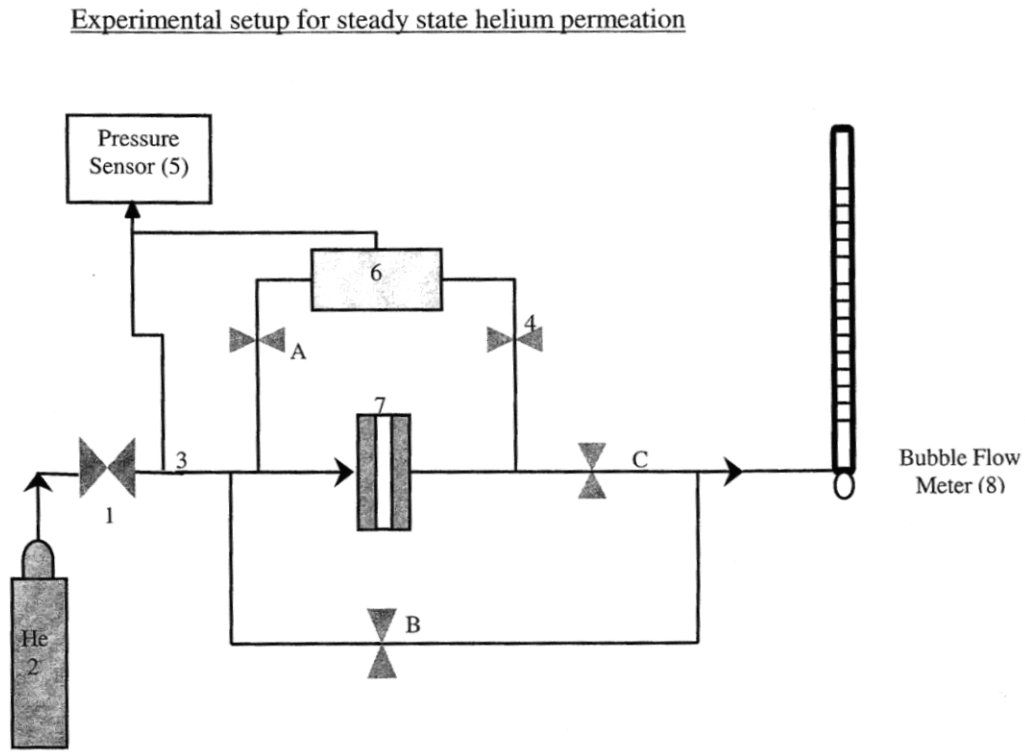

Figure H.1 Steady state permeation diagram

APPENDIX I

UNSTEADY STATE HELIUM PERMEATION

1. Mount the membrane in the stainless steel permeation cell (PC). Be sure that each side of the membrane is sealed with a rubber (Viton, Buna etc.) o-ring. A schematic of the unsteady state system can be found in Figure I.1.
2. Completely seal the membrane by tightening the bolts around the edges.. However, do not tighten the cell so much that is causes your membrane to break
3. Evacuate the system with the vacuum pump. Leave the vacuum pump on until the pressure in the system reaches a minimum value. At this point, close the valves to seal the system under the vacuum
4. Once finished using the vacuum pump, turn it off. Leaving it on can cause the pump to either overheat or emit fumes into the surrounding area.
5. Before gathering permeance data, it is a good idea to check and make sure that there is no leak within the permeation cell by isolating the permeation cell. Let the system set for a couple of minutes and monitor the pressure readout (PR). If the pressure does not change or the change is very minimal, then there is no leak and you can proceed to check the permeance of the membrane.
6. Open the valve which will allow helium gas to enter the system. Increase or decrease the pressure in the system by adjusting the flow rate of helium in the system. Monitor the upstream pressure gauge until the pressure in the system has reached the desired value.
7. On the computer that is attached to the unsteady state system, open Labview.

8. Type in a name that you want to save the file as. Keep in mind, it is usually a good idea to indicate some important parameters in the test file, such as the permeating gas, the gauge pressure of the system and the temperature at which the test was conducted.
9. Indicate the desired time step for data collection
10. Click $\rightarrow$ and after about 1 second, open the valve to let the helium gas permeation through the membrane. Allow the system to take data for as long as it is necessary to gain an accurate measure of dP/dt, which is the slope of the line in the Labview window. Stop collecting data by clicking the red stop sign in the Labview window.
11. Export the data to a program, such as Excel, and graph it. Fit a line to the data and get the slope. As mentioned previously, the slope of this line is the dP/dt. Be sure to remember that dP/dt from this data is in units of mmHg/s.
12. Using the following equation, one can solve for the permeance of the membrane:

$$Q = \left(\frac{dP}{dt}\right)\left(\frac{V_c}{S \cdot R \cdot T \cdot (P_h - P_l)}\right)$$

where Q is the permeance (*usually in moles/$m^2 \cdot Pa \cdot s$*), dP/dt is change in pressure versus time, V_c is volume of the cylinder (*in this case, the cylinder is 1L or $10^{-3} m^3$*), S is the area of the membrane, R is the gas constant and T is temperature. P_h and Pl represent the up and downstream pressures. In this case, downstream pressure is assumed to be 0 (vacuum).

13. After completing all of the necessary experiments, be sure to relieve the pressure on the system. To do this, shut off the helium to the system and open all valves to the atmosphere.

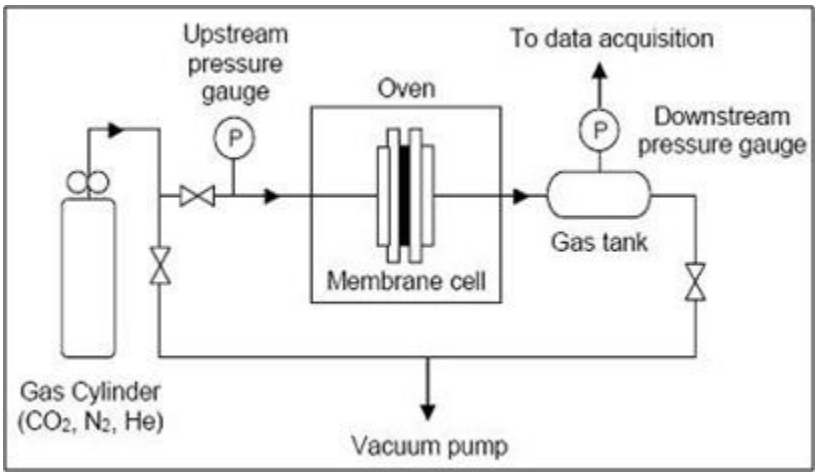

Figure I.1 Unsteady state helium permeation diagram

APPENDIX J

DEVELOPMENT OF ORIGINAL MODEL FOR CO2 PERMEATION

A theoretical model was developed to help describe and predict high temperature CO_2 permeation through the LSCF dual-phase membrane. The step by step methodology used to develop the model is described here, beginning with the fluxes of the two charged species of interests in the dual-phase membrane, $CO_3^{=}$ and $O^{=}$, denoted as 1 and 2 respectively. A geometric factor, ϕ, has been added to solid phase to account for the effect of support porosity.

$$J_1 = -\frac{\sigma_1}{z_1^{\,2}F}\left(\nabla\mu_1 + z_1F\nabla\phi_1\right) \tag{J.1}$$

$$J_2 = -\frac{\phi\sigma_2}{z_2^{\,2}F}\left(\nabla\mu_2 + z_2F\nabla\phi_2\right) \tag{J.2}$$

Since there is no external current for the dual-phase membrane, the charge within the system remains balanced:

$$z_1J_1 + z_2J_2 = 0 \tag{J.3}$$

Combination of Equations J.1-J.3 provides:

$$J_1 = -\frac{\phi\sigma_1\sigma_2}{\left(\sigma_1+\sigma_2\right)z_1^{\,2}F^2}\left(\nabla\mu_1 - \frac{z_1}{z_2}\nabla\mu_2\right) \tag{J.4}$$

Since $z_1 = z_2$, the Equation 4 becomes:

$$J_1 = -\frac{\phi\sigma_1\sigma_2}{\left(\sigma_1+\sigma_2\right)z_1^{\,2}F^2}\left(\nabla\mu_1 - \nabla\mu_2\right) \tag{J.5}$$

Before going further, it is important to define a geometric correction factor, ϕ. Theoretical equations used to model the ionic conductivity of LSCF assume that the material is dense. However, the structure of LSCF used in the dual-phase membrane is composed of a highly porous and tortuous network of

pores. The geometric correction factor is used to relate the conductivities (electronic and ionic) in a dense material to that in a porous material:

$$J_1 = -\frac{\phi\sigma_1\sigma_2}{(\phi\sigma_1 + \sigma_2)z_1^{\,2}F^2}(\nabla\mu_1 - \nabla\mu_2) \tag{J.6}$$

The reaction that governs separation of CO_2 for the dual-phase membrane in a low P_{O_2} environment can be used to relate the chemical potentials of the charged species present. The governing equation for permeation must be solved for CO_2:

$$CO_2 = CO_3^{=} - O^{=} \tag{J.7}$$

$$\nabla\mu_{CO_2} = \nabla\mu_{CO_3^{=}} - \nabla\mu_{O^{=}} = \nabla\mu_1 - \nabla\mu_2 \tag{J.8}$$

Combining Equations J.6 and J.8 simplifies to:

$$J_1 = -\frac{\phi^2\sigma_1\sigma_2}{\phi(\sigma_1 + \sigma_2)z_1^{\,2}F^2}(\nabla\mu_{CO_2}) \tag{J.9}$$

The chemical potential ($\nabla\mu_i$) and thermodynamic factor (i_f) are defined as:

$$\nabla\mu_i = \frac{RT}{c_i}\left(\frac{\partial \ln a_i}{\partial \ln c_i}\right)\nabla c_i \tag{J.10}$$

$$fi = \frac{\partial \ln a_i}{\partial \ln c_i} \tag{J.11}$$

By combining Equations J.10 and J.12, the chemical potential of CO_2 can be written as:

$$\nabla\mu_{CO_2} = \frac{RT}{c_{CO_2}} f_{CO_2}\nabla c_{CO_2} \tag{J.12}$$

To simplify matters, it is assumed that this system follows ideal thermodynamic behavior; therefore, the value of f_{CO_2} can be assumed to be 1. Finally, Equation J.7 states that $J_{CO_3^{=}}$ equals J_{CO_2}:

$$J_{CO_2} = -\frac{\phi\sigma_1\sigma_2}{(\sigma_1+\sigma_2)z_1^{\,2}F^2}\left(\frac{RT}{c_{CO_2}}\nabla c_{CO_2}\right) \tag{J.13}$$

The CO_2:Ar ratio of gas in the feed is 1:1. From the ideal gas law, the concentration and change in concentration of carbon dioxide can be written as:

$$c_{CO_2} = \frac{1}{2}\left(\frac{P_t}{RT}\right) \tag{J.14}$$

$$\nabla c_{CO_2} = \frac{1}{2}\left(\frac{1}{RT}\right)\left(\frac{dP_{CO_2}}{dL}\right) \tag{J.15}$$

Insertion of Equations J.14 and J.15 into J.13 beholds:

$$J_{CO_2} = -\frac{RT\phi\sigma_1\sigma_2}{(\sigma_1+\sigma_2)z_1^{\,2}F^2}\frac{1}{P_{CO_2}}\left(\frac{dP_{CO_2}}{dL}\right) \tag{J.16}$$

To integrate, it is assumed that σ_1 and σ_2 are independent of P_{CO_2}.

$$\int_0^L J_{CO_2}\,dL = -\int_{P'_{CO_2}}^{P''_{CO_2}} \frac{RT\phi\sigma_1\sigma_2}{(\sigma_1+\sigma_2)z_1^{\,2}F^2}\left(\frac{dP_{CO_2}}{P_{CO_2}}\right) \tag{J.17}$$

P'_{CO_2} and P''_{CO_2} are the upstream and downstream partial pressures of CO_2. Integration yields:

$$J_{CO_2} = -\frac{RT\phi\sigma_1\sigma_2}{(\sigma_1+\sigma_2)z_1^{\,2}F^2L}\ln\left(\frac{P''_{CO_2}}{P'_{CO_2}}\right) \tag{J.18}$$

The ionic conductivity of $CO_3^{=}$ (σ_1) is much greater than the ionic conductivity of the oxide ion, $O^{=}$ (σ_2), leading to the following simplification:

$$J_{CO_2} = -\frac{RT\phi\sigma_2}{z_1^{\,2}F^2L}\ln\left(\frac{P''_{CO_2}}{P'_{CO_2}}\right) \qquad \text{(J.19)}$$

Equation J.19 reports the particle flux of CO_2 in $mol\cdot cm^{-2}\cdot s^{-1}$. However, it is desired to report the data in terms of high temperature permeance. To convert to units of $mol\cdot m^{-2}\cdot s^{-1}\cdot Pa^{-1}$, the pressure difference between the upstream and downstream side of the membrane (ΔP_{CO_2}) and the porosity/tortuosity factor (ε/τ). Finally, Equation J.20 predicts the theoretical high temperature permeance of CO_2 through the dual-phase membrane as a function of temperature, membrane thickness and the up and downstream partial pressures of CO_2:

$$F_{CO_2} = -\left(\frac{\varepsilon}{\tau}\right)\frac{RT\phi\sigma_2}{\Delta P_{CO_2} z_1^{\,2}F^2L}\ln\left(\frac{P''_{CO_2}}{P'_{CO_2}}\right) \qquad \text{(J.20)}$$